EFFECTS OF DETAILED FINITE RATE CHEMISTRY IN TURBULENT COMBUSTION

A Dissertation
Presented to
The Academic Faculty

by

Suo Yang

In Partial Fulfillment
of the Requirements for the Degree
of Doctor of Philosophy in the
School of Aerospace Engineering

Georgia Institute of Technology
August 2017

EFFECTS OF DETAILED FINITE RATE CHEMISTRY IN TURBULENT COMBUSTION

Approved by:

Dr. Wenting Sun, Advisor
School of Aerospace Engineering
Georgia Institute of Technology

Dr. Yiguang Ju
Department of Mechanical and Aerospace Engineering
Princeton University

Dr. Vigor Yang, co-Advisor
School of Aerospace Engineering
Georgia Institute of Technology

Dr. Yingjie Liu
School of Mathematics
Georgia Institute of Technology

Dr. Suresh Menon
School of Aerospace Engineering
Georgia Institute of Technology

Date Approved: May 05, 2017

To my parents and wife for their love, encouragement, and support

ACKNOWLEDGEMENTS

I would like to thank my thesis advisors, Dr. Wenting Sun and Dr. Vigor Yang for their precious guidance and continuous support throughout the course of my Ph.D. Working with them, as one of their disciples, has been a pleasant and memorable experience.

Thanks also to Dr. Suresh Menon, Dr. Yiguang Ju, and Dr. Yingjie Liu for their invaluable help and encouragement on my research for the past years, and for serving on my thesis committee and providing helpful suggestions on my work.

Special thanks to Dr. Sharath Nagaraja, Dr. Reetesh Ranjan, and Dr. Xingjian Wang for the time and energy they have spent with me for many enlightening discussions and enormous help. I would like to thank my co-authors, Dr. Alexander Kurganov, Dr. Joseph K. Lefkowitz, Dr. Hongfa Huo, Xiang Gao, Weiqi Sun, and Aric Rousso for the great collaboration.

I would also like to thank my colleagues and friends, Dr. Yanxing Wang, Dr. Liwei Zhang, Dr. Prashant Khare, Dr. Dilip Sundaram, Shine Xiaomeng Zhai, Xiaohang Yuan, Ximing Gao, Zhihang Liu, Chung-Han Wu, Murali Gopal Muraleedharan, Christopher Lioi, Shiang-Ting Yeh, Travis Smith, Principio Tudisco, Yixing Li, Yu-Hung Chang, Phoebe Yao Zhang, Bin Wu, Miad Karimi, Umesh Unnikrishnan, Achyut Panchal, Simon Tsz Fung Mak, Peter Chao Ma, and Hao Wu for many discussions and wonderful times.

I would like to thank the following sponsors: Georgia Institute of Technology, Federal Aviation Administration, National Aeronautics and Space Administration, Department of Energy, and Air Force Office of Scientific Research.

My deepest appreciation goes to my parents, Zhigang Yang and Lanping Liang, and to my wife, Yuan Wang, for their love and support.

TABLE OF CONTENTS

ACKNOWLEDGEMENTS ..... **iv**

LIST OF TABLES ..... **viii**

LIST OF FIGURES ..... **ix**

LIST OF SYMBOLS AND ABBREVIATIONS ..... **xiv**

SUMMARY ..... **xviii**

CHAPTER 1 INTRODUCTION **1**

1.1 Background and Motivation 1
1.2 Literature Review 4
1.2.1 Reduction of Detailed Chemical Kinetics Mechanisms 4
1.2.2 Stiff ODE Solvers 6
1.2.3 Turbulence/Combustion Interaction Models 6
1.2.4 Analysis Tool for Combustion Simulation Results 8
1.3 Research Objectives 10
1.4 Dissertation Outline 11

CHAPTER 2 THEORETICAL FRAMEWORK **12**

2.1 Governing Equations 12
2.2 Finite Rate Chemistry 14
2.3 Thermo-physical Properties 15
2.3.1 Equation of State (EOS) 15
2.3.2 Thermodynamic Properties 16
2.4 Transport Properties 17
2.4.1 Dynamic Viscosity and Thermal Conductivity 17
2.4.2 Binary Mass Diffusivity 18

CHAPTER 3 NUMERICAL FRAMEWORK **20**

3.1 Direct Numerical Simulation 20
3.1.1 Compressible Reacting Flow Solver 21
3.2 Larger Eddy Simulation 21
3.2.1 Filtered Governing Equations 23
3.2.2 Subgrid-Scale Models 25
3.2.3 Turbulence/Combustion Interaction Models 29
3.2.4 Preconditioning Scheme 36
3.2.5 Spatial Discretization 44
3.2.6 Temporal Discretization 58
3.3 Boundary Conditions 60
3.3.1 Characteristic Boundary Conditions 60

3.4 Parallel Implementation 64

CHAPTER 4 EFFICIENT APPROACHES TO SIMULATE FINITE RATE CHEMISTRY 66

4.1 Point-Implicit Stiff ODE Solver (ODEPIM) 66
4.2 Correlated Dynamic Adaptive Chemistry (CoDAC) 69
4.2.1 Path Flux Analysis (PFA) Method for Kinetic Mechanism Reduction 69
4.2.2 Space-Time Correlations 71
4.3 Correlated Evaluation of Transport Properties (CoTran) 74

CHAPTER 5 NUMERICAL VERIFICATION 77

5.1 Laminar Plasma Discharge of Gas Mixture 77
5.1.1 Introduction 78
5.1.2 Theoretical Framework 81
5.1.3 Results and Discussions 85
5.1.4 Conclusion 95
5.2 Turbulent Premixed Flame 96
5.2.1 Introduction 97
5.2.2 Theoretical Framework 99
5.2.3 Results and Discussions 101
5.2.4 Conclusion 110
5.3 Turbulent Non-premixed Flame 111
5.3.1 Introduction 111
5.3.2 Physical Model and Flow Conditions 113
5.3.3 Chemical Kinetics Models 116
5.3.4 Results and Discussions 116
5.3.5 Conclusion 122

CHAPTER 6 EXPERIMENTAL VALIDATION AND COMPARISON OF FINITE RATE AND FLAMELET MODELS 123

6.1 Introduction 123
6.2 Theoretical Framework 128
6.2.1 Physical Configurations: Sandia Flame D 128
6.2.2 Boundary Conditions 129
6.2.3 Combustion Chemistry 130
6.3 Results and Discussions 131
6.3.1 Performance Analysis 131
6.3.2 Spatial Distribution 134
6.3.3 Axial Profiles 139
6.3.4 Radial Profiles 143
6.3.5 Conditional Statistics 146
6.4 Conclusion 152

CHAPTER 7 SENSITIVITY OF PREDICTIONS TO CHEMICAL KINETICS . 154

7.1 Introduction 155
7.2 Physical Model and Flow Conditions 155
7.3 Chemical Kinetics Models 156
7.4 Results and Discussions 158
7.4.1 Instantaneous Reacting Flow Features 158
7.4.2 Comparison of the Two Kinetics Models 160
7.4.3 Global Pathway Analysis (GPA) 193
7.5 Conclusions 196

CHAPTER 8 CONCLUSIONS 199

CHAPTER 9 FUTURE RECOMMENDATION 204

9.1 More Efficient Approaches to Simulate Finite Rate Chemistry 204
9.2 Future Development of FRC and FGM Models 205
9.3 Better Selection and Global Reduction of Chemical Kinetics 208

REFERENCES 209

LIST OF TABLES

Table 5.1: Speed up and saving of total CPU time by five combinations of new methods w.r.t. VODE with detailed kinetics. 88

Table 5.2: Average time per step for different components of total CPU time and their percentages during the simulation of ODEPIM+CoDAC+CoTran framework. 93

Table 5.3: CPU time distribution of the four methods..... 104

Table 5.4: $\boldsymbol{L2}$ and $\boldsymbol{L\infty}$ errors of the three frameworks. 108

Table 5.5: Simulation case of a canonical temporally evolving non-premixed flame.... 114

Table 5.6: Errors of CoDAC and CoTran at Local Extinction ($\boldsymbol{20\ tj}$) and Re-ignition ($\boldsymbol{40\ tj}$). 121

Table 6.1: Flow boundary conditions of Sandia Flame D. 129

Table 7.1: Statistics of the PDF of temperature on the stoichiometric surface ($\boldsymbol{Zst}$) for the two chemical kinetics models. 162

Table 7.2: Maximal (over time) deviations/errors of the 11-species model (11-sp), GRI-Mech 3.0 using CoDAC+CoTran, and GRIred11, with respect to GRI-Mech 3.0. Mean values of temperature and mass fractions of representative species on the stoichiometric surface. 164

Table 7.3: Contribution from the global reduction of reaction pathways to the maximal (over time) absolute deviations between GRI-Mech 3.0 and 11-species model; absolute deviation magnification factors for (a) global reduction of reaction pathways, (b) different reaction rate coefficients, and total. Based on mean values of temperature and mass fractions of representative species on the stoichiometric surface. 168

Table 7.4: Maximal (over mixture fraction Z) deviations/errors of the conditional means in the 11-species model (11-sp), GRI-Mech 3.0 using CoDAC+CoTran, and GRIred11, with respect to GRI-Mech 3.0: temperature and mass fractions of representative species. 178

Table 7.5: Contribution from the global reduction of reaction pathways to the maximal (over mixture fraction Z) absolute deviations between GRI-Mech 3.0 and the 11-species model; absolute deviation magnification factors for (a) global reduction of reaction pathways, (b) different reaction rate coefficients, and total. Temperature and mass fractions of representative species. 181

Table 7.6: Statistics of non-normalized PDFs of scalar dissipation rate on stoichiometric surface ($\boldsymbol{Zst}$) from the two chemical kinetics models. 189

LIST OF FIGURES

Figure 3.1: Schematic of three-dimensional computational cell 45

Figure 3.2: Schematic diagram of the stencil used in evaluating inviscid flux terms in the plane. 49

Figure 3.3: Schematic diagram for a three-dimensional auxiliary cell. 50

Figure 3.4: Schematic of a two-dimensional sub-domain with ghost cells. 65

Figure 4.1: Flow chart of the point-implicit stiff ODE solver (ODEPIM). 68

Figure 4.2: Flow chart of PFA method for kinetic mechanism reduction. 71

Figure 4.3: Flow chart of the time-space correlation algorithm in CoDAC method. 72

Figure 5.1: Geometry of the simulation model for plasma discharge of gas mixtures. 83

Figure 5.2: Gaussian fit to experimental pulse waveform used in simulation. 84

Figure 5.3: Temporal evolution of active species number (green solid line) and gap voltage (blue dashed line) at the center of discharge gap. 86

Figure 5.4: Spatial distribution of active species number. 87

Figure 5.5: Temporal evolution of CPU time speed up of kinetic source term by CoDAC method (blue dashed line), and that of active species number (green solid line) at the center of discharge gap. 89

Figure 5.6: Comparison of average CPU time distribution per time step of VODE, VODE+CoDAC, ODEPIM+CoDAC, and ODEPIM+CoDAC+CoTran. 90

Figure 5.7: Temporal evolution of different components of CPU time per time step other than kinetics and transport properties during the simulation of ODEPIM+CoDAC+CoTran framework. 92

Figure 5.8: Comparison of VODE (blue solid line), VODE+CoDAC (green dashed line), ODEPIM (red dash-dot line), ODEPIM+CoDAC (cyan dotted line), ODEPIM+CoTran (magenta solid line with cycle), and ODEPIM+CoDAC+CoTran (gold dashed line with cycle) for the temporal evolution of C_2H_2, CH_4, H_2O, and gas temperature. 94

Figure 5.9: Comparison of VODE with detailed chemistry (solid line) and ODEPIM+CoDAC+CoTran (dashed line) for spatial distribution of C_2H_2, CH_4, H_2O, and gas temperature. Blue: 1^{st} pulse; green: 15^{th} pulse; red: 50^{th} pulse; cyan: 100^{th} pulse; magenta: 150^{th} pulse. 95

Figure 5.10: A canonical turbulent premixed flame configuration. 101

Figure 5.11: Spatial distribution of the number of active species at the center plane (z = 0.75 cm). 102

Figure 5.12: Average CPU time distribution per cell per step ($\boldsymbol{\mu s}$) for four methods (from left to right): DVODE, ODEPIM, ODEPIM+CoDAC, and ODEPIM + CoDAC + CoTran. 103

Figure 5.13: Left: weak scaling of the speed-up (w.r.t. DVODE) of the three new frameworks; right: strong scaling of ODEPIM+CoDAC+CoTran. 104

Figure 5.14: Temperature (upper) and vorticity (lower) at the center plane (z = 0.75 cm) using conventional DNS (left) and proposed framework (right). 105

Figure 5.15: Mass fraction (upper) and reaction rate (lower) of fuel at the center plane (z = 0.75 cm) from conventional DNS (left) and proposed framework (right). 106

Figure 5.16: Stream-wise profiles of spatially-averaged scaled temperature, fuel mass fraction, and fuel reaction (In the legend, OAK=CoDAC). 107

Figure 5.17: PDF profiles of mass fraction (upper left) and reaction rate (lower left) of fuel, mass fraction (upper right) and absolute reaction rate (lower right) of OH. In the legend, OAK=CoDAC. 107

Figure 5.18: Relative errors of ODEPIM+CoDAC+CoTran at the mean flame plane (x = 0.75 cm). 109

Figure 5.19: Spatial (left) and temporal (right) distribution of errors of ODEPIM+CoDAC+CoTran. 110

Figure 5.20: Schematic of the canonical temporally evolving non-premixed flame. 113

Figure 5.21: Grid convergence test: comparison of GRI-Mech 3.0 (blue) and 11-species model (red) by the conditional means (left) and spatially averaged transverse profiles (right) of T (top), and mass fractions of H_2O (middle) and H (bottom), using grids of $\mathbf{256 \times 512 \times 128}$ (resolution of ~2$\boldsymbol{\eta}$: solid line) and $\mathbf{128 \times 256 \times 64}$ (resolution of ~4$\boldsymbol{\eta}$: dashed line) at $\mathbf{15}\boldsymbol{tj}$ 115

Figure 5.22: (a) Comparison of computational time use distribution for benchmark and CoDAC+CoTran ('New'); (b) 2D contours of active species number at local extinction ($\mathbf{20}\ \boldsymbol{tj}$). 117

Figure 5.23: Comparison of benchmark and CoDAC+CoTran ('New') at centerline of computational domain under local extinction ($\mathbf{20}\ \boldsymbol{tj}$) for (a) temperature, (b) vorticity magnitude, (c) mass fraction of OH, and (d) reaction rate of OH. 118

Figure 5.24: (a) PDF of mass fraction errors of OH under local extinction ($\boldsymbol{20\ tj}$), and (b) temporal evolution of relative $\boldsymbol{L2}$ errors of temperature, vorticity magnitude, and mass fraction of OH through 3D computational domain for CoDAC+CoTran..... 120

Figure 5.25: Transverse variation of mass fraction (left) and reaction rate (right) of OH on five arbitrary transverse lines at local extinction ($\boldsymbol{20\ tj}$). 121

Figure 6.1: Numerical verification of GRIred20 by homogeneous auto-ignition delays. 130

Figure 6.2: Numerical verification of GRIred20 by extinction curves in the perfectly stirred reactor. 131

Figure 6.3: Instantons spatial distribution of numbers of active species (upper) and reactions (lower), generated from the CoDAC method with the FRC-LES approach. .. 132

Figure 6.4: Average computation time distribution of the four models: FPV, Frozen (multi-species transport equations without chemical kinetics source terms), New (new FRC model using ODEPIM and CoDAC), Old (conventional FRC model using DVODE). 133

Figure 6.5: Time-averaged temperature distribution from the FRC-LES approach (left) and the FPV-LES approach (right). 135

Figure 6.6: Instantaneous temperature distribution from the FRC-LES approach (left) and the FPV-LES approach (right) at a same time. 136

Figure 6.7: Instantaneous $\boldsymbol{YOH}$ distribution from the FRC-LES approach (left) and the FPV-LES approach (right) at a same time. 137

Figure 6.8: Instantaneous $\boldsymbol{YCO}$ distribution from the FRC-LES approach (left) and the FPV-LES approach (right) at a same time. 138

Figure 6.9: Axial profiles of mean (left) and RMS (right) of temperature (upper) and $\boldsymbol{YOH}$ (lower), from the experiment, the FRC-LES approach, and the FPV-LES approach. 141

Figure 6.10: Axial profiles of mean (left) and RMS (right) of mixture fraction (upper) and progress variable (lower), from the experiment, the FRC-LES approach, and the FPV-LES approach. 143

Figure 6.11: Radial profiles of time-averaged temperature at x/d = 7.5 (upper-left), 15 (upper-right), 30 (lower-left), 45 (lower-right), from the experiment, the FRC-LES approach, and the FPV-LES approach. 144

Figure 6.12: Radial profiles of time-averaged mixture fraction at x/d = 7.5 (upper-left), 15 (upper-right), 30 (lower-left), 45 (lower-right), from the experiment, the FRC-LES approach, and the FPV-LES approach. 145

Figure 6.13: Conditional average of temperature at x/d = 7.5 (upper-left), 15 (upper-right), 30 (lower-left), 45 (lower-right), from the experiment, the FRC-LES approach, and the FPV-LES approach. 148

Figure 6.14: Conditional average of $\boldsymbol{YH2O}$ at x/d = 7.5 (upper-left), 15 (upper-right), 30 (lower-left), 45 (lower-right), from the experiment, the FRC-LES approach, and the FPV-LES approach. 149

Figure 6.15: Conditional average of $\boldsymbol{YCH4}$ at x/d = 7.5 (upper-left), 15 (upper-right), 30 (lower-left), 45 (lower-right), from the experiment, the FRC-LES approach, and the FPV-LES approach. 150

Figure 6.16: Conditional average of $\boldsymbol{YCO}$ at x/d = 7.5 (upper-left), 15 (upper-right), 30 (lower-left), 45 (lower-right), from the experiment, the FRC-LES approach, and the FPV-LES approach. 151

Figure 7.1: Comparison of GRI-Mech 3.0 and the 11-species model by (a) homogeneous ignition delay times, (b) extinction curves in the perfectly stirred reactor, and (c) laminar flame speeds. 158

Figure 7.2: Contours of OH mass fraction overlaid with stoichiometric mixture fraction (upper) and vorticity magnitude (lower) in 3D computational domain at local extinction ($\boldsymbol{20\,tj}$, left) and re-ignition ($\boldsymbol{40\,tj}$, right) from GRI-Mech 3.0. 160

Figure 7.3: (a) Temporal evolution of mean temperature on the stoichiometric surface obtained from GRI-Mech 3.0 and 11-species model; (b) PDF of temperature on the stoichiometric surface at local extinction ($\boldsymbol{20\,tj}$) and re-ignition ($\boldsymbol{40\,tj}$) from GRI-Mech 3.0 and 11-species model. 161

Figure 7.4: Temporal evolution of mean temperature on the stoichiometric surface obtained from 11-species model with $\pm\mathbf{5}\%$ perturbations to initial temperatures. 163

Figure 7.5: Instantaneous 2D contours of temperature at $\boldsymbol{20\,tj}$ (left) and $\boldsymbol{40\,tj}$ (right) on center plane (Z = 4H); GRI-Mech 3.0 (upper) and 11-species model (lower). 170

Figure 7.6 Comparison of GRI-Mech 3.0 (solid line) and 11-species model (dashed line) in 1D steady laminar solutions (initial data and laminar flamelet values at extinction) and 3D turbulent simulations (at $\boldsymbol{20tj}$ and $\boldsymbol{40tj}$): the conditional means of (a) T, (b) Y_{OH}, (c) Y_O, and (d) Y_H. 171

Figure 7.7 Comparison of GRI-Mech 3.0 (red solid line) and 11-species model (blue dashed line) in 3D turbulent simulations (at $40\boldsymbol{tj}$): conditional statistics of heat release rate 172

Figure 7.8 Mass fractions of (a) CO, (b) H_2, (c) CO_2, and (d) H_2O, in 1D steady laminar solution (initial data and laminar flamelet values at extinction) and 3D turbulent simulations (at $\boldsymbol{20tj}$ and $\boldsymbol{40tj}$); GRI-Mech 3.0 (solid line) and 11-species model (dashed line). 174

Figure 7.9: Comparison of GRI-Mech 3.0 (upper) and 11-species model (lower): instantaneous 2D contours of vorticity magnitude at $\mathbf{20}\ \boldsymbol{tj}$ (left) and $\mathbf{40}\ \boldsymbol{tj}$ (right) on center plane (Z = 4H). 182

Figure 7.10: Comparison of GRI-Mech 3.0 (upper) and 11-species model (lower): instantaneous 2D contours of mixture fraction at $\mathbf{20}\ \boldsymbol{tj}$ (left) and $\mathbf{40}\ \boldsymbol{tj}$ (right) on center plane (Z = 4H). 184

Figure 7.11: Instantaneous 2D contours of CO mass fraction at $\mathbf{20}\ \boldsymbol{tj}$ (left) and $\mathbf{40}\ \boldsymbol{tj}$ (right) on the center plane (Z = 4H): GRI-Mech 3.0 (upper) and 11-species model (lower). 184

Figure 7.12: Instantaneous 2D contours of H_2 mass fraction at $\mathbf{20}\ \boldsymbol{tj}$ (left) and $\mathbf{40}\ \boldsymbol{tj}$ (right) on the center plane (Z = 4H): GRI-Mech 3.0 (upper) and 11-species model (lower). 186

Figure 7.13: Instantaneous 2D contours of OH mass fraction at $\mathbf{20}\ \boldsymbol{tj}$ (left) and $\mathbf{40}\ \boldsymbol{tj}$ (right) on the center plane (Z = 4H): GRI-Mech 3.0 (upper) and 11-species model (lower). 187

Figure 7.14: Instantaneous 2D contours of $\mathbf{log10}(\boldsymbol{\chi/\chi q})$ at $\mathbf{20}\ \boldsymbol{tj}$ (left) and $\mathbf{40}\ \boldsymbol{tj}$ (right) on the center plane (Z = 4H): GRI-Mech 3.0 (upper) and 11-species model (lower). ... 188

Figure 7.15: PDF of normalized logarithm of scalar dissipation rate on the stoichiometric surface at $\mathbf{20}\ \boldsymbol{tj}$ (blue) and $\mathbf{40}\ \boldsymbol{tj}$ (red): GRI-Mech 3.0 (solid lines), 11-species model (dashed lines), and log-normal distribution (dash-lot line). 189

Figure 7.16: PDF of (a) $\boldsymbol{\chi/\chi q}$, (b) $\boldsymbol{\chi CO}$, and (c) $\boldsymbol{\chi OH}$ on the stoichiometric surface at $\mathbf{20}\ \boldsymbol{tj}$ (blue) and $\mathbf{40}\ \boldsymbol{tj}$ (red), calculated using GRI-Mech 3.0 (solid lines) and 11-species model (dashed lines). 192

Figure 7.17: Instantaneous 2D contours of net radical production rate, R_{GP}, associated with GP-H_2-1, at 20 t_j (left) and 40 t_j (right) on center plane (Z = 4H): GRI-Mech 3.0 (upper) and 11-species model (=SKE: lower). 194

Figure 7.18: Instantaneous 2D contours of net radical production rate, R_{GP}, associated with GP-H_2-3, at 20 t_j (left) and 40 t_j (right) on center plane (Z = 4H): GRI-Mech 3.0 (upper) and 11-species model (=SKE: lower). 195

LIST OF SYMBOLS AND ABBREVIATIONS

$\boldsymbol{A}_i$	Jacobian matrix of convection flux w.r.t. primitive state variables
$\boldsymbol{A}_i^v$	Jacobian matrix of diffusion flux w.r.t. primitive state variables
a	flow strain rate (s^{-1})
C	progress variable
C_p	specific heat at constant pressure ($J \cdot kg^{-1} \cdot K^{-1}$)
D	mass diffusivity ($m^2 \cdot s^{-1}$)
Da	Damköhler number
d	jet diameter (m)
dip	dipole moment
$\boldsymbol{E}$	electric field ($V \cdot m^{-1}$)
E	specific total energy ($J \cdot kg^{-1}$)
e	specific internal energy ($J \cdot kg^{-1}$)
$\boldsymbol{F}$	convection flux vector of conservative state variables
$\boldsymbol{F}^{\mathrm{v}}$	diffusion flux vector of conservative state variables
F_i^{EHD}	electro-hydrodynamic force per unit volume ($kg \cdot m^{-2} \cdot s^{-1}$)
f	mixture fraction
$G(t)$	non-dimensional heat transfer parameter
H	energy flux ($J \cdot m^{-2} \cdot s^{-1}$)
h	specific enthalpy ($J \cdot kg^{-1}$)
I	total reactions count
$\boldsymbol{J}$	flux ($m^{-2} \cdot s^{-1}$)
k	thermal conductivity ($W \cdot m^{-1} \cdot K^{-1}$)
k_B	Boltzmann constant ($m^2 \cdot kg \cdot s^{-2} \cdot K^{-1}$)
k_i	reaction rate constant of reaction i

L	gap length (m)
L_k	number of reactions involving species k
l	thickness (m)
M	Mach number
m_k	molecular mass of species k (kg·mol^{-1})
$\dot{m}$	mass flow rate (kg·s^{-1})
N	total number of species
N_i	number of species involved in reaction i
$\boldsymbol{n}_s$	outward unit normal vector
n	number density (m^{-3})
Pr	Prandtl number
p	pressure (Torr/Pa/kg·m^{-1}·s^{-1})
$\boldsymbol{Q}$	state vector of conservative variables
$\widehat{\boldsymbol{Q}}$	state vector of primitive variables
$\dot{Q}$	production rate (cm^{-3}·s^{-1})
$\dot{Q}^{JH}$	heat release rate from Joule heating (kg·m^{-1}·s^{-3})
Q_i	heat flux on the i^{th} direction (J · m^{-2} · s^{-1})
$\dot{q}$	heat release rate (kg·m^{-1}·s^{-3})
q_i	energy flux from heat conduction and diffusion in the direction of i (kg·s^{-3})
R_u	universal gas constant (J · K^{-1} · mol^{-1})
r	spatial coordinate on the radial direction (m)
$\boldsymbol{S}$	source term vector of conservative equations
SGS/sgs	subgrid scale
Sc	Schmidt number
$\boldsymbol{T}$	Jacobian matrix of conservative variables w.r.t. primitive variables

T	temperature (K)
t	physical time (s)
u	velocity component ($m \cdot s^{-1}$)
$U_{k,j}$	diffusive velocity of species k in j direction ($m \cdot s^{-1}$)
MW/W	molecular weight ($kg \cdot mol^{-1}$)
X_k	mole fraction of species k
x	physical coordinate (m)
Y_k	mass fraction of species k
Z	compressibility factor / mixture fraction

Greek Symbols

α	diffusivity ($m^2 \cdot s^{-1}$)
$\boldsymbol{\Gamma}$	preconditioning matrix
γ	secondary electron emission coefficient for ions colliding with electrode
δ	Dirac delta
ϵ	electric permittivity ($F \cdot m^{-1}$) / Lennard-Jones potential well depth
ϵ_e	electron energy (eV)
ϵ_T, ϵ_χ	threshold of temperature (K) and mole fraction, respectively
λ	thermal conductivity ($W \cdot m^{-1} \cdot K^{-1}$)
μ	molecular dynamic viscosity ($Pa \cdot s$)
$\nu_{A,i}$	stoichiometric coefficient of species A in the i th reaction
ν_t	turbulent eddy viscosity ($m^2 \cdot s^{-1}$)
ρ	density ($kg \cdot m^{-3}$)
σ	stress tensor / viscous work ($J \cdot m^{-2} \cdot s^{-1}$)
σ_k	Lennard-Jones collision diameter (m)
τ	pseudo time (s)

τ_{ij}	viscous stress tensor ($kg \cdot m^{-1} \cdot s^{-2}$)
$\Phi_{k,j}$	species flux of the k^{th} species on the j^{th} direction ($kg \cdot m^{-2} \cdot s^{-1}$)
ϕ	electric potential (V) / equivalence ratio
χ	scalar dissipation rate (s^{-1})
$\dot{\omega}$	mass production rate ($kg \cdot m^{-3} \cdot s^{-1}$)
Subscripts	
amb	ambient
app	applied
b	boundary / backward
C	progress variable
ci	critical properties of species *i*
d	dielectric layer
e	electron
ext	extinction
f	forward
g	gauge
gw	at a distance Δx from the solid wall
i, j, k	dummy indexes / reaction *i* / species *k*
ign	ignition
s	wall boundary
se	secondary electrons ejected from the electrode surface
t	turbulent
Z	mixture fraction
ϵ	electron energy (eV)
+,-	positive and negative ions

SUMMARY

The development of advanced combustion energy-conversion systems requires accurate simulation tools, such as Direct Numerical Simulation (DNS) and Large Eddy Simulation (LES), for capturing and understanding ignition, combustion instability, lean blowout, and emissions. However, the characteristic timescales in combustion systems can range from milliseconds to picoseconds or even lower. This renders the use of detailed finite rate chemistry prohibitive in DNS/LES of turbulent combustion, which requires the calculation of a large number of species and reactions on a large number of grid cells. Due to these high computational costs, DNS and LES typically employ either a flamelet model with detailed chemistry or a simplified/reduced finite rate chemistry with non-stiff reactions. Both approaches, however, are of limited accuracy and may reduce the overall prediction quality. To address this, a framework with high fidelity by incorporating finite rate chemistry, while mitigating additional computational cost, is necessary for the development of advanced combustion systems.

In this dissertation, a new numerical framework for DNS and LES of turbulent combustion is established employing correlated dynamic adaptive chemistry (CoDAC), correlated evaluation of transport properties (CoTran), and a point-implicit stiff ODE solver (ODEPIM). CoDAC utilizes a path flux analysis (PFA) method to reduce the large chemical kinetics mechanism to a smaller size for each location and time step. Thermo-chemical correlation zones are introduced and only one PFA calculation is required for each zone, which diminishes the CPU overhead of CoDAC to negligible computation costs. CoTran uses a similar correlation method to accelerate the evaluation of mixture-averaged diffusion (MAD) coefficients.

This framework is firstly applied to investigate the non-equilibrium plasma discharge of $C_2H_4/O_2/Ar$ mixtures in a low-temperature flow reactor. The accelerated

case has been verified against the benchmark case by both temporal evolution and spatial distribution of several key species and gas temperature. Simulation results show that it accelerates the total computation time by a factor of 3.16, the calculation of chemical kinetics by a factor of 80, and the evaluation of MAD coefficients by a factor of 836. The high accuracy and efficiency of this proposed framework illustrate its promise in the simulation of diverse combustion problems.

Secondly, this framework is evaluated for a canonical turbulent premixed flame employing a conventional jet fuel kinetics model. Again, the results show that the new framework provides a significant speed-up of chemical kinetics and transport computation, enabling DNS with large kinetics mechanisms while maintaining high accuracy and good parallel scalability. Detailed diagnostics show that, for this test case, calculation of the chemical source term with ODEPIM is 17 times faster than that of a pure implicit solver. CoDAC further speeds up the calculation of chemical source terms by 2.7 times. CoTran makes the evaluation of MAD coefficients 72 times faster. Comparing to the conventional DNS, the total computation time of this framework in this test is 20 times faster, with that of chemical kinetics 46 times faster, and that of the evaluation of transport properties 72 times faster.

Based on the above DNS framework, an efficient finite-rate chemistry (FRC) - LES formulation is developed for numerical modeling of a turbulent jet flame. Comparing to the conventional FRC-LES, this framework provides a speed-up of 8.6 times for the chemistry calculation, and 6.4 times for the total computation, using a 20 species kinetics model. Both the new FRC-LES and flamelet/progress-variable (FPV)-LES are conducted for a piloted partially premixed methane/air flame (Sandia Flame D). The two approaches provide similar predictions in terms of time-averaged flame field and statistics, which agree well with the experimental data. For the instantaneous flame field, FPV-LES predicts significantly smaller regions with high temperature than the FRC-LES case, especially in the downstream region. Near the stoichiometric region, FPV-LES

over-predicts the radical generation with respect to the experimental data, but under-predicts the CO generation and heat release, which explains its under-prediction of temperature. In contrast, on the fuel rich side, CO is no longer the bottleneck species, thus the FPV-LES predicts a higher temperature than FRC-LES. With respect to the experimental data, FRC-LES provides overall better predictions than FPV-LES for both temperature and species.

Most existing chemical kinetics models offer similar predictions of ignition and extinction in 0D/1D finite-rate simulations of laminar combustion processes. Is it appropriate, therefore, to extend this observation to a 3D turbulent combustion environment? In order to investigate the sensitivity of predictions to chemical kinetics models, two different kinetics models, GRI-Mech 3.0 and an 11-species syngas model, are compared by performing 3D finite-rate kinetics-based DNS of a temporally evolving turbulent non-premixed syngas flame. The framework enables computationally efficient simulation incorporating the detailed GRI-Mech 3.0. Both chemical kinetics models provide comparable qualitative trends, and capture local extinction/re-ignition events. However, significant quantitative discrepancies (e.g. 86~100 K difference in the temperature field) indicate high sensitivity to the chemical kinetics model. The 11-species model predicts a lower radicals-to-products conversion rate, causing more local extinction and less re-ignition. This sensitivity to the chemical kinetics model is amplified relative to a 1D steady laminar simulation by the effects of unsteadiness and turbulence (up to 7 times for temperature, up to 12 times for CO, up to 13 times for H_2, up to 7 times for O_2, up to 5 times for CO_2, and up to 13 times for H_2O), with the deviations in species concentrations, temperature, and reaction rates forming a nonlinear positive feedback loop under reacting flow conditions. The differences between the results from the two models are primarily due to: (a) the larger number of species and related kinetic pathways in GRI-Mech 3.0, and (b) the differences in reaction rate coefficients for the same reactions in the two models. Both (a) and (b) are sensitive to

unsteadiness and other turbulence effects, but (b) is more pronounced. During local extinction events, the major differences between the results from the two chemical kinetics models are in the peak values and the volume occupied by the peak values, which is dominated by unsteady effects. During re-ignition events, differences are mainly observed in the spatial distribution of the reacting flow field, which is primarily dominated by the complex turbulence-chemistry interaction. Further analysis shows that GRI-Mech 3.0 predicts more net radical production associated with the major global pathways, explaining the prediction of less local extinction and more re-ignition.

CHAPTER 1

INTRODUCTION

1.1 Background and Motivation

Increasing demand in an energy economy still dominated by the combustion of fossil fuels, coupled with concerns regarding the long-term environmental effects of these processes make detailed understanding of the physics and chemistry of turbulent combustion a scientific and engineering priority. Particularly, the development of advanced propulsion and combustion-energy conversion systems requires accurate computational tools, such as Direct Numerical Simulation (DNS) and Large Eddy Simulation (LES), which provide a powerful way to investigate the complex interplay of turbulent mixing, molecular diffusion, and finite-rate kinetics. However, DNS/LES suffers from a bottleneck in the calculation of the stiff finite-rate chemical reactions and mixture-averaged transport properties, when moderately complex to detailed chemical kinetics models are employed [1-3]. For this reason, except for those consuming excessive computational resources and time [4-6], most DNS/LES studies of turbulent combustion have used either a flamelet model with detailed chemistry (~50 species or more) [7-10] or a simplified/reduced finite-rate chemical kinetics model with non-stiff reactions (~10 species) [11-16]. Both approaches, however, are of limited accuracy and may reduce the overall accuracy of prediction [17], especially in low-temperature ignition zones [17-19]. Therefore, accelerating the computation of chemical kinetics and transport properties is required to enable computationally efficient and accurate simulations with the DNS/LES approach employing detailed finite-rate chemical kinetics models. In combustion systems, the characteristic timescales can range from milliseconds to picoseconds or lower. This renders the use of detailed finite rate chemistry prohibitive in DNS/LES of turbulent combustion, due to the large number of chemical species and

reactions. As a result, chemistry and transport dominate the resource requirements in most combustion DNS studies [2, 3, 20, 21].

Molecular diffusion transport modeling is another obstacle to accurate and efficient DNS of turbulent combustion. Bruno *et al.* [2] compared three models in DNS of a partially premixed flame, and concluded that the mixture-averaged diffusion (MAD) model predicts essentially the same fluid-dynamic and thermo-chemical field as the fully multi-component diffusion (MCD) model. However, the fast constant Lewis number model predicts a significantly different flow-field. Therefore, the MAD model or a higher fidelity model is needed to guarantee accurate predictions. Although MAD is much faster than the MCD model, applying it at every time step and every grid cell is still expensive; it is often the second largest component of the required CPU time for a given computation, and could dominate CPU use when the kinetic source term is no longer the bottleneck.

For any practical simulation method, the key is to provide quantitative solutions with minimal empirical constants. LES has drawn significant attention during the past three decades, and its predictive capability is continuously enhanced. In LES, the energy-contained large-eddy motions are resolved with sufficient grid resolution, while motions of scales smaller than the grid sizes, i.e. subgrid scale (SGS) motions, are not resolved but modeled. In LES of turbulent combustion, turbulent mixing and chemical reactions are closely coupled to each other. The chemical reaction rates are highly nonlinear functions of species concentrations and temperature, which in turn heavily depend on the turbulent mixing. On the other hand, chemical reactions also release heat and subsequently affect species concentrations and temperature, which in turn change the turbulent mixing. Chemical reactions occurring at different time scales may interact with eddies of different length/time scales, further complicating both the physical and chemical processes. For these reasons, turbulence/chemistry interaction is considered the most challenging topic in turbulent combustion modeling.

Due to the mathematical nature of the governing equations, there are primarily three categories of computational fluid dynamics (CFD) solvers: incompressible solvers, low Mach solvers, and fully compressible solvers. The intense heat release and subsequent gas expansion in turbulent combustion make incompressible solvers less preferable. In low Mach solvers, density is decoupled from pressure (acoustics), which makes the solvers inaccurate or unstable near the instability limit or at high Mach numbers. In fully compressible solvers, conservation equations are closely coupled under moderate or high Mach numbers, but become poorly coupled and numerically stiff at low Mach numbers. Many fluid flow problems involve a wide range of Mach numbers, which poses a great challenge for all three categories.

Furthermore, the sensitivity of simulation results to different chemical kinetics models is still unclear, particularly concerning the prediction of local extinction and re-ignition events in highly turbulent combustion environments. These phenomena are associated with increased emissions, combustion instability, and flame blowout, so their accurate prediction is critical

Numerical analysis plays an increasingly important role in the understanding of combustion simulation results. However, due to the large sizes and complicated coupled relations of chemical kinetics, it remains a formidable task to extract insights from the reaction system. Systematic and rigorous analytic tools are necessary to obtain useful information from massive simulation datasets.

This dissertation attempts to address the above challenging key issues related to the numerical modeling and understanding of turbulent combustion and its underlying fundamental physicochemical processes at a wide range of fuel types and conditions. Specifically, this dissertation (a) establishes an efficient framework to calculate detailed finite rate chemistry in DNS/LES of turbulent combustion, (b) studies the influence of global mechanism reduction and choices of chemical kinetics mechanisms, and (c) investigates the necessity of finite rate chemistry.

1.2 Literature Review

1.2.1 Reduction of Detailed Chemical Kinetics Mechanisms

Global Reduction

In order to reduce computational cost, several mechanism reduction methods have been proposed. Typical examples include the visualization method [22], the direct relation graph (DRG) method [23], the DRG with error propagation (DRGEP) method [24], the multi-generation path flux analysis (PFA) method [25], and the global pathway selection (GPS) method [26]. These models essentially reduce the number of species in the chemical kinetics models.

Well-verified by homogeneous ignition delays, extinction curves in the perfectly stirred reactor, and laminar flame speeds, globally reduced models for hydrocarbons generally require at least ~40 species to cover all user-defined conditions of interest (fuel type, oxidizer type, equivalence ratio, initial pressure and temperature). Any further reduction would introduce significant errors, because globally reduced mechanisms typically have to be produced based on conditions of interest in practice. Unfortunately, the least number of required species is still too large for DNS/LES using the finite-rate kinetics approach.

Dynamic Local Reduction

To deal with this issue, several adaptive combustion models have been proposed by a number of investigators.

To tackle this challenge, dynamic adaptive chemistry (DAC) [27, 28] was proposed to utilize detailed stiff finite-rate chemistry. DAC generates locally optimized reduced kinetics for each spatial location and time step, and only the reaction rates of active species are calculated. DAC has been applied to accelerate the kinetics computation in DNS of 0D/1D reactors [29], 2D RANS of DI engines [30], and 3D

URANS and LES of spray flames [31]. Liang *et al.* [32] proposed a pre-partitioned adaptive chemistry methodology for 0D partially-stirred reactor using particle probability density function (PDF) methods. In contrast, Wu *et al.* [33] designed a sub-model assignment framework to assign different flamelet/finite rate sub-models rather than different kinetics to different zones of the simulation domain for a 2D laminar triple flame, which matches the boundaries of zones by only conserving the interested quantities.

Both the DAC and zone partition in all the above methods contain significant CPU overhead for mechanism reduction/zone partition. In order to reduce the CPU overhead, Liang *et al.* [32] and Wu *et al.* [33] proposed pre-generating look-up tables for the zone partition. However, covering all conditions through tabulation is very challenging, and the large tables make important demands on memory resources.

Recently, Sun *et al.* [34, 35] proposed a simple zone-partition criterion to decide whether a new on-the-fly reduction was required or not, and this significantly reduced CPU overhead. Employing the correlated version of DAC (CoDAC) technique, Sun *et al.* [34, 35] showed significant reduction of CPU time for chemistry in 0D/1D laminar flames. To improve the computation of transport properties, Sun and Ju [36] developed a correlated transport (CoTran) technique, and obtained significant further speed-up for extensive 0D/1D laminar flames.

Both the CoDAC and CoTran techniques have been applied only to 0D and 1D simulations of laminar flames. Generalization of these techniques to 3D DNS/LES of turbulent combustion gives rise to several critical questions: 1) how to efficiently scan and form the correlation zones in 3D space; 2) whether existing CPU overhead reduction methods are adequate for 3D turbulent flames; 3) whether correlation grouping is valid under high intensity turbulence; 4) how to maintain good parallel scaling performance on a large number of processors. In addition, optimized combinations of the above methods to provide the best possible computational speed have not yet been developed.

CoDAC and CoTran has not been implemented via parallel high performance computing (HPC), which is necessary for high dimensional simulation with immensely fine grid. The zoning of CoDAC and CoTran method is convenient for parallelization because there is no need to communicate reduced mechanism of one local zone with other processors. Ideally, parallel CoDAC and CoTran can resolve the efficiency degeneracy issue of CoDAC and CoTran when the number of correlated spatial zones increases. In particular, larger number of zones can be distributed to more processors, which results in a relatively fixed number of zones on each processor to guarantee the efficiency of CoDAC and CoTran.

1.2.2 Stiff ODE Solvers

In a combustion system, the characteristic timescales of different phases can range from milliseconds to picoseconds and even smaller. In most of the previous literature, the variable-coefficient ODE solver (VODE) [37] is applied to solve the stiff ODE system. However, the computation time of VODE solver increases as cubic of the number of species due to the iterative "Jacobian matrix decomposition". For this reason, it is almost impossible to involve large detailed mechanisms or moderate mechanisms in simulations with a large number of grid points, especially in the high dimensional computational domain.

In order to enable the detailed combustion chemistry in comprehensive modeling, one can directly reduce the stiffness of the ODE system, such as the computational singular perturbation (CSP) method [38, 39], the intrinsic low-dimensional manifold (ILDM) method [40], the dynamic stiffness removal method [41] and the hybrid multi-timescale (HMTS) method [42]. The highly reduced kinetics will still keep the multi-timescale nature of combustion, therefore, much faster stiff ODE solvers, such as the point-implicit stiff ODE solver (ODEPIM) [43, 44], are preferred.

1.2.3 Turbulence/Combustion Interaction Models

Many LES turbulent combustion models have been developed, which can be classified into two major categories: the finite-rate chemistry (FRC) models, and the flamelet generated manifold (FGM) models. The FRC models category includes laminar chemistry model [45-47], perfectly-stirred reactor (PSR) model [48], partially-stirred reactor (PaSR) model [49], linear-eddy model (LEM) [50], Monte Carlo method for Lagrangian filtered probability density function (FDF) transport equations [51], thickened flame model (TFM) [52], etc. The FGM models category includes steady laminar flamelet model [53], Lagrangian flamelet model [54, 55], flamelet/progress-variable (FPV) model [56], etc.

Among different FGM models, the steady laminar flamelet model pioneered by Peters [53] provides the advantages of easy implementation and low computational cost. However, there are limitations. Firstly, the mixture fraction essentially does not carry any information about the chemical states. The model chooses the filtered dissipation rate of mixture fraction as an additional parameter to account for the flame stretching effect, but does not provide a unique mapping from mixture fraction to the corresponding reaction state. A pure mixing of fuel and oxidizer cannot be accounted by the steady laminar flamelet model if the local scalar dissipation rate is close to the quenching limit. In addition, the coexistence and interaction between auto-ignition kernels and flame sheet [57-59] cannot be captured.

In order to overcome the drawbacks of the steady laminar flamelet model, the FPV model [56, 60] was proposed by incorporating a transport equation to track a progress variable. This model has been developed to account for low-level of extinction, ignition, and unsteady mixing effect [56] to some extent. However, it cannot handle multiple-feed streams unless adding a third parameter, which makes the look-up table very difficult to handle due to the large computer memory requirement and time to build up the table. In addition, the higher-dimension look-up table results in a more

complicated data retrieval process and coarser table grid, which could introduce higher interpolation errors.

The main assumption of many FGM models is that the chemical reactions are faster than all turbulent flow eddies, such that the combustion process can be decoupled from the turbulent flow field. This assumption becomes invalid in three important categories of operating conditions. (1) When the turbulence intensity is high enough, the local Reynolds number may increase to such a level that small turbulent eddies become faster than chemical reactions to penetrate into the flame zone and greatly enhance the mixing process. (2) Most chemical reactions related to combustion emissions (NO_x, soot, aerosol, etc.) are very slow, thus FGM models normally cannot capture emissions accurately. (3) For processes of ignition, extinction, and conditions close to flammability limits, chemical reactions are often slower than small turbulent eddies. In addition, since each FGM model is optimized for one single regime, they are problematic to handle turbulent combustion with multiple regimes, like lean blowout (LBO) in partially premixed fames. To overcome these limitations, detailed finite-rate chemistry (FRC) is desirable.

Many fluid flow problems involve a wide range of Mach numbers, which poses a great challenge for all these three categories. To resolve this issue, a preconditioning method [61-66] was proposed for fully compressible solver to allow a broad range of Mach numbers simultaneously in the simulation.

1.2.4 Analysis Tool for Combustion Simulation Results

Realistic chemical kinetic mechanisms describing the combustion process typically involve hundreds of species and thousands of reactions. Due to their large sizes and complicated coupled relations, it remains a formidable task to extract insights from the reaction system. Systematic and rigorous analytic tools are necessary to obtain useful information from massive simulation datasets.

The analysis of chemical kinetics may start from timescale decoupling. One prominent example is the Computational Singular Perturbation (CSP) [67]developed in the mid-1980s. CSP decouples fast and slow subspaces (modes) based on Jacobian analysis. The involvement of species and reactions in the fast processes can be identified by the radical pointer and the participation index [68], respectively. The wide applications of CSP include mechanism reduction [69, 70], analysis of flow-chemistry interactions [71], and biochemical systems [72]. Intrinsic low-dimensional manifold (ILDM) [73] is another. The identified manifolds represent attractors for the chemical kinetics, thus separating the fast processes, which relax towards the attractors, and the slow ones, which move within the manifolds [74]. This method is then extended to reaction–diffusion manifolds (REDIMs) to tackle the coupling of reaction and diffusion processes [75, 76]. A more recent kinetic analysis method is Chemical Explosive Mode Analysis (CEMA) proposed by Lu *et al.* [77]. It quantifies the timescales related to chemical explosive modes (CEM) based on the eigenvalue analysis of the Jacobian matrix of the chemical source term. Methods to evaluate the contribution of each species or elementary reaction to CEM are provided [77-79]. Such diagnostic techniques provide insights to analyze complex flame dynamics, such as turbulent lifted jet flames associated with auto-ignition [79-83]. Besides the methods based on eigenvalue analysis of Jacobian matrix, approaches representing the results with basic physical quantities are available as well. In an investigation of diffusion flame extinction, Won *et al.* [84] introduced the concept of radical index, which is the normalized OH radical formation rate, to quantify the impact of chemical kinetics, and a transport weighted enthalpy, to assess the mass transfer effect. For fuels with distinct chemical properties, a universal correlation between diffusion flame extinction strain rates and the product of radical index and transport-weighted enthalpy has been demonstrated in that work. Sensitivity analysis [85] is another method to analyze the reacting system. However, this method is brute-force

and very time-consuming, especially when the number of variables is significant. Furthermore, the coupling relations between variables may not be discovered.

Recently, a Global Pathway Selection algorithm (GPS) [26] is proposed to identify important chemical pathways that converting initial reactants to final products, based on atomic flux analysis. Different from the classical Path Flux Analysis algorithm (PFA) [25, 86-88], which only considers one or two generations, GPS provides a way to consider the relation between species through all generations (reaction steps). GPS has been used for effective chemical kinetic mechanism reduction [26, 89]. GPS is further extended as an analytic tool, Global Pathway Analysis (GPA) [90-92]. By analyzing the dominancy and effects on radical production and consumption of different reaction pathways, GPA provide insights to understand the complex reacting system. It has been demonstrated using zero-dimensional (0D) simulation results [90].

1.3 Research Objectives

The first objective of this dissertation is to develop a new regime-independent framework for 3D DNS of turbulent combustion with detailed kinetics by incorporating CoDAC, CoTran, and ODEPIM into conventional DNS platforms. All three methods are modified and optimized to adapt to 3D turbulent combustion and parallel high performance computing (HPC). The new framework is tested on a non-equilibrium plasma discharge of $C_2H_4/O_2/Ar$ mixtures in a low-temperature flow reactor, a canonical premixed flame interacting with decaying isotropic turbulence, a temporally evolving turbulent non-premixed syngas flame to evaluate its accuracy for both species and temperature evolution, speed-up and parallel performance.

The second objective of this dissertation is to incorporate the framework into a preconditioning scheme to allow an Eulerian FRC-LES approach in a fully compressible CFD solver. The established FRC-LES framework is then used to investigate a low Mach piloted turbulent partially premixed flame (Sandia Flame D) as a benchmark case. The

results from the FRC model are compared to those from both the FPV model and the experiment, in terms of both computational performance and accuracy. For self-consistency, all LES combustion models are coupled with a fully compressible CFD solver using a preconditioning scheme.

The last objective of this dissertation is to investigate the sensitivity of simulation results to different chemical kinetics models, particularly with regard to the prediction of local extinction and re-ignition events. In particular, two different chemical kinetics models (GRI-Mech 3.0 [93] and an 11-species model [13]) are used to simulate a temporally evolving turbulent non-premixed syngas flame, and the results are compared. GPA is applied to investigate the underlying physical processes for this sensitivity.

1.4 Dissertation Outline

The dissertation is organized into eight chapters. Chapter 2 describes the theoretical framework including governing equations, finite rate chemistry, thermos-physical and transport properties. Chapter 3 presents the numerical framework for both DNS and LES, as well the boundary conditions and parallel implementation. Chapter 4 focuses on the development of efficient numerical framework for detailed finite rate chemistry in turbulent combustion, using ODEPIM, CoDAC, and CoTran. Chapter 5 numerically verifies the framework for plasma assisted combustion, turbulent premixed and non-premixed flames. This is followed by the experimental validation of the framework via LES for a turbulent partially premixed jet flame in Chapter 6, in which the FRC and FPV models are compared in detail. Chapter 7 systematically investigate the sensitivity of simulation prediction to chemical kinetics models. Finally, the conclusions of this dissertation and recommendations for the future work are provided in Chapter 8.

CHAPTER 2

THEORETICAL FRAMEWORK

2.1 Governing Equations

The theoretical framework is based on the full conservation equations of mass, momentum, energy, and species concentrations in Cartesian coordinate systems. In fluid mechanics, assuming continuum and negligible body forces, the differential form of Navier-Stokes equations are given by

$$\frac{\partial \rho}{\partial t} + \frac{\partial \rho u_i}{\partial x_i} = 0 \,, \tag{2.1}$$

$$\frac{\partial \rho u_i}{\partial t} + \frac{\partial (\rho u_i u_j)}{\partial x_j} = \frac{\partial \sigma_{ij}}{\partial x_j}, \quad (i = 1,\ 2,\ 3) \tag{2.2}$$

$$\frac{\partial \rho E}{\partial t} + \frac{\partial \left[(\rho E + p) u_i \right]}{\partial x_i} = -\frac{\partial q_i}{\partial x_i} + \frac{\partial (u_i \tau_{ij})}{\partial x_j}, \tag{2.3}$$

$$\frac{\partial \rho Y_k}{\partial t} + \frac{\partial \rho Y_k u_j}{\partial x_j} = \dot{\omega}_k + \frac{\partial \left(\rho D_k \nabla_j Y_k \right)}{\partial x_j}, \qquad (k = 1,\ \cdots,\ N\text{-}1) \tag{2.4}$$

here *i*, *j*, and *k* are indexes of spatial coordinate, summation, and species. For a Newtonian fluid with Stokes' hypothesis, the viscous stress tensor, σ_{ij} in Eq. 2.2 is expressed as

$$\sigma_{ij} = -p\delta_{ij} + \tau_{ij} = -p\delta_{ij} + \mu \left(\frac{\partial u_i}{\partial x_j} + \frac{\partial u_j}{\partial x_i} \right) - \frac{2}{3} \mu \frac{\partial u_k}{\partial x_k} \delta_{ij} \,. \tag{2.5}$$

The Dufour effect, which is the heat flux due to concentration gradient, is generally very small and thus neglected in the current study. Then q_j in Eq. 2.3 is defined as

$$q_j = -\lambda \frac{\partial T}{\partial x_j} + \rho \sum_{k=1}^{N} \hat{h}_k Y_k U_{k,j} \,. \tag{2.6}$$

The specific total energy is defined as the sum of specific internal energy and kinetic energy, given by

$$E = e + \frac{u_j u_j}{2} \ , \tag{2.7}$$

where the specific internal energy is calculated from specific enthalpy, pressure, and density, given by

$$e = h - \frac{p}{\rho} \ , \tag{2.8}$$

where h is determined by the mixture concentration and partial-mass based enthalpies, $\hat{h}_k$, for which the definition will be given later.

$$h = \sum_{k=1}^{N} Y_K \hat{h}_k \ . \tag{2.9}$$

In non-premixed combustion studies, mixture fraction is an important conserved variable and often used. The definition of mixture fraction is not unique. In a two-feed system, mixture fraction is simply defined as the ratio of the local mass originating from the fuel (denoted by 1) to total mass (with mass from the oxidizer stream denoted by 2),

$$Z = \frac{\dot{m}_1}{\dot{m}_1 + \dot{m}_2} \ . \tag{2.10}$$

Although the definition based on Eq. 2.10 is straightforward, it becomes ambiguous when there are multiple inlets. In such a case, a more general definition based on elemental conservation is used. If a_{ij} denote the number of atoms of element j in a molecule of species i, then the mass of all atoms j in the system of interest is given by:

$$m_j = \sum_{k=1}^{N} \frac{a_{ij} MW_j}{MW_i} m_i \tag{2.11}$$

Dividing Eq. 2.11 by the total mass, one has the mixture fraction of element j as:

$$Z_j = \frac{m_j}{m} = \sum_{k=1}^{N} \frac{a_{ij} MW_j}{MW_i} Y_i \tag{2.12}$$

It is obviously that Z_j is a linear function of species, Y_i. Multiplying Eq. 2.4 by $\frac{a_{ij}MW_j}{MW_i}$ and summing over all the species, it gives:

$$\frac{\partial \rho Z_k}{\partial t} + \frac{\partial (\rho u_j Z_k)}{\partial x_j} = \frac{\partial}{\partial x_j}\left(\rho D_k \frac{\partial Z_k}{\partial x_j} \right). \tag{2.13}$$

The source term vanishes because of the conservation of chemical elements. If we assume that the mass diffusivity for all the species equal to D, the balance equation becomes

$$\frac{\partial \rho Z_k}{\partial t} + \frac{\partial (\rho u_j Z_k)}{\partial x_j} = \frac{\partial}{\partial x_j}\left(\rho D \frac{\partial Z_k}{\partial x_j} \right). \tag{2.14}$$

For hydrocarbon fuels ($C_m H_n$), the coupling function can be defined as: (Burke and Schumann 1928):

$$\beta = \frac{Z_C}{mMW_C} + \frac{Z_H}{nMW_H} - \frac{2Z_O}{\nu'_{O_2} MW_{O_2}}, \tag{2.15}$$

where β is a conserved scalar. It can be normalized between 0 and 1 to obtain Bilger's (1988) definition of the mixture fraction:

$$f = \frac{\frac{Z_C}{mMW_C} + \frac{Z_H}{nMW_H} + \frac{2\left(Y_{O_2,2} - Z_O\right)}{\nu'_{O_2} MW_{O_2}}}{\frac{Z_{C,1}}{mMW_C} + \frac{Z_{H,1}}{nMW_H} + \frac{2Y_{O_2}}{\nu'_{O_2} MW_{O_2}}}. \tag{2.16}$$

From Eq. 2.17 and Eq. 2.19, one can get the transport equation for the mixture fraction:

$$\frac{\partial \rho f}{\partial t} + \frac{\partial (\rho u_j f)}{\partial x_j} = \frac{\partial}{\partial x_j}\left(\rho D \frac{\partial f}{\partial x_j} \right). \tag{2.17}$$

2.2 Finite Rate Chemistry

The chemical source term in Eq. 2.4 is determined from the selected chemistry kinetics. For an elementary reaction mechanism, with L-step reaction and N species,

$$\sum_{k=1}^{N} \nu'_{kl} X_k \underset{k_{bl}}{\overset{k_{fl}}{\Longleftrightarrow}} \sum_{k=1}^{N} \nu''_{kl}, \quad l = 1, 2, \cdots, L \tag{2.18}$$

the reaction rate constants of the forward and backward reactions, k_{fl} and k_{bl}, may take the following form according to the modified Arrhenius's equation:

$$k_l(T) = A_l T^b \exp\left(-E_l / R_u T\right). \tag{2.19}$$

The net production rate for each species in a multi-step mechanism is given by,

$$\dot{\omega}_k = MW_k \sum_{i=1}^{L} (\nu''_{kl} - \nu'_{kl}) \left[k_{fl} \prod_{k=1}^{N} [X_k]^{\nu'_{kl}} - k_{bl} \prod_{k=1}^{N} [X_k]^{\nu'_{kl}} \right] k = 1, 2, \cdots, N. \tag{2.20}$$

where $[X_k]$ is the molar concentration of species k.

2.3 Thermo-physical Properties

In order to close the aforementioned governing equations, thermodynamic and transport properties require to be defined and an equation of state (EOS) is needed to correlate pressure, temperature, and density. In this section, first, the EOS is presented, and then thermodynamics treatments, including the derivatives appearing in the preconditioning matrix are summarized.

2.3.1 Equation of State (EOS)

In the present study, the EOS used is that of an ideal, multi-fluid gas. The formula of ideal gas EOS is given by,

$$p = \rho RT = \frac{\rho R_u T}{MW} \tag{2.21}$$

where the mean mass density is defined by,

$$\rho = \sum_{k=1}^{N} [X_k] MW_k \tag{2.22}$$

The mean molecular weight MW is given by,

$$MW = \frac{1}{\sum_{k=1}^{N} Y_k/MW_k} = \sum_{k=1}^{N} X_k MW_k = \frac{\sum_{k=1}^{N}[X_k]MW_k}{\sum_{k=1}^{N}[X_k]} \tag{2.23}$$

2.3.2 Thermodynamic Properties

In this study, the thermodynamic properties are assumed thermally perfect, i.e. they are only functions of temperature. Practically, it is convenient to fit the molar heat capacities at constant pressure for species k in terms of polynomial of temperature:

$$\frac{C_{p,k}}{R} = \sum_{n=1}^{N} a_{n,k} T^{n-1} . \tag{2.24}$$

Other thermodynamic properties are given in terms of integrals of the molar heat capacities. First, the standard-state molar enthalpy for species k is given by,

$$H_k = \int_{298\ K}^{T} C_{p,k}(T)dT + H_k(298\ K) = RT\left(\sum_{n=1}^{N} \frac{a_{n,k}T^{n-1}}{n} + \frac{a_{N+1,k}}{T}\right), \tag{2.25}$$

where the parameter $a_{N+1,k}R$ represents the standard heat of formation at 298 K.

Similarly, the molar entropy for species k is written as,

$$\begin{aligned} S_k &= \int_{298\ K}^{T} \frac{C_{p,k}(T)}{T} dT + S_k(298\ K) \\ &= R\left(a_{1,k} lnT + \sum_{n=2}^{N} \frac{a_{n,k}T^{n-1}}{n-1} + a_{N+2,k}\right), \end{aligned} \tag{2.26}$$

where the parameter $a_{N+2,k}R$ represents the standard molar entropy at 298 K.

Other thermodynamic properties are given in terms of $C_{p,k}$, H_k, and S_k. The specific heat capacity at constant volume $C_{v,k}$ is defined as:

$$C_{v,k} = C_{p,k} - R, \tag{2.27}$$

The internal energy U_k is defined as:

$$U_k = H_k - RT. \tag{2.28}$$

For gas mixtures, the mixture-averaged thermodynamic properties are defined as:

$$C_p = \sum_{k=1}^{N} C_{p,k} X_k, \tag{2.29}$$

$$C_v = \sum_{k=1}^{N} C_{v,k} X_k, \tag{2.30}$$

$$H = \sum_{k=1}^{N} H_k X_k, \tag{2.31}$$

$$U = \sum_{k=1}^{N} U_k X_k. \tag{2.32}$$

The mixture-averaged entropy is more complicated:

$$S = \sum_{k=1}^{N} \left(S_k - RlnX_k - Rln\left(\frac{p}{p_{atm}}\right)\right) X_k. \tag{2.33}$$

2.4 Transport Properties

Accurate calculation of transport properties, including dynamic viscosity, thermal conductivity, and binary mass diffusivity, is very important for fluid mixing and combustion characteristics. They determine not only the flow dynamics, but also the heat and mass transfer rates.

2.4.1 Dynamic Viscosity and Thermal Conductivity

The single component viscosity is given by the standard kinetic theory expression:

$$\eta_k = \frac{5}{16} \frac{\sqrt{\pi m_k k_B T}}{\pi \sigma_k^2 \Omega^{(2.2)*}}, \tag{2.34}$$

where the collision integral $\boldsymbol{\Omega}^{(2.2)*}$ depends on the reduced temperature $T_k^* = k_B T/\epsilon_k$ and the reduced dipole moment $\delta_k^* = \frac{\frac{1}{2}\mu_k^2}{\epsilon_k \sigma_k^3}$. It is determined by a quadratic interpolation of the tables based on Stockmayer potentials given in Monchick and Mason [94].

The individual species thermal conductivities are assume to be composed of translational, rotational, and vibrational modes given by Warnatz [95]:

$$\lambda_k = \frac{\eta_k}{MW_k}\left(f_{tran}C_{v,tran} + f_{rot}C_{v,rot} + f_{vib}C_{v,vib}\right), \tag{2.35}$$

To expedite the evaluation of transport properties in a computer program, people often fit the temperature dependent parts of the pure species transport properties. The viscosity and conductivity are independent of pressure. Practically, a polynomial fit of the logarithm of the property versus the logarithm of the temperature is often employed. For the viscosity, the fitting is:

$$ln\eta_k = \sum_{n=1}^{N} a_{n,k}(lnT)^{n-1}, \tag{2.36}$$

and the fitting of thermal conductivity is:

$$ln\lambda_k = \sum_{n=1}^{N} b_{n,k}(lnT)^{n-1}. \tag{2.37}$$

For gas mixtures, we need to get the mixture-averaged transport properties from those of single species. The Wilke formula [96] of viscosity is given by:

$$\eta = \sum_{k=1}^{N} \frac{X_k\eta_k}{\sum_{j=1}^{N} X_j\Phi_{kj}}, \tag{2.38}$$

where,

$$\Phi_{kj} = \frac{1}{\sqrt{8}}\left(1 + \frac{MW_k}{MW_j}\right)^{-\frac{1}{2}}\left(1 + \left(\frac{\eta_k}{\eta_j}\right)^{\frac{1}{2}}\left(\frac{MW_j}{MW_k}\right)^{\frac{1}{4}}\right)^2 \tag{2.39}$$

The mixture-averaged thermal conductivity uses a combination averaging formula [97]:

$$\lambda = \frac{1}{2}\left(\sum_{k=1}^{N} X_k\lambda_k + \frac{1}{\sum_{k=1}^{N}\frac{X_k}{\lambda_k}}\right). \tag{2.40}$$

2.4.2 Binary Mass Diffusivity

The binary mass diffusion coefficients are given as function of both temperature and pressure:

$$D_{jk} = \frac{3}{16}\frac{\sqrt{2\pi k_B^3 T^3/m_{jk}}}{p\pi\sigma_{jk}^2\Omega^{(1,1)*}}, \tag{2.41}$$

where the reduced molecular mass m_{jk} is defined as:

$$m_{jk} = \frac{m_j m_k}{m_j + m_k}, \tag{2.42}$$

To expedite the evaluation of transport properties in a computer program, people often fit the temperature dependent parts of the pure species transport properties. Practically, a polynomial fit of the logarithm of the property versus the logarithm of the temperature is often employed. For binary mass diffusion coefficients:

$$lnD_{jk} = \sum_{n=1}^{N} d_{n,jk}(lnT)^{n-1}. \tag{2.43}$$

The diffusion coefficients depend inversely on pressure. The diffusion coefficient fits are computed at unit pressure; the later evaluation of a diffusion coefficient is obtained by simply dividing the diffusion coefficient as evaluated from the fit by the actual pressure.

For gas mixture, the mixture-averaged diffusion coefficient for species k is given by:

$$D_k = \frac{1 - Y_k}{\sum_{j\neq k} X_j/D_{jk}} = \frac{\sum_{j\neq k} X_j MW_j}{MW \sum_{j\neq k} X_j/D_{jk}}. \tag{2.44}$$

CHAPTER 3

NUMERICAL FRAMEWORK

Although turbulence has been studied for more than ten decades after Osborne Reynolds' experiments, it is still a big challenge in fluid mechanics due to its strong nonlinear behavior [98]. Numerical simulations of turbulent motions fall into three major categories: Direct Numerical Simulation (DNS), Reynolds-Aaveraged Navier-Stokes Equation (RANS), and Large-Eddy Simulation (LES) [99].

Numerical simulations of turbulent combustion bear a series of difficulties. This chapter outlines the intrinsic challenges and the corresponding methodologies to handle these problems. The numerical schemes are capable of solving the three dimensional governing equations in a general curvilinear coordinate system. The solvers use finite volume approach with structured grid system. Message passing interface (MPI) - parallelization is used to expedite the calculation and reduce the turnaround time.

3.1 Direct Numerical Simulation

DNS is the most straightforward method. The governing equations are discretized with enough resolution and solved numerically; it resolves the smallest scales of motion and does not require any modeling. This makes it possible to compute and visualize any quantity of interest, and it has been a very useful research tool to obtain insight on detailed kinematics and dynamics of turbulent flows [100]. DNS has been applied to combustion studies [101] to reveal physical and/or chemical processes that would not have been possibly revealed with other approaches. The database created by DNS can be used to validate existing turbulent models and turbulent/combustion models. However, the implementation of DNS requires extensively computational resources. To resolve all scales of motion in three-dimensional space, the number of grid points are proportional

to Re_L^3, e.g., 9 billion grid points for Re_L= 10000. Therefore, DNS is limited to relatively small Reynolds number flows and is infeasible for industry-interested applications.

3.1.1 Compressible Reacting Flow Solver

In this study, the well-established reacting flow solver AVF-LESLIE [102, 103] was used. It is a multi-physics and multi-species compressible flow solver for DNS/LES of non-reacting/reacting flows in canonical and moderately complex flow configurations. It has been extensively used in the past to investigate a wide range of combustion problems, including acoustic flame-vortex interactions, premixed flame turbulence interactions, and scalar mixing [103-105]. The solver uses the $2^{nd}/4^{th}$-order accurate MacCormack finite volume scheme [106] on generalized curvilinear coordinates, and an explicit 2nd-order accurate scheme for time-integration. A fractional-step method [107, 108] is used to treat the convection-diffusion term and the kinetics source term separately. The solver can handle arbitrarily complex finite-rate chemical kinetics, where the thermodynamic properties are computed based on a thermally perfect gas assumption, and the transport properties are computed using a mixture-averaged (MAD) formulation. The solver has been demonstrated in large-scale turbulent combustion simulations on HPC platforms exhibiting strongly scalable parallel performance [87, 109]. Our tests show that the simulation results are not affected by HPC architecture, processor counts, and processors topology obtained from MPI domain decomposition.

3.2 Larger Eddy Simulation

In contrast to DNS, RANS has been commonly applied method to solve turbulent flow problems, especially in engineering applications. In RANS, only statistical quantities, i.e., the ensemble or time-averaged mean quantities are predicted. The effect of all the scales of motion is modeled (except for Unsteady-RANS, in which coherent motions are partially resolved) [99]. Although RANS is inherently less expensive and has

moderate success in industrial applications, it fails to account for a very wide range of scales. Based on Kolmogorov's hypothesis, at sufficiently high Reynolds number, the small-scale motions are statistically isotropic and tend to be universal to model [110]. However, the large-scale motions are strongly dependent on flow conditions and geometric boundaries, thus it is impossible for RANS to achieve a universal model that can cover a wide range of scales in turbulent flows [98].

As a trade-off between the accuracy and computational cost of RANS and DNS, an intermediate technique known as Large-Eddy Simulation (LES) has been developed. LES features higher accuracy than RANS, while it requires much less computational effort compared to DNS. In LES, energy-containing large-scale motions are fully resolved with the grid and filter employed, while the effect of the smallest-scale motions of turbulence is modeled [98]. Since the small-scale motions are more isotropic and universal, they can be modeled in a universal manner with much less adjustments in model coefficients, as compared to the turbulent models for RANS simulations. The demanding computational cost to resolve all scales of motions explicitly and accurately in DNS is avoided.

LES seems promising to solve turbulent flow problems. However, difficulties arise near the wall region, where a series of important events occur. The production and dissipation of turbulent kinetic energy achieve peak values at less than 30 wall units [110]. The energy-containing scales depend on Reynolds number, but the growth of the small scales is prohibited by the presence of the wall, making the exchange mechanisms between large and small scales different from unconstrained flows. To capture the important energy-production events in the near-wall layer, an extremely fine grid is necessary, especially for high Reynolds number flows. Based on Chapman’s estimate [111], the boundary layer can be divided into outer and inner layers: the number of grid points scales with $Re^{0.4}$ for the outer layer, and scales with $Re^{1.8}$ for the inner layer. So for a boundary layer flow with a Reynolds number of 10^6, 99% of the grid points are

required to resolve the inner layer, whose thickness is only about 10% of the boundary layer. As pointed out by Piomelli [98], the wall layer modeling is probably the most urgent challenge when it is intended to apply LES to industrially interested flows. Wall-modeled LES (WMLES) have been studied by many researchers. Cabot [112] and Balaras et. al. [113] used two-layer boundary layer equations to model the near-wall region in LES of wall bounded shear flows. Spalart [114] proposed a Detached-Eddy Simulation (DES). It used Spalart-Allmaras turbulence model or k-omega SST model for the Reynolds stress and the sub-grid stress modeling. DES has been applied to massively separated flows and seems promising for wall bounded flows. More discussion on wall layer models can be found in review papers by Piomelli [98] and Spalart [114].

The small-scale motions are not resolved in LES; however, based on the energy cascade analysis, in this range of scales, viscous dissipations drain turbulent kinetic energy to internal energy. This part of turbulent motions has to be modeled with appropriate SGS models.

3.2.1 Filtered Governing Equations

In LES, large-scale motions, which carry most of the kinetic energy, are fully resolved, while small-scale motions, which are universal and appropriate to model, are simulated with SGS models. To separate the large-scale motions from the small-scale ones, a low-pass filtering operation is performed explicitly or implicitly. A filtered (or resolved) variable is defined as,

$$\tilde{f}(\boldsymbol{x}) = \int_{\infty} f(\boldsymbol{x}) G_f(\boldsymbol{x} - \boldsymbol{x}') d\boldsymbol{x}' , \tag{3.1}$$

where G_f is the filter function and satisfies $\int G_f(x')dx' = 1$. The filter function determines the size and structure of the small scales. Leonard [115] indicated that if G_f is only a function of $\boldsymbol{x} - \boldsymbol{x}'$, the differentiation and filtering operations could commute with each other. Although for stretched grids, the commutation between filtering and

differentiation is not strictly valid [116, 117], the commutation error is usually neglected for moderately stretched grids [118, 119]. The modeling error is found to be generally smaller than the discretization error [118]. One of the most commonly used filter functions, the box filter, which is also used in the current study, is defined as:

$$\overline{f}(\mathbf{x}) = \frac{1}{\Delta V}\int_{\Delta V} f(\mathbf{x})\, d\mathbf{x} \,. \tag{3.2}$$

With the box filter, any filtered quantity is simply its average in the control volume. A detailed description of properties of various filters can be found in standard textbooks [110].

Based on the Favre-averaging [120], any instantaneous variable (f) can be expressed as the sum of a Favre-averaged filtered scale ($\tilde{f}$) and a sub-filter scale (f'')

$$f = \tilde{f} + f'' \,, \tag{3.3}$$

where

$$\tilde{f} = \frac{\overline{\rho f}}{\overline{\rho}} \,. \tag{3.4}$$

Since $\overline{f}' \neq 0$ and $\tilde{f}'' \neq 0$, the filtering operation in LES is different from the conventional Reynolds averaging in time domain. The filtered Favre-averaged mass, momentum, energy, mixture fraction, and progress variable transport equations in conservative form can be written as

$$\frac{\partial \overline{\rho}}{\partial t} + \frac{\partial \overline{\rho}\tilde{u}_i}{\partial x_i} = 0 \,, \tag{3.5}$$

$$\frac{\partial \overline{\rho}\tilde{u}_i}{\partial t} + \frac{\partial (\overline{\rho}\tilde{u}_i\tilde{u}_j)}{\partial x_j} = -\frac{\partial \overline{p}}{\partial x_i} + \frac{\partial (\tilde{\tau}_{ij} - \tau_{ij}^{SGS})}{\partial x_j} \,,\ i = 1,2,3, \tag{3.6}$$

$$\frac{\partial \overline{\rho}\tilde{E}}{\partial t} + \frac{\partial \left[(\overline{\rho}\tilde{E} + \overline{p})\tilde{u}_i \right]}{\partial x_i} = \frac{\partial}{\partial x_i}\left(\overline{q}_i + \tilde{u}_j\tilde{\tau}_{ij} - Q_i^{SGS} - H_i^{SGS} + \sigma_i^{SGS} \right) \,, \tag{3.7}$$

where the SGS terms are defined as:

$$\tau_{ij}^{SGS} = \overline{\rho u_i u_j} - \bar{\rho}\tilde{u}_i\tilde{u}_j \ , \tag{3.8}$$

$$Q_i^{sgs} = (\overline{q}_i - \tilde{q}_i) \ , \tag{3.9}$$

$$H_i^{SGS} = \left(\overline{\rho E u_i} - \bar{\rho}\tilde{E}\tilde{u}_i\right) + \left(\overline{p u_i} - \bar{p}\tilde{u}_i\right) \ , \tag{3.10}$$

$$\sigma_{ij}^{SGS} = \left(\overline{u_j \tau_{ij}} - \tilde{u}_j\tilde{\tau}_{ij}\right) \ , \tag{3.11}$$

The pressure gradient term $\partial\bar{p}\delta_{ij}/\partial x_j$ is proportional to $1/M^2$. In low Mach flows, this term becomes singular and creates great numerical challenges, which makes preconditioning scheme necessary for fully compressible solver. The SGS stress term τ_{ij}^{SGS}, SGS energy flux term H_i^{SGS}, and SGS scalar flux terms Φ_j^{SGS} and Ψ_j^{SGS}, result from filtering the corresponding convective terms. The SGS viscous work term, σ_{ij}^{SGS}, comes from correlations of the velocity field with the viscous stress tensor. The modeling of these SGS terms is discussed in detail in the following subsections.

In addition to the conservation equations, the equation of state must also be filtered. The form of EOS can be written as

$$p = \rho RT = \rho R_u T/MW \tag{3.12}$$

Filtering EOS [121] gives us

$$\bar{p} = \bar{\rho}R\tilde{T} = \bar{\rho}R_u\tilde{T}/MW \tag{3.13}$$

The filtered total energy, $\tilde{E}$ can be approximated as

$$\tilde{E} = \tilde{h} - \frac{\bar{p}}{\bar{\rho}} + \frac{\tilde{u}_k^2}{2} + k^{SGS} = \tilde{\Psi} + \int_{p_0}^{p}\left[\frac{1}{\rho} + \frac{T}{\rho^2}\left(\frac{\partial\rho}{\partial T}\right)_p\right]dp - \frac{\bar{p}}{\bar{\rho}} + \frac{\tilde{u}_k^2}{2} + k^{SGS}, \tag{3.14}$$

where $\Psi = \sum_{k=1}^{N} Y_k h_k^0$ and $k^{SGS} = \frac{\tau_{kk}^{SGS}}{2\bar{\rho}} = \frac{1}{2}\left(\frac{\overline{\rho u_k u_k}}{\bar{\rho}} - u_k^2\right)$.

3.2.2 Subgrid-Scale Models

In LES, the unresolved motions of sub-grid scales have to be represented by an appropriate SGS model. Most of SGS models use the concept of eddy viscosity, ν_t,

which is similar to dynamic viscosity but generally with much higher value. Using eddy viscosity, the subgrid viscous shear stress can be written as,

$$\tau_{ij}^{SGS} - \frac{\delta_{ij}}{3}\tau_{kk}^{SGS} = -2\nu_t \tilde{S}_{ij}, \tag{3.15}$$

where $\tilde{S}_{ij}$ is the symmetric part of velocity gradient tensor, $S_{ij} = \frac{1}{2}\left(\frac{\partial u_i}{\partial x_j} + \frac{\partial u_j}{\partial x_i}\right)$. In the following section, two commonly used SGS models are introduced.

3.2.2.1 Algebraic Smagorinsky Model

The Smagorinsky SGS model [122] has been widely used because of its simplicity and good accuracy. The eddy viscosity is obtained algebraically to avoid solving additional equations. The model uses the equilibrium hypothesis, which claims that the small-scale motions with much short time scales, can rapidly adjust to the flow perturbations and recover equilibrium nearly instantaneously. A balance equation between turbulent kinetic energy production and viscous dissipation thus exists: $-\tau_{ij}\tilde{S}_{ij} = \epsilon_\nu$. Followed by this assumption, the Smagorinsky model is written as,

$$\nu_t = \left(C_S \bar{\Delta}\right)^2 \left|\tilde{S}\right|, \tag{3.16}$$

$$\left|\tilde{S}\right| = \sqrt{2\tilde{S}_{ij}\tilde{S}_{ij}}, \tag{3.17}$$

$$\bar{\Delta} = \sqrt[3]{\Delta_1 \Delta_2 \Delta_3}, \tag{3.18}$$

where $\bar{\Delta}$ is the filter width, which is usually proportional to the grid size. The coefficient C_s can be determined from a priori test on decaying isotropic turbulence [123] with C_s=0.16. Erlebacher et al. [124] extended the above model to compressible flows,

$$\tau_{ij}^{SGS} = -2\bar{\rho}\nu_t\left(\tilde{S}_{ij} - \frac{\delta_{ij}}{3}\tilde{S}_{kk}\right) + \frac{2}{3}\bar{\rho}k^{SGS}\delta_{ij}, \tag{3.19}$$

$$\nu_t = \left(C_R \Delta D\right)^2 \left|\tilde{S}\right|, \tag{3.20}$$

$$k^{SGS} = C_I(\Delta D)^2 \tilde{S}_{ij}\tilde{S}_{ij}, \tag{3.21}$$

where the dimensionless quantities C_R and C_I represent the compressible Smagorinsky constants. The Van-Driest damping function (D) is used to take into account the inhomogeneities near the wall [125], and is expressed as

$$D = 1 - \exp\left(-\left(y^+/25\right)^2\right), \tag{3.22}$$

where $y^+ = yu_\tau/\nu$ and u_t is friction velocity.

The subgrid energy flux term H_j^{SGS} is modeled based on the gradient transport assumption

$$H_i^{SGS} = --\bar{\rho}\frac{\nu_t}{Pr_t}\frac{\partial \tilde{H}}{\partial x_i} = -\bar{\rho}\frac{\nu_t}{Pr_t}\left(\frac{\partial \tilde{h}}{\partial x_i} + \tilde{u}_j\frac{\partial \tilde{u}_j}{\partial x_i} + \frac{1}{2}\frac{\partial k^{SGS}}{\partial x_i}\right) \tag{3.23}$$

where Pr_t represents the turbulent Prandtl number, and a standard value 1.0 is used. The SGS viscous work term, σ_{ij}^{sgs} , is neglected due to its small contribution to the total energy equation [98, 126].

The convective mixture fraction flux term is usually approximated as

$$\Phi_j^{sgs} = -\bar{\rho}\frac{\nu_t}{Sc_t}\frac{\partial \tilde{f}}{\partial x_j} \tag{3.24}$$

where Sc_t is the turbulent Schmidt number. However, the use of the gradient transport assumption for reactive species is questionable.

The algebraic Smagorinsky model described above is the most widely used model in LES. However, as pointed out by Germano et al. [127], it has several limitations. First, the optimal model constant must be changed for a different class of flows. The model does not have the accurate limiting behavior near the wall [128]. The SGS stress does not vanish in laminar flow and the model is found to be very dissipative in the laminar/transition region. In addition, the model does not account for the backscatter of

energy from small to large scale, which has been shown to be of importance in the transition region.

3.2.2.2 Dynamic Smagorinsky Model

The dynamic model introduced by Germano et al. [127] improves some of the aforementioned deficiencies in algebraic models. The dynamic model uses the assumption of scale invariance by applying the coefficient measured from the resolved scales to the SGS range. It calculates the model coefficients dynamically from the information already contained in the resolved velocity field during the simulation. Apply the test-filter $\tilde{\bar{G}}$, with characteristic $\tilde{\bar{\Delta}} > \bar{\Delta}$ (typically, $\tilde{\bar{\Delta}} = 2\bar{\Delta}$), to the equations of motion, one obtains filtered governing equations similar to Eqns. 3.5-3.7, but replacing $\tilde{f} = \overline{\rho f} / \bar{\rho}$ with $\tilde{\bar{f}} = \overline{\rho f}/\tilde{\bar{\rho}}$, yields the sub-test scale stress T_{ij}, defined as:

$$T_{ij} = \overline{\rho u_i u_j} - \bar{\rho}\bar{u}_i\bar{u}_j. \tag{3.25}$$

Formally, the dynamical procedure is based on the Germano identity [129]

$$L_{ij} = T_{ij} - \tau_{ij}^{SGS} = \bar{\rho}\tilde{u}_i\tilde{u}_j - \bar{\rho}\bar{u}_i\bar{u}_j. \tag{3.26}$$

The following expressions can be derived for the dynamic evaluation of C_R and C_I using the least square minimization approach of Lilly [130] for the momentum SGS stress tensor.

$$C_R = \frac{\langle L_{ij} M_{ij} \rangle}{\langle M_{kl} M_{kl} \rangle} - \frac{1}{3} \frac{\langle M_{mn} M_{mn} \rangle}{\langle M_{kl} M_{kl} \rangle} \tag{3.27}$$

$$C_I = \frac{\langle L_{kk} \rangle}{\langle \beta - \langle \alpha \rangle \rangle} \tag{3.28}$$

The forms of M_{ij}, β and α are given as follows

$$M_{ij} = \beta_{ij} - \langle \alpha_{ij} \rangle \tag{3.29}$$

$$\beta_{ij} = -2\hat{\Delta}^2 \langle \bar{\rho} \rangle \left| \bar{\tilde{S}} \right| (\bar{\tilde{S}}_{ij} - \frac{\delta_{ij}}{3} \bar{\tilde{S}}_{kk}) \tag{3.30}$$

$$\alpha_{ij} = -2\Delta^2 \bar{\rho} \left| \tilde{S} \right| (\tilde{S}_{ij} - \frac{\delta_{ij}}{3} \tilde{S}_{kk}) \tag{3.31}$$

$$\alpha = 2\bar{\rho}\Delta^2 \left| \tilde{S} \right|^2 \tag{3.32}$$

$$\beta = 2\hat{\Delta}^2 \langle \bar{\rho} \rangle \left| \bar{\tilde{S}} \right|^2 \tag{3.33}$$

The same idea can be applied to model SGS turbulent stress to dynamically calculate the turbulent Prandtl number and Schmidt number in Eq. 3.23 and Eq. 3.24.

3.2.3 Turbulence/Combustion Interaction Models

In LES, although the energy-carrying eddy motions are resolved with sufficient grid resolution, motions of small scales, such as the Kolmogorov scale, are not resolved, which plays a crucial role in reactant mixing at molecular levels. The chemical reaction rate is a very strong nonlinear function of local species concentration and temperature at the molecular level, which are highly dependent on the turbulent mixing. Chemical reactions release heat and alter species concentration and temperature gradients of the smallest turbulent eddies, which in turn change the turbulent mixing process. Chemical reaction occurring at different time scales may interact with turbulence eddies of different length/time scales, which further complicates the picture. The interaction of these two processes occurs at length scales from the smallest turbulent scales to much larger inertial sub-range scales, which cannot be completely resolved in LES studies. The physical processes associated with these interactions are modeled with turbulent combustion models.

3.2.3.1 Finite Rate Chemistry (FRC) Models

The FRC models are preferred to handle flows that involve variable Lewis number mixing, extinction, ignition, emissions, fuel modulation, and combustion with

multiple modes. In this study, to avoid interpolation between grids and particles in Lagrangian formulation, an Eulerian formulation is employed to track the detailed species transport. The Favre-filtered transport equation of species concentrations in fully compressible flow is given as follows:

$$\frac{\partial \bar{\rho}\tilde{Y}_k}{\partial t} + \frac{\partial (\bar{\rho}\tilde{u}_j \tilde{Y}_k)}{\partial x_j} = \frac{\partial}{\partial x_j}\left(\bar{\rho}\widetilde{U}_{k,j}\tilde{Y}_k - \Phi_{k,j}^{sgs}\right) + \bar{\dot{\omega}}_k \tag{3.34}$$

The unclosed filtered species net mass production rate $\bar{\dot{\omega}}_k$ is the key for turbulence/combustion modeling. There are several finite rate combustion models for the LES of turbulent combustion.

The most straightforward way is to evaluate the filtered reaction rate from the filtered quantities, without consideration of the sub-grid interactions of turbulence and chemistry. This method is called “laminar chemistry model” or “no model”, which has been used by several researchers due to its simplicity [131, 132]. As shown in the past studies, it actually has similar accuracy as many other major Eulerian SGS closure models [45, 46]. In addition, if the simple laminar chemistry FRC model could provide more accurate predictions than FGM models, more advanced FRC models are also expected to be more accurate than FGM models. Therefore, this model is adopted in the present study.

Conditioned Momentum Closure (CMC) was developed by Klimenko [133] and Bilger [134] independently for non-premixed turbulent combustion. Variables of interest are conditioned with mixture fraction before the Favre averaging to obtain conditional moment equations. CMC has been used in homogenous and boundary layer flows. With those applications, CMC can be related to flamelet equations [135]. However, this method solves conditional species equations for all species; the computational cost increases with the number of species, which may become prohibitively costly when detailed chemical mechanism is used.

The Linear-Eddy Model (LEM) was developed by Kerstein [136, 137] has been used by the author, Menon and colleagues [104, 138]. The one-dimensional laminar reactive scalar field is combined with stochastically independent rearrangement events to mimic turbulence/chemistry interactions. However, this model suffers from prohibitive computational costs in applications.

The Monte Carlo method for PDF transport equations was developed by Pope and extensively tested in RANS and LES [135]. However, the formulation is very complicated, and the computation cost is considerably high for even a moderate number of species.

Dynamically thickened flame was developed by Légier et al. [139] for both premixed- and non-premixed combustion. This model can account for unsteady combustion such as extinction, re-ignition etc. However, it has similar difficulties when detailed chemistry is used.

3.2.3.2 Laminar Flamelet Model

Flamelet concept and flamelet generated manifold (FGM) models proposed by Peters [135] has been extensively studied. The basic assumption of the laminar flamelet model is that the chemical time scales are shorter than that of the smallest turbulent eddies: Kolmogorov scales. Consequently, a turbulent flame can be envisioned as a synthesis of thin reaction zones (i.e., flamelets) embedded in an otherwise inert turbulent flow field. The inner structure of the flame can be handled separately from turbulent flow simulations. Instead of directly treating the reactive scalar (i.e., species concentration), the focus is placed on the identification of the flame surface in the flow-field, which can be obtained by solving the conservation equation of the mixture fraction together with the mass, momentum, and energy equations.

The flame thickness is smaller than the grid size employed in LES and is not actually resolved. Therefore, the filtered species mass fraction of the i^{th} species, $\tilde{Y}_i(x,t)$,

in each computational cell should be evaluated by convoluting the state relationships, $Y_i(f,\chi_{\mathrm{st}})$, with the *SGS* Filtered Density Function (*FDF*) of mixture fraction, $\tilde{P}(f)$, and the *SGS FDF* of scalar dissipation rate, $\tilde{P}(\chi_{st})$, as shown below:

$$\tilde{Y}_i(x,t)=\int_0^1\int_0^\infty Y_i(f,\chi_{st})\tilde{P}(\chi_{st})\tilde{P}(f)d\chi_{st}df. \tag{3.35}$$

It should be noted that a statistical independence is intrinsically assumed in above relation between the *SGS* variations of mixture fraction and scalar dissipation. A presumed β-shaped Probability Density Function (PDF) parameterized by the filtered mixture fraction and its SGS variance commonly represents the unresolved SGS fluctuation of the mixture fraction. The full equation is shown in the following where Γ is the γ-function.

$$P\left(f;\tilde{f},f''^2\right)=\frac{f^{\alpha-1}(1-f)^{\beta-1}}{\Gamma(\alpha)\Gamma(\beta)}\Gamma(\alpha+\beta), \tag{3.36}$$

The parameters α and β are defined as

$$\alpha=\tilde{f}\left[\frac{\tilde{f}\left(1-\tilde{f}\right)}{f''^2}-1\right], \tag{3.37}$$

$$\beta=\left(1-\tilde{f}\right)\left[\frac{\tilde{f}\left(1-\tilde{f}\right)}{f''^2}-1\right]. \tag{3.38}$$

The *SGS* variance of mixture fraction, f''^2 , is modeled based on the scale similarity assumption [140],

$$f''^2=K_b\bar{\rho}\overline{\left(\tilde{f}-\tilde{\bar{f}}\right)^2}/\bar{\bar{\rho}}, \tag{3.39}$$

where K_b is a model constant chosen as 3. It has been validated by many researchers that the β -function *PDF* provides an excellent estimation of the *SGS* mixture fraction distribution for non-premixed reacting turbulent flows [141]. For simplicity, the *SGS* FDF of the scalar dissipation rate, $\tilde{P}(\chi_{st})$, which is typically assumed to be lognormal, is considered as a Dirac peak at the filtered scalar dissipation rate. Further investigation is

required to validate this assumption. The filtered rate of scalar dissipation, $\tilde{\chi}$, is modeled based on the eddy viscosity approach as suggested by Girimaji and Zhou [142]

$$\tilde{\chi} = 2(\frac{\nu}{Sc} + \frac{\nu_t}{Sc_t})(\frac{\partial f}{\partial x_j}\frac{\partial f}{\partial x_j}) \ . \tag{3.40}$$

The thermo-chemistry state relation is established through a steady-state flamelet approach. Taking advantage of the fact that the flamelet library only needs to be calculated once for every specified case, chemistry kinetics with any number of species and reaction steps can be used to establish the flamelet library. The flamelet library should cover a broad range of strain rates, from near chemistry equilibrium to near-extinction limit. For all the calculations, the pressure is set fixed as the application; and the inlet temperatures of the fuel and oxidizer take the corresponding inlet temperature of the application cases. Consistent with the flamelet assumption, the corresponding scalar dissipation rate, χ , for each solution is evaluated as a function of filtered mixture fraction. The solutions are then integrated based on Eq. 3.35 and tabulated as functions of $\tilde{\chi}$, $\tilde{f}$, and f''^2. The calculated filtered mixture fraction, mixture fraction variance, and the scalar dissipation rate from LES simulation are used to determine the appropriate entry in the table. In particular, the filtered mixture fraction $\tilde{f}$ is solved from the following transport equation:

$$\frac{\partial \bar{\rho}\tilde{f}}{\partial t} + \frac{\partial(\bar{\rho}\tilde{u}_j\tilde{f})}{\partial x_j} = \frac{\partial}{\partial x_j}\left(\bar{\rho}D\frac{\partial \tilde{f}}{\partial x_j} - \Phi_j^{SGS}\right) , \tag{3.41}$$

where the SGS term is defined as:

$$\Phi_j^{SGS} = \left(\overline{\rho u_j f} - \bar{\rho}\tilde{u}_j\tilde{f}\right) , \tag{3.42}$$

In the present study, the flamelet library is generated from steady-state laminar counter-flow diffusion flames. Thus, the species profile does not include the history effect of the chemical reactions, i.e. the time taken to achieve the steady state flame

profile. In a real turbulent flame, slow chemistry reactions, such as CO oxidation, take a much longer time compared to other reactions. Following Peters' argument, if the scalar dissipation rate is changing slowly enough so that the change of chemical reactions can follow the pace of the local flow variations, the steady flamelet is a valid assumption [135]. Otherwise, the unsteady effect may become important. According to Pitsch *et al.* [143], it is valid to apply a steady flamelet within the range of 30 nozzle diameter from the fuel nozzle exit. Extreme caution must be taken in the further downstream, where the scalar dissipation rate becomes small and the chemistry may not be fast enough to follow the flow variations.

As pointed out by Poinsot and Veynante [144], the effect of external mixing (turbulent flow) is lumped into the scalar dissipation rate, while chemistry is decoupled from the flow and retrieved from the lookup table. Consequently, the scalar dissipation rate accounts for the effect of turbulent mixing as an external parameter on the laminar flamelet structures. The procedure to estimate this variable directly affects the chemical species distribution, the flame structure, and the combustion dynamics. Instead of assuming a pre-assumed shape of scalar dissipation as proposed by Peters, the scalar dissipation as a function of the mixture fraction is calculated from the laminar counter-flow flamelets, which are generated in physical space using a one-dimensional code [145, 146]. This is different from Pitsch's methods, which are conducted in the mixture fraction space, and the dependence of scalar dissipation is modeled by an exponential function of the mixture fraction.

3.2.3.3 Flamelet/Progress-Variable (FPV) Model

Although the laminar flamelet method is easy to implement and inexpensive, it has several drawbacks. Firstly, the mixture fraction essentially does not carry information about the chemical reaction state. The flamelet method uses the scalar dissipation rate as an additional parameter to account for the flame stretching and quenching effect.

However, the scalar dissipation rate does not provide a unique mapping from the mixture fraction to the corresponding chemical state. A pure mixing of fuel and oxidizer cannot be accounted for in the flamelet method if the local scalar dissipation is smaller than the quenching limit. This drawback is due to the lack of information regarding the local chemical state in the flow field. The Flamelet/Progress-Variable (FPV) method is able to overcome the limitations of the flamelet method by incorporating an additional transport equation for tracking a scalar in the form of a progress variable.

$$\frac{\partial \bar{\rho}\tilde{C}}{\partial t}+\frac{\partial(\bar{\rho}\tilde{u}_j\tilde{C})}{\partial x_j}=\frac{\partial}{\partial x_j}\left(\bar{\rho}D\frac{\partial \tilde{C}}{\partial x_j}-\Psi_j^{SGS}\right)+\overline{\dot{\omega}_C}\ , \tag{3.43}$$

Where the progress variable C is often defined as:

$$C = Y_{CO} + Y_{CO_2} + Y_{H_2} + Y_{H_2O}, \tag{3.44}$$

and the SGS term is defined as:

$$\Psi_j^{SGS}=\left(\overline{\rho u_j C}-\bar{\rho}\tilde{u}_j\tilde{C}\right)\ . \tag{3.45}$$

The resolved-scale progress variable production rate, $\overline{\dot{\omega}_C}$, is also unclosed. The source term $\bar{\dot{\omega}}_C$ for the filtered progress variable $\tilde{C}$ can only be roughly estimated, and is integrated explicitly assuming the timescale of progress variable is larger than Δt, which may not be true.

From the implementation point of view, the FPV library differs from the steady laminar flamelet library mainly as follows. (1) The library is parametrized by filtered progress variable instead of filtered dissipation rate of mixture fraction. (2) The library needs to cover part of the unstable branch of the S-shaped curve of ignition and extinction to account for the unsteady effects to some extent. During the simulation, the filtered mass fractions and their gradients are retrieved from the library as functions of filtered mixture fraction, its variance, and the filtered progress variable.

This method has been developed to account for extinction, ignition, and unsteady mixing effect [56].

3.2.3.4 Differential Diffusion Effect

Without solving the species transport equation, constant Lewis number has to be assumed to derive the mixture fraction and progress variable equation for FGM models, including laminar flamelet and FPV models [135]. It is interesting to know how much accuracy of numerical solution is sacrificed by this assumption. The effect of differential diffusion has been examined by Pitsch and Peters [147]. They found that the existence of a laminar region in the near field of the jet exit causes the differential diffusion effect, which is only important within a 10-diameter distance from the jet exit. However, the temperature and the species concentration distributions are influenced by the differential diffusion effect farther downstream. Generally, in the regions with low turbulence intensity, α_t is smaller than $\tilde{\alpha}_Z$ and $\tilde{\alpha}_C$, thus differential diffusion effects become important, which is likely to introduce relatively larger errors to FPV model. In the process of building the flamelet library, the differential diffusion effect is considered within the model used herein [148].

3.2.4 Preconditioning Scheme

Using laminar flamelet model as an example, the three-dimensional, unsteady, Favre-filtered governing equations listed in Chapter 2 can be re-written in a vector form:

$$\frac{\partial \mathbf{Q}}{\partial \mathrm{t}}+\frac{\partial(\mathbf{E}-\mathbf{E}_{\mathrm{v}})}{\partial \mathrm{x}}+\frac{\partial(\mathbf{F}-\mathbf{F}_{\mathrm{v}})}{\partial \mathrm{y}}+\frac{\partial(\mathbf{G}-\mathbf{G}_{\mathrm{v}})}{\partial \mathrm{z}}=\mathbf{H}, \tag{3.46}$$

where the vectors $\mathbf{Q}, \mathbf{E}, \mathbf{F}, \mathbf{G}, \mathbf{E}_{\mathrm{v}}, \mathbf{F}_{\mathrm{v}}, \mathbf{G}_{\mathrm{v}}$ and $\mathbf{H}$ are defined as:

$$\mathbf{Q}=\left(\bar{\rho}, \bar{\rho}\tilde{u}, \bar{\rho}\tilde{v}, \bar{\rho}\tilde{w}, \bar{\rho}\tilde{E}, \bar{\rho}\tilde{f}\right)^{T}, \tag{3.47}$$

$$\mathbf{E}=\left(\bar{\rho}\tilde{u}, \bar{\rho}\tilde{u}^{2}+\bar{p}, \bar{\rho}\tilde{u}\tilde{v}, \bar{\rho}\tilde{u}\tilde{w}, \left(\bar{\rho}\tilde{E}+\bar{p}\right)\tilde{u}, \bar{\rho}\tilde{u}\tilde{f}\right)^{T}, \tag{3.48}$$

$$\mathbf{F} = \left(\bar{\rho}\tilde{v}, \bar{\rho}\tilde{u}\tilde{v}, \bar{\rho}\tilde{v}^2 + \bar{p}, \bar{\rho}\tilde{v}\tilde{w}, \left(\bar{\rho}\tilde{E} + \bar{p} \right) \tilde{v}, \bar{\rho}\tilde{v}\tilde{f} \right)^T \quad , \tag{3.49}$$

$$\mathbf{G} = \left(\bar{\rho}\tilde{w}, \bar{\rho}\tilde{u}\tilde{w}, \bar{\rho}\tilde{v}\tilde{w}, \bar{\rho}\tilde{w}^2 + \bar{p}, \left(\bar{\rho}\tilde{E} + \bar{p} \right) \tilde{w}, \bar{\rho}\tilde{w}\tilde{f} \right)^T \quad , \tag{3.50}$$

$$\mathbf{E}_v = \begin{pmatrix} 0, \bar{\tau}_{xx} - \tau_{xx}^{sgs}, \bar{\tau}_{xy} - \tau_{xy}^{sgs}, \bar{\tau}_{xz} - \tau_{xz}^{sgs}, \tilde{u}\bar{\tau}_{xx} + \tilde{v}\bar{\tau}_{xy} + \tilde{w}\bar{\tau}_{xz} + \bar{q}_x - H_x^{sgs} + \sigma_x^{sgs}, \\ \bar{\rho}D\tilde{f}_x + \bar{\rho}\dfrac{\nu_t}{Sc_t}\tilde{f}_x \end{pmatrix}^T \quad , \tag{3.51}$$

$$\mathbf{F}_v = \begin{pmatrix} 0, \bar{\tau}_{xy} - \tau_{xy}^{sgs}, \bar{\tau}_{yy} - \tau_{yy}^{sgs}, \bar{\tau}_{yz} - \tau_{yz}^{sgs}, \tilde{u}\bar{\tau}_{xy} + \tilde{v}\bar{\tau}_{yy} + \tilde{w}\bar{\tau}_{yz} + \bar{q}_y - H_y^{sgs} + \sigma_y^{sgs}, \\ \bar{\rho}D\tilde{f}_y + \bar{\rho}\dfrac{\nu_t}{Sc_t}\tilde{f}_y \end{pmatrix}^T \quad , \tag{3.52}$$

$$\mathbf{G}_v = \begin{pmatrix} 0, \bar{\tau}_{xz} - \tau_{xz}^{sgs}, \bar{\tau}_{yz} - \tau_{yz}^{sgs}, \bar{\tau}_{zz} - \tau_{zz}^{sgs}, \tilde{u}\bar{\tau}_{xz} + \tilde{v}\bar{\tau}_{yz} + \tilde{w}\bar{\tau}_{zz} + \bar{q}_z - H_z^{sgs} + \sigma_z^{sgs}, \\ \bar{\rho}D\tilde{f}_z + \bar{\rho}\dfrac{\nu_t}{Sc_t}\tilde{f}_z \end{pmatrix}^T \quad , \tag{3.53}$$

$$\mathbf{H} = \left(0, 0, 0, 0, 0, 0 \right)^T \quad , \tag{3.54}$$

where the superscript T stands for the transpose of the vector.

There are severe numerical challenges in solving these equations for high-pressure mixing and combustion. The rapid variation of the fluid state and wide range of characteristic time and length scales pose the well-known stiffness problem. The stiffness of the system results from: 1) ill-conditioned eigenvalues; 2) competing convective and diffusion processes; and 3) pressure singularities in the momentum equation.

The Mach number in present simulations is relatively small, and thus the dynamic pressure is negligibly smaller than the static pressure (high-pressure situations). This could cause the computer round-off error override the dynamic pressure in the momentum equation, thus raise the pressure singularity problem. To overcome this difficulty, the static pressure is decomposed into a constant reference pressure and a gauge pressure [149, 150],

$$p = p_0 + p_g \quad . \tag{3.55}$$

Here the averaged pressure in the flow field is generally selected as the reference pressure, while the gauge pressure is the fluctuating part induced by unstable flow motions. With this decomposition, p is replaced with p_g in the momentum equations. By this way, the acoustic waves can be captured accurately.

To solve the ill-conditioned eigenvalue problem, let us look at the following equation:

$$\frac{\partial \boldsymbol{Q}}{\partial \boldsymbol{t}} + \mathbf{A}\frac{\partial \boldsymbol{Q}}{\partial \boldsymbol{x}} + \mathbf{B}\frac{\partial \boldsymbol{Q}}{\partial \boldsymbol{y}} + \mathbf{C}\frac{\partial \boldsymbol{Q}}{\partial \boldsymbol{z}} = 0 \,, \tag{3.56}$$

where $\mathrm{A} = \partial \mathrm{E}/\partial \mathrm{Q}$, $\mathbf{B} = \partial \mathbf{F}/\partial \mathbf{Q}$, and $\mathbf{C} = \partial \mathbf{G}/\partial \mathbf{Q}$ are the Jacobian matrices. Analysis shows that the eigenvalues of matrix **A** is:

$$\lambda_1 = \tilde{u} + \tilde{c}, \lambda_2 = \tilde{u} - \tilde{c}, \lambda_{3,4,5,6} = \tilde{u} \,. \tag{3.57}$$

In low Mach number flows, $M \ll 1$, the ratio of the largest eigenvalue to the smallest one is close to inverse of Mach number, indicating that the eigenvalues are differed by order of magnitude. For a given CFL number, the maximum local time step determined by the largest eigenvalue hence is extremely small, resulting in a very slow convergence. It becomes unacceptable for even lower-Mach number or time accurate simulations.

To cure the eigenvalue disparity problem in low Mach number flows, the time-derivative preconditioning method [149-152] are implemented. Zong and Yang [153] made further improvement by changing primitive variable *h* to *T*, getting rid of the cost intensive computation associated with iterative calculations to get temperature from enthalpy. A unified treatment of thermodynamic properties and associated preconditioning matrix makes the numerical scheme accurate, robust, and efficient.

The basic idea of the preconditioning method is to add a pseudo-time differential term, with multiplication factor of a preconditioning matrix:

$$\Gamma\frac{\partial \mathbf{Z}}{\partial t}+\frac{\partial \mathbf{Q}}{\partial t}+\frac{\partial\left(\mathbf{E}-\mathbf{E}_{\mathbf{v}}\right)}{\partial x}+\frac{\partial\left(\mathbf{F}-\mathbf{F}_{\mathbf{v}}\right)}{\partial y}+\frac{\partial\left(\mathbf{G}-\mathbf{G}_{\mathbf{n}}\right)}{\partial z}=\mathbf{H}, \tag{3.58}$$

$$\mathbf{Z}=\left(\bar{\mathbf{p}}_{\mathbf{g}}, \tilde{u}, \tilde{v}, \tilde{w}, \tilde{T}, \tilde{f}\right)^{T} . \tag{3.59}$$

If Γ is chosen carefully so that the eigenvalues of these matrixes are of the same order of magnitude, the resulting equations have well-conditioned eigenvalues and converge efficiently in all Mach number flows. An implicitly iterative process is conducted for the asymptotic time advancing in the pseudo-time inner loop. When the pseudo-time iteration converges, i.e. steady state solutions with respect to pseudo-time stepping are achieved, the physical time-accurate solutions of the original governing equations are recovered. Practically, 40~60 pseudo-time iterations are enough for convergence. It can be seen that the efficiency of preconditioning method is largely determined by the selection of the preconditioning matrix.

Following Zong [154], the transfer matrix is derived as:

$$T=\frac{\partial \mathbf{Q}}{\partial \mathbf{Z}} . \tag{3.60}$$

In this matrix, a common term $\left(\frac{\partial \rho}{\partial p}\right)_{T,Y_i}$ can be related to speed of sound and specific heat capacity ratio:

$$\left(\frac{\partial \rho}{\partial p}\right)_{T,Y_i}=\frac{C_p}{C_v}\left(\frac{\partial \rho}{\partial p}\right)_{s,Y_i}=\frac{\gamma}{a^2} . \tag{3.61}$$

Here, a^2 is replaced with β to define the preconditioning matrix,

$$\Gamma = \begin{pmatrix} \frac{\gamma}{\beta} & 0 & 0 & 0 & \rho_T & \rho_f \\ \frac{\gamma}{\beta}\tilde{u} & \bar{\rho} & 0 & 0 & \tilde{u}\rho_T & \tilde{u}\rho_f \\ \frac{\gamma}{\beta}\tilde{v} & 0 & \bar{\rho} & 0 & \tilde{v}\rho_T & \tilde{v}\rho_f \\ \frac{\gamma}{\beta}\tilde{w} & 0 & 0 & \bar{\rho} & \tilde{w}\rho_T & \tilde{w}\rho_f \\ \frac{\gamma}{\beta}\tilde{h}_t + \frac{\tilde{T}}{\bar{\rho}}\rho_T & \bar{\rho}\tilde{u} & \bar{\rho}\tilde{v} & \bar{\rho}\tilde{w} & \bar{\rho}c_p + h_t\rho_T & \rho_f E + \bar{\rho}E_f \\ \frac{\gamma}{\beta}\tilde{f} & 0 & 0 & 0 & \rho_T\tilde{f} & \bar{\rho} + \tilde{f}\rho_f \end{pmatrix}, \quad (3.62)$$

where $\tilde{h}_t$ is the total specific enthalpy, and β is defined as

$$\beta = \frac{\gamma\varepsilon a^2}{1+(\gamma-1)\varepsilon}, \quad (3.63)$$

where ϵ ($0 < \epsilon \leq 1$) is the preconditioning factor. Unlike the definition of preconditioning matrix by other researchers, all of the off-diagonal terms have been retained. By keeping these terms, the unaltered system is identically restored as $\epsilon \to 1$;

$$\lim_{\varepsilon \to 1} \Gamma = T . \quad (3.64)$$

The conditioned governing equations in the pseudo-time space are characterized by the new Jacobian matrices, $\Gamma^{-1}A_v$, $\Gamma^{-1}B_v$, $\Gamma^{-1}C_v$, the eigenvalues of which are given by:

$$\begin{aligned} \lambda_1 &= \frac{1}{2}[U(\varepsilon+1) + \sqrt{U^2(1-\varepsilon)^2 + 4\varepsilon a^2}], \\ \lambda_2 &= \frac{1}{2}[U(\varepsilon+1) - \sqrt{U^2(1-\varepsilon)^2 + 4\varepsilon a^2}], \\ \lambda_{3,4,5,6} &= U , \end{aligned} \quad (3.65)$$

where U represents $\tilde{u}$, $\tilde{v}$, and $\tilde{w}$ in x-, y- and z-direction, respectively. If ε is small enough, the first two eigenvalues can achieve the same order of magnitude as others.

Note that no assumption is made to the form of the EOS, it can be applied to any fluid state without loss of accuracy.

3.2.4.1 Determination of the Preconditioning Factor

From the definition of the preconditioning matrix, and the resulting system eigenvalues, it is clear that the effectiveness of the preconditioning method is totally determined by the choice of the preconditioning factor, ε. The value of ε in each computational cell is crucial to get well-conditioned eigenvalues and thus the fast convergence of the numerical scheme.

Various time scales are associated with each computational cell in each direction, due to local flow convection, acoustic propagation, momentum, and thermal and mass diffusion processes. These processes have to be taken into account when choosing the preconditioning factor. The non-dimensional numbers characterizing the time scales associated with these physical processes are CFL number, Mach number, von Neumann number, cell Reynolds number, Prandtl number, and Schmidt number.

The CFL number, which characterizes the local convective propagation rates in the three coordinate directions are defined as:

$$CFL_x = \frac{\rho(\lambda_x)\Delta\tau}{\Delta x},\ CFL_y = \frac{\rho(\lambda_y)\Delta\tau}{\Delta y},\ CFL_z = \frac{\rho(\lambda_z)\Delta\tau}{\Delta z}, \tag{3.66}$$

where $\rho(\lambda_x)$, $\rho(\lambda_y)$, $\rho(\lambda_z)$ are the maximum eigenvalues in each direction, respectively.

The von Neumann number, which characterizes the diffusion propagation rates, is defined as:

$$VNN_x = \frac{\nu\Delta\tau}{\Delta x^2},\ VNN_y = \frac{\nu\Delta\tau}{\Delta y^2},\ VNN_z = \frac{\nu\Delta\tau}{\Delta z^2}, \tag{3.67}$$

The cell Reynolds number, which indicates the ratio of local velocities to momentum diffusion velocity, is defined as:

$$\mathrm{Re}_x = \frac{\tilde{u}\Delta x}{\nu},\ \mathrm{Re}_y = \frac{\tilde{v}\Delta y}{\nu},\ \mathrm{Re}_z = \frac{\tilde{w}\Delta z}{\nu}, \tag{3.68}$$

If the respective quantities *Re, RePr,* and *ReSc* exceed unity in one of directions, the convection velocity is larger than the corresponding velocity scale, thus convective effects dominant and the conservation equations exhibit a hyperbolic character. For this situation, an inviscid criterion must be employed. If *Re, RePr,*or *ReSc* are less than or equal to unity, diffusive effects dominate, a parabolic character is exhibited and a viscous criteria must be employed.

The final preconditioning factor is selected based on the methodology developed by Choi and Merkel [149], Buelow et al. [155], and Venkateswaran and Merkel [156]. Optimal values are specified locally as:

$$\varepsilon = \min[1, \max(\varepsilon_{inv}, \varepsilon_{vis})]\ . \tag{3.69}$$

The subscripts refer to the inviscid and viscous preconditioning factors, respectively. The criteria employed to evaluate these terms are discussed below.

In the limit of infinitely large Reynolds numbers, or inviscid flows, following Choi and Merkle [149], ε is assigned a value proportional to the local Mach number to ensure that the pseudo acoustic speed and flow velocity are of the same order of magnitude. To achieve correct limiting behavior, as Mach number approaches zero (e.g. in the stagnant region), a minimum value (typically 10^{-5}) is used. The resulting preconditioning factor is defined as:

$$\varepsilon_{inv} = \begin{cases} \varepsilon^2, & M < \varepsilon\ ; \\ 2M^2, & \varepsilon < M < 1\ ; \\ 1, & M \geq 1\ . \end{cases} \tag{3.70}$$

In inviscid flows, above equation gives minimal disparity in system eigenvalues and optimal damping rates. The convergence rate is primarily dependent on the local pseudo CFL number, which is determined by the stability criterion.

In regions where diffusion processes are important, the effect of diffusion on the preconditioning factor has to be considered. Buelow et al. [155, 157] have conducted a variety of studies to determine an optimal viscous preconditioning factor for the Navier-Stokes equations. Results from stability analysis indicate that three different requirements must be addressed in order to specify a generalized criterion. For high cell Reynolds numbers ($Re \gg 1$), the acoustic wave speeds should be scaled to the same order of magnitude as the particle speeds, as is accomplished by the inviscid preconditioning factor defined by Eq. 3.70. For low cell Reynolds numbers ($Re \ll 1$) and high acoustic cell Reynolds numbers ($\frac{Re}{M} \gg 1$), the diffusion rates should be scaled to the same order of magnitude as the acoustic speeds. For low cell Reynolds numbers and low acoustic cell Reynolds numbers, the diffusion rates should be scaled to the particle speeds. The only way to satisfy these conditions simultaneously is to define a viscous preconditioning factor that is dependent on the Fourier wavenumber. Such a definition is not appropriate for implementation in a CFD code. To overcome the difficulties outlined above, a preconditioning factor based on local length scales, which is tuned to damp the low wavenumber modes, has been developed. This definition requires a priori assumption of the orientation of dominating convective and diffusion processes within a given grid configuration and the choice of ε_{vis} is somewhat more involved. In three dimensions, there are three possible CFL numbers, and two possible VNN numbers, and six possible values of ε_{vis}. The most restrictive of the CFL and VNN numbers are usually chosen for stability reasons and these values are the most likely candidates for determining ε_{vis}.

In practice, the grid system is stretched near the wall, so that predominating diffusion processes, which are in a direction normal to the predominating convective processes, are resolved. Under these conditions, the rate limiting diffusion processes typically coincide with the maximum von Neumann number in a given cell. To retain the benefits of the time step given by CFL conditions, this quantity must be optimized with

respect to the minimum CFL number. Performing this operation yields an expression of the form

$$\varepsilon_{vis} = \max\left[\frac{\tilde{u}^2 \delta_x (\delta_x - 1)}{\tilde{u}^2 \delta_x^2 + a^2}, \ \frac{\tilde{v}^2 \delta_y (\delta_y - 1)}{\tilde{v}^2 \delta_y^2 + a^2}, \ \frac{\tilde{w}^2 \delta_z (\delta_z - 1)}{\tilde{w}^2 \delta_z^2 + a^2} \right], \tag{3.71}$$

where

$$\begin{aligned} \delta_x &= \max(\nu, \ \frac{\nu}{\mathrm{Pr}}, \ \frac{\nu}{Sc_i}) \frac{1}{\tilde{u}} \frac{CFL}{VNN} \ , \\ \delta_y &= \max(\nu, \ \frac{\nu}{\mathrm{Pr}}, \ \frac{\nu}{Sc_i}) \frac{1}{\tilde{v}} \frac{CFL}{VNN} \ , \\ \delta_z &= \max(\nu, \ \frac{\nu}{\mathrm{Pr}}, \ \frac{\nu}{Sc_i}) \frac{1}{\tilde{w}} \frac{CFL}{VNN} \ . \end{aligned} \tag{3.72}$$

This equation takes into account the effects of momentum, energy, and mass diffusion processes on the overall convergence rate.

The pseudo-time step size $\Delta\tau$ is determined based on the numerical stability of the algorithm and could be modified to provide the optimal convergence rate for the pseudo-time iteration process. Practically, pseudo-time CFL numbers between 5 and 10 are chosen.

3.2.5 Spatial Discretization

3.2.5.1 Finite Volume Approach

The conservation laws of fluid motion presented in Chapter 2 can be expressed in differential or integral form. The former can be solved by finite differencing approach, but it has inherent difficulties associated with irregular gird system [158]. Integral methods, including finite volume and finite element methods, can ensure the conservation of properties in each computational cell. In the current study, finite volume approach is thus implemented.

To utilize the finite-volume approach, the governing equations are integrated over the control volume V enclosed by the surface S in the physical domain as

$$\iiint \left(\Gamma \frac{\partial \boldsymbol{Z}}{\partial \tau} + \frac{\partial \boldsymbol{Q}}{\partial t} + \frac{\partial (\boldsymbol{E} - \boldsymbol{E}_v)}{\partial x} + \frac{\partial (\boldsymbol{F} - \boldsymbol{F}_v)}{\partial y} + \frac{\partial (\boldsymbol{G} - \boldsymbol{G}_v)}{\partial z} - \boldsymbol{H} \right) dV = \boldsymbol{0}. \qquad (3.73)$$

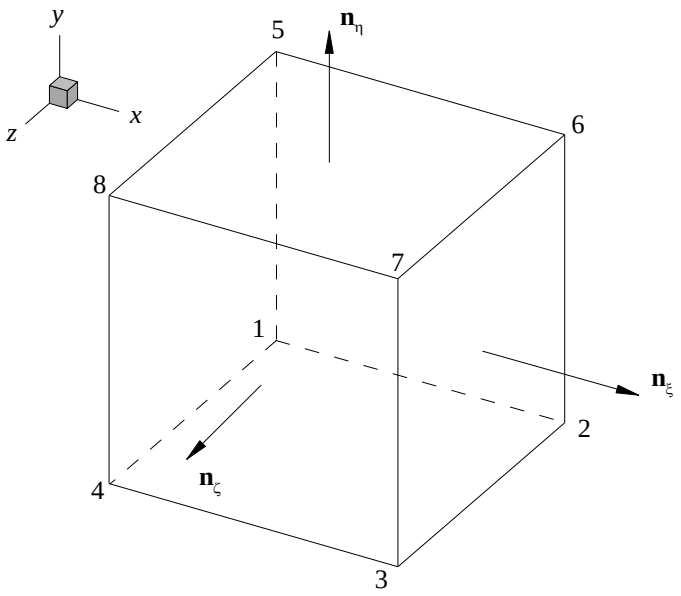

Figure 3.1: Schematic of three-dimensional computational cell

The generalized control volume in a structured grid system is a hexahedron formed by eight nodes as shown in Fig. 3.1, where $\vec{n}_\xi$, $\vec{n}_\eta$, and $\vec{n}_\zeta$ are area unit vectors normal to the surfaces in the ξ-, η-, and ζ-directions, respectively. In order to enhance numerical efficiency and minimize the complexity arising from the irregular shape of the computational mesh, a grid transformation is made to convert a curvilinear coordinate system in the physical space into a uniform grid system in the computational space.

Upon applying the Gauss' divergence theorem over a hexahedral cell as shown in Fig. 3.1, the Eq. 3.73 can be re-written as:

$$\iiint \left(\Gamma \frac{\partial \boldsymbol{Z}}{\partial \tau} + \frac{\partial \boldsymbol{Q}}{\partial t}\right) dV + \iint \vec{\boldsymbol{W}} \cdot \vec{\boldsymbol{n}}_{\xi} dS_{\xi} + \iint \vec{\boldsymbol{W}} \cdot \vec{\boldsymbol{n}}_{\eta} dS_{\eta} + \iint \vec{\boldsymbol{W}} \cdot \vec{\boldsymbol{n}}_{\zeta} dS_{\zeta} = \iiint \boldsymbol{H} dV, \tag{3.74}$$

where

$$\vec{\mathbf{W}} = \left(\mathbf{E} - \mathbf{E}_v\right)\vec{\mathbf{i}} + \left(\mathbf{F} - \mathbf{F}_v\right)\vec{\mathbf{j}} + \left(\mathbf{G} - \mathbf{G}_v\right)\vec{\mathbf{k}} \,. \tag{3.75}$$

And S_{ξ}, S_{η}, and S_{ζ} are the surface areas that are perpendicular to the surface vectors $\vec{n}_{\xi}$, $\vec{n}_{\eta}$ and $\vec{n}_{\zeta}$, respectively. These areas can be combined with the area unit vectors $\vec{n}_{\xi}$, $\vec{n}_{\eta}$ and $\vec{n}_{\zeta}$ into a vector form given by:

$$\begin{aligned} \vec{S}_{\xi} &= S_{\xi}\vec{n}_{\xi} = S_{\xi x}\vec{i} + S_{\xi y}\vec{j} + S_{\xi z}\vec{k} \,, \\ \vec{S}_{\eta} &= S_{\eta}\vec{n}_{\eta} = S_{\eta x}\vec{i} + S_{\eta y}\vec{j} + S_{\eta z}\vec{k} \,, \\ \vec{S}_{\zeta} &= S_{\zeta}\vec{n}_{\zeta} = S_{\zeta x}\vec{i} + S_{\zeta y}\vec{j} + S_{\zeta z}\vec{k} \,. \end{aligned} \tag{3.76}$$

And the unit area vectors are related to cell surface areas as

$$\vec{\boldsymbol{n}}_{\xi} = \frac{\vec{\boldsymbol{S}}_{\xi}}{\left|\vec{\boldsymbol{S}}_{\xi}\right|}, \vec{\boldsymbol{n}}_{\eta} = \frac{\vec{\boldsymbol{S}}_{\eta}}{\left|\vec{\boldsymbol{S}}_{\eta}\right|}, \vec{\boldsymbol{n}}_{\zeta} = \frac{\vec{\boldsymbol{S}}_{\zeta}}{\left|\vec{\boldsymbol{S}}_{\zeta}\right|} \tag{3.77}$$

The surface vectors and the cell volume can be calculated directly from the grid points [159]:

$$\begin{aligned} \vec{S}_{\xi} &= \frac{1}{2}\left(\vec{r}_{72} \times \vec{r}_{36}\right) = \frac{1}{2}\begin{vmatrix} \vec{i} & \vec{j} & \vec{k} \\ x_2 - x_7 & y_2 - y_7 & z_2 - z_7 \\ x_6 - x_3 & y_6 - y_3 & z_6 - z_3 \end{vmatrix}, \\ \vec{S}_{\eta} &= \frac{1}{2}\left(\vec{r}_{86} \times \vec{r}_{75}\right) = \frac{1}{2}\begin{vmatrix} \vec{i} & \vec{j} & \vec{k} \\ x_6 - x_8 & y_6 - y_8 & z_6 - z_8 \\ x_5 - x_7 & y_5 - y_7 & z_5 - z_7 \end{vmatrix}, \end{aligned} \tag{3.78}$$

$$\vec{S}_\zeta = \frac{1}{2}\left(\vec{r}_{74} \times \vec{r}_{83}\right) = \frac{1}{2}\begin{vmatrix} \vec{i} & \vec{j} & \vec{k} \\ x_4 - x_7 & y_4 - y_7 & z_4 - z_7 \\ x_3 - x_8 & y_3 - y_8 & z_3 - z_8 \end{vmatrix},$$

$$\Delta V = \frac{1}{3}\vec{r}_{17}\left(\vec{S}_\xi + \vec{S}_\eta + \vec{S}_\zeta\right).$$

Assuming that the increments $\Delta\xi=\Delta\eta=\Delta\zeta=1$ in the body-fitted coordinate system yields the following governing equation in the general coordinates

$$\left\{\Gamma\frac{\partial \boldsymbol{Z}}{\partial \tau} + \frac{\partial \boldsymbol{Q}}{\partial t}\right\} + \left(\boldsymbol{E}_\xi - \boldsymbol{E}_{\xi v}\right)\Big|_{i-\frac{1}{2},j,k}^{i+\frac{1}{2},j,k} + \left(\boldsymbol{F}_\eta - \boldsymbol{F}_{\eta v}\right)\Big|_{i,j-\frac{1}{2},k}^{i.j+\frac{1}{2},k} + \left(\boldsymbol{G}_\zeta - \boldsymbol{G}_{\zeta v}\right)\Big|_{i,j,k-\frac{1}{2}}^{i.j,k+\frac{1}{2}} = \boldsymbol{H}, \quad (3.79)$$

where the vectors $\boldsymbol{E}_\xi, \boldsymbol{E}_{\xi v}, \boldsymbol{F}_\eta, \boldsymbol{F}_{\eta v}, \boldsymbol{G}_\zeta, \boldsymbol{G}_{\zeta v}$ are defined as

$$\begin{aligned}
\mathbf{E}_\xi &= \left(\tilde{S}_{\xi x}\mathbf{E} + \tilde{S}_{\xi y}\mathbf{F} + \tilde{S}_{\xi z}\mathbf{G}\right), \quad & \mathbf{E}_{\xi v} &= \left(\tilde{S}_{\xi x}\mathbf{E}_v + \tilde{S}_{\xi y}\mathbf{F}_v + \tilde{S}_{\xi z}\mathbf{G}_v\right), \\
\mathbf{F}_\eta &= \left(\tilde{S}_{\eta x}\mathbf{E} + \tilde{S}_{\eta y}\mathbf{F} + \tilde{S}_{\eta z}\mathbf{G}\right), \quad & \mathbf{F}_{\eta v} &= \left(\tilde{S}_{\eta x}\mathbf{E}_v + \tilde{S}_{\eta y}\mathbf{F}_v + \tilde{S}_{\eta z}\mathbf{G}_v\right), \\
\mathbf{G}_\zeta &= \left(\tilde{S}_{\zeta x}\mathbf{E} + \tilde{S}_{\zeta y}\mathbf{F} + \tilde{S}_{\zeta z}\mathbf{G}\right), \quad & \mathbf{G}_{\zeta v} &= \left(\tilde{S}_{\zeta x}\mathbf{E}_v + \tilde{S}_{\zeta y}\mathbf{F}_v + \tilde{S}_{\zeta z}\mathbf{G}_v\right),
\end{aligned} \quad (3.80)$$

and the quantities $\boldsymbol{E}_{\xi(v),i\pm\frac{1}{2},j,k}, \boldsymbol{F}_{\eta(v),i,j\pm\frac{1}{2},k}, \boldsymbol{G}_{\zeta(v),i,j,k\pm\frac{1}{2}}$ represent the numerical fluxes associated with each cell interface. $\tilde{S}$ represents cell surface areas per cell volume. In fact, the above analysis describes the transformation of a quadrilateral cell with a volume ΔV in *x-y-z* coordinates to a cubic cell with unit volume in the general coordinate (i.e., ξ-η-ζ coordinates).

To accelerate convergence, the pseudo-time integration is based on the local time step in the computational domain. The maximum pseudo-time increment $\Delta\tau$ of each cell can be evaluated by

$$\Delta\tau = \frac{\Delta\tau_\xi \quad \Delta\tau_\eta \quad \Delta\tau_\zeta}{\Delta\tau_\xi \quad \Delta\tau_\eta + \Delta\tau_\eta \quad \Delta\tau_\zeta + \Delta\tau_\zeta \quad \Delta\tau_\xi}, \quad (3.81)$$

where

$$\Delta\tau_\xi = \frac{CFL\cdot\ \Delta V}{\left|\rho(\lambda_x)S_{\xi x} + \rho(\lambda_y)S_{\xi y} + \rho(\lambda_z)S_{\xi z}\right| / \left|\vec{S}_\xi\right|},$$
$$\Delta\tau_\eta = \frac{CFL\ \cdot\Delta V}{\left|\rho(\lambda_x)S_{\eta x} + \rho(\lambda_y)S_{\eta y} + \rho(\lambda_z)S_{\eta z}\right| / \left|\vec{S}_\eta\right|}, \tag{3.82}$$
$$\Delta\tau_\zeta = \frac{CFL\ \cdot\Delta V}{\left|\rho(\lambda_x)S_{\zeta x} + \rho(\lambda_y)S_{\zeta y} + \rho(\lambda_z)S_{\zeta z}\right| / \left|\vec{S}_\zeta\right|}.$$

3.2.5.2 Evaluation of Inviscid Fluxes

Different approaches in evaluating the numerical fluxes lead to disparate numerical characteristics. In the central difference scheme, the convective flux at a cell face in the ξ-direction can be written as

$$\hat{\mathbf{E}}_{\xi,i+1/2,j} = \frac{1}{2}\left[\mathbf{E}_\xi(\mathrm{Z}^L) + \mathbf{E}_\xi(\mathrm{Z}^R)\right], \tag{3.83}$$

The above equation corresponds to the stencil illustrated in Fig. 3.2. The superscripts *L* and *R* represent the left and right cells, respectively. Depending on how these terms are evaluated, a wide variety of central and upwind schemes can be obtained. According to Rai and Chakravarthy [160], the numerical flux is computed as

$$\boldsymbol{E}_{\xi,i+\frac{1}{2},j,k} = \boldsymbol{E}_{\xi,i+\frac{1}{2},j,k} - \phi^{(4)}_{i+\frac{1}{2},j,k}\left(\frac{\boldsymbol{E}_{\xi,i+\frac{3}{2},j,k} - 2\boldsymbol{E}_{\xi,i+\frac{1}{2},j,k} + \boldsymbol{E}_{\xi,i-\frac{1}{2},j,k}}{24}\right), \tag{3.84}$$

where $\phi^{(4)}$ is the flux limiter. This term switches the truncation error associated with the flux-difference from fourth-order accuracy when $\phi^{(4)} = 1$, to second-order accuracy when $\phi^{(4)} = 0$. For uniform grid system, these terms are written as follows to facilitate easy switching and make the scheme TVD (total-variation-diminishing).

$$\begin{aligned} Z^L_{i+1/2,j,k} = Z_{i,j,k} &+ \phi^{(2)}_{i+1/,j,k}\left(\frac{3\nabla Z_{i+1,j,k} + \nabla Z_{i,j,k}}{8}\right) \\ &+ \phi^{(4)}_{i+1/2,j,k}\left(\frac{-5\nabla Z_{i+2,j,k} + 7\nabla Z_{i+1,j,k} + \nabla Z_{i,j,k} - 3\nabla Z_{i-1,j,k}}{128}\right), \end{aligned} \tag{3.85}$$

$$Z^{R}_{i+1/2,j,k} = Z_{i,j,k} - \phi^{(2)}_{i+1/,j,k}\left(\frac{\nabla Z_{i+2,j,k} + 3\nabla Z_{i+1,j,k}}{8}\right) + \phi^{(4)}_{i+1/2,j,k}\left(\frac{3\nabla Z_{i+3,j,k} - \nabla Z_{i+2,j,k} - 7\nabla Z_{i+1,j,k} + 5\nabla Z_{i,j,k}}{128}\right), \tag{3.86}$$

$$\nabla Z_{i,j} = Z_{i,j} - Z_{i-1,j} \ . \tag{3.87}$$

These stencils are fifth-order accuracy ($\phi^{(4)} = 1, \phi^{(2)} = 1$), third order accuracy ($\phi^{(4)} = 0, \phi^{(2)} = 1$), and first-order accuracy ($\phi^{(4)} = 0, \phi^{(2)} = 0$), respectively. The present work utilizes second-order overall accuracy for spatial discretization with the exception of first order accuracy close to the physical boundaries. The third-order accurate evaluation of the left and right states is thus employed. The fluxes in η-, and ζ-directions can be computed in a similar fashion as above.

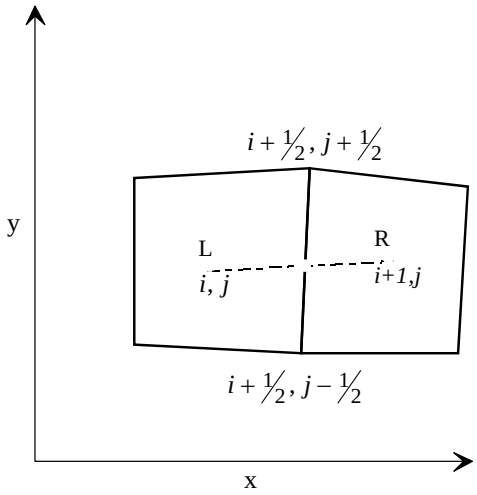

Figure 3.2: Schematic diagram of the stencil used in evaluating inviscid flux terms in the plane.

In practical applications, non-uniform grids are generally used. If the same procedure is used to evaluate the left and right state terms, Taylor series expansion shows

that there is a truncation error of first order. This will significantly reduce the overall order of accuracy of the numerical scheme. Extremely refined grids are used to diminish such side effect.

Fosso et al. [161] proposed higher-order accurate compact interpolation for curvilinear finite volume schemes to take into account the effect of grid non-uniformity. The values of interest at cell surfaces can be estimated from the cell average values in its neighborhood, by applying Taylor series expansion and solving the linear equations. Appropriate boundary treatment procedures have been developed for multi-block applications. However, this method is more expensive due to extra calculations of the surface values in each iteration. The current study compromises by mimicking the so-called Cartesian-like scheme using curvilinear abscissa scheme in the cited work. Instead of implicit equations, explicit equations are obtained to improve the numerical accuracy of spatial differencing for convective flux evaluation.

3.2.5.3 Evaluation of Viscous and SGS Fluxes

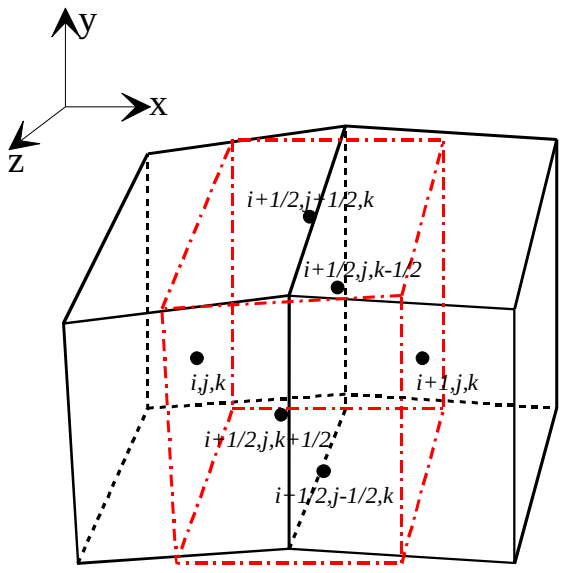

Figure 3.3: Schematic diagram for a three-dimensional auxiliary cell.

The dash-dotted lines in Fig. 3.3 show a three-dimensional auxiliary cell schematically. The viscous fluxes need to be evaluated at the center of the cell faces, i.e., $i+\frac{1}{2}, j, k$ for the viscous flux in the axial direction. Using divergence theorem and applying it to a small control volume ΔV, the viscous fluxes can be approximated as

$$\nabla \cdot \vec{f} = \frac{1}{\Delta V} \oint \vec{f} \cdot \vec{n} dS. \tag{3.88}$$

Applying the above formulation to the auxiliary cell at $(i+1/2, j, k)$ gives

$$\begin{aligned} \left(\frac{\partial f}{\partial x}\right)_{i+1/2,j,k} = \frac{1}{\Delta V_{i+1/2,j,k}} \Big[& f \quad S_{\xi x_x}\Big|_{i+1,j,k} - f \quad S_{\xi x}\Big|_{i,j,k} + f \quad S_{\eta x}\Big|_{i+1/2,j+1/2,k} \\ & - f \quad S_{\eta x}\Big|_{i+1/2,j-1/2,k} + f \quad S_{\zeta x}\Big|_{i+1/2,j,k+1/2} - f \quad S_{\zeta x}\Big|_{i+1/2,j,k-1/2} \Big] . \end{aligned} \tag{3.89}$$

Similarly

$$\begin{aligned} \left(\frac{\partial f}{\partial y}\right)_{i+1/2,j,k} = \frac{1}{\Delta V_{i+1/2,j,k}} \Big[& f \quad S_{\xi y}\Big|_{i+1,j,k} - f \quad S_{\xi y}\Big|_{i,j,k} + f \quad S_{\eta y}\Big|_{i+1/2,j+1/2,k} \\ & - f \quad S_{\eta y}\Big|_{i+1/2,j-1/2,k} + f \quad S_{\zeta y}\Big|_{i+1/2,j,k+1/2} - f \quad S_{\zeta y}\Big|_{i+1/2,j,k-1/2} \Big] , \end{aligned} \tag{3.90}$$

$$\begin{aligned} \left(\frac{\partial f}{\partial z}\right)_{i+1/2,j,k} = \frac{1}{\Delta V_{i+1/2,j,k}} \Big[& f \quad S_{\xi z}\Big|_{i+1,j,k} - f \quad S_{\xi z}\Big|_{i,j,k} + f \quad S_{\eta z}\Big|_{i+1/2,j+1/2,k} \\ & - f \quad S_{\eta z}\Big|_{i+1/2,j-1/2,k} + f \quad S_{\zeta z}\Big|_{i+1/2,j,k+1/2} - f \quad S_{\zeta z}\Big|_{i+1/2,j,k-1/2} \Big] . \end{aligned} \tag{3.91}$$

Note that f in the above equations are elements of the viscous flux vectors, $\mathbf{E}_{\xi v}$, $\mathbf{F}_{\eta v}$, or $\mathbf{G}_{\zeta v}$. Physical variables with one-half indices need to be interpolated from the quantities at the neighboring cell centers and are given by

$$\begin{aligned} f_{i+1/2,j\pm1/2,k} &= \frac{1}{4}(f_{i,j,k} + f_{i+1,j,k} + f_{i+1,j\pm1,k} + f_{i,j\pm1,k}) , \\ f_{i+1/2,j,k\pm1/2} &= \frac{1}{4}(f_{i,j,k} + f_{i+1,j,k} + f_{i+1,j,k\pm1} + f_{i,j,k\pm1}) . \end{aligned} \tag{3.92}$$

The evaluation of SGS fluxes follows a similar procedure as for the viscous and diffusive fluxes.

The viscous term evaluation procedure outlined above results in lower order of accuracy for non-uniform grids for reasons similar to the convective flux terms. However, in large Reynolds number flows, convection is dominant, and the effect of grid uniformity is neglected in the current study. Further study is warranted to consistently improve the numerical accuracy.

3.2.5.4 Evaluation of Artificial Dissipation

Artificial dissipation plays a crucial role in the stability of a numerical scheme. The form of dissipation terms must be higher order of accuracy than that of the numerical scheme to keep their magnitude minimal. For the present case, the numerical differentiation of the flux vectors is fourth-order accurate in the core region of the computational domain. Accordingly, the artificial dissipation is fourth-order accurate. The accuracy order of the numerical scheme decreases near the physical boundary, and the artificial dissipation also goes to a lower order. The form of numerical dissipation is quite often a blending of second- and fourth-order dissipation terms. The second-order terms are used near shock waves and flame zones to prevent spurious oscillations, while the fourth-order terms are important for stability and convergence. The standard dissipation model can be written as

$$\begin{aligned} \mathrm{AD} &= \textit{artificial} \quad \textit{dissipation} \\ &= \mathbf{d}_{i+1/2,j,k} - \mathbf{d}_{i-1/2,j,k} \ , \end{aligned} \tag{3.93}$$

where

$$\mathrm{d}_{i\pm1/2,j,k} = \frac{\varepsilon_2}{8}\frac{1}{\Delta t}\frac{\partial Z}{\partial \xi}\bigg|_{i\pm1/2,j,k} - \frac{\varepsilon_4}{8}\frac{1}{\Delta t}\frac{\partial^3 Z}{\partial \xi^3}\bigg|_{i\pm1/2,j,k} + \frac{\varepsilon_6}{8}\frac{1}{\Delta t}\frac{\partial^5 Z}{\partial \xi^5}\bigg|_{i\pm1/2,j,k} \ , \tag{3.94}$$

ε_2, ε_4, and ε_6 correspond to the coefficients of the second-, fourth- and sixth-order accurate artificial dissipation terms and in the present formulation, $\Delta\xi = 1$.

Even though the standard dissipation model has been proven to be reasonably effective in many cases, there are strong motivations for reducing the numerical

dissipation being produced. The standard model also has difficulties in hypersonic flows and in density stratified supercritical fluids with steep discontinuities as it occurs in the present case. A scalar dissipation model was constructed by Swanson and Turkel [162] and by Jorgenson and Turkel [163] to overcome the above difficulties. In their model

$$d_{i+\frac{1}{2},j,k} = \epsilon^{(2)}_{i+\frac{1}{2},j,k}\rho_{i+\frac{1}{2},j,k}(\lambda)\frac{\partial Z}{\partial \xi}\Big|_{i+\frac{1}{2},j,k} - \epsilon^{(4)}_{i+\frac{1}{2},j,k}\rho_{i+\frac{1}{2},j,k}(\lambda)\frac{\partial^3 Z}{\partial \xi^3}\Big|_{i+\frac{1}{2},j,k}. \qquad (3.95)$$

The modified eigenvalues are given by

$$\tilde{\lambda}_1 = \tilde{\lambda}_2 = \tilde{\lambda}_3 = \tilde{\lambda}_4 = \tilde{\lambda}_5 = \tilde{\lambda}_6 = \rho(\lambda)\,, \qquad (3.96)$$

where $\rho(\lambda)$ is the spectral radius of the flux Jacobian matrix $\Gamma^{-1}\mathrm{A}$.

$$\varepsilon^{(2)}_{i+1/2,\,j,k} = \kappa^{(2)}\max(\nu_{i-1,j,k},\ \nu_{i,j,k},\ \nu_{i+1,j,k},\ \nu_{i+2,j,k})\,, \qquad (3.97)$$

$$\nu_{i,j,k} = \left|\frac{p_{i-1,j,k} - 2p_{i,j,k} + p_{i+2,j,k}}{p_{i-1,j,k} + 2p_{i,j,k} + p_{i+1,j,k}}\right|\,, \qquad (3.98)$$

$$\varepsilon^{(4)}_{i+1/2,\,j,k} = \max\left(0,\ (\kappa^{(4)} - \varepsilon^{(2)}_{i+1/2,\,j,k}\right)\,, \qquad (3.99)$$

$$\kappa^{(2)} = \frac{1}{4} \sim \frac{1}{2}, \quad \kappa^{(4)} = \frac{1}{64} \sim \frac{1}{32}\,. \qquad (3.100)$$

The first term on RHS given in Eq. 3.95 is nonlinear. Its purpose is to introduce an entropy-like condition and to suppress oscillations in the neighborhood of shock discontinuities. This term is small in the smooth portion of the flow field. The switch $\nu_{i,j,k}$ is important near discontinuities, in which large pressure gradients exist. For high-pressure fluid mixing and combustion, however, this switch is tuned to include temperature or density gradients other than pressure gradients, as pressure may still be uniform across the boundary between different fluid layers. The fourth-order term is basically linear and is included to damp high-frequency modes and allow the scheme to approach a steady state. Only this term affects the linear stability of the scheme and is reduced to zero near the discontinuity.

Although effective for numerical stability, the scalar dissipation model results in much dissipation and probably contaminates the accuracy of the simulation. Because the scalar dissipation model uses the same artificial dissipation coefficient for all the equations regardless of the actual wave speeds, resulting in excessive smearing. This situation deteriorates in locations where the local preconditioning factor is not optimized such that the eigenvalues of the Jacobian matrix are in different orders of magnitude. Furthermore, the scalar dissipation is not conservative, and leads to mass conservation problem in practice.

To overcome the difficulties with the scalar dissipation model, matrix dissipation formulations are derived for real-fluid mixture systems following Swanson and Turkel [162] and by Jorgenson and Turkel [163]. To demonstrate the procedure of adding matrix artificial dissipation, backward differencing in time is applied to the governing equations, giving:

$$\left\{\mathbf{\Gamma}+a\frac{\Delta\tau}{\Delta t}\mathbf{T}\right\}\frac{\partial\mathbf{Z}}{\partial\tau}+\frac{\partial\mathbf{E}}{\partial x}+\frac{\partial\mathbf{F}}{\partial y}+\frac{\partial\mathbf{G}}{\partial x}=-\frac{1}{\Delta t}\left(a\mathbf{Q}^{m}-\phi\right)\,, \tag{3.101}$$

or equivalently:

$$\frac{\partial}{\partial x}\left(\rho uY_k\right)+\frac{1}{r}\frac{\partial}{\partial r}\left(r\rho vY_k\right)+\dot{m}''_{k,diff}=MW_k\dot{\omega}_k \tag{3.102}$$

where $a=3/2$, $\phi=(2\boldsymbol{Q}^{n}-\boldsymbol{Q}^{n-1})/2$.

At this point, the eigenvalues and eigenvectors of the preconditioned system can be derived. Let

$$\boldsymbol{S} = \boldsymbol{\Gamma} + a\frac{\Delta\tau}{\Delta t}\boldsymbol{T}$$

$$= \left(1 + \frac{2}{3}\frac{\Delta\tau}{\Delta t}\right)\begin{pmatrix} \rho_p'' & 0 & 0 & 0 & \rho_T & \rho_f \\ \rho_p'' u & \rho & 0 & 0 & u\rho_T & u\rho_f \\ \rho_p'' v & 0 & \rho & 0 & v\rho_T & v\rho_f \\ \rho_p'' w & 0 & 0 & \rho & w\rho_T & w\rho_f \\ \rho_p'' h_t + \dfrac{T}{\rho}\rho_T & \rho u & \rho v & \rho w & \rho c_p + h_t\rho_T & \rho_f E + \rho E_f \\ \rho_p'' f & 0 & 0 & 0 & \rho_T f & \rho + f\rho_f \end{pmatrix}, \tag{3.103}$$

where $\rho_p'' = \left(\frac{\gamma}{\beta} + \frac{3}{2}\frac{\Delta\tau}{\Delta t}\left(\frac{\partial\rho}{\partial p}\right)_{T,Y_i}\right) / \left(1 + \frac{2}{3}\frac{\Delta\tau}{\Delta t}\right)$. Then $\mathbf{S}^{-1}$ can be derived as:

$$\mathbf{S}^{-1} = \frac{1}{1+\frac{3}{2}\frac{\Delta\tau}{\Delta t}}\begin{pmatrix} g_{11} & \frac{u\rho_T}{d} & \frac{v\rho_T}{d} & \frac{w\rho_T}{d} & -\frac{\rho_T}{d} & g_{16} \\ -\frac{u}{\rho} & \frac{1}{\rho} & 0 & 0 & 0 & 0 \\ -\frac{v}{\rho} & 0 & \frac{1}{\rho} & 0 & 0 & 0 \\ -\frac{w}{\rho} & 0 & 0 & \frac{1}{\rho} & 0 & 0 \\ g_{51} & -\frac{u\rho_p''}{d} & -\frac{u\rho_p''}{d} & -\frac{u\rho_p''}{d} & \frac{\rho_p''}{d} & g_{56} \\ -\frac{f}{\rho} & 0 & 0 & 0 & 0 & \frac{1}{\rho} \end{pmatrix}, \tag{3.104}$$

where

$$\begin{aligned} g_{11} &= \frac{1}{d}\left\{\rho c_p + \rho_T\left[h - \frac{1}{2}\left(u^2+v^2+w^2\right)\right] + \left(\rho_f c_p - f\rho_T h_f\right)\right\}, \\ g_{16} &= \frac{1}{d}\left(\rho_T h_f - c_p\rho_f\right), \\ g_{51} &= \frac{1}{d}\left\{\begin{aligned} &-\frac{T}{\rho}\rho_T + \rho_p''\left[h - \frac{1}{2}\left(u^2+v^2+w^2\right)\right] \\ &+\left(f\rho'' h_f - \frac{T}{\rho^2}\rho_f\rho_T f\right) \end{aligned}\right\}\left(\rho_T h_f - c_p\rho_f\right), \end{aligned} \tag{3.105}$$

$$g_{16} = \frac{1}{d}\left(\frac{T}{\rho^2}\rho_f \rho_T - \rho_p'' h_f \right)$$

$$\mathbf{S}^{-1}\mathbf{A}_v = \frac{1}{1+\frac{3}{2}\frac{\Delta\tau}{\Delta t}} \begin{pmatrix} U\varepsilon' & \frac{\rho^2 c_p}{d} l_x & \frac{\rho^2 c_p}{d} l_y & \frac{\rho^2 c_p}{d} l_z & 0 & 0 \\ \frac{l_x}{\rho} & U & 0 & 0 & 0 & 0 \\ \frac{l_y}{\rho} & 0 & U & 0 & 0 & 0 \\ \frac{l_z}{\rho} & 0 & 0 & U & 0 & 0 \\ \frac{U}{d}\left(-\frac{T}{\rho}\rho_T\right)\left(\rho_p - \rho_p''\right) & -\frac{T\rho_T}{d} l_x & -\frac{T\rho_T}{d} l_y & -\frac{T\rho_T}{d} l_z & U & 0 \\ 0 & 0 & 0 & 0 & 0 & U \end{pmatrix}. \quad (3.106)$$

The eigenvalues are:

$$\lambda_{1,2,3,6} = Ub$$

$$\lambda_{4,5} = \frac{b}{2}\left[U\left(1+\varepsilon'\right) \pm \sqrt{U^2\left(1-\varepsilon'\right)^2 + 4\frac{\rho c_p}{d}\left|\nabla l\right|^2} \right] \quad (3.107)$$

$$b = 1 \Big/ \left(1 + \frac{3}{2}\frac{\Delta\tau}{\Delta t} \right).$$

The left and right eigenvectors, which correspond to each of the eigenvalues are given by:

$$\mathbf{M} = \begin{pmatrix} 0 & 0 & 0 & \frac{\lambda_5 - \varepsilon' U b}{\lambda_5 - \lambda_4} & \frac{\lambda_5 - \varepsilon' U b}{\lambda_4 - \lambda_5} & 0 \\ 0 & \tilde{m}_1/\rho & \tilde{n}_1/\rho & \frac{l_x b}{\rho\left(\lambda_4 - \lambda_5\right)} & \frac{l_x b}{\rho\left(\lambda_5 - \lambda_4\right)} & 0 \\ 0 & \tilde{m}_2/\rho & \tilde{n}_2/\rho & \frac{l_y b}{\rho\left(\lambda_4 - \lambda_5\right)} & \frac{l_y b}{\rho\left(\lambda_5 - \lambda_4\right)} & 0 \\ 0 & \tilde{m}_3/\rho & \tilde{n}_3/\rho & \frac{l_z b}{\rho\left(\lambda_4 - \lambda_5\right)} & \frac{l_z b}{\rho\left(\lambda_5 - \lambda_4\right)} & 0 \\ \frac{T\rho_T}{\rho^2 c_p} & 0 & 0 & B_1 & B_2 & 0 \\ 0 & 0 & 0 & 0 & 0 & 1 \end{pmatrix}, \quad (3.108)$$

$$\mathbf{M}^{-1} = \begin{pmatrix} 1 & 0 & 0 & 0 & \dfrac{\rho^2 c_p}{T\rho_T} & 0 \\ 0 & \rho\tilde{m}_1 & \rho\tilde{m}_2 & \rho\tilde{m}_3 & 0 & 0 \\ 0 & \rho\tilde{n}_1 & \rho\tilde{n}_2 & \rho\tilde{n}_3 & 0 & 0 \\ 1 & \rho\left(\lambda_4/b-\varepsilon' U\right)l_x & \rho\left(\lambda_4/b-\varepsilon' U\right)l_y & \rho\left(\lambda_4/b-\varepsilon' U\right)l_z & 0 & 0 \\ 1 & \rho\left(\lambda_5/b-\varepsilon' U\right)l_x & \rho\left(\lambda_5/b-\varepsilon' U\right)l_y & \rho\left(\lambda_5/b-\varepsilon' U\right)l_z & 0 & 0 \\ 0 & 0 & 0 & 0 & 0 & 1 \end{pmatrix}, \tag{3.109}$$

where $B_1 = -\frac{T\rho_T}{\rho^2 c_p}\frac{\lambda_5-\epsilon' Ub}{\lambda_5-\lambda_4}$ and $B_2 = -\frac{T\rho_T}{\rho^2 c_p}\frac{\lambda_4-\epsilon' Ub}{\lambda_4-\lambda_5}$.

Following Swanson and Turkel [162], the matrix dissipation term in ξ direction is given by:

$$\mathbf{AD}_i = \mathbf{d}_{i+1/2} - \mathbf{d}_{i-1/2}\ , \tag{3.110}$$

$$\mathbf{d}_{i+1/2} = \mathbf{\Gamma}_{i+1/2}\left|\mathbf{A}\right|_{i+1/2}\left(\varepsilon^{(2)}_{i+1/2}\left.\frac{\partial \mathbf{Z}}{\partial \xi}\right|_{i+1/2} - \varepsilon^{(4)}_{i+1/2}\left.\frac{\partial^3 \mathbf{Z}}{\partial \xi^3}\right|_{i+1/2}\right), \tag{3.111}$$

$$\left|\mathbf{A}\right|_{i+1/2} = \mathbf{M}_{i+1/2}\left|\mathbf{\Lambda}\right|_{i+1/2}\mathbf{M}^{-1}{}_{i+1/2}\ , \tag{3.112}$$

where $\mathbf{\Lambda} = diag(\lambda_1, \lambda_2, \lambda_3, \lambda_4, \lambda_5, \lambda_6)$. The half point values are evaluated using Roe averaging technique. To avoid numerical difficulties caused by zero artificial viscosity at stagnation points or sonic regions, the eigenvalues are limited by:

$$\left|\lambda_i\right| = \max\left(\left|\lambda_i\right|, V_n\rho\left(\mathbf{A}\right)\right),\ \text{with}\ \rho\left(\mathbf{A}\right) = \max\left(\lambda_i\right), i = 1,6\ . \tag{3.113}$$

The higher-order term is not helpful to TVD or up-winding property, but is intended to eliminate high frequencies and to accelerate numerical convergence.

The artificial dissipation coefficient $\varepsilon^{(2)}$ is based on the following switch:

$$\varepsilon^{(2)}_{i+1/2} = \kappa^{(2)} \max\left(\nu_i, \nu_{i+1}\right) ,$$

$$\nu_i = \max\left(\begin{array}{c} \dfrac{\left(p_{i+1} - 2p_i + p_{i-1}\right)}{\left[(1-\omega)\left(\left|p_{i+1} - p_i\right| + \left|p_i - p_{i-1}\right|\right) + \omega\left(p_{i+1} - 2p_i + p_{i-1}\right)\right]}, \\ \dfrac{\left(T_{i+1} - 2T_i + T_{i-1}\right)}{\left[(1-\omega)\left(\left|T_{i+1} - T_i\right| + \left|T_i - T_{i-1}\right|\right) + \omega\left(T_{i+1} - 2T_i + T_{i-1}\right)\right]}, \\ \dfrac{\left(\rho_{i+1} - 2\rho_i + \rho_{i-1}\right)}{\left[(1-\omega)\left(\left|\rho_{i+1} - \rho_i\right| + \left|\rho_i - \rho_{i-1}\right|\right) + \omega\left(\rho_{i+1} - 2\rho_i + \rho_{i-1}\right)\right]} \end{array} \right) , \qquad (3.114)$$

$$\varepsilon^{(4)}_{i+1/2} = \max\left[0, \left(\kappa^{(4)} - \varepsilon^{(2)}_{i+1/2}\right)\right] ,$$

where $\frac{1}{4} \le \kappa^{(2)} \le \frac{1}{2}$, $\frac{1}{64} \le \kappa^{(4)} \le \frac{1}{32}$, $0.05 \le \omega \le 0.5$. The resulting scheme is TVD given the switches above.

3.2.6 Temporal Discretization

The physical time derivatives are evaluated by backward differencing

$$\frac{\partial Q}{\partial t} = \frac{1}{\Delta t}\left[a_1 Q^{m+1} - \phi(Q^n, Q^{n-1}, \cdots)\right] . \qquad (3.115)$$

The coefficient a_1 and function ϕ can be specified to any level of temporal accuracy desired. In the current work, a three-point backward difference with second-order accuracy is employed. For this situation

$$a_1 = \frac{3}{2}, \;\; \phi = \frac{1}{2}(4Q^n - Q^{n-1}) . \qquad (3.116)$$

The superscripts m and n denote iterations within the pseudo-time domain (inner-loop) and physical time domain (outer-loop), respectively. The physical time term Q^{m+1} can be linearized as

$$Q^{m+1} = Q^m + T\Delta Z^{m+1} . \qquad (3.117)$$

Then we get the following discretized system

$$\left\{\Gamma + a\frac{\Delta\tau}{\Delta t}T\right\}\Delta Z + \frac{\Delta\tau}{\Delta V}\left(\left(\mathrm{E}_{\xi} - \mathrm{E}_{\xi v}\right)\Big|_{i-1/2,j,k}^{i+1/2,j,k} + \left(\mathrm{F}_{\eta} - \mathrm{F}_{\eta v}\right)\Big|_{i,j-1/2,k}^{i,j+1/2,k} + \left(\mathrm{G}_{\zeta} - \mathrm{G}_{\zeta v}\right)\Big|_{i,j,k-1/2}^{i,j,k+1/2}\right) = \mathrm{H}^{\mathrm{m}+1}\Delta\tau - \frac{\Delta\tau}{\Delta t}(a_1 Q^m - \phi)\ . \tag{3.118}$$

To solve this equation implicitly, matrix "inversion" of $\left(\Gamma + a\frac{\Delta\tau}{\Delta t}T\right)$ is required.

A fourth-order Runge-Kutta (RK-4) scheme is used to solve the governing equation in the pseudo-time space due to its higher temporal accuracy and relatively larger CFL number requirement (i.e., $2\sqrt{2}$ for an Euler calculation using RK-4). A thorough investigation of the stability characteristics of the RK-4 method, based on convection of the turbulence energy-spectrum, has been performed by Apt and Yang [164] to establish its creditability and accuracy. Using the four-step Runge-Kutta scheme, each pseudo-time integration is completed through four consecutive intermediate steps, as given below:

$$\begin{aligned} Z_0 &= Z^m, \\ Z_1 &= Z^m + \Delta Z_1, \left(\Gamma + \frac{\Delta\tau}{\Delta t}T - \Delta\tau D\right)\Delta Z_1 = \alpha_1\Delta\tau\cdot R(Z_0), \\ Z_2 &= Z^m + \Delta Z_2, \left(\Gamma + \frac{\Delta\tau}{\Delta t}T - \Delta\tau D\right)\Delta Z_2 = \alpha_2\Delta\tau\cdot R(Z_1), \\ Z_3 &= Z^m + \Delta Z_3, \left(\Gamma + \frac{\Delta\tau}{\Delta t}T - \Delta\tau D\right)\Delta Z_3 = \alpha_3\Delta\tau\cdot R(Z_2), \\ Z^{m+1} &= Z^m + \Delta Z^{m+1}, \left(\Gamma + \frac{\Delta\tau}{\Delta t}T - \Delta\tau D\right)\Delta Z^{m+1} = \Delta\tau\cdot R(Z_3), \end{aligned} \tag{3.119}$$

where

$$R(z) = \mathrm{H}^{\mathrm{m}} - \frac{1}{\Delta t}(a_1 Q^m - \phi) - \left[\left(\mathrm{E}_{\xi} - \mathrm{E}_{\xi v}\right)\Big|_{i-1/2,j,k}^{i+1/2,j,k} + \left(\mathrm{F}_{\eta} - \mathrm{F}_{\eta v}\right)\Big|_{i,j-1/2,k}^{i,j+1/2,k} + \left(\mathrm{G}_{\zeta} - \mathrm{G}_{\zeta v}\right)\Big|_{i,j,k-1/2}^{i,j,k+1/2}\right]. \tag{3.120}$$

Superscripts 'm' and 'm+1' stand for the solution at the 'm^{th}' and '$(m+1)^{\mathrm{th}}$' pseudo-time steps, respectively. The coefficients α_1, α_2, and α_3 can be varied to obtain a variety of schemes with different stability properties. The standard four-step scheme has the following values (Jameson, 1983)

$$\alpha_1 = \frac{1}{4} \quad , \quad \alpha_2 = \frac{1}{3} \, , \quad \alpha_3 = \frac{1}{2} \, . \tag{3.121}$$

The iteration begins from pseudo-time steps (inner-loop). At convergence in pseudo-time step, the solution proceeds one physical time step (outer-loop). Due to the unconditional numerical stability of implicit solvers, the dual-time advancing process provides flexibility in the selection of time step sizes. In particular, the physical-time step size Δt is determined based on the evolution of the unsteady flow. To capture the small chemical timescales of most species, Δt should not be larger than ~0.5 μs, then the sub-cycling of pseudo-time steps could guarantee the capture of small chemical timescales of ~10 ns. On the other hand, the pseudo-time step size $\Delta \tau$ is determined based on the numerical stability of the algorithm and could be modified to provide the optimal convergence rate for the pseudo-time iteration process. Practically, pseudo-time CFL numbers between 5 and 10 are chosen for most simulations.

3.3 Boundary Conditions

In all cases considered, second-order accurate boundary conditions are implemented. The inlet and exit conditions are specified using the method-of-characteristics (MOC). Adiabatic and no-slip conditions are imposed at the solid wall. Elsewhere conditions are specified using second-order extrapolated values. These conditions produce zero normal gradients with respect to pressure, velocity, temperature, and species mass fraction.

3.3.1 Characteristic Boundary Conditions

At the inlet and outlet boundaries, care must be taken when specifying the numerical boundary conditions. One has to ensure that the unphysical spurious wave reflections are avoided at the boundary and the flow is capable of relaxing to ambient conditions in the prescribed ways, which can be satisfied using the MOC proposed by Poinsot and Lele [165]. In the absence of a significant diffusion processes, the MOC

method provides correct number of conditions that must be specified, as well as conditioned information from the interior domain.

Implementation of the MOC procedure involves diagonalizing the governing system to a quasi-one-dimensional characteristic form

$$[S + LM^{-1}\Gamma^{-1}(\Gamma + \frac{\Delta\tau}{\Delta t}T - \Delta\tau D)]\Delta Z = -LM^{-1}\Gamma^{-1}$$
$$\left\{(\frac{\partial E}{\partial x} + \frac{\partial F}{\partial y} + \frac{\partial G}{\partial z}) + \tilde{\Omega} + \frac{\Delta\tau}{\Delta t}(a_1 Q^m - \phi) - H\right\} . \qquad (3.122)$$

All of the terms in above equation are evaluated at cell centroids using the finite difference methodology. The term $\tilde{\Omega}$ is the vector of specified boundary conditions. The term L is a selection matrix that singles out the desired characteristics at respective boundaries. The Jabobian matrix S is defined as $S = \partial\Omega/\partial Z$.

In the absence of significant diffusion processes, the MOC procedure dictates the correct number of conditions that must be specified at each boundary and provides well-conditioned information from the interior domain. In this study, the conditions imposed at the inlet and exit planes remain subsonic. At the inlet, there is one outgoing characteristic and N+3 conditions must be specified. Here the temperature, velocity, and species concentrations are employed assuming fully-developed turbulent channel flow. These conditions are given by

$$\tilde{\Omega}_{inlet} = \Delta V \begin{pmatrix} 0 \\ \tilde{u} - \tilde{u}_{ref} \\ \tilde{v} - \tilde{v}_{ref} \\ \tilde{w} - \tilde{w}_{ref} \\ \tilde{T} - \tilde{T}_{ref} \\ \tilde{Y}_1 - \tilde{Y}_{1_{ref}} \\ \vdots \\ \tilde{Y}_N - \tilde{Y}_{N-1_{ref}} \end{pmatrix} , \; L_{inlet} = \begin{pmatrix} 1 & 0 & 0 & 0 & 0 & 0 & \cdots & 0 \\ 0 & 0 & 0 & 0 & 0 & 0 & \cdots & 0 \\ 0 & 0 & 0 & 0 & 0 & 0 & \cdots & 0 \\ 0 & 0 & 0 & 0 & 0 & 0 & \cdots & 0 \\ 0 & 0 & 0 & 0 & 0 & 0 & \cdots & 0 \\ 0 & 0 & 0 & 0 & 0 & 0 & \cdots & 0 \\ \vdots & \vdots & \vdots & \vdots & \vdots & \vdots & \ddots & \vdots \\ 0 & 0 & 0 & 0 & 0 & 0 & \cdots & 0 \end{pmatrix} . \qquad (3.123)$$

where $\tilde{u}_{ref}$, $\tilde{v}_{ref}$, $\tilde{w}_{ref}$, and $\tilde{T}_{ref}$, $\tilde{Y}_{1_{ref}}$, …, $\tilde{Y}_{N-1_{ref}}$ represent the specified values of velocity components, temperature, and species mass fraction, respectively. At the exit, there are N+3 outgoing characteristics and one condition must be specified. Here a far-field pressure condition is simulated using the methodologies proposed by Rudy and Strikwerda [166], Poinsot and Lele [165], and Baum et al. [167].

To simulate the far-field boundary, the incoming characteristic is modified to provide a nonreflecting outflow condition. The equation of interest is given by the selection matrix

$$L = \begin{pmatrix} 1 & 0 & 0 & 0 & 0 & 0 & \cdots & 0 \\ 0 & 0 & 0 & 0 & 0 & 0 & \cdots & 0 \\ 0 & 0 & 0 & 0 & 0 & 0 & \cdots & 0 \\ 0 & 0 & 0 & 0 & 0 & 0 & \cdots & 0 \\ 0 & 0 & 0 & 0 & 0 & 0 & \cdots & 0 \\ 0 & 0 & 0 & 0 & 0 & 0 & \cdots & 0 \\ \vdots & \vdots & \vdots & \vdots & \vdots & \vdots & \ddots & \vdots \\ 0 & 0 & 0 & 0 & 0 & 0 & \cdots & 0 \end{pmatrix}. \tag{3.124}$$

Associated with this equation is the term

$$\Pi_2 = \lambda_2 \left[\frac{1}{\epsilon} \frac{u - \lambda_2}{a} \frac{\partial p}{\partial x} - \rho a \frac{\partial u}{\partial x} \right], \tag{3.125}$$

which characterizes the time variation of the normal component of acoustic waves that propagate from an infinitely distant downstream source into the computational domain. The term λ_2 is the acoustic eigenvalue. Conceptually, a perfectly non-reflecting subsonic outflow condition can be obtained if this term is set equal to zero. Specifying such a condition, however, eliminates the information provided by the acoustic waves and leads to an ill-posed problem. To simulate this information Rudy and Strikwerda [166], Poinsot and Lele [165], and Baum et al. [167] proposed that Eq. 3.81 be replaced with

$$\Pi_2^k = k(p - p_\infty), \tag{3.126}$$

where k is a constant that determines the speed with which the average pressure in the computational domain relaxes towards the imposed pressure at infinity p_∞. This condition introduces small amplitude acoustic waves using scaling arguments that are based on known quantities at the exit. Rudy and Strikwerda [166] proposed that optimal values of k are given by

$$k = 2\frac{\sigma}{x_c}\frac{\epsilon a^2(1-\bar{M}^2)}{\sqrt{u(1-\epsilon)^2+4\epsilon a^2}}. \tag{3.127}$$

The factor presented here has been modified from that given by Rudy and Strikwerda [166] to accommodate the dual-time preconditioned system. Here $\bar{M}^2$ represents the maximum Mach number in the computational domain, x_c is the characteristic axial length of the domain, ϵ is the local preconditioning factor, and a is the local speed of sound. The term σ is a scaling factor used for optimization. Poinsot and Lele [165], and Baum et al. [167] have shown that values ranging from 0.25 to 0.5 provide the best results. When lower values are specified, solutions tend to drift away from the reference pressure. When larger values are specified, flow oscillations are introduced.

To implement the MOC methodology with the far field pressure condition described above, the $N+3$ outgoing characteristics are selected and the incoming characteristic is modified by replacing the incoming wave amplitude. These conditions are given by

$$\tilde{\Omega}_{outlet} = \Delta V \begin{pmatrix} p-p_{ref} \\ 0 \\ 0 \\ 0 \\ 0 \\ 0 \\ \vdots \\ 0 \end{pmatrix}, \; L_{outlet} = \begin{pmatrix} 0 & 0 & 0 & 0 & 0 & 0 & \cdots & 0 \\ 0 & 1 & 0 & 0 & 0 & 0 & \cdots & 0 \\ 0 & 0 & 1 & 0 & 0 & 0 & \cdots & 0 \\ 0 & 0 & 0 & 1 & 0 & 0 & \cdots & 0 \\ 0 & 0 & 0 & 0 & 1 & 0 & \cdots & 0 \\ 0 & 0 & 0 & 0 & 0 & 1 & \cdots & 0 \\ \vdots & \vdots & \vdots & \vdots & \vdots & \vdots & \ddots & \vdots \\ 0 & 0 & 0 & 0 & 0 & 0 & \cdots & 1 \end{pmatrix}. \tag{3.128}$$

The far-field pressure condition has been shown to be effective in reducing reflections at the subsonic exit boundary and is relatively accurate and stable.

3.4 Parallel Implementation

Since the explicit time-stepping numerical scheme is applied in the current study, only the data from neighboring cells instead of the whole computational domain were required during the calculation of variables in each cell. Since the data dependence is weak, the domain decomposition technique is best suited for this kind of application. It is also commonly implemented in distributed-memory parallel computer systems. In the field of computational fluid dynamics (CFD), it is generally referred to as mesh partitioning, based on the geometric substructure of the computational domain. In the domain-decomposition technique, the physical domain is divided into several sub-domains. Variables in each cell are updated to the next time step simultaneously. In order to calculate the spatial derivatives at the sub-domain boundaries, ghost cells or halo data around the computing cells are introduced. Figure 3.4 shows an example of a two-dimensional sub-domain with ghost cells. Because the variables in the ghost cell are updated in another sub-domain, message passing is required to synchronize data between different sub-domains. The communication overhead is directly proportional to the volume-to-surface ratio of the grid system in that sub-domain. Maximizing the computation-to-communication ratio leads to higher parallel execution efficiency.

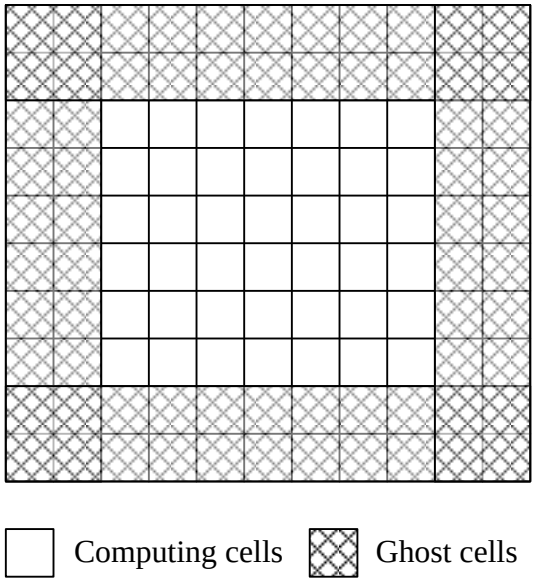

Figure 3.4: Schematic of a two-dimensional sub-domain with ghost cells.

High Performance Computing (HPC) clusters are used to conduct the large-scale computations required in the current studies. The in-house program is highly paralleled, and each decomposed sub-domain is computed by one CPU core. Communication at the domain boundary is made through a message passing interface (MPI).

CHAPTER 4

EFFICIENT APPROACHES TO SIMULATE FINITE RATE CHEMISTRY

The chemical source terms introduce a large and stiff ODE system, which is the main reason why detailed FRC calculation is very expensive. In the implementation, techniques of ODEPIM [43, 44] and CoDAC [35, 86-88] are utilized to accelerate the calculation of chemical source terms.

4.1 Point-Implicit Stiff ODE Solver (ODEPIM)

There are generally 3 categories of ODE solvers available for the calculation of chemical kinetics: (1) pure implicit solvers, such as the variable-coefficient stiff ODE solver (VODE) [37]; (2) semi-implicit solvers, such as the point-implicit stiff ODE solver (ODEPIM) [43, 44]; and (3) pure explicit solvers, such as the 4th-order Runge-Kutta (RK4) solver and Euler explicit solver with sub-cycling. Pure implicit solvers, although accurate even for stiff mechanisms, are computationally expensive. For example, VODE is more than 40 times slower than ODEPIM while employing GRI-Mech 3.0. Pure explicit solvers require time step sizes smaller than the smallest chemical timescales; otherwise significant errors or even numerical instability may be triggered. For the turbulent flames using stiff mechanisms (such as GRI-Mech 3.0), the minimum chemical timescales are O (0.1 ns), while the time step sizes from the CFL condition are O (10 ns). Numerical experiments show that using RK4 for stiff mechanisms can introduce significant errors and incorrect results (for example, the average temperature error was more than 400 K in our investigation). For reasons of both accuracy and computational speed, ODEPIM is selected in this study.

The reaction rate $\dot{\omega}_k$ can be decomposed to two parts: production P_k and destruction D_k. Therefore ODE system of chemical kinetics can be rewritten as:

$$\frac{dY_k}{dt} = P_k - D_k \tag{4.1}$$

Above decomposition can be explicitly discretized to the following from, note that the superscript n means these terms are evaluated using the states at time $t = t^n$.

$$\frac{Y_k^{n+1} - Y_k^n}{\Delta t} = P_k^n - D_k^n \frac{Y_k^{n+1}}{Y_k^n} \tag{4.2}$$

Rearrange above discrete form, we can get a pointwise explicit formula for Y_k^{n+1}.

$$Y_k^{n+1} = \frac{Y_k^n + \Delta t P_k^n}{1 + \frac{\Delta t D_k^n}{Y_k^n}} \tag{4.3}$$

Explicitly time advance using above equation is both unstable and inaccurate unless using extremely small time steps approximately the smallest timescale of the plasma-combustion kinetics. For this reason, point-implicit stiff ODE solver (ODEPIM) introduces an inner iteration to solve the ODE system implicitly. The states at time $t = t^n$ are utilized as the initial values ($m = l$) for the inner iteration:

$$Y_k^{n,m=1} = Y_k^n \tag{4.4}$$

The iteration from state $Y_k^{n,m}$ to $Y_k^{n,m+1}$ is conducted based on Eq. (4.3):

$$Y_k^{n,m+1} = \frac{Y_k^n + \Delta t P_k^{n,m}}{1 + \frac{\Delta t D_k^{n,m}}{Y_k^{n,m}}} \tag{4.5}$$

Iteration stops once

$$\max_{1 \le k \le NS} \left(\left| \frac{\log_{10} Y_k^{n,m+1}}{\log_{10} Y_k^{n,m}} - 1 \right| \right) < \epsilon_{iter} = 10^{-5} \tag{4.6}$$

In the implementation, species with too low mole fractions ($< 10^{-3}\ ppm$) has large uncertainty thus should be ruled out from above maximum calculation to improve convergence. As a result, the updated states at next time step $t = t^{n+1} = t^n + \Delta t$ is

$$Y_k^{n+1} = Y_k^{n,m+1} \tag{4.7}$$

Note that energy equation can also be decomposed to production and destruction by the same manner. Then temperature is also combined into above inner iteration and the iteration convergence criteria need to include the following condition for temperature:

$$|T^{n,m+1} - T^{n,m}| < 10^{-3}K \tag{4.8}$$

The flow chart of ODEPIM is summarized in Fig. 4.1.

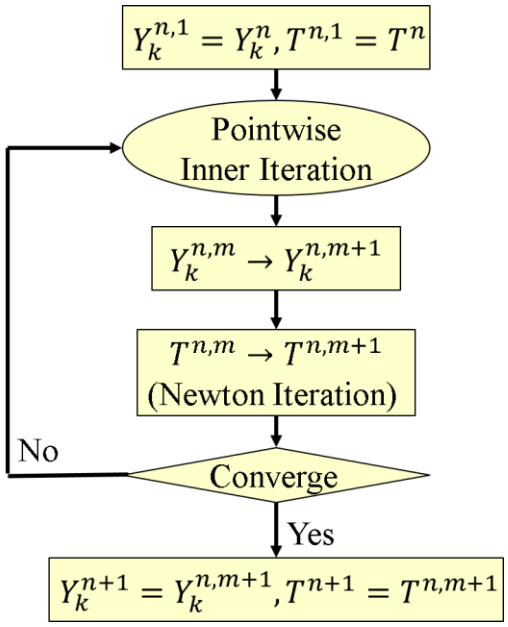

Figure 4.1: Flow chart of the point-implicit stiff ODE solver (ODEPIM).

ODEPIM is a semi-implicit stiff ODE solver. It is much faster than purely implicit solvers (e.g. double precision variable coefficient stiff ODE solver (DVODE)) because of its pointwise decoupling during the inner iteration. For the same reason, its accuracy should stay between purely explicit solvers (e.g. 4th order Runge-Kutta (RK4) and Euler Explicit with sub-cycling) and purely implicit solvers. Past studies [43, 44] show that its accuracy is close to that of pure implicit solvers but its speed is close to that of pure

explicit solves, especially for detailed stiff chemical kinetics. Its numerical stability allows Δt up to O(100 ns), which is enough for DNS and high-fidelity LES. Therefore, ODEPIM is a good balance between efficiency and accuracy.

4.2 Correlated Dynamic Adaptive Chemistry (CoDAC)

4.2.1 Path Flux Analysis (PFA) Method for Kinetic Mechanism Reduction

The kernel engine of CoDAC is a path flux analysis (PFA) method [25] for kinetic mechanism reduction. The PFA method can select important species and reactions based on both production and destruction fluxes. The PFA reduction procedure begins with a list of preselected important species, typically fuel, and oxygen, and then selects all species with significant correlation to the selected species to form a sub-mechanism.

To illustrate it, consider an arbitrary species A. Its net production and consumption fluxes are Eqs. (4.9) and (4.10), respectively:

$$P_A = \sum_{i=1}^{I} \max\left(\nu_{A,i}\dot{\omega}_i, 0\right) \tag{4.9}$$

$$C_A = \sum_{i=1}^{I} \max\left(-\nu_{A,i}\dot{\omega}_i, 0\right) \tag{4.10}$$

The production and consumption fluxes between species A and B are Eqs. (4.11) and (4.12), respectively:

$$P_{AB} = \sum_{i=1}^{I} \max\left(\nu_{A,i}\dot{\omega}_i\delta_B^i, 0\right) \tag{4.11}$$

$$C_{AB} = \sum_{i=1}^{I} \max\left(-\nu_{A,i}\dot{\omega}_i\delta_B^i, 0\right) \tag{4.12}$$

Based on Eq. (4.9-4.12), we can obtain the 1st generation normalized fluxes for production and consumption of species A requiring species B:

$$r_{AB}^{pro-1st} = \frac{P_{AB}}{\max(P_A, C_A)} \tag{4.13}$$

$$r_{AB}^{con-1st} = \frac{C_{AB}}{\max(P_A, C_A)} \tag{4.14}$$

Using the 1st generation, the 2nd generation normalized fluxes between A and B via any intermediate M are defined as:

$$r_{AB}^{pro-2nd} = \sum_{M \neq A,B} r_{AM}^{pro-1st} \times r_{MB}^{pro-1st} \tag{4.15}$$

$$r_{AB}^{con-2nd} = \sum_{M \neq A,B} r_{AM}^{con-1st} \times r_{MB}^{con-1st} \tag{4.16}$$

Theoretically, each normalized flux can be assigned a corresponding threshold. For simplicity, above 4 normalized fluxes can be agglomerate together which only need one threshold value:

$$r_{AB} = r_{AB}^{pro-1st} + r_{AB}^{pro-2nd} + r_{AB}^{con-1st} + r_{AB}^{con-2nd} \tag{4.17}$$

Then r_{AB} is utilized to evaluate the correlation of species B to species A. PFA kinetics reduction starts from a list of preselected important species and selects any species with correlation to one of the selected species larger than a threshold ϵ_r. This procedure is conducted iteratively until no new species can be added to the list. Then a reduced kinetics is generated. In this study, 0.02 is chosen as the threshold value ϵ_r for PFA, which is a compromise between computational efficiency and accuracy [28, 34, 35]. The flow chart of ODEPIM is summarized in Fig. 4.2.

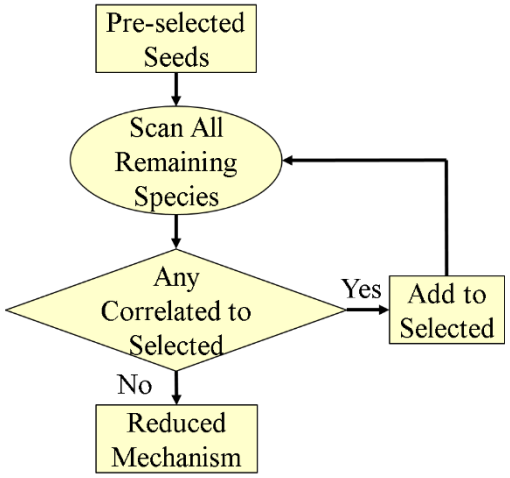

Figure 4.2: Flow chart of PFA method for kinetic mechanism reduction.

4.2.2 Space-Time Correlations

The basic idea of DAC is to generate reduced kinetics for each spatial location and time step (via the PFA method). To guarantee conservation of species, transport equations of inactive species are still solved but their chemical source terms are frozen to zero. Unfortunately, doing on-the-fly reduction by simply applying the PFA method for each grid cell and time step demands significant CPU overhead, which severely reduces the benefits of DAC [28]. In fact, many spatial locations and time steps have similar thermo-chemical states, thus could share the same reduced kinetics. Therefore, it is more efficient to group grid points in space-time hyperspace into zones of the chemical thermodynamic state space. The PFA calculation is required for only one point in each space-time zone of similar thermo-chemical state, and other points can copy and use the same reduced kinetics decreasing the CPU overhead requirements [34, 35].

This idea of CoDAC is schematically presented in Fig. 4.3. During the calculation, the reduced kinetics is firstly generated on the fly based on the chemical thermodynamic state of the centroid grid on each parallel processor. Then CoDAC scans

all grid cells in dictionary order. Adjacent time steps and spatial neighbors are likely to correlate to each other. Therefore, the correlation checking procedure is conducted on a 7-point stencil (center, upper, lower, front, back, left, and right) for each 3D grid cell. In particular, CoDAC checks the time correlation first by comparing the thermo-chemical states between the present and previous time steps at this grid cell. If they are correlated according to a pre-specified criterion (i.e. their difference is smaller than a user-specified threshold), then the reduced kinetics on this grid cell do not need to change. Otherwise, CoDAC will check the 3D space correlation by comparing the thermo-chemical state of the present grid cell with the most updated states of its 6 neighbors. If any one of them is correlated to the present grid cell, then its most updated reduced kinetics will be copied and used for the present grid cell. Otherwise a new locally reduced mechanism must be generated from the detailed kinetics on that grid point, and search its neighbors on the same processor to form a new spatial correlation zone. As the time advances, less and less new reduction is required due to the increase of space and time correlations.

Note that each processor generates its own reduced kinetics without the need to communicate with each other, which efficiently reduces the total simulation time.

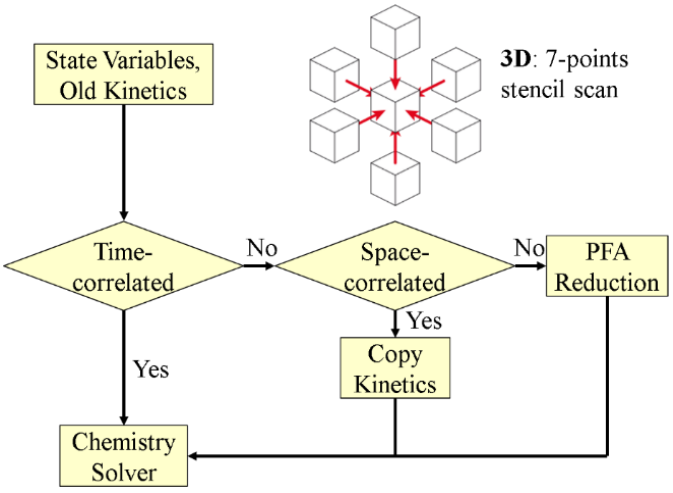

Figure 4.3: Flow chart of the time-space correlation algorithm in CoDAC method.

The key for time and space correlation is a reasonable pre-specified criterion. In order to form a suitable criterion, important marker species and thermodynamic state variables need to be selected. For plasma simulations, electron number density and energy dominate the plasma kinetics and indirectly affect chemical kinetics, so electron number density must be considered in the criterion. According to equivalence ratio effects and the Arrhenius law, fuel, oxidizer, and temperature should be considered in this criterion. Radicals and intermediate species are critical for combustion. Radicals, fuel fragments and excited species, primarily sustain combustion. For this reason, OH is adopted as a representative of radicals in the criterion, and as the marker of high temperature chemistry. Actually, other important radicals like O also can serve as the representative. In addition, low temperature chemistry (LTC) is important for phenomena like cool flame, low-temperature ignition (LTI), and lean blow-out (LBO), thus CH_2O and HO_2 should be considered in the criterion as explained by Sun et al. [35]. Therefore, the resulted criterion is the following (quantities with superscript 'o' represent the values at candidate time step/grid cell):

$$\boldsymbol{\Delta} = \left(\frac{|T - T^o|}{\epsilon_T}, \frac{|lnX_{elec} - lnX_{elec}^o|}{\epsilon_X}, \frac{\left|lnX_{fuel} - lnX_{fuel}^o\right|}{\epsilon_X}, \frac{|lnX_{ox} - lnX_{ox}^o|}{\epsilon_X}, \frac{|lnX_{OH} - lnX_{OH}^o|}{\epsilon_X}, \frac{\left|lnX_{CH_2O} - lnX_{CH_2O}^o\right|}{\epsilon_X}, \frac{\left|lnX_{HO_2} - lnX_{HO_2}^o\right|}{\epsilon_X}\right) \tag{4.18}$$

For space correlation, quantities with superscript circle represent the values at the centroid grid point; for time correlation, they represent the values at previous time step at the same grid point. When $\|\boldsymbol{\Delta}\|_\infty \leq 1$, the two states are considered as correlated to each other, and can share the same reduced kinetic mechanisms. The thresholds are set as $\epsilon_T = 20K$ and $\epsilon_Y = 25\%$. Past work shows that the accuracy of OAK is not sensitive to these

thresholds [35]. When the concentration of a species is too small, large relative uncertainty arises. Therefore any of the above five species with a very small mass fraction ($< 10^{-6}$) should be removed from the criterion to avoid unnecessary reduction.

It is noteworthy that the performance of CoDAC is independent of ODE solver.

4.3 Correlated Evaluation of Transport Properties (CoTran)

Mixture-averaged (MAD) transport coefficients are employed for the computation of viscous, thermally conductive, and species diffusion fluxes, and to capture differential diffusion and the strong interaction among molecular diffusion, turbulent mixing, and finite-rate kinetics.

In conventional simulations, transport properties based on the MAD model are computed at every time step and grid point, and this takes a significant amount of CPU time. As shown in past works [36], the CPU time of diffusion coefficients is often the 2nd largest for serial simulations, and can become the largest if CPU time of chemical source term is significantly reduced by CoDAC, ODEPIM, etc. On the other hand, diffusion coefficients, in fact, also contain time and space correlations. For instance, the unburnt/burnt regions far from the premixed flame should have similar transport properties. In plane-to-plane plasma discharge reactor, chemical thermodynamic state of the plasma is proved relatively uniform except the sheath layers near the walls (i.e. space correlation). In the quasi-steady state, the diffusion coefficients from one time step to the next change only slightly. Therefore, by the same idea as CoDAC, only one time computation is needed in each space-time correlation zone for transport properties, and the calculated diffusion coefficients are copied to every point in the zone [36]. Again, the copy operations are confined within each processor to eliminate MPI communication, and a 7-point stencil is adopted for time and space correlation checking.

Just like CoDAC, the idea of CoTran is to agglomerate space and time correlation groups in phase space defined by few parameters and a user-specified threshold ϵ_{tran} (set

to be 0.05 in this study). Then the transport properties can be calculated only once for each correlation group, as shown in Fig. 2. For computational efficiency, time correlation is always applied first, and space correlation is applied only if time correlation is not applicable. In the parallel implementation, to minimize MPI communication time, each processor calculates its own diffusion coefficients even if its chemical thermodynamic states are spatially correlated with some other processors. In another words, spatially correlated transport (CoTran) only applies within each processor instead of all processors together.

The primary difference between CoTran and the correlation grouping in OAK is the selection of marker parameters in the correlation criterion, which should reasonably represent the transport properties rather than kinetic reactivity. In most models [95], viscosity μ_k and conductivity k_k of the pure k^{th} species depend only on temperature, whereas mass diffusivity D_k depends on both temperature and pressure, but ρD_k only depends on temperature. Therefore, temperature must be considered in the criterion while the pressure need not be, if ρD_{mix} rather than D_{mix} is calculated and copied during CoTran. In addition, based on the Wilke formula [96] of the MAD model, diffusion coefficients of gas mixture are nonlinear combinations of those of pure species weighted by their concentrations. Therefore, species with larger concentration make a greater contribution to the transport properties of the gas mixture, even if they are inertial. In this study, diluent (N_2, Ar, etc.), oxidizer (in most cases: O_2), fuel, H_2, H_2O, CO, and CO_2 contribute more than 95% of the total mole fraction, and contribution from the rest is at the same level as the threshold ϵ_{tran}. Therefore, the correlation criterion for CoTran is designed as the following:

$$\boldsymbol{dist} = \left(\frac{T - T^o}{T^o}, \frac{X_{diluent} - X^o_{diluent}}{X^o_{diluent}}, \frac{X_{fuel} - X^o_{fuel}}{X^o_{fuel}}, \frac{X_{ox} - X^o_{ox}}{X^o_{ox}}, \frac{X_{H_2} - X^o_{H_2}}{X^o_{H_2}}, \frac{X_{H_2O} - X^o_{H_2O}}{X^o_{H_2O}}, \frac{X_{CO} - X^o_{CO}}{X^o_{CO}}, \frac{X_{CO_2} - X^o_{CO_2}}{X^o_{CO_2}}\right) \tag{4.19}$$

where superscript "o" represents the quantities evaluated at the center of the CoTran group. When $\|\boldsymbol{dist}\|_\infty \leq \epsilon_{tran}$, the CoTran threshold, the two states are considered as correlated to each other with respect to transport properties, and their transport properties are taken to be equal. In this study ϵ_{tran} is 5%, which is larger than the contribution from species other than the above seven.

Unlike CoDAC, CoTran has no CPU overhead except for the correlation checking, so it is highly efficient. The performance of CoTran is also independent of ODE solver.

CHAPTER 5

NUMERICAL VERIFICATION

In Chapter 4, we introduce several numerical techniques (ODEPIM, CoDAC, CoTran) to accelerate the calculation of detailed finite-rate chemistry and multi-species transport in turbulent combustion. Before applying these innovative techniques to investigate the physics of turbulent combustion, both accuracy and efficiency of these techniques need to be numerically verified and experimentally validated in a comprehensive and solid manner. In this chapter, numerical verification is conducted on three cases: a laminar plasma discharge of gas mixture, a canonical turbulent premixed flame, and a turbulent non-premixed flame in shear layers. The experimental validation will be conducted in the next chapter on a partially premixed jet flame case.

5.1 Laminar Plasma Discharge of Gas Mixture

To enhance the computational efficiency for the simulation of plasma assisted combustion (PAC) models, three new techniques, correlated dynamic adaptive chemistry (CoDAC), point-implicit stiff ODE solver (ODEPIM), and correlated transport (CoTran), are combined together to generate a new simulation framework. This framework is applied to non-equilibrium plasma assisted oxidation of $C_2H_4/O_2/Ar$ mixtures in a low-temperature flow reactor. The new framework is extensively verified by both temporal evolution and spatial distribution of several key species and gas temperature. Simulation results show that it accelerates the total CPU time by 3.16 times, accelerates the calculation of kinetics by 80 times, and accelerates the calculation of transport properties by 836 times. The high accuracy and performance of the new framework indicates that it has great application potentials to many different areas in the modeling and simulation of plasma-assisted combustion.

5.1.1 Introduction

Recent years, non-equilibrium plasma discharges have drawn great attention due to its potential to enhance and stabilize combustion in internal combustion engines, gas turbines, and scramjet engines [18, 168-170]. Experimental studies have demonstrated that plasmas can shorten the ignition delays [171-173], extend extinction limits [174], improve flame stabilization [174], increase flame speed [175] and suppress soot formation [176, 177]. However, the understanding of the mechanism of plasma/combustion interaction is still lacking due to the complicated thermal, kinetic and transport coupling between plasma and combustion. In particular, it is still unclear which reaction pathways are dominant, and what reaction pathways are still missing. In order to answer this question, a combination of both computational and experimental efforts with detailed kinetics is required.

In contrast to experimental efforts, there have been only a few detailed numerical studies of plasma assisted combustion (PAC). Numerical simulation can be immensely advantageous in complementing the experimental efforts and in providing significant insights into the mechanism of plasma enhancement of combustion. The multi-scale nature of PAC, however, creates significant difficulties of stiffness for comprehensive modeling studies. As a result, many studies have resorted to simplified 0D models to gain understanding of the plasma kinetic and thermal effects in fuel-air mixtures [178-181]. In such models, plasma discharge was assumed to be uniform in the entire volume during each discharge pulse. The electric field and electron density were pre-tuned such that the coupled energy can match that in experiments. These models did not consider sheath formation, and charge accumulation on the dielectric layers. In addition, species and thermal diffusion effects were ignored. In the past few years, Nagaraja et al. [86, 172, 173, 182-184] developed a self-consistent, 1D parallel model to simulate pulsed, nanosecond discharges in fuel-air mixtures. The framework is capable of resolving

electric field transients from pulse to pulse, as well as the cumulative effects of multiple pulses on fuel oxidation and combustion. However, the comprehensiveness of this model results in significant computational difficulties even on our supercomputer capable of peta-scale and beyond. For example, the simulation of 150 discharge pulses for $C_2H_4/O_2/Ar$ mixtures took more than 3 weeks. One of the major computational challenges comes from the large number of species and the dramatic stiffness of the detailed plasma-combustion kinetics which need to be calculated on every grid point and every time step. In a plasma-combustion system, the characteristic timescales of different phases can range from millisecond to picosecond and even beyond. In most past works, the variable-coefficient ODE solver (VODE) [37] is usually applied to solve the stiff ODE system. However, the computation time of VODE solver increases as cubic of the number of species due to the iterative "Jacobian matrix decomposition". For this reason, it is almost impossible to involve large detailed mechanisms or moderate mechanisms in simulations with large number of grid points, especially in the high dimensional computational domain.

In order to enable the detailed plasma-combustion kinetics in comprehensive modeling, people can either reduce the stiffness of the ODE system, such as the computational singular perturbation (CSP) method [38, 39], the intrinsic low-dimensional manifold (ILDM) method [40], the dynamic stiffness removal method [41] and the hybrid multi-timescale (HMTS) method [42], or reduce the size of the kinetic mechanism, such as the visualization method [22], the direct relation graph (DRG) method [23], the DRG with error propagation (DRGEP) method [24], and the multi-generation path flux analysis (PFA) method [25]. Recently, Sun et al. [34-36, 185] integrated correlated dynamic adaptive chemistry and transport (CO-DACT) method with the HMTS method and successfully addressed the challenge of utilizing large detailed chemical kinetics in combustion modeling. In CO-DACT, correlated reduced chemical mechanisms in time and space are generated on-the-fly from the detailed one by the multi-generation PFA

method, and the calculation of mixture-averaged transport coefficients is also grouped by correlations in space and time. Then HMTS is adopted to replace the VODE method to time advance the chemical source term based on the local reduced chemical mechanism. The efficiency and accuracy of CO-DACT has been demonstrated by comprehensive numerical tests.

Despite above efforts, the correlated dynamic adaptive chemistry (CoDAC) and correlated transport (CoTran) methods have never been integrated with non-equilibrium plasma discharges of gas mixtures. There is a need to investigate whether chemical mechanism reduction methods are also valid for plasma kinetics. Furthermore, even the highly reduced kinetics will keep the multi-timescale nature of plasma-assisted oxidation. For this reason, much faster stiff ODE solvers like point-implicit stiff ODE solver (ODEPIM) [43, 44] are preferred. In addition, CoDAC and CoTran have not been implemented via parallel high performance computing (HPC), which is necessary for high dimensional simulation with immensely fine grid. The zoning of CoDAC and CoTran method has advantage for parallelization because there is no need to communicate reduced mechanism of local zone with other processors. Ideally, parallel CoDAC and CoTran can resolve the efficiency degeneracy issue of CoDAC and CoTran when the number of correlated spatial zones increases. In particular, larger number of zones can be distributed to more processors, which results in relatively fixed number of zones on each processor to guarantee the efficiency of CoDAC and CoTran.

This work incorporates CoDAC, ODEPIM, and CoTran to the time-accurate 1D model for parallel simulation of non-equilibrium plasma assisted oxidation of $C_2H_4/O_2/Ar$ mixtures in a low-temperature flow reactor. In the reactor, the gas mixtures are activated by nano-second pulsed discharge at 60 Torr. The simulation can resolve the species and temperature evolution across the discharge gap. Detailed analysis is conducted to evaluate the efficiency and accuracy of CoDAC, ODEPIM, and CoTran for PAC model.

5.1.2 Theoretical Framework

5.1.2.1 Governing Equations and Numerical Methods

The model contains Poisson equation for electric potential, electron energy equation, and N species continuity equations for all charged and neutral species given by Eqs. (5.1-5.3), respectively,

$$\nabla \cdot (\epsilon \nabla \phi) = -e(n_+ - n_- - n_e) \tag{5.1}$$

$$\frac{\partial n_\epsilon}{\partial t} + \nabla \cdot J_\epsilon = \dot{\mathrm{Q}}_\epsilon \tag{5.2}$$

$$\frac{\partial n_k}{\partial t} + \nabla \cdot J_k = \dot{\omega}_k \tag{5.3}$$

where the electron energy density n_ϵ is given by the product of electron density n_e and electron energy ϵ_e. The drift (mobility)-diffusion model is used to calculate the transport of energy and species.

Furthermore, the gas mixture flow is modeled by solving mass, momentum and energy conservation equations simultaneously, given by Eqs. (5.4-5.6), respectively,

$$\frac{\partial \rho}{\partial t} + \frac{\partial \rho u_i}{\partial x_i} = 0 \tag{5.4}$$

$$\frac{\partial \rho u_i}{\partial t} + \frac{\partial (\rho u_i u_j)}{\partial x_j} = -\frac{\partial p}{\partial x_i} + \frac{\partial \tau_{ij}}{\partial x_j} + F_i^{EHD} \tag{5.5}$$

$$\frac{\partial \rho E}{\partial t} + \frac{\partial [(\rho E + p) u_i]}{\partial x_i} = -\frac{\partial q_i}{\partial x_i} + \frac{\partial \left(u_i \tau_{ij}\right)}{\partial x_j} + \dot{Q}^{JH} \tag{5.6}$$

The 2nd order Strang splitting scheme [61, 107, 108] is used to treat the convection-diffusion term and the kinetic source term separately in Eq. (3) and (6). In particular, the convection-diffusion term is integrated for half time step. Then the resulted state variables are used as initial condition to integrate the ODE system with kinetic source for one time step. Its results are regarded as the new initial conditions to integrate

the convection-diffusion term for another half time step to reach the 2nd order accuracy. The ODE system in the second fractional step consists of the followings:

$$\frac{dn_k}{dt} = \dot{\omega}_k \tag{5.7}$$

$$\frac{dT}{dt} = -\frac{1}{\rho C_p}\sum_{k=1}^{N} h_k \dot{\omega}_k \tag{5.8}$$

As we can see, the dimension of above ODE system is (N+1), and the objective of the CoDAC approach is to generate zoned reduced kinetics on-the-fly to decrease the number of species and thus the size of above ODE system.

5.1.2.2 Physical Configurations

The geometry of the numerical model is shown in Fig. 5.1. The model considers a particular cross-section of the flow reactor, and the computational domain is 14 mm long from the left electrode to the right electrode (the dashed line in Fig. 5.1). The voltage pulses are applied at the right electrode, whereas the left one is connected to the ground. The dielectric constants of quartz and silicone rubber dielectric layers are chosen to be 3.8 and 9.0, respectively. An adaptive mesh is utilized to provide more grid points near the boundary to resolve the sheath formation. 48 processors are used for parallel computing.

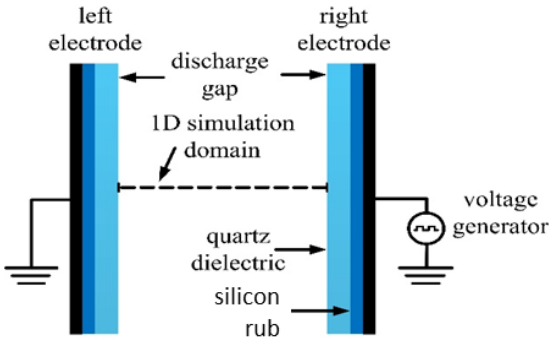

Figure 5.1: Geometry of the simulation model for plasma discharge of gas mixtures.

5.1.2.3 Nanosecond Voltage Waveforms

In the simulations, a Gaussian fit of the experimental high voltage pulse waveform is used, as shown in Fig. 5.2. Note that the curve-fit used in the present simulations uses only two voltage peaks, whereas the measured waveform has additional smaller peaks. It is found that the input energy coupled after the first two peaks of the voltage waveform is negligible, so the latter peaks are neglected in the simulation, in order to improve computational efficiency. To tackle the multi-scale nature of the problem, adaptive time-stepping is implemented with small time-steps (10^{-13} - 10^{-12} s) during each voltage pulse, and larger time-steps (10^{-10} s) in the gap between two consecutive pulses. More details about the numerical methods can be found in Nagaraja *et al.* [108, 182, 186].

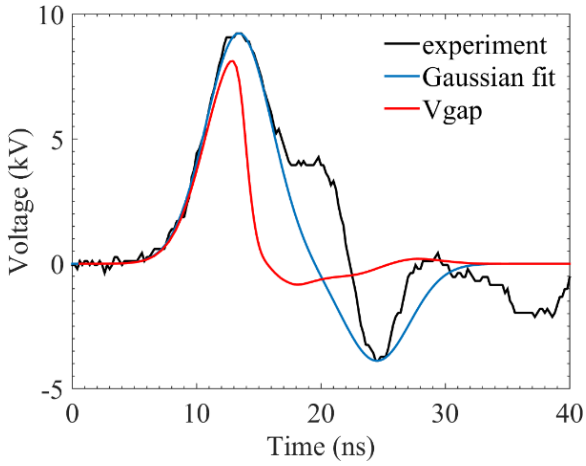

Figure 5.2: Gaussian fit to experimental pulse waveform used in simulation.

5.1.2.4 Plasma-Combustion Chemistry and Gas Mixtures

The plasma-combustion kinetics used in the present work is assembled by combining the new low temperature (below 700~800 K) plasma-combustion mechanism (HP-Mech) [187-189] with Ar and O_2 plasma reactions taken from ZDPlasKin [190] database. The rate constants of reactions between excited Ar species and ground state O_2 molecules were taken from Sun *et al.* [191]. In addition, reactions between $O(^1D)$ and hydrocarbons are added in the kinetic mechanism because they dominate the $O(^1D)$ pathways and significantly contribute the hydrocarbon oxidation as shown in our past studies [183]. The detailed mechanism (85 species) is globally pre-reduced by second-generation PFA method and validated based on the comprehensive physical conditions of present reactor. The resulted kinetics containing 60 species, 375 chemical reactions and 161 plasma reactions. This is a moderate size kinetic model, but requirement to calculate it on each grid point at each time step makes it still extremely expensive even equipped with parallel HPC. The simulations are conducted at 60 Torr pressure, and 300 K initial

temperature. The initial mixture composition was C_2H_4:Ar:O_2 = 0.062:0.75:0.18 in mole-fractions.

5.1.3 Results and Discussions

In this study, simulation results generated by VODE with detailed kinetics are considered as benchmark for verification.

5.1.3.1 Performance Analysis

To understand why CoDAC method can work, we need to investigate the temporal and spatial behavior of active species number.

Figure 5.3 illustrates the temporal evolution of active species number and gap voltage at the center of discharge gap. Profile of active species number shows periodic oscillation following that of gap voltage, but both its crest and trough roughly increase with time as more active species are generated by the plasma discharges. Therefore, CoDAC can efficiently reduce the size of ODE system benefiting from the periodical oscillation phenomenon, but the reduced size gradually increases with time due to the progress of chemical reactions. The profile also indicates that the crest and trough of active species number finally reach a quasi-equilibrium of 52 and 37, respectively. Our tests indicate that electron energy equation is extremely sensitive to total charge and plasma kinetics. In particular, even if only one or two plasma reactions are reduced, the electron energy can diverge during the simulation. For this reason, CoDAC is not directly applicable to plasma kinetics and thereby all charged and excited species have to be kept in the pre-selection list. Therefore, the evolution of active species number primarily represents the change in chemical species. An interesting fact is that most surges of active species number happen during the gap between two adjacent discharge pulses. The reason is that chemical reactions are much slower than plasma reactions, which results in a relaxation lag for chemical response, i.e. a hysteresis phenomenon.

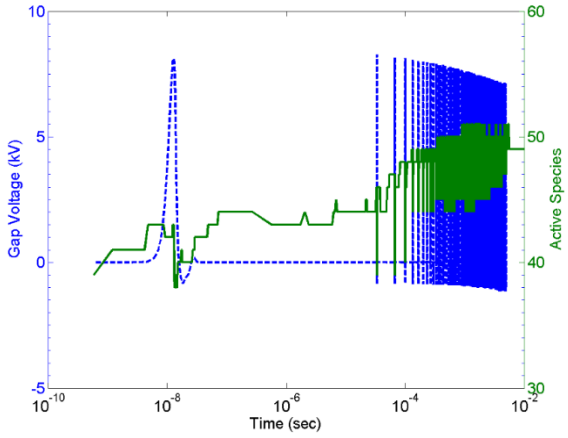

Figure 5.3: Temporal evolution of active species number (green solid line) and gap voltage (blue dashed line) at the center of discharge gap.

Figure 5.4 shows the spatial distribution of active species number at the peak of the 1st, 15th, 50th, 100th, and 150th discharge voltage pulse. Regions close to boundaries often have larger active species number because the higher concentration of reactive species in the sheath layers causes more progress of fuel oxidation. Unlike the flat profiles of species in bulk plasma as shown in previous study [183], the active species number profile is not always uniform. The non-uniformity does not appear in species profile because active species number in bulk plasma only varies one or two. This observation also justifies the importance of one-dimensional simulations compared to zero-dimensional ones. 48 processors are used in the simulation, so averagely only 0.03 cm of computational domain is allocated in a processor. On the other hand, the spatial distribution profile is piecewise constant with each piece much larger than 0.03 cm. Therefore, most processors only contain one spatial correlation zone, and only require PFA reduction once per time step. The profiles of the 100th pulse and the 150th pulse

almost coincide with each other, which indicates that the spatial distribution of active species number also reaches a quasi-equilibrium just like temporal evolution in Fig. 5.3.

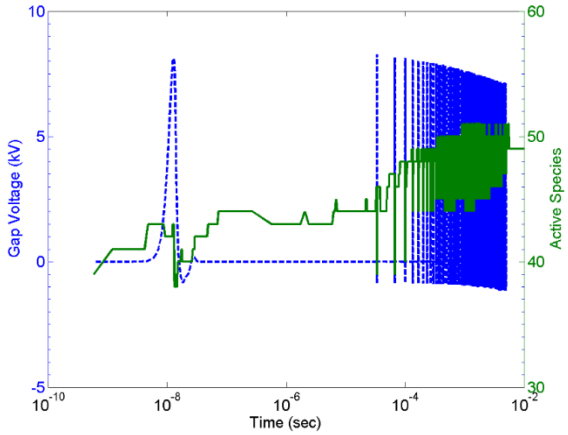

Figure 5.4: Spatial distribution of active species number.

Note that the peak values in Fig. 5.4 are smaller than those in Fig. 5.3. This is because each spatial distribution in Fig. 5.4 is evaluated at the peak of each discharge voltage pulse, while the surge of active species number is mainly during the gap between two adjacent pulses as shown in Fig. 5.3. In addition, due to the spatial homogeneity of plasma, number of active species/reactions mainly changes with time rather than space. Therefore, the time saving from CoDAC also mainly varies with time rather than space. In both temporal evolution and spatial distribution, 60 species in detailed kinetics are never active together at the same time and space. Furthermore, number of active species are significantly smaller than 60 at most time and space. This is where the better performance of CoDAC method comes from.

Table 5.1 lists the CPU time speed up and saving for five combinations of new methods. Among all three methods, ODEPIM provides the most significant speed up of more than two for total CPU time. In contrast, CoDAC reduces the total CPU time by

21% and CoTran reduces the total CPU time by 17%. To understand the speed up and time saving, CPU time components and their distribution must be diagnosed in detail.

Table 5.1: Speed up and saving of total CPU time by five combinations of new methods w.r.t. VODE with detailed kinetics.

w.r.t. VODE	VODE +CoDAC	ODEPIM	ODEPIM +CoDAC	ODEPIM +CoTran	ODEPIM +CoDAC +CoTran
Speed up	1.267291	2.388692	2.651159	2.892417	3.160962
Saving	21.0915%	58.1361%	62.2806%	65.4268%	68.3641%

CoDAC method only directly affect the performance of kinetic source term, which is the largest component of CPU time in VODE with detailed kinetics. Figure 5.5 shows the time evolution of CPU time speed up of kinetic source term by CoDAC method, and compare it with that of active species number. For the case with CoDAC method, PFA time is added into time of kinetic source term for a fair comparison. It is seen that CoDAC method can speed up the kinetics up to approximately 3 times. The average speed up is 1.55, which saves 35.5% CPU time of kinetics. The main reason for this relatively low speed up is that plasma mechanism cannot be reduced, and all charged and excited species are preselected. The periodic oscillation and time variation of cusp and trough of speed up roughly follows that of active species number. As the number of active species increases with time, the speed up is reduced accordingly. This demonstrate the theoretical conclusion that CPU time of kinetics is a monotonically function of active species number. The speed up does not strictly follow active species number and is much more oscillated. The reason is that for ODE systems with the same dimension, some physical conditions (range of timescales) are harder to converge (i.e. stiffer) while some others are easier.

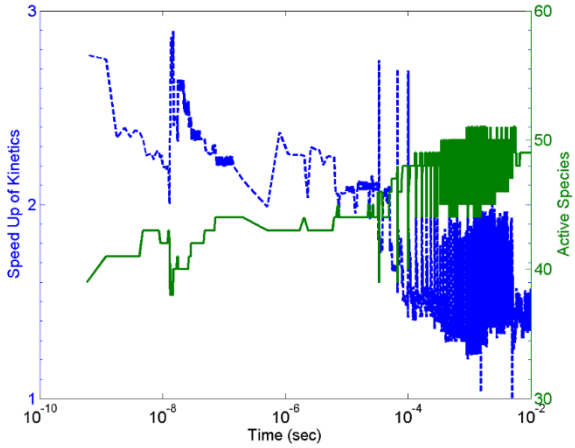

Figure 5.5: Temporal evolution of CPU time speed up of kinetic source term by CoDAC method (blue dashed line), and that of active species number (green solid line) at the center of discharge gap.

To obtain a more clear idea about the performance of CoDAC, ODEPIM, and CoTran. Figure 5.6 compares the average CPU time distribution per time step of four combinations of methods. Unlike the previous studies [34, 35], PFA time is negligible in this work due to the computational intensity of one-dimensional plasma simulation. For both VODE and VODE+CoDAC, kinetics solver time dominate the total CPU time. More precisely, kinetics solver time accounts for 54% of total CPU time for VODE with detailed kinetics, and it accounts for 44% of total time for VODE+CoDAC. For this reason, ODEPIM is applied to further improve the performance of kinetics solver, and kinetics time is further reduced to only 1.82% of the total CPU time. In particular, ODEPIM further speeds up the kinetics calculation by 60 times, which saves 98% of the kinetics calculation time. For ODEPIM+CoDAC, CPU time of calculating transport properties becomes 16.6% of the total CPU time. To deal with the CPU time for transport, CoTran is applied to speed up the transport calculation by 836 times, which reduces the percentage of transport time to negligible amount (0.03%) of the total CPU

time. In addition, unlike the PFA overhead of CoDAC method, CoTran has no overhead at all. Since the calculation other than kinetics and transport dominates the total CPU time for both ODEPIM+CoDAC and ODEPIM+CoDAC+CoTran, which significantly dilutes the effects of new methods, we need to further investigate which components dominate. The total CPU time includes update time, Input/Output (I/O) communication time to write data, calculation time of electric field equation, electron energy equation, and Navier-Stokes (NS) equations (species, mass, momentum and energy equations). In particular, NS time includes the calculation time of convection, diffusion, transport properties, kinetic source term, PFA overhead time and MPI communication between parallel processors. Since Fig. 5.6 already illustrate the percentage of CPU time for kinetics source term, transport properties and PFA overhead, some of the rest must dominate the total CPU time for cases of ODEPIM+CoDAC and ODEPIM+CoDAC+CoTran.

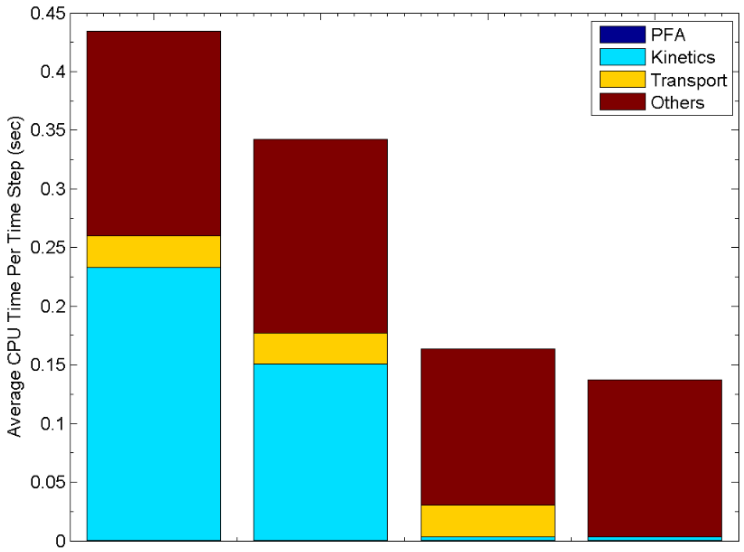

Figure 5.6: Comparison of average CPU time distribution per time step of VODE, VODE+CoDAC, ODEPIM+CoDAC, and ODEPIM+CoDAC+CoTran.

Figure 5.7 shows the temporal evolution of CPU time per time step for update time (include I/O), calculation time of electric field equation, electron energy equation, convection, diffusion, and MPI communication time during the simulation of ODEPIM+OAK+CoTran framework. The last three components are measured together, because they are interlocked to each other in the code and thereby difficult to measure separately. As expected, CPU times of both electric field and electron energy equations are nonzero during the discharge pulses, and zero during the gap between two adjacent pulses. Time of electric field equation is extremely small, while that of update and electron energy equation can be significant during discharge pulses. The profile of both update time (include I/O) and time of convection, diffusion and MPI are highly oscillated. Since update, convection, and diffusion have relatively fixed amount of calculation, such strong oscillations must come from the unstable performance of MPI and I/O communications, which heavily depend on the traffic of cluster network and its scheduler. At some extreme situation of heavy traffic, MPI communication time can be 4 times that of the rest, which dominate the performance and may result in either increase or decrease of total time. Also notice that this is a new issue originated from parallel computing which does not exist in serial simulations of previous studies [34, 35]. In addition, past studies [36] indicate that the CPU time of convection and diffusion calculation are much smaller than that of transport properties. Therefore, MPI communication must be much larger than the CPU time of convection and diffusion.

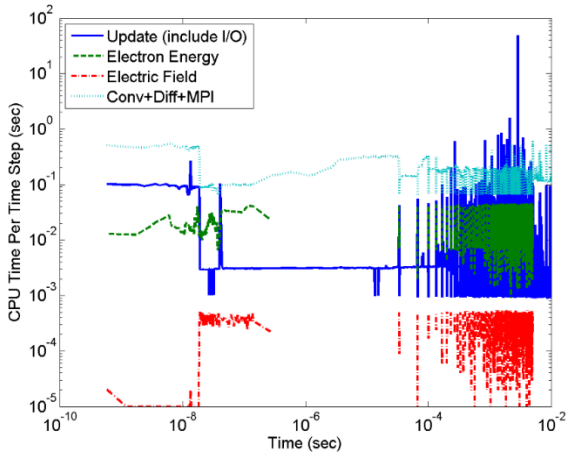

Figure 5.7: Temporal evolution of different components of CPU time per time step other than kinetics and transport properties during the simulation of ODEPIM+CoDAC+CoTran framework.

The oscillating profiles in Fig. 5.7 cannot illustrate the overall distribution of CPU time. In particular, Figure 5.7 shows that the CPU time to compute electric field is very small, but it is still unknown, which of the other three components is the dominant one. For this reason, Table 5.2 shows the average time per step for each component of total CPU time and their percentages during the simulation of ODEPIM+CoDAC+CoTran framework. Now it is clear that convection+diffusion+MPI is the dominant component. Since MPI communication time is much larger than the CPU time of both convection and diffusion as mentioned above, MPI communication time must dominate the total CPU time. Therefore, to reduce the dilution effects and further enhance the computational efficiency, we must optimize the MPI communication between parallel processors in the future.

Table 5.2: Average time per step for different components of total CPU time and their percentages during the simulation of ODEPIM+CoDAC+CoTran framework.

Components of CPU time	Update (include I/O)	Electron Energy	Electric Field	Convetion +Diffusion +MPI
Average time per step (sec)	0.003613	0.011262	0.000179	0.118677
Percentage (%)	2.701941	8.421148	0.134147	88.74276

5.1.3.2 Verification of Accuracy

Figure 5.8 shows the comparison of temporal evolution of C_2H_2, CH_4, H_2O concentrations and gas temperature calculated by six combinations of methods: VODE, VODE+CoDAC, ODEPIM, ODEPIM+CoDAC, ODEPIM+CoTran, ODEPIM+CoDAC+CoTran. It can be seen that the new methods reproduces the results of VODE and detailed kinetics well in most predictions, considering each simulation took nearly nine million time steps. Overall, CH_4 and H_2O have relatively larger errors than C_2H_2 and gas temperature because they have smaller concentrations and thus are more sensitive to errors introduced by the new methods. For C_2H_2 and H_2O, both CoDAC and CoTran show good accuracy, but ODEPIM shows slightly under-predictions. For CH_4, ODEPIM and CoTran present good agreement with VODE and detailed kinetics, but CoDAC introduces some small errors. For gas temperature, all cases show good accuracy except VODE+CoDAC, which seems to indicate that CoDAC is more compatible with ODEPIM than with VODE.

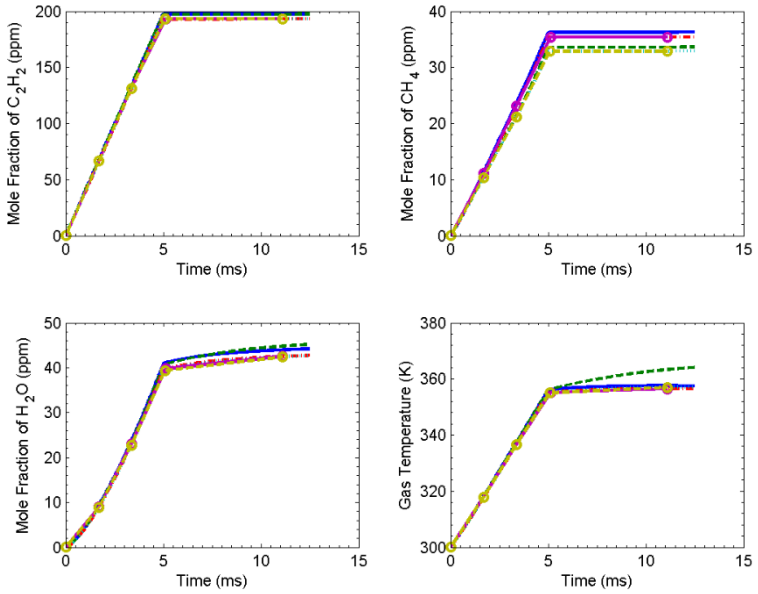

Figure 5.8: Comparison of VODE (blue solid line), VODE+CoDAC (green dashed line), ODEPIM (red dash-dot line), ODEPIM+CoDAC (cyan dotted line), ODEPIM+CoTran (magenta solid line with cycle), and ODEPIM+CoDAC+CoTran (gold dashed line with cycle) for the temporal evolution of C_2H_2, CH_4, H_2O, and gas temperature.

Figure 5.9 shows the spatial distribution of C_2H_2, CH_4, H_2O concentrations and gas temperature predicted by VODE with detailed chemistry (benchmark) and ODEPIM+CoDAC+CoTran, which is both the fastest version and the one with largest errors introduced among all possible combinations. It can be seen that most profiles are almost the same, verifying that the precision is maintained by all the three methods. However, CH_4 profile of the 1st pulse shows significant deviation. Note that this deviation is magnified by the log scale and the actual size is much less than 0.1 ppm, which is very sensitive and has large uncertainty. On the contrary, later pulses do not contain such deviation due to their relatively large concentrations. This is also why species with too small concentrations are ruled out from correlation grouping criteria. In addition, this significant deviation vanishes as the simulation advance to larger number of pulses, which shows that the new framework is both stable and robust. Temperature has

relatively larger deviation than species since all errors of species accumulate to that of temperature.

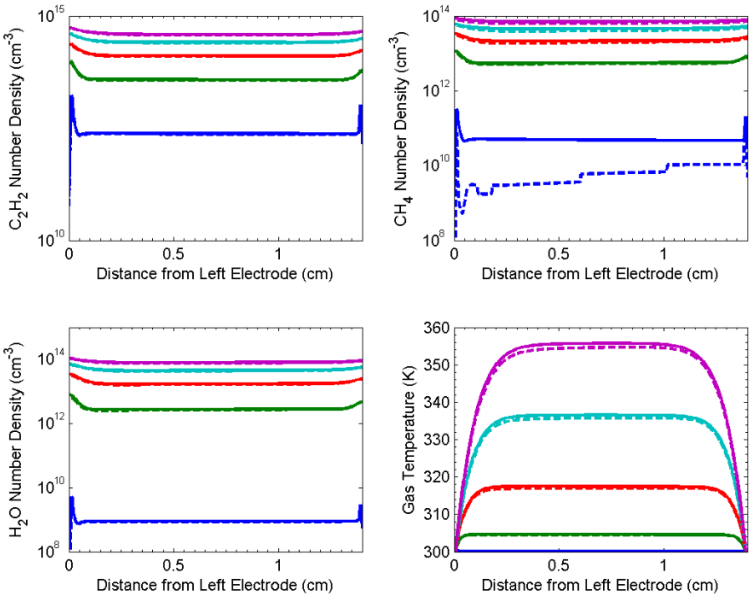

Figure 5.9: Comparison of VODE with detailed chemistry (solid line) and ODEPIM+CoDAC+CoTran (dashed line) for spatial distribution of C_2H_2, CH_4, H_2O, and gas temperature. Blue: 1st pulse; green: 15th pulse; red: 50th pulse; cyan: 100th pulse; magenta: 150th pulse.

The excellent agreement in both temporal evolution and spatial distribution demonstrates that CoDAC is valid to capture the primary phenomena of plasma discharges of gas mixtures.

5.1.4 Conclusion

Correlated dynamic adaptive chemistry (CoDAC), point-implicit stiff ODE solver (ODEPIM), and correlated transport (CoTran) are combined together to accelerate the simulation of non-equilibrium plasma assisted oxidation of $C_2H_4/O_2/Ar$ mixtures in a low-temperature flow reactor. The accuracy and robustness of the new framework are

extensively verified by comparing its results with those of previous simulations without the new methods. In particular, temporal evolution and spatial distribution of several key species and gas temperature are compared to verify the new framework. Temporal evolution of active species number shows periodic oscillation following that of gap voltage pulses. For this reason, CoDAC can efficiently reduce the size of ODE system benefiting from the periodical oscillation phenomena. Spatial distribution of active species number is not always uniform, which justifies the importance of one-dimensional simulations compared to zero-dimensional ones. Simulation results indicate that the new framework provides a speed up of 3.16 times in total, 80 times in kinetics, and 836 times in transport. Therefore, the new framework largely enhance the computational efficiency for simulations of plasma-assisted combustion with detailed plasma-combustion kinetics. Further analysis indicate that MPI communication between parallel processors dominate the total CPU time of the new framework. MPI communication heavily depends on the traffic of cluster network and its scheduler, and its highly unstable performance significantly dilutes the effects of new methods. If the MPI communication can be optimized in the future, the new framework would provide even more significant speed up for total CPU time.

5.2 Turbulent Premixed Flame

A new numerical framework for direct numerical simulation (DNS) of turbulent combustion is developed employing correlated dynamic adaptive chemistry (CoDAC), correlated transport (CoTran), and a point-implicit ODE solver (ODEPIM). The new framework is tested on a canonical turbulent premixed flame employing a real conventional jet fuel mechanism. The results show that the new framework provides a significant speed-up of kinetics and transport computation, which allows DNS with large kinetic mechanisms, and at the same time maintains high accuracy and good parallel scalability. Detailed diagnostics show that calculation of the chemical source term with

ODEPIM is 17 times faster than with a pure implicit solver in this test. CoDAC utilizes a path flux analysis (PFA) method to reduce the large kinetic mechanism to a smaller size for each location and time step, and it can further speed up the chemical source calculation by 2.7 times in this test. CoTran uses a similar correlation method to make the calculation of mixture-averaged diffusion (MAD) coefficients 72 times faster in this test. Compared to conventional DNS, the final framework is 20 times faster in total, kinetics is 46 times faster, and transport is 72 times faster in this test.

5.2.1 Introduction

The development of advanced combustion-energy conversion systems requires accurate simulation tools, such as Direct Numerical Simulation (DNS) and Large Eddy Simulation (LES), for ignition, combustion instability, lean blowout, and emissions. Because of high computational cost, DNS and LES typically employ simplified kinetic mechanisms. Oversimplified kinetic mechanisms, however, are known to be of limited functions and may significantly reduce the quality of prediction [17]. Detailed kinetic mechanisms must be considered for accurate prediction, which normally contain a large number of species. In combustion systems, the characteristic timescales can range from millisecond to picosecond or even beyond, so it is prohibitive to use detailed kinetic mechanisms in DNS/LES of turbulent combustion with a large number of grid cells. As a result, chemistry and transport dominate the resource requirements in most combustion DNS studies [2, 3, 20, 21].

In order to reduce the number of species in detailed kinetic mechanisms, several methods [23-25] have been proposed. Although the globally reduced kinetic mechanisms of around 40 species are small enough for most 0D/1D simulations, they are still too large for 3D simulations of turbulent combustion. On the other hand, any further reduction would introduce significant errors, because globally reduced mechanisms typically have

to be produced based on conditions of interest in practice. To deal with this issue, several adaptive combustion models have been proposed by a number of investigators. Gou *et al.* [28] proposed a dynamic adaptive chemistry method with error control for 0D/1D laminar flames, reducing kinetics locally for each grid point and time step. Liang *et al.* [32] proposed a pre-partitioned adaptive chemistry methodology for 0D partially-stirred reactor using particle probability density function (PDF) methods. In contrast, Wu *et al.* [33] designed a sub-model assignment framework to assign different flamelet/finite rate sub-models rather than different kinetics to different zones of the simulation domain for a 2D laminar triple flame. This method matches the boundaries of zones by only conserving the interested quantities. Both the on-the-fly reduction and zone partition in methods above contain significant CPU overhead for mechanism reduction/zone partition. In order to reduce the CPU overhead, Liang *et al.* [32] and Wu *et al.* [33] proposed pre-generating look-up tables for the zone partition. Covering all conditions through tabulation, however, presents challenges, and the large tables make important demands on memory resources. Recently, Sun *et al.* [34, 35] proposed a simple zone-partition criterion to decide whether a new on-the-fly reduction was required or not, and this significantly reduced CPU overhead. Employing the correlated dynamic adaptive chemistry (CoDAC) technique, Sun *et al.* [34, 35] showed significant reduction of CPU time for chemistry in 1D laminar flames.

Molecular diffusion transport modeling is another obstacle to accurate and efficient DNS of turbulent combustion. Bruno *et al.* [2] compared three models in DNS of a partially premixed flame, and concluded that the mixture-averaged diffusion (MAD) model predicts essentially the same fluid-dynamic and thermo-chemical field as the fully multi-component diffusion (MCD) model, but the fast constant Lewis number model predicts a significantly different flow field. Therefore, the MAD, or a higher fidelity model is needed to guarantee accurate predictions. Although much faster than the MCD

model, applying the MAD model at every time step and every grid cell is still expensive; it is often the 2nd largest component of the CPU time for a given computation, and could dominate CPU use if the kinetic source term is accelerated. To improve the computation of transport properties, Sun and Ju [36] developed a correlated transport (CoTran) technique, and obtained significant further speed-up for extensive 0D/1D laminar flames.

Both the CoDAC and CoTran techniques have been applied only to 0D and 1D simulations of laminar flames. Generalization of these techniques to 3D DNS of turbulent combustion gives rise to several critical questions. 1) How to efficiently scan and form the correlation zones in 3D space. 2) Whether existing CPU overhead reduction methods are adequate for 3D turbulent flames. 3) Whether correlation grouping is valid under high intensity turbulence. 4) How to maintain good parallel scaling performance on a large number of processors. In addition, optimized combinations of the above methods to provide the best possible speed have not yet been developed.

In the present work, a new regime-independent framework for 3D DNS of turbulent combustion with detailed kinetics is developed by incorporating correlated dynamic adaptive chemistry (CoDAC), correlated transport (CoTran) techniques, and an efficient point-implicit ODE solver (ODEPIM) into a conventional DNS platform. All three methods are modified and optimized to adapt to 3D turbulent combustion and parallel high performance computing (HPC). The new framework is tested on a canonical premixed flame interacting with decaying isotropic turbulence to evaluate its accuracy, speed-up and parallel performance.

5.2.2 Theoretical Framework

5.2.2.1 Physical Configurations

A canonical turbulent premixed flame configuration (Figure 5.10) corresponding to the thin reaction-zone regime based on the initial conditions ($\frac{u'}{S_L} = 15,\ \frac{l}{\delta_f} = 0.87$, where u' is the root-mean-square velocity fluctuations, S_L is the flame speed, l is the integral length-scale, and δ_f is the thermal flame thickness) is considered, where an initially planar premixed flame front interacts with a decaying isotropic turbulence. The computational domain consists of a cube with length 0.015 m. Periodic boundary conditions are specified in the span-wise (z) and transverse (y) directions, whereas a characteristic based inflow/outflow boundary condition [192] is specified in the x-direction with a mean flow velocity of 1.5 m/s. The initial isotropic turbulence is generated following the Kraichnan spectrum [193] and the planar flame solution is obtained at equivalence ratio of 0.8 (unburnt temperature is 300 K, and pressure is 1 atm). All the simulations are conducted to 1.5 times initial eddy turn-over time (0.127 ms) to allow flame-turbulence interactions to evolve.

Full-scale DNS simulations with grid size smaller than the Kolmogorov length-scales and large kinetic mechanism is prohibitive for conventional brute force DNS with DVODE solver, so the verification is conducted on a coarse grid of 64^3 cells ($\frac{\delta_f}{\Delta x} = 1.8, k_{max}\eta = 0.178$, where k_{max} is the grid wavenumber, and η is the Kolmogorov length-scale). Therefore, the results presented here should be considered as coarse DNS. Note that ODEPIM+CoDAC+CoTran has run on a fine grid of 384^3 grid cells ($\frac{\delta_f}{\Delta x} = 11, k_{max}\eta = 1.069$) using 1728 processors and finished 1.5 initial eddy turnover time within two days.

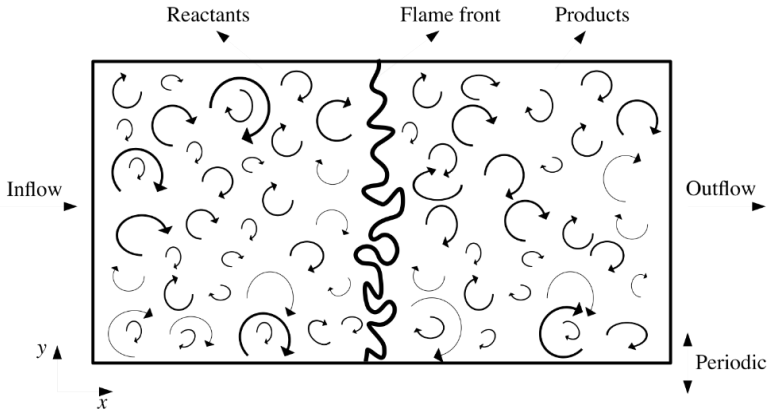

Figure 5.10: A canonical turbulent premixed flame configuration.

5.2.2.2 Combustion Chemistry

The kinetic mechanism used in this study is a real jet fuel pyrolysis mechanism ($C_{11}H_{22}$, Hai Wang, Stanford University, personal communication, 2015). The detailed kinetic mechanism contains 112 species and 790 elementary reactions, and so is prohibitively large for use in DNS. For validation purposes, therefore, a globally reduced kinetic mechanism from this detailed kinetic mechanism is used instead. The globally reduced kinetic model (Y. Gao, T. Lu, R. Xu, H. Wang, D.F. Davidson, C.T. Bowman, R.K. Hanson, personal communication, 2015) contains 38 species and 185 elementary reactions, and has been extensively validated against the detailed kinetic mechanism for parameters such as flame speed, ignition delay, and blowout.

5.2.3 Results and Discussions

To verify the new DNS framework proposed in this study, simulation results from the conventional brute force DNS with the DVODE solver and the new DNS framework integrating ODEPIM, CoDAC, and CoTran methods are compared at the end of the simulation time.

5.2.3.1 Performance Analysis

To understand the performance of CoDAC, it is necessary to visualize the correlation zones of local kinetics. Figure 5.11 shows the spatial distribution of active species number. Both the cold reactants side and the hot products side have small active species numbers. The cold unburnt side ($0 \leq x \leq 0.006\,m$) has two active species (preselected fuel and O_2) and zero active reaction. Therefore, the kinetics in the unburnt side is reduced completely. The hot side ($0.009\,m \leq x \leq 0.015\,m$) contains 10 active species and 27 active reactions, which is a size tolerable to conventional DNS/LES. In particular, the burnt side has more active species and reactions, due to the long lifespan of some minor species like OH. Large active species numbers only exist near the flame surface, and the buffer layers between the flame and non-flame regions have intermediate active species numbers. The brush of large kinetics is significantly wrinkled by flow turbulence.

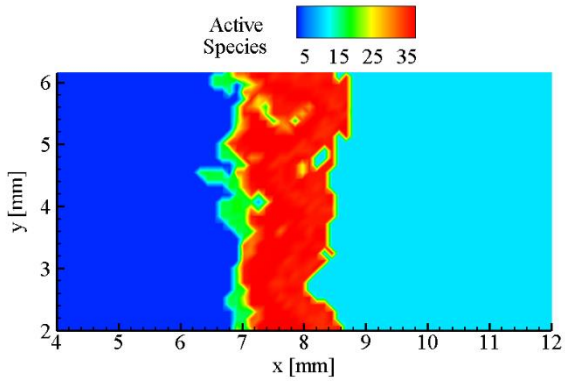

Figure 5.11: Spatial distribution of the number of active species at the center plane (z = 0.75 cm).

Figure 5.12 shows the CPU time distribution of the four methods, to illustrate the speed-up of each component, and conventional DNS with DVODE solver are used as the benchmark case. The CPU time contains the CoDAC overhead, time for calculating

chemical source terms, thermal and transport properties, and other components. With ODEPIM, calculation of the chemical source term is 17 times faster, and the total calculation is 6 times faster. With ODEPIM+CoDAC, the chemical source calculation is 46 times faster, but the total calculation is only 8 times faster. This is because calculation of transport properties becomes the dominant component of total CPU time when ODEPIM is applied, so the significant further acceleration of chemistry calculation cannot provide a much better total speed-up. Also, note that the CPU overhead of CoDAC is negligible, due to the space and time correlation grouping. With ODEPIM+CoDAC+CoTran, calculation of transport properties is 72 times faster without overhead, and the total calculation is 20 times faster. Quantified CPU time distribution can be found in Table 5.3.

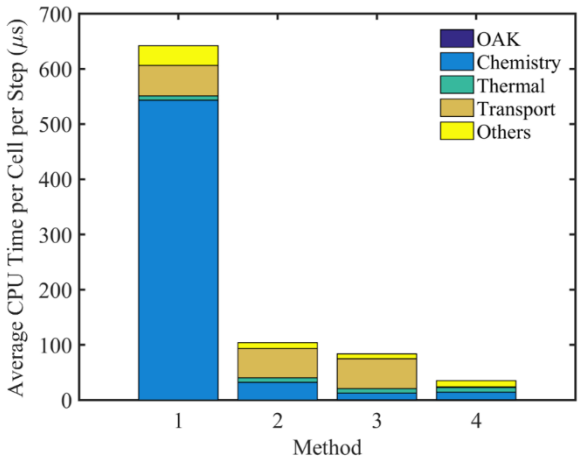

Figure 5.12: Average CPU time distribution per cell per step (μs) for four methods (from left to right): DVODE, ODEPIM, ODEPIM+CoDAC, and ODEPIM + CoDAC + CoTran.

Table 5.3: CPU time distribution of the four methods.

CPU time distribution (%)	CoDAC overhead	Chemistry	Thermal	Transport	Others
DVODE	0	84.61	1.23	8.62	5.54
ODEPIM	0	30.84	7.89	50.92	10.35
ODEPIM+CoDAC	0.67	14.18	9.87	64.73	10.54
ODEPIM+CoDAC+CoTran	1.90	38.38	24.26	3.07	32.40

Full scale DNS requires a large number of processors, so it is important to evaluate the parallel scalability performance of the new frameworks. Figure 5.13 shows the weak scaling of the speed-up for all three new frameworks, and the strong scaling of ODEPIM+CoDAC+CoTran. 32^3 grid cells/processor are used in weak scaling test, and the profiles of the speed-up of all three new frameworks are roughly flat, which indicates a good weak scaling of speed-up. The strong scaling test utilizes a grid of 256^3 cells ($\frac{\delta_f}{\Delta x} = 7.3, k_{max}\eta = 0.713$), and uses the CPU time of 64 processors as the benchmark. The strong scaling profile fluctuates slightly around the ideal curve, which indicates a good strong scaling.

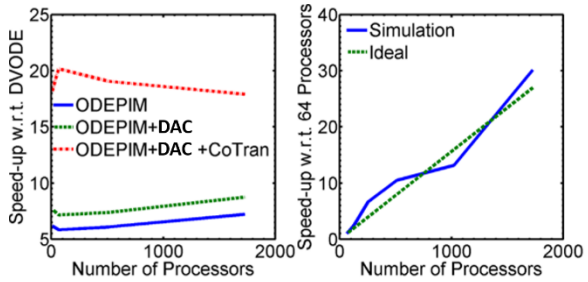

Figure 5.13: Left: weak scaling of the speed-up (w.r.t. DVODE) of the three new frameworks; right: strong scaling of ODEPIM+CoDAC+CoTran.

5.2.3.2 Verification of Accuracy

Figure 5.14 shows a comparison of temperature and vorticity from the two methods. Both methods capture the same wrinkled flame as shown by temperature field and density field. Due to gas expansion, turbulence is damped on the products side. This phenomenon is captured by both methods as shown by the vorticity field. Therefore, the new framework well reproduces results for thermodynamic state and flow field.

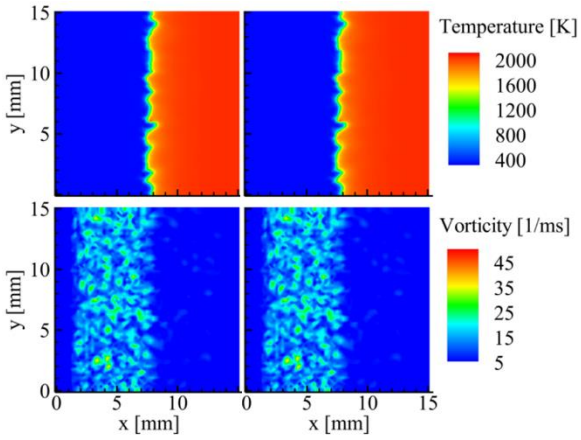

Figure 5.14: Temperature (upper) and vorticity (lower) at the center plane (z = 0.75 cm) using conventional DNS (left) and proposed framework (right).

It is important to verify that the locally reduced kinetics from CoDAC can provide accurate reaction rates and concentrations. Fuel mass fraction and reaction rate for the two methods are shown in Fig. 5.15. Wrinkling of the flame surface can be observed in both quantities, but the flame remains contiguous while the reaction rate contour is disconnected, due to turbulence fluctuations. For both mass fraction and reaction rate, there is no observable difference between the two methods.

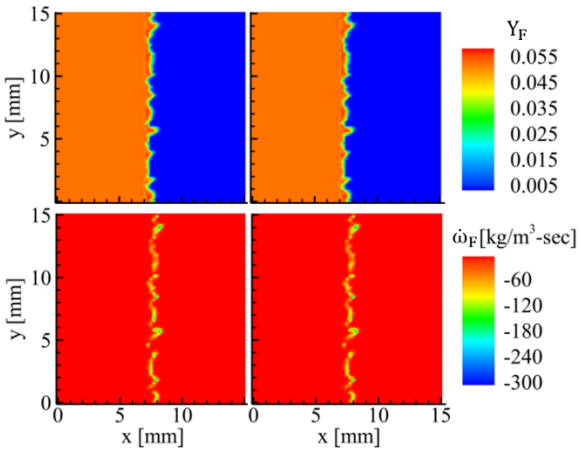

Figure 5.15: Mass fraction (upper) and reaction rate (lower) of fuel at the center plane (z = 0.75 cm) from conventional DNS (left) and proposed framework (right).

Since there is no observable difference between the two methods based on 2D contours, more quantitative comparison is conducted to further evaluate the accuracy of the new frameworks. In Fig. 5.16, stream-wise profiles of the spatially-averaged flame structure of the conventional DNS with DVODE solver and three new frameworks ODEPIM, ODEPIM+CoDAC, ODEPIM+CoDAC+CoTran are compared, and results show no observable difference. Based on the fuel mass fraction profile in Fig. 5.16, unburned mixture, reaction region, and burned mixture account for 46.76%, 19.36%, and 33.88% of the computational domain, respectively.

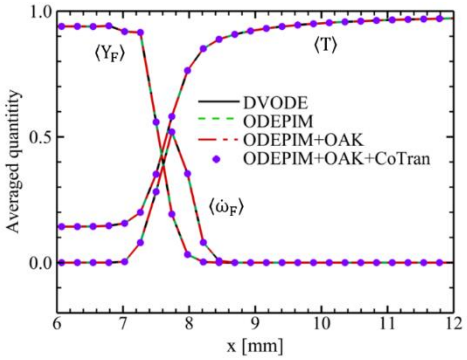

Figure 5.16: Stream-wise profiles of spatially-averaged scaled temperature, fuel mass fraction, and fuel reaction (In the legend, OAK=CoDAC).

In Fig. 5.17, PDF profiles of mass fractions and reaction rates are compared among the conventional DNS with DVODE solver and three new frameworks. The complete PDF profiles show almost no difference among the four methods. Note that all profiles are also zoomed in to show detailed differences.

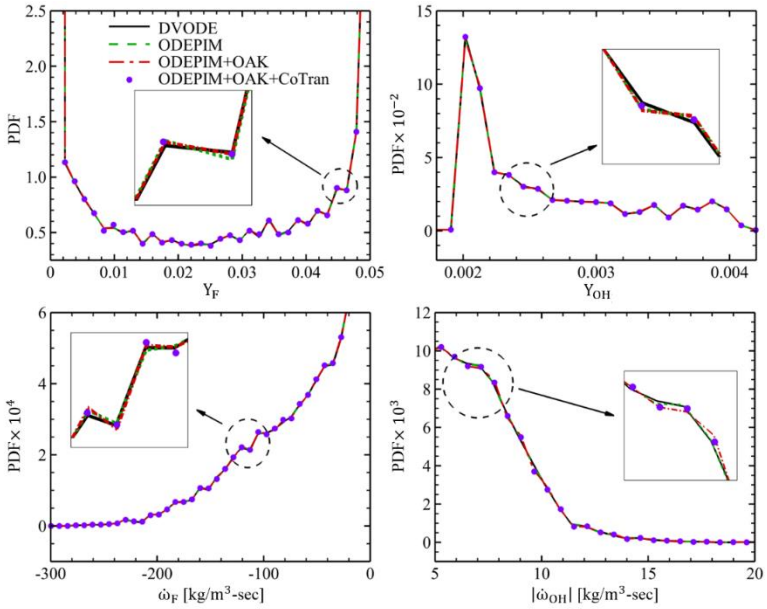

Figure 5.17: PDF profiles of mass fraction (upper left) and reaction rate (lower left) of fuel, mass fraction (upper right) and absolute reaction rate (lower right) of OH. In the legend, OAK=CoDAC.

To further quantify errors introduced by the new methods, L_2 and L_∞ errors are calculated using the conventional DNS with DVODE solver as the benchmark case. L_2 error is the root-mean-square of errors at all locations, and L_∞ error is the maximal error. Table 5.4 shows both L_2 and L_∞ errors of the three new frameworks. All L_2 errors are very small, and increase slightly from ODEPIM to ODEPIM+CoDAC to ODEPIM+CoDAC +CoTran. L_∞ errors show some rare but extreme behaviors of the new methods concealed by L_2 errors. As expected, L_∞ errors are significantly larger than the corresponding L_2 errors. From ODEPIM to ODEPIM+CoDAC to ODEPIM+CoDAC+CoTran, L_∞ errors are not monotonically increasing, and even decrease for temperature, Y_{OH}, and $\dot{\omega}_F$.

Table 5.4: L_2 and L_∞ errors of the three frameworks.

Error	Temperature (K)	Y_F	Y_{OH}	$\dot{\omega}_F$ $\left[\frac{kg}{m^3 \cdot sec}\right]$	$\dot{\omega}_{OH}$ $\left[\frac{kg}{m^3 \cdot sec}\right]$
ODEPIM (L_2)	1.19E-4	5.91E-09	9.50E-10	1.30E-4	1.01E-05
ODEPIM+CoDAC (L_2)	1.27E-4	6.46E-09	1.09E-09	1.36E-4	2.77E-05
ODEPIM+CoDAC +CoTran (L_2)	3.52E-4	1.02E-08	1.59E-09	1.62E-4	2.85E-05
ODEPIM (L_∞)	9.83	1.80E-04	7.89E-05	12.83	7.22E-01
ODEPIM+CoDAC (L_∞)	9.74	1.92E-04	7.75E-05	12.83	1.05E+00
ODEPIM+CoDAC +CoTran (L_∞)	9.36	2.28E-04	7.44E-05	12.38	1.09E+00

Relative errors of ODEPIM+CoDAC+CoTran at mean flame plane (x = 0.75 cm) is shown in Fig. 5.18. Relative errors of temperature are always smaller than 0.5%. All locations with large relative errors of mass fractions and reaction rates only contain negligible corresponding values. Spatial and temporal distributions of errors are shown in Fig. 5.19 in the supplemental material. Most large errors appear on the flame, and they are not sensitive to time.

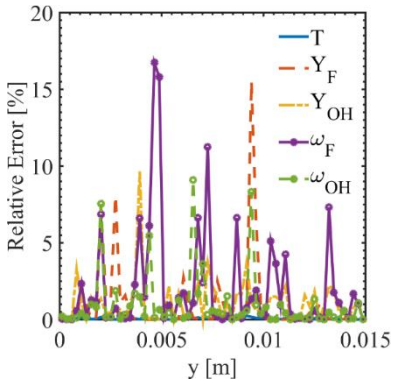

Figure 5.18: Relative errors of ODEPIM+CoDAC+CoTran at the mean flame plane (x = 0.75 cm).

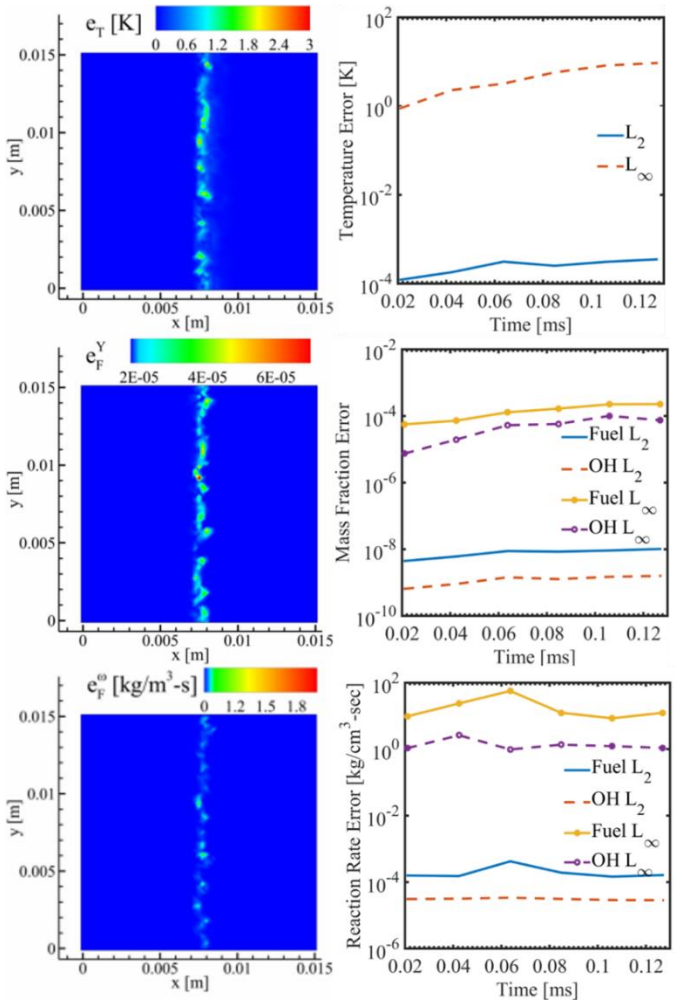

Figure 5.19: Spatial (left) and temporal (right) distribution of errors of ODEPIM+CoDAC+CoTran.

5.2.4 Conclusion

A new framework for 3D DNS of turbulent combustion is developed by combining CoDAC, CoTran, and ODEPIM strategies. ODEPIM is a fast semi-implicit stiff ODE solver, which has accuracy similar to that of an implicit solver, and speed similar to that of an explicit solver. Simulation results show that in this test, calculation of the chemical source term is 17 times faster with ODEPIM as compared to DVODE, a pure implicit solver. CoDAC utilizes the PFA method to reduce the kinetic mechanism

for each location and time step, which significantly reduces the stiffness of the highly nonlinear kinetic system and greatly accelerates the calculation of the chemical source term. The kinetics in the cold unburnt side is reduced to zero reaction, which indicates that CoDAC provides an optimized local reduction. Thermo-chemical zones are introduced and only one PFA calculation is required for each zone, which diminishes the CPU overhead of CoDAC to negligible. Overall, in this test, with ODEPIM+CoDAC, the chemical source calculation is 2.7 times faster than ODEPIM, and 46 times faster than DVODE. CoTran uses a similar correlation technique to reduce the calculation of MAD transport properties, which is the dominant component of total CPU time after application of ODEPIM. In this test, calculation of the transport properties is 72 times faster, and the total calculation is 20 times faster than DVODE. A turbulent premixed flame is utilized to test both the accuracy and the performance of the new framework. Verifications, including 2D contours, stream-wise spatially averaged flame structure, PDF profiles, and quantified errors indicate that the new framework provides highly accurate results. In addition, parallel scaling tests show that the new framework has good weak scaling of speed-up and good strong scaling due to the minimization of MPI communication. In summary, the new framework provides a significant speed-up of calculation of both chemistry and transport, which enables DNS with detailed kinetics and at the same time, maintains high accuracy and good parallel scaling performance.

5.3 Turbulent Non-premixed Flame

Two different kinetics models, GRI-Mech 3.0 and an 11-species syngas model, are compared by performing 3D finite-rate kinetics-based direct numerical simulations (DNS) of a temporally evolving turbulent non-premixed syngas flame. Dynamic adaptive chemistry and correlated transport techniques are applied to enable computationally efficient simulation with the detailed GRI-Mech 3.0.

5.3.1 Introduction

Direct numerical simulation (DNS) and large eddy simulation (LES) are powerful tools for understanding the complex interplay of turbulent mixing, molecular diffusion, and finite-rate kinetics. These approaches are critical to analyzing and improving the design and development of advanced energy conversion and propulsion systems. However, DNS/LES suffers from a bottleneck in the calculation of the stiff finite-rate chemical reactions and transport properties, when moderately complex to detailed chemical kinetics models are employed to account for a wide range of combustion processes.

Detailed finite-rate chemistry and mixture-averaged transport are computationally intensive, especially in 3D turbulent combustion simulations [1-3]. For this reason, except for those consuming excessive computational resources and time [4-6], most past DNS/LES studies of turbulent combustion have used either a flamelet model with detailed chemistry (~50 species or more) [7-10] or a simplified/reduced finite-rate chemical kinetics model with non-stiff reactions (~10 species) [11-16]. Both approaches, however, are of limited accuracy and may reduce the overall quality of prediction [17]. Therefore, acceleration of the computation of chemical kinetics and transport properties will be required to enable computationally efficient and accurate simulations with the DNS/LES approach employing detailed finite-rate chemical kinetics models.

In order to reduce computational cost, several mechanism reduction methods [23-26] have been proposed. These models essentially reduce the number of species in the chemical kinetics models. Well-verified by homogeneous ignition delays, extinction curves in the perfectly stirred reactor, and laminar flame speeds, globally reduced models for hydrocarbons generally require at least ~40 species to cover all user-defined conditions of interest (fuel type, oxidizer type, equivalence ratio, initial pressure and temperature). Unfortunately, such a large number of species is still too large for DNS/LES using the finite-rate kinetics approach. To tackle this challenge, dynamic adaptive chemistry (DAC) [27, 28] was proposed to utilize detailed stiff finite-rate

chemistry. DAC generates locally optimized reduced kinetics for each spatial location and time step, and only the reaction rates of active species are calculated. DAC has been applied to accelerate the kinetics computation in DNS of 0D/1D reactors [29], 2D RANS of DI engines [30], and 3D URANS and LES of spray flames [31]. To further reduce the large computational overhead of DAC in mechanism reduction, Correlated - DAC (CO-DAC) [35] and Correlated - DAC & Transport (CO-DACT) [36] were introduced to further accelerate both chemistry and transport calculation in 0D/1D simulation of laminar flames. Recently, Yang *et al.* rigorously verified and optimized CO-DACT in DNS of a turbulent premixed flame in the thin reaction zone regime [87], and in LES of a turbulent partially premixed flame [80], to allow computationally efficient DNS/LES with detailed finite-rate chemistry.

5.3.2 Physical Model and Flow Conditions

In this study, we consider a canonical temporally evolving non-premixed flame (Figure 5.20). This type of flame has been extensively studied in the past, using DNS [12, 13, 15] and LES [14, 16].

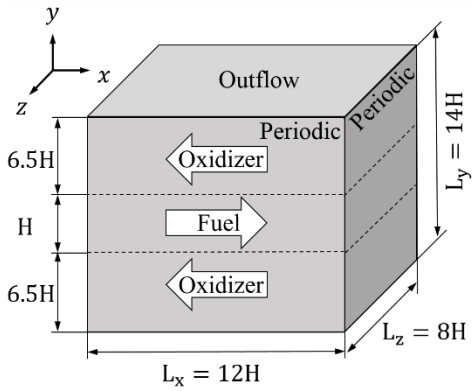

Figure 5.20: Schematic of the canonical temporally evolving non-premixed flame.

The flow parameters and the grid information are provided in Table 5.5. We consider a reduced characteristic jet velocity U = 100 m/s to allow for simulations with a coarse grid. All the simulations are conducted at pressure P = 1 atm. The canonical flow configuration comprises an inner fuel jet (50% CO, 10% H_2, and 40% N_2 by volume) and an outer oxidizer stream (25% O_2 and 75% N_2 by volume), which are counter-flowing in the stream-wise direction. The jet has a Reynolds number (Re_{jet}) of 2315 and a Damkohler number (*Da*) of 0.01, which is low enough to induce local extinction during turbulence-chemistry interaction and evolution.

Table 5.5: Simulation case of a canonical temporally evolving non-premixed flame.

	Mach	Re_{jet}	Da	η (m)	Δx (m)	Grid points
Simulation Case	0.11	2315	0.01	1.2×10^{-5}	5.25×10^{-5}	$128 \times 256 \times 64$

The extent of the computational domain is $L_x \times L_y \times L_z \equiv 12H \times 14H \times 8H$, where H = 0.96 mm is the initial width of the fuel jet. The simulations in this study employ about 18 uniformly spaced points along H, which leads to approximately 2.1M grid points total, with a minimum resolution of approximately 4η, where η is the Kolmogorov length-scale. A past DNS study [13] reports that η grows with time and becomes comparable to the grid size Δx; the grid resolution considered in this study is therefore adequate to capture the extinction and re-ignition dynamics. Figure 5.21 is a grid convergence test to show that the observations in this study are insensitive to grid resolution.

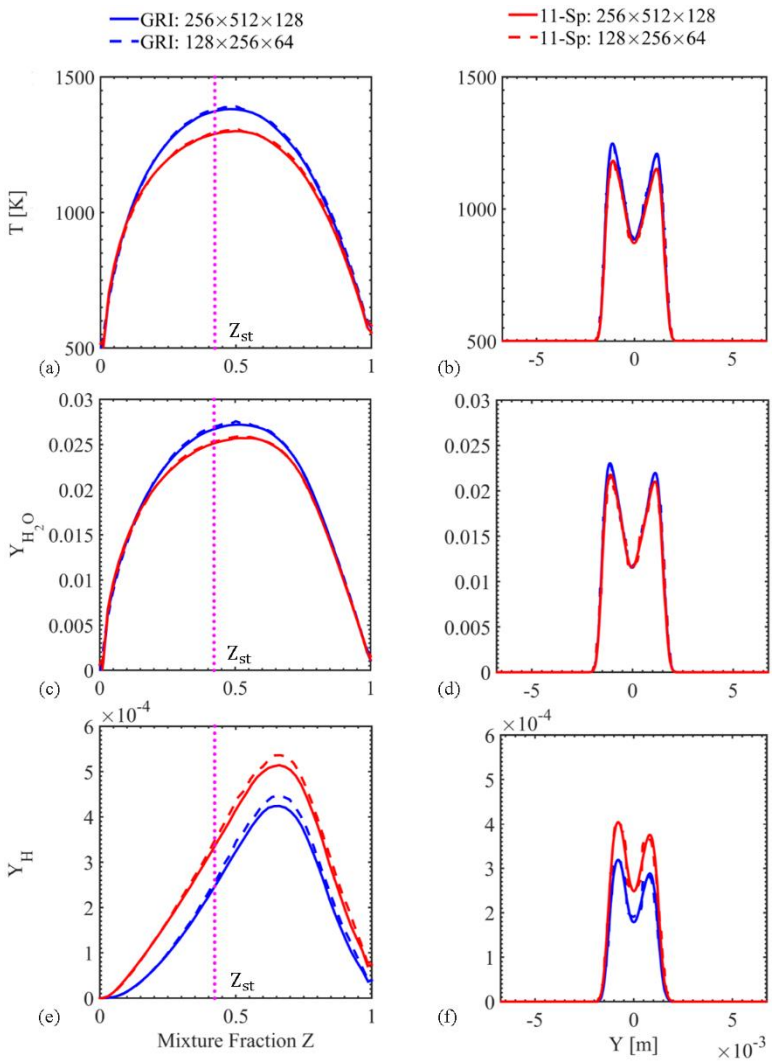

Figure 5.21: Grid convergence test: comparison of GRI-Mech 3.0 (blue) and 11-species model (red) by the conditional means (left) and spatially averaged transverse profiles (right) of T (top), and mass fractions of H_2O (middle) and H (bottom), using grids of $256 \times 512 \times 128$ (resolution of ~2η: solid line) and $128 \times 256 \times 64$ (resolution of ~4η: dashed line) at $15t_j$.

The reacting flow field is initialized with a laminar flamelet solution [53] at a bulk strain rate $\kappa = 0.75\kappa_q$, where $\kappa_q = 1295\ s^{-1}$ is the extinction bulk strain rate. Here, κ_q is obtained by gradually increasing the bulk strain rate in the laminar flamelet calculation until extinction occurs. To allow for the evolution of shear layer turbulence, broadband isotropic turbulence is superimposed on the mean flow with an initial integral length-

scale of H/3, and turbulence intensity of 0.05U. A perfectly non-reflecting, characteristic-based outflow boundary condition is used in the transverse (y) direction, whereas a periodic boundary condition is specified along the streamwise (x) and spanwise (z) directions. The characteristic transient jet time is defined as $t_j = H/U$, and the simulations are conducted up to $40\ t_j$ to capture both the extinction and re-ignition events.

5.3.3 Chemical Kinetics Models

Two chemical kinetics models are compared in this study. The first model, GRI-Mech 3.0 [93], comprises 325 steps and 53 species, and serves as a detailed stiff mechanism for syngas. The second is a 21-step, 11-species non-stiff mechanism [13] developed by Hawkes et al., which has been used in past DNS [13] and LES [14, 16] studies.

5.3.4 Results and Discussions

5.3.4.1 Assessment of Computational Cost

Figure 5.22(a) shows the speed-up using CoDAC and CoTran versus the ODEPIM benchmark. Notably, CoDAC speeds up the calculation of chemical kinetics by 3.4 times, and CoTran speeds up the calculation of mixture-averaged transport properties by 32 times. Together, they provide a net speed-up of a factor of four. Since ODEPIM is used for the time-integration of chemical reactions, it is the calculation of transport properties that dominates the total computational time of the benchmark simulation, and, therefore, CoTran contributes most to the net speed-up.

The speed-up from CoDAC depends heavily on the stiffness of the chemical kinetics models. This is apparent from Fig. 5.22(b), which shows the distribution of the number of active species at local extinction ($20\ t_j$). Outside the shear layers, there are no active reactions but only 3 "hibernating" species, fuels (CO and H_2) and oxygen, which

are the seeds of the chemical mechanism reduction [25]. Inside the shear layers, the high temperature region has no more than 40 reactions and 10 species, while the relatively low temperature regions have a greater number of active reactions and species.

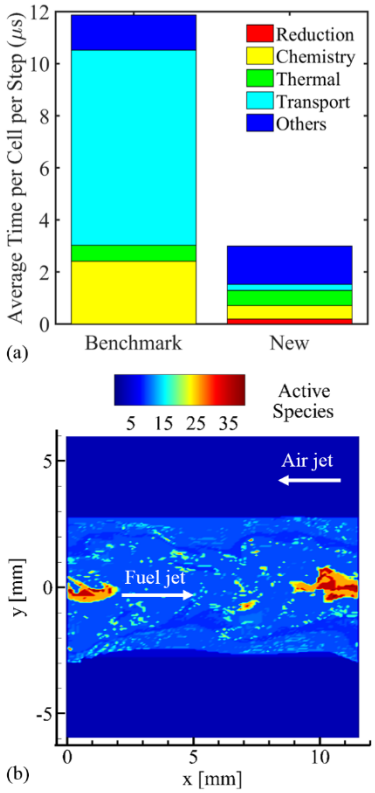

Figure 5.22: (a) Comparison of computational time use distribution for benchmark and CoDAC+CoTran ('New'); (b) 2D contours of active species number at local extinction ($20\ t_j$).

5.3.4.2 Assessment of Accuracy

CoDAC and CoTran have been rigorously verified in the past by simulating 0D/1D laminar flames [35, 36], a turbulent premixed flame [87], and a turbulent partially premixed flame [80]. In the present study, the accuracy of CoDAC and CoTran is verified

for a turbulent non-premixed flame. Figure 5.23 shows a comparison of the benchmark (using ODEPIM) and CoDAC+CoTran ('New') at the centerline of the computational domain under local extinction ($20\ t_j$) for temperature, vorticity magnitude, mass fraction, and reaction rate of OH. There are no observable differences in the quantities under comparison. The same results were confirmed by comparison of the 2D contours, which are omitted here for the sake of brevity.

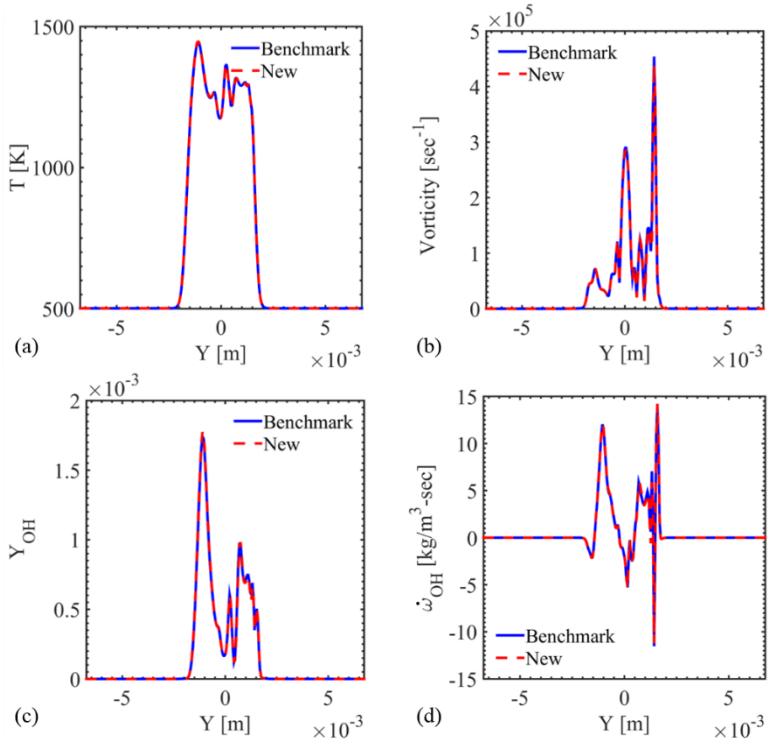

Figure 5.23: Comparison of benchmark and CoDAC+CoTran ('New') at centerline of computational domain under local extinction ($20\ t_j$) for (a) temperature, (b) vorticity magnitude, (c) mass fraction of OH, and (d) reaction rate of OH.

To further quantify errors, the absolute L^2 error is defined as:

$$\epsilon_{abs} = \frac{1}{V}\sqrt{\int \left(Y_k^{New} - Y_k^{Benchmark}\right)^2 dV}, \tag{5.9}$$

and the relative L^2 error is defined as:

$$\epsilon_{rel} = \sqrt{\frac{\int (Y_k^{New} - Y_k^{Benchmark})^2 dV}{\int (Y_k^{Benchmark})^2 dV}}. \quad (5.10)$$

These metrics provide the most stringent test, since local point-wise errors can be made even if the benchmark and the new method have similar means and PDFs. Figure 5.24 presents the PDF of errors of Y_{OH} at local extinction $(20\ t_j)$, and the temporal evolution of relative errors of temperature, vorticity magnitude, and Y_{OH}. The error distribution is highly concentrated at its mean value near zero, and large errors are rare events. There is some error accumulation for all quantities, but it is slow considering the long run time of $40\ t_j$. In addition, the error of temperature grows much slower than that of Y_{OH} and vorticity magnitude.

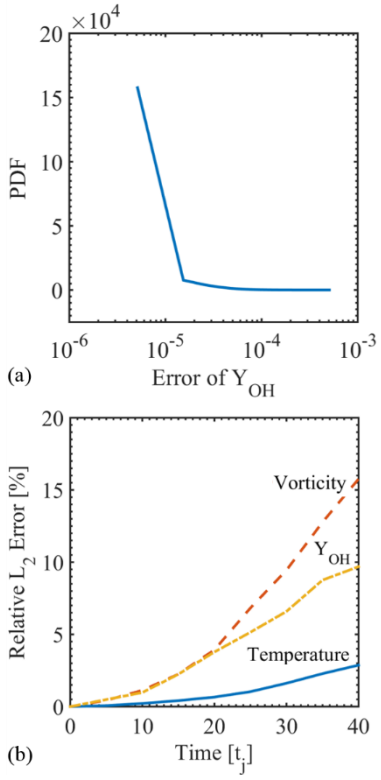

Figure 5.24: (a) PDF of mass fraction errors of OH under local extinction ($20\ t_j$), and (b) temporal evolution of relative L^2 errors of temperature, vorticity magnitude, and mass fraction of OH through 3D computational domain for CoDAC+CoTran.

Table 5.6 shows the quantified errors of CoDAC+CoTran at local extinction ($20\ t_j$) and re-ignition ($40\ t_j$) for temperature, vorticity magnitude, and mass fraction of representative species. The error is small even at the end of the simulation, especially for temperature (0.02 K) and major species (within 6%). In summary, CoDAC+CoTran provides an accurate prediction of the 3D turbulent non-premixed flame.

Table 5.6: Errors of CoDAC and CoTran at Local Extinction ($20\,t_j$) and Re-ignition ($40\,t_j$).

Error	T (K)	Vor. (s^{-1})	Y_{CO}	Y_{H_2}	Y_{O_2}	Y_H	Y_O	Y_{OH}	Y_{CO_2}	Y_{H_2O}
ϵ_{abs} : 20 t_j	0.003	1.70	1.68×10^{-6}	1.22×10^{-8}	7.64×10^{-7}	2.24×10^{-9}	2.27×10^{-8}	1.04×10^{-8}	7.73×10^{-7}	1.08×10^{-7}
ϵ_{abs} : 40 t_j	0.021	4.65	5.38×10^{-6}	2.61×10^{-8}	4.72×10^{-6}	1.04×10^{-8}	1.87×10^{-7}	7.84×10^{-8}	5.22×10^{-6}	3.68×10^{-7}
ϵ_{rel} (%) : 20 t_j	0.66	3.93	1.48	1.49	0.47	1.79	3.46	3.78	2.05	1.46
ϵ_{rel} (%) : 40 t_j	2.87	15.76	6.14	5.64	3.29	4.79	11.23	9.69	6.18	3.99

Figure 5.25 shows the transverse variation of mass fraction and reaction rate of OH on 5 arbitrary transverse lines through the flame region at local extinction time, i.e., $20\,t_j$. It can be observed that the use of CoDAC and CoTran does not lead to any numerical instabilities and the profiles of Y_{OH} show expected behavior across the flame region, where peaks are observed corresponding to the region of peaks of reaction rate of OH.

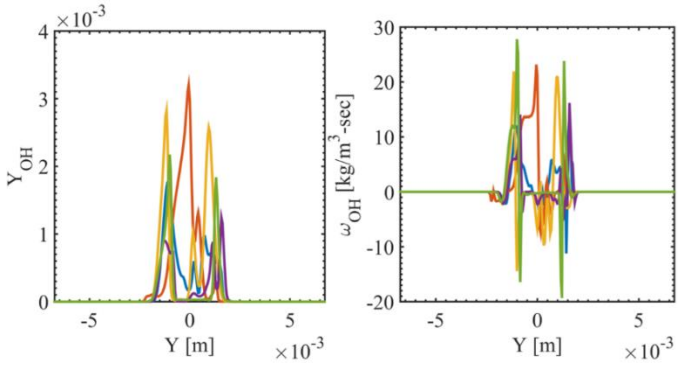

Figure 5.25: Transverse variation of mass fraction (left) and reaction rate (right) of OH on five arbitrary transverse lines at local extinction ($20\,t_j$).

5.3.5 Conclusion

Using the ODEPIM solver, techniques of correlated dynamic adaptive chemistry (CoDAC) and correlated transport (CoTran) are verified and applied in a 3D finite-rate simulation of a temporally evolving turbulent non-premixed syngas flame with extinction and re-ignition, and are found to allow 4 times more efficient computation of 3D finite-rate simulations of turbulent combustion using detailed GRI-Mech 3.0. Comprehensive verifications indicate that CoDAC+CoTran provides accurate results that allow for comparison of predictions by the two chemical kinetics models.

CHAPTER 6

EXPERIMENTAL VALIDATION AND COMPARISON OF FINITE RATE AND FLAMELET MODELS

An efficient finite-rate chemistry (FRC) - large-eddy simulation (LES) formulation is developed for numerical modeling of turbulent combustion, using a point-implicit stiff ODE solver (ODEPIM) and a correlated dynamic adaptive chemistry algorithm (CoDAC). Compared to conventional FRC-LES, this new version provides a speed-up of 8.6 times for chemistry, and 6.4 times for total computation using a 20 species kinetics model. Both the new FRC-LES and flamelet/progress-variable (FPV)-LES are conducted for a piloted partially premixed methane/air flame, which contains relatively low-level of local extinction and re-ignition. Although the two approaches predict similar time-averaged flame fields and statistics, which agree well with the experimental data, the instantaneous prediction for high temperature region from FPV-LES is significantly smaller than that from FRC-LES case, especially in the downstream. Near the stoichiometric region, with respect to experimental data, FPV-LES over-predicts the radical generation, but under-predicts the CO generation and heat release, which explains its under-prediction of temperature. In contrast, on the fuel rich side, CO is no more the bottleneck, thus FPV-LES predicts higher temperature. Comparing to experimental data, FRC-LES provides better predictions for both temperature and species.

6.1 Introduction

Due to the increasing combustion-based energy demand and its environmental concerns, high-fidelity simulation of turbulent combustion becomes highly important. For any practical simulation method, the key is to provide quantitative solutions with minimal empirical constants. Large-eddy simulation (LES) has drawn significant attention during

the past three decades, and its predictive capability is continuously increasing. In LES, the energy-contained large-eddy motions are resolved with sufficient grid resolution, while motions of scales smaller than the grid sizes, i.e. sub-grid scale (SGS) motions, are not resolved. The chemical reaction rates are highly nonlinear functions of species concentrations and temperature, which heavily depend on the turbulent mixing. On the other hand, chemical reactions also release heat and subsequently affect species concentrations and temperature, which in turn change the turbulent mixing. Chemical reactions occurring at different time scales may interact with eddies of different length/time scales, which further complicates both the physical and chemical processes. Therefore, turbulence/chemistry interaction is considered the most challenging topic in turbulent combustion modeling.

Many LES turbulent combustion models have been developed, which can be classified into two major categories: the finite-rate chemistry (FRC) models, and the flamelet generated manifold (FGM) models. The FRC models category includes laminar chemistry model [45-47], perfectly-stirred reactor (PSR) model [48], partially-stirred reactor (PaSR) model [49], linear-eddy model (LEM) [50], Monte Carlo method for Lagrangian filtered probability density function (FDF) transport equations [51], thickened flame model (TFM) [52], etc. The FGM models category includes steady laminar flamelet model [53], Lagrangian flamelet model [54, 55], flamelet/progress-variable (FPV) model [56], etc.

Among different FGM models, the steady laminar flamelet model pioneered by Peters [53] provides advantages of easy implementation and low computational cost, however, there are limitations. Firstly, the mixture fraction essentially does not carry any information about the chemical states. The model chooses the filtered dissipation rate of mixture fraction as an additional parameter to account for the flame stretching effect. However, it does not provide a unique mapping from mixture fraction to the corresponding reaction state. A pure mixing of fuel and oxidizer cannot be accounted by

the steady laminar flamelet model if the local scalar dissipation rate is close to the quenching limit. In addition, the coexistence and interaction between auto-ignition kernels and flame sheet [57-59] cannot be captured. In order to overcome the drawbacks of the steady laminar flamelet model, the FPV model [56, 60] was proposed by incorporating a transport equation to track a progress variable. This model has been developed to account for low-level of extinction, ignition, and unsteady mixing effect [56] to some extent. However, it cannot handle multiple-feed streams unless adding a third parameter, which makes the look-up table very difficult to handle due to the large computer memory requirement and time to build up the table. In addition, the higher-dimension look-up table results in a more complicated data retrieval process and coarser table grid, which could introduce higher interpolation errors.

The main assumption of many FGM models is that the chemical reactions are faster than all turbulent flow eddies, such that the combustion process can be decoupled from the turbulent flow field. This assumption becomes invalid in three important categories of operating conditions. (1) When the turbulence intensity is high enough, the local Reynolds number may increase to such a level that small turbulent eddies become faster than chemical reactions to penetrate into the flame zone and greatly enhance the mixing process. (2) Most chemical reactions related to combustion emissions (NOx, soot, aerosol, etc.) are very slow, thus FGM models normally cannot capture emissions accurately. (3) For processes of ignition, extinction, and conditions close to flammability limits, chemical reactions are often slower than small turbulent eddies. In addition, since each FGM model is optimized for one single regime, they are problematic to handle turbulent combustion with multiple regimes, like lean blowout (LBO) in partially premixed fames.

To overcome these limitations, detailed FRC models are desirable. Among all FRC models, one of the most popular models is the Lagrangian FDF model, due to the reason that Lagrangian approaches do not introduce errors associated with the

discretization of spatial gradients. However, these errors can be re-introduced by the interpolation between particles and grid points. In addition, for most Lagrangian FRC models, standard Eulerian approaches are still employed for the velocity components. For this reason, Lagrangian FRC models introduce complicated couplings between the Eulerian and Lagrangian solvers, which can be critical in the feedback of chemistry into the flow solver, and some "correction" methods are often required in the LES context. Thus, Eulerian FRC models are simpler to implement than Lagrangian models, and are easier to extend to a multi-scalar situation in any grid. Among different Eulerian FRC models, many past studies has shown that the simple laminar chemistry model actually has similar accuracy as many other major Eulerian SGS closure models [45, 46]. For this reason, the laminar chemistry model is adopted in this study.

Compared to FGM model, the detailed kinetics models in FRC models are computationally prohibitive for LES application due to the large number of species and stiffness. For this reason, conventional finite-rate LES often employs over-simplified kinetics models, which may significantly increase the uncertainties, especially in low-temperature ignition zones [17-19]. To resolve this issue, a regime-independent framework of a point-implicit stiff ODE solver (ODEPIM) [43, 44] and a correlated dynamic adaptive chemistry (CoDAC) [35] were proposed. In particular, CoDAC generates locally reduced chemical kinetics for each spatial location and time step, and only calculates the reaction rates of active species and reactions. This framework has been comprehensively evaluated in the simulations of laminar plasma-assisted combustion [18, 19, 86, 172, 183], and in the direct numerical simulations (DNS) of turbulent premixed [87] and non-premixed [88] flames. The new approach provides a significant speed-up (20~50 times), which allows FRC simulations using kinetics models with a reasonable number of species in a computationally manageable manner.

Due to the mathematical nature of the governing equations, there are primarily three categories of computational fluid dynamics (CFD) solvers: incompressible solvers,

low Mach solvers, and fully compressible solvers. The intense heat release and subsequent gas expansion in turbulent combustion make incompressible solvers less preferable. In low Mach solvers, density is decoupled from pressure (acoustics), which makes the solvers problematic near the instability limit or at high Mach numbers. In fully compressible solvers, conservation equations are closely coupled under moderate or high Mach numbers, but become poorly coupled and numerically stiff at low Mach numbers. Many fluid flow problems involve a wide range of Mach numbers, which poses a great challenge for all these three categories. To resolve this issue, a preconditioning method [61-66] was proposed for fully compressible solver to allow a broad range of Mach numbers simultaneously in the simulation.

In the present study, for the first time, the highly efficient framework of ODEPIM and CoDAC is incorporated into a preconditioning scheme to allow an Eulerian FRC-LES approach in a fully compressible CFD solver. The established FRC-LES framework is then used to investigate a low Mach piloted turbulent partially premixed flame (Sandia Flame D) as a benchmark case. In the past, Sandia Flame D has been widely investigated using both FGM and FRC models, mostly with low Mach CFD solvers. For FGM models, steady laminar flamelet [194, 195], Lagrangian flamelet [54, 55, 196], and FPV [8, 197] have been employed. For FRC models, most work employed transported FDF models, including both Lagrangian [198-200] and Eulerian [201, 202] FDF models, while few others employed other Eulerian models such as laminar chemistry [47], PSR [48] and PaSR [49] models. In addition, most FRC studies use global kinetics models with only a few reactions due to the high computational cost of finite-rate calculation. In this study, a relatively more detailed chemical kinetics model is employed.

There are only very few direct comparisons between FGM and FRC models for Sandia Flame D [47], and only the steady laminar flamelet model instead of more advanced FGM models (e.g. FPV model) is compared, thus it is less conclusive on the comparison of these two models. In this study, the results from the laminar chemistry

FRC model are compared to those from both the FPV model and the experiment, in terms of both computational performance and accuracy. For self-consistency, all LES combustion models are coupled with a fully compressible CFD solver using a preconditioning scheme.

6.2 Theoretical Framework

In this study, two turbulence/chemistry interaction models are considered: FPV model and FRC model.

6.2.1 Physical Configurations: Sandia Flame D

The Sandia flames [203] include a series of experiments employing a piloted turbulent partially premixed methane/air flame configuration, which provides detailed experimental data and has been widely simulated for validation purpose [54, 198, 202]. Sandia flame series are low Mach flames, in which the preconditioning scheme becomes necessary for fully compressible solvers. In this study, Sandia Flame D is simulated as a benchmark using both FPV and FRC models. To our best knowledge, this work is the first attempt to employ a fully compressible solver with Eulerian FRC model for Sandia Flame D. Previous work [8, 60] on Sandia Flame D shows that FPV can predict experimental results well, therefore, Sandia Flame D is employed in this study as a starting point for model comparison and validation. In addition, most previous studies employ low Mach CFD solvers, but this study employs a fully compressible CFD solver with a preconditioning scheme. Therefore, when the results from present and previous studies are compared, the choice of CFD solvers is a possible source of difference.

In the simulations, the computation domain is designed as 6 mm upstream the nozzle exit of the inlet injector, 600 mm downstream the exit, 36 mm in radial direction at inlet, and 150 mm in radial direction at the end of the domain. There are 310 grid points in axial direction, 130 points in radial direction, and 64 points in azimuthal

direction. Grid clustering is employed to resolve the high gradient regions near both inner and outer shear layers. The total grid number is approximately 2.6 million. Following the grid structure, 231 AMD Abu Dhabi processors are employed to perform parallel computing via Massage Passing Interface (MPI) system. All time-averaged statistics are taken after three flow-through-time, to ensure that the flow field has reached its statistically stationary state.

6.2.2 Boundary Conditions

The Reynolds number in this case is 22400, which is relatively low. The detailed flow boundary conditions are presented in Table 6.1.

Table 6.1: Flow boundary conditions of Sandia Flame D.

	Components	Inner diameter	Outer diameter	Bulk velocity	Temperature
Fuel jet	25% CH_4 / 75% air (by volume)	7.2 mm	7.7 mm	49.6 m/s	294 K
Piloted flame	Equilibrium: CH_4/air mixture ($\phi = 0.77$)	7.7 mm	18.2 mm	11.4 m/s	1880 K
Co-flow	Air	18.9 mm	N/A	0.9 m/s	291 K

Experimental velocity profile and specified turbulence intensity are enforced as the inlet boundary conditions, while the outlet flow is enforced with fixed backpressure.

In this study, mixture fraction Z is defined as:

$$Z = \frac{0.5 \times \frac{Y_H - Y_{H,coflow}}{W_H} + 2 \times \frac{Y_C - Y_{C,coflow}}{W_C}}{0.5 \times \frac{Y_{H,jet} - Y_{H,coflow}}{W_H} + 2 \times \frac{Y_{C,jet} - Y_{C,coflow}}{W_C}}, \quad (6.1)$$

where the ‘coflow’ subscript represents the quantities in the co-flow stream, the ‘jet’ subscript represents the quantities in the main jet stream, and the rest quantities are measured samples.

6.2.3 Combustion Chemistry

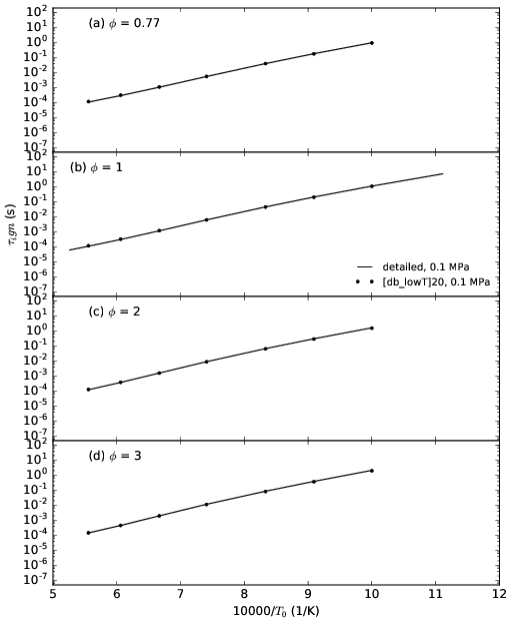

Figure 6.1: Numerical verification of GRIred20 by homogeneous auto-ignition delays.

A methane kinetics model with 20 species and 84 reactions (GRIred20) is utilized in both FPV and FRC models, which is globally reduced from GRI-Mech 3.0 [93] via Global Pathway Selection (GPS) algorithm [26, 58, 204] and verified in terms of homogeneous ignition delays, extinction curves in the perfectly-stirred reactor (PSR), and laminar flame speeds [205]. The reduced methane kinetics model and its verification plots are provided as the Supplemental Materials.

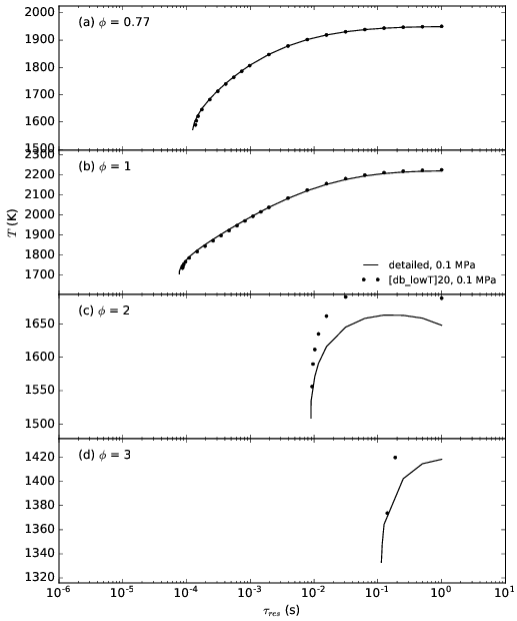

Figure 6.2: Numerical verification of GRIred20 by extinction curves in the perfectly stirred reactor.

6.3 Results and Discussions

6.3.1 Performance Analysis

6.3.1.1 Local reduction

Figure 6.3 shows the snapshots of the spatial distribution of number of active species and number of active reactions, generated from the local PFA mechanism reduction of CoDAC method. Outside the jet brush, only 2 species (preselected seed species: fuel and oxidizer) and none of the reactions are selected, because no chemical reactions occur there. Near the highly distributed turbulent partially premixed flame, a large number of species and reactions are selected, which is close to the full mechanism (20 species and 84 reactions). There is a large buffer zone between above two regions, which has intermediate number of selected species and reactions. The reduction of

number of species and reactions in most spatial locations is responsible for the acceleration of chemistry calculation from the CoDAC method. Due to the highly efficient correlation techniques, the PFA mechanism reduction time is more than 500 times smaller than the chemistry calculation time, and only occupies 0.135% of the total computation time. Therefore, the computational overhead of CoDAC is negligible.

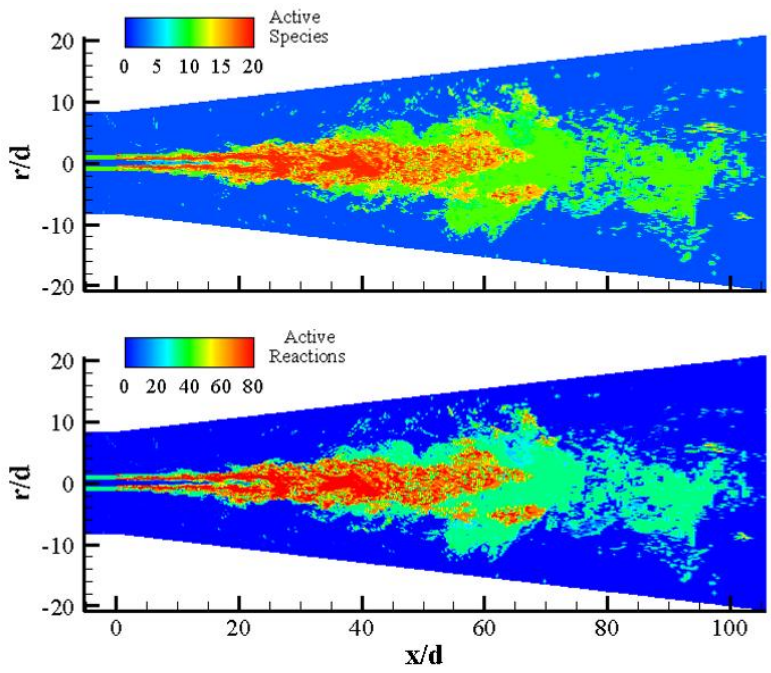

Figure 6.3: Instantons spatial distribution of numbers of active species (upper) and reactions (lower), generated from the CoDAC method with the FRC-LES approach.

6.3.1.2 Speed-up

Figure 6.4 shows the computation time distribution. The Frozen case (multi-species transport equations without chemical kinetics source terms) serves as the theoretical upper limit for the computation speed of all FRC models. From FPV to Frozen, the number of equations rises up from 7 to 24 by a factor of 3.4. For this reason,

the total computation time increases by a factor of 2.7 from FPV to Frozen, which is even better than the ideal linear computational complexity. The time for preconditioning matrix inversion increases by a factor of $11.2 \approx 3.4^2$, which is much better than the theoretical cubic computational complexity. This super-scaling maybe due to the relatively small size of chemical kinetics mechanism used in this study. The chemistry calculation is very expensive, and dominates the total computation time. With respect to the conventional FRC model using DVODE, the new FRC model using ODEPIM and CoDAC significantly accelerates the chemistry calculation by a factor of 8.6, and reduces the total computation by a factor of 6.4. The chemistry time, however, still occupying 70% of the computation time in the new FRC model, which is the largest portion of the total computation time. In contrast, preconditioning matrix inversion only accounts for 7.4% of the total computational time. Therefore, the reduction of computational time in this part is not at high priority. In summary, the computation time of the new FRC model is within 3 times of that of the Frozen model without chemistry, within 8 times of that of the FPV model, and 6.4 times smaller than the conventional FRC model.

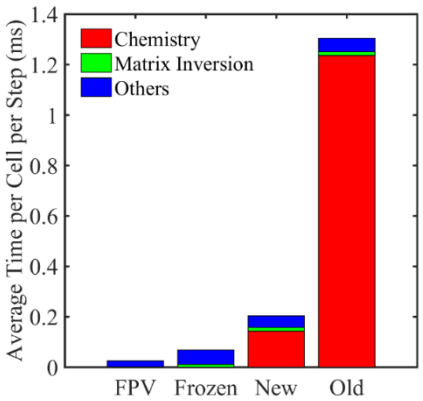

Figure 6.4: Average computation time distribution of the four models: FPV, Frozen (multi-species transport equations without chemical kinetics source terms), New (new FRC model using ODEPIM and CoDAC), Old (conventional FRC model using DVODE).

6.3.2 Spatial Distribution

Figure 6.5 shows the time-averaged temperature distribution calculated by FRC-LES and FPV-LES approaches. Note that the contours in previous studies [8, 48] are smoother because the additional azimuthal average performed based on the time-averaged data. Both simulation results resemble a simple diffusion flame, and agree with Nd:YAG laser beam images from the experiment [203]. The flame has relatively simple flow characteristics, and the chemical reactions interlink to the local strain in both inner and outer shear layers. At approximately x/d = 40, an intense flame region can be observed, where the mixing and combustion are close to complete such that peak temperatures are achieved there. The flame length is approximately 65d, which is very close to experiment (67d). The two models predict similar time-averaged temperature field, but flame temperature prediction from FPV-LES are lower than that from FRC-LES.

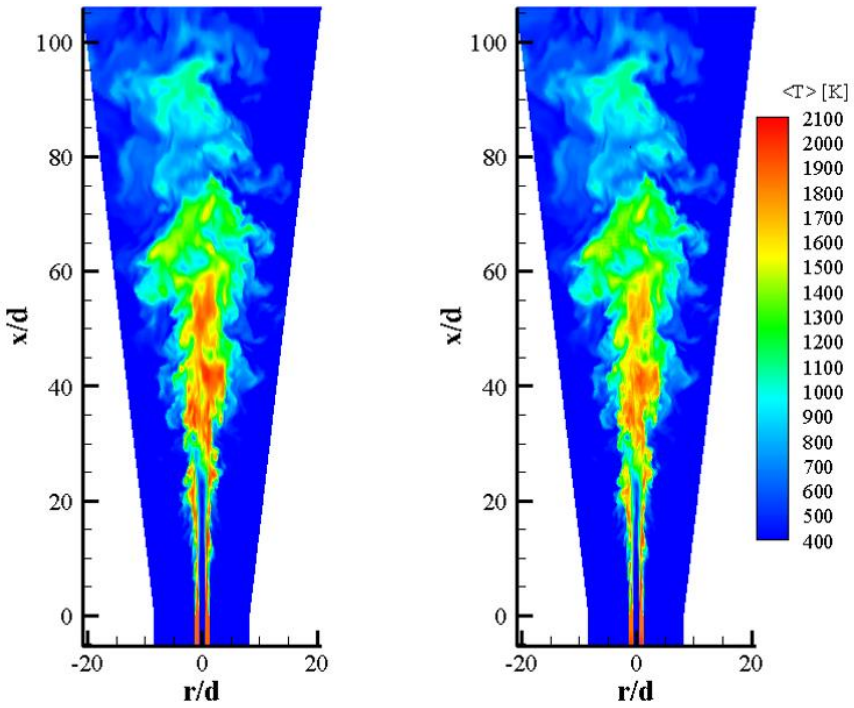

Figure 6.5: Time-averaged temperature distribution from the FRC-LES approach (left) and the FPV-LES approach (right).

In contrast to time-averaged temperature distributions, the instantaneous temperature distributions of the two models are much more different (Figure 6.6). Particularly, results from FRC-LES agree well with those from previous Eulerian FRC studies [48], and results from FPV-LES approach agree with those from previous FPV studies [8]. It is not obvious which one is closer to the experiment here, because a quantitative experimental measurement of instantaneous temperature distribution is not available. Therefore, even though both models could predict similar time-averaged statistics or spatial distributions, the prediction of unsteady/un-stationary evolution between FRC-LES and FPV-LES approaches could still be significantly different from each other. In view of the unsteady/un-stationary phenomena (e.g. ignition, extinction,

combustion instability), such magnification of deviation between the two models becomes an important issue.

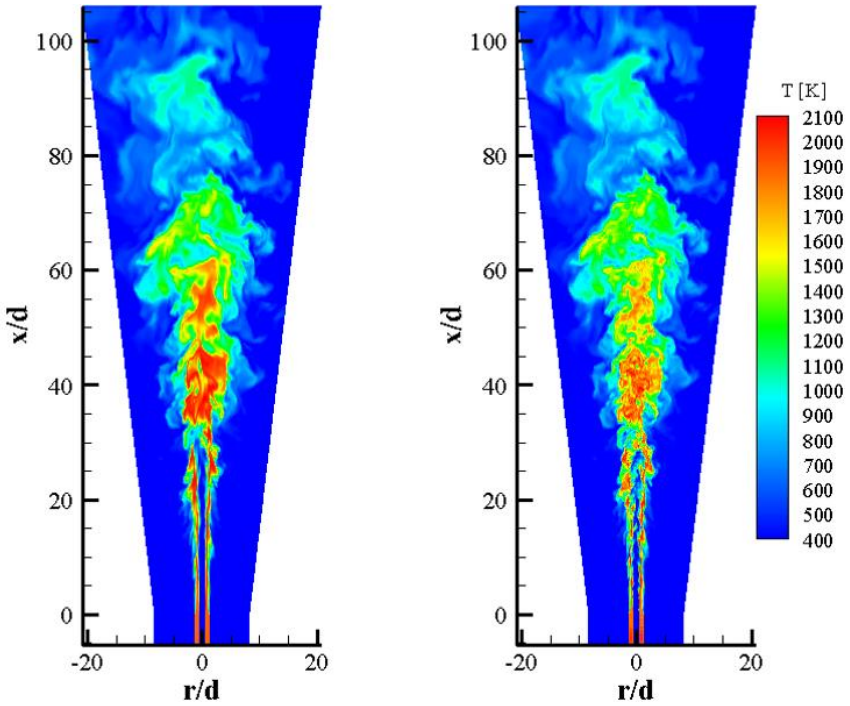

Figure 6.6: Instantaneous temperature distribution from the FRC-LES approach (left) and the FPV-LES approach (right) at a same time.

Both models predict very dynamic jet flow and flame structures and low levels of local extinction. Near the inlet, the broad pilot flame enhances the stability of the flame and results in minimal local extinction. In addition, turbulence intensity is very low in this region, and the flow field is close to laminar. This means that multi-species differential diffusion effect should be important [54], which cannot be captured by the FPV-LES approach. In the downstream region, the outer co-flow and the inner fuel jet interact with each other in the high temperature region of the shear layer, which results more local extinction. In this region, the FPV-LES approach predicts significantly smaller regions with high temperature than the FRC-LES approach. Note that the large

deviations between the two models is mainly in the downstream region. This indicates that FRC model is only necessary for certain combustion regimes, and the cheaper FPV model is accurate enough for the rest part of Sandia Flame D.

To better understand the deviations between the two models, detailed species distributions are investigated. Figure 6.7 compares the distributions of OH radical predicted by the two models. FPV-LES predicts more regions with high OH concentration, although it is more distributed. However, FPV-LES actually predicts less regions with high temperature. This contradicts with the general understanding that higher radical levels will result a stronger heat release and higher temperature.

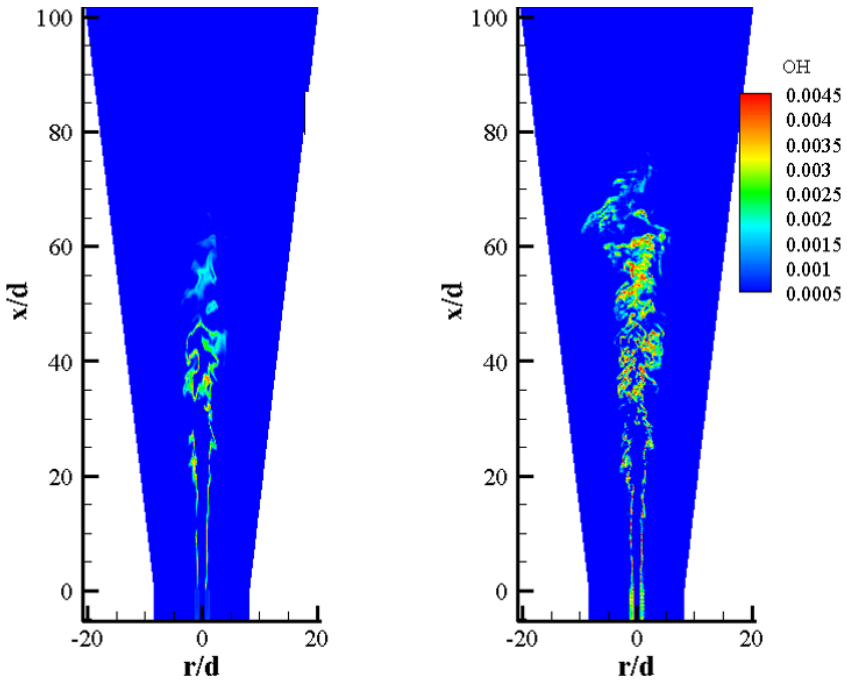

Figure 6.7: Instantaneous Y_{OH} distribution from the FRC-LES approach (left) and the FPV-LES approach (right) at a same time.

To explain this phenomenon, distributions of CO from the two models (Figure 6.8) are compared. FPV-LES predicts both smaller peak CO level and smaller regions

with high CO levels. CO+OH=CO_2+H is one of the primary heat release reactions for methane flame. For this reason, CO oxidation becomes the rate-controlling step for the heat release in FPV-LES model, which explains why it predicts significantly smaller regions with high temperature and partially explains its over-prediction of OH. The comparison of concentrations of major products (CO_2 and H_2O) between the two models (not show here for succinct) indicates that the FPV-LES approach predicts both lower peak product level and smaller regions with high product levels, which further confirms the above conclusion.

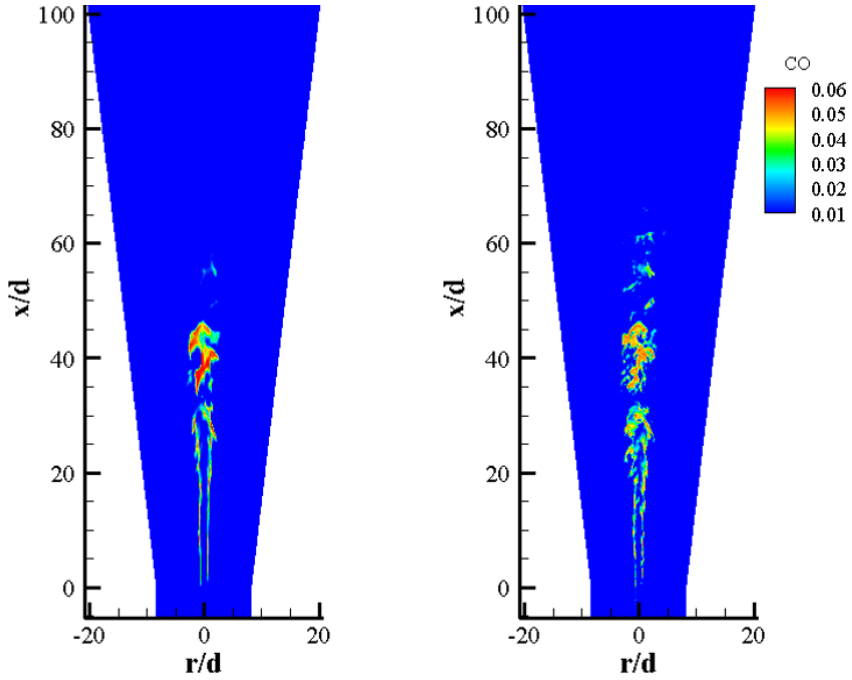

Figure 6.8: Instantaneous Y_{CO} distribution from the FRC-LES approach (left) and the FPV-LES approach (right) at a same time.

On the other hand, FPV-LES predicts smaller regions with high level of CH_4 (not show here for succinct). Therefore, in the prediction of FPV-LES, part of the carbon

element must be stuck at some intermediate species between CH_4 and CO, which mainly includes CH_2O and HCO. The conversion from HCO to CO is very fast, thus, only very low level of HCO can be accumulated in the flames (up to mass fractions of 10^{-5} level in this problem). In the generation of FPV table using 1D steady counter-flow configurations, the flame temperature is higher than the real unsteady conditions in turbulent combustion, thus $CH_2O+OH=HCO+H_2O$ tends to dominate the conversion from CH_2O to HCO. However, according to Fig. 6.6, there are many holes in the intense flame regions with lower temperature of ~1200 K, in which $CH_2O+O_2=HCO+HO_2$ should dominate the conversion from CH_2O to HCO. In the S-curve of ignition and extinction, this intermediate-temperature region is primarily located on the unstable middle branch and thus $CH_2O+O_2=HCO+HO_2$ is more likely to occur during the unsteady evolution. However, the steady FPV table cannot capture the unsteady evolution history of the flame, and has difficulty to predict the unstable branch accurately, thus could easily overlook this important reaction. As a result, in those holes, carbon element in FPV case is partially stuck at CH_2O and has difficulty to convert into HCO and CO. In this problem, CH_2O is accumulated up to mass fractions of 10^{-3} level.

The deviations between the two models could come from the FPV library, the unsteady evolution of filtered mixture fraction and progress variable in the FPV-LES approach, or some combinations of them. For this reason, in the following sections, predictions from the two models will be compared to experimental data in terms of (1) axial and radial distribution of both mixture fraction and progress variable, and (2) the conditional statistics in mixture fraction space.

6.3.3 Axial Profiles

Figure 6.9 shows the axial profiles of time-averaged statistics for temperature and Y_{OH} (to represent minor species). For temperature, the deviation between FRC-LES and FPV-LES approaches are small. Both models predict the axial location of the peak

temperature reasonably well, indicating the capture of turbulence and its interaction with heat release. Similar to previous Eulerian FRC studies [48, 201], FRC-LES matches the experimental mean temperature (3% uncertainty) very well, while FPV-LES over-predicts the upstream mean temperatures and under-predicts the peak mean temperatures near the intense flame region (x/d = 40~60). This is consistent with the observations in the snapshots of temperature distribution (Fig. 6.5-6.6). In contrast, the temperatures from both experiment and FRC model are lower than those from FGM models in previous studies (both steady laminar flamelet [47] and FPV [8, 197]), possibly because previous studies employed low Mach CFD solvers but this work employ a fully compressible CFD solver with a preconditioning scheme. However, both present and previous [47] studies show that FRC models agree with experimental data better than FGM models, even if the simple laminar chemistry FRC model is employed and the SGS composition fluctuations are neglected. In fact, the influence of the SGS composition fluctuations in Sandia Flame D have been proved to be very limited in previous studies [201]. For normalized root-mean-square (RMS), FRC-LES matches well with the experimental data in the upstream region, while FPV-LES over-predicts RMS in the same region. However, both models under-predict RMS in the downstream region. In addition, all models in both present and some previous [47] studies over-predict peak RMS, but some other studies [8] only slightly under-predict peak RMS. It is known that RMS is composed of fluctuations, which are very sensitive and much more difficult to capture than mean quantities. Comparing to temperature, significantly larger deviation between the two models shows up for Y_{OH}, in terms of both mean values and RMS. The FRC-LES case matches the experimental data well, but the FPV-LES case significantly over-predicts both mean and RMS in the downstream region, which is limited by the significantly lower CO prediction from FPV-LES case, as discussed previously. This is consistent with previous FRC [201] and FPV [197] studies. The uncertainty of the experimental data is 10% for mean Y_{OH}. Therefore, the errors of the FPV-LES approach are significantly beyond the experimental

uncertainty, while those of the FRC-LES approach are within the uncertainty level for most axial locations. In addition, the OH prediction in present study is much more accurate than previous Eulerian FRC study using PSR model [48], which implies that the PSR assumption is too strong such that even the simple laminar chemistry model could be more accurate than PSR model.

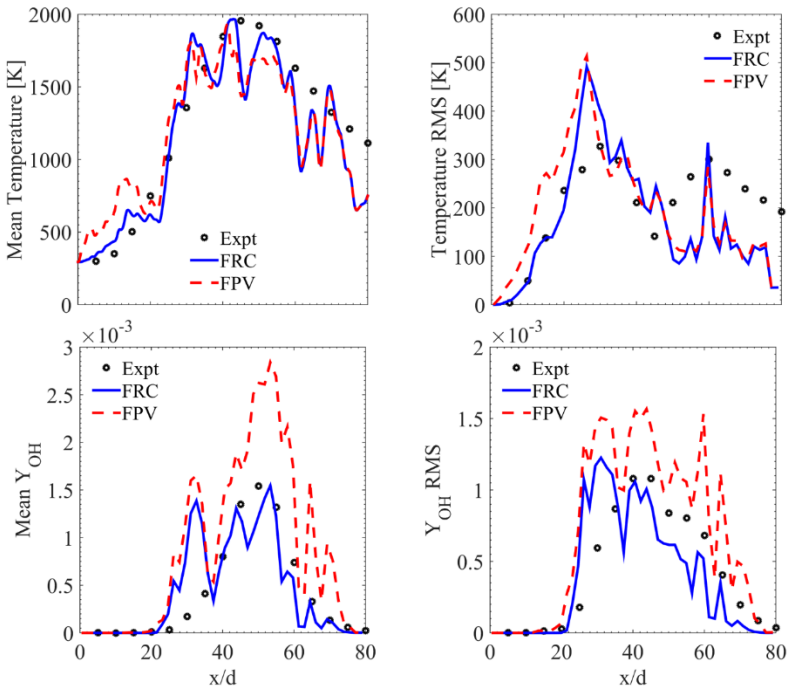

Figure 6.9: Axial profiles of mean (left) and RMS (right) of temperature (upper) and Y_{OH} (lower), from the experiment, the FRC-LES approach, and the FPV-LES approach.

Figure 6.10 shows the axial profiles of time-averaged statistics for mixture fraction and progress variable (to represent major species). Similar to previous Eulerian FRC studies [201], FRC-LES matches the experimental mean values very well, while FPV-LES, under-predicts the upstream mean mixture fraction, over-predicts the upstream mean progress variable, and slightly under-predicts the peak mean progress variable near

the intense flame region (x/d = 40). This is consistent with the under-prediction of temperature from FPV model in the intense flame region (Fig. 4-5), and is also consistent with some previous FPV studies [197]. In contrast, in some other previous studies [8], FPV-LES only slightly over-predicts the mean mixture fraction, which employed a more detailed chemical kinetics (GRI 2.11 mechanism: 49 species and 279 reactions) model than both the present study and most other previous FPV studies. The largest error of mean mixture fraction occurs near x/d=30. For the RMS of mixture fraction, both models cannot provide a good prediction for most axial locations. For the RMS of progress variable, FRC-LES matches well with the experimental data in the upstream region and the intense flame region, while FPV-LES over-predicts in the upstream region but under-predicts in the intense flame region. However, both models under-predicts the RMS of progress variable in the downstream region.

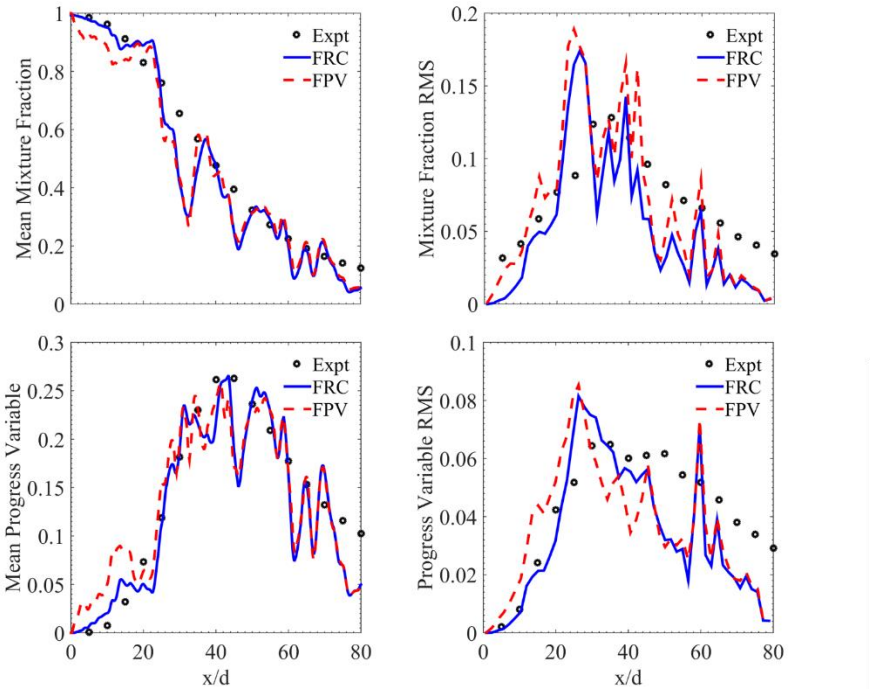

Figure 6.10: Axial profiles of mean (left) and RMS (right) of mixture fraction (upper) and progress variable (lower), from the experiment, the FRC-LES approach, and the FPV-LES approach.

In summary, the FRC-LES approach provides better prediction than the FPV-LES approach on both temperature and species, and this superiority is even larger for minor species. Note that in spite of this limitation of the FPV-LES approach, the time evolution of filtered progress variable significantly enhances the prediction capability of the model compared to steady laminar flamelet model.

6.3.4 Radial Profiles

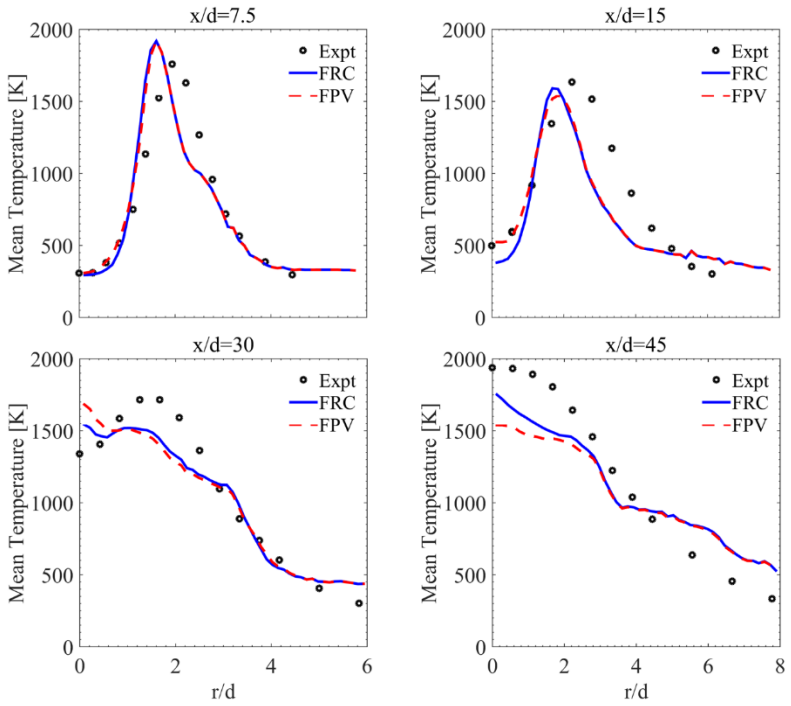

Figure 6.11: Radial profiles of time-averaged temperature at x/d = 7.5 (upper-left), 15 (upper-right), 30 (lower-left), 45 (lower-right), from the experiment, the FRC-LES approach, and the FPV-LES approach.

Figure 6.11 shows the radial profile of mean temperature at four representative axial locations. Simulation results from both FRC and FPV models are very close to each other except near the centerline, and in roughly good agreement with experimental data (3% uncertainty) and previous Eulerian FRC studies [201]. At x/d=7.5, the errors of both models are much smaller than the other three axial locations. At x/d=15, FRC-LES slightly under-predicts the mean temperature near the centerline, while FPV-LES slightly under-predicts the mean temperature of the pilot flame. At x/d=30, both models not only over-predict the mean temperatures near the centerline, but also show a different trend from the experimental data. Therefore, the mean temperature prediction at x/d=30 is the most unreliable one among all these four representative axial locations. At x/d=45, both models under-predict the mean temperature near the centerline and over-predict it near the co-flow, but show a consistent trend with the experimental data. In addition, FPV-

LES predicts several hundred Kelvin lower than FRC-LES case near the centerline (intense flame region), which is consistent with their comparison in both time-averaged and instantaneous snapshots (Fig. 6.5-6.6).

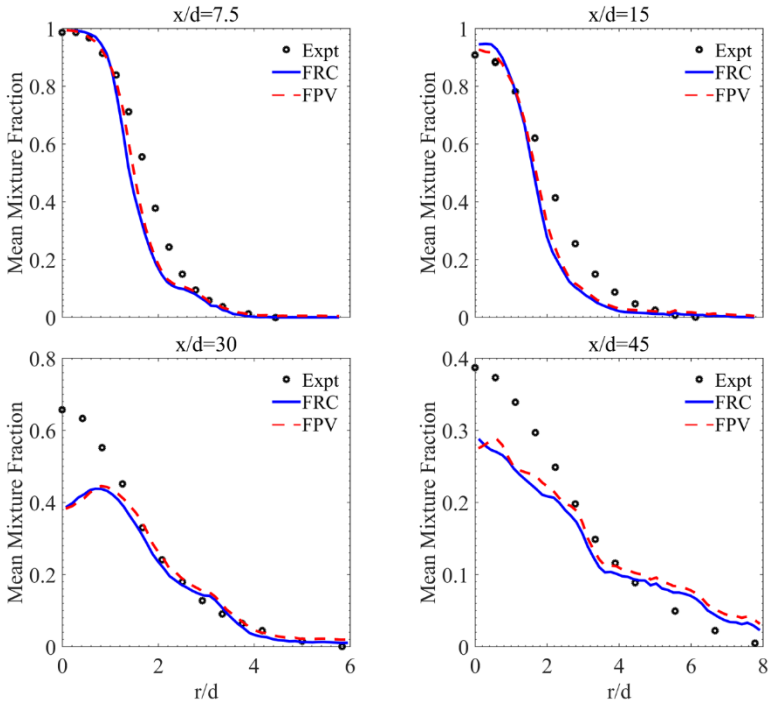

Figure 6.12: Radial profiles of time-averaged mixture fraction at x/d = 7.5 (upper-left), 15 (upper-right), 30 (lower-left), 45 (lower-right), from the experiment, the FRC-LES approach, and the FPV-LES approach.

Figure 6.12 shows the radial profile of mean mixture fraction at four representative axial locations. Mean mixture fraction near the centerline gradually decreases from the upstream region to the downstream region, indicating significant breakup and consumption of the main fuel jet. Simulation results from both FRC and FPV models are very close to each other, and in roughly good agreement with the experimental data and previous Eulerian FRC studies [201]. The deviation between the simulation results and the experimental data gradually increase from the upstream to the

downstream. Near the centerline, mean mixture fraction agrees perfectly with that of the experimental data at x/d = 7.5; it is slightly over-predicted at x/d = 15, but significantly under-predicted further downstream (at x/d = 30, 45), possibly due to their over-prediction of fuel jet-breakup and consumption there. These trends are consistent with those in previous FPV studies [197]. At x/d=30, the simulation data not only contains the largest errors, but also provides a trend different from that of experimental data. Therefore, the mean mixture fraction prediction at x/d=30 is the most unreliable one among all these four representative axial locations. There are several possible reasons for this phenomenon: (1) in the simulations, the inlet velocity and turbulence are specified using the experimental data, while the outlet flow is enforced with fixed backpressure. For this reason, predictions in the upstream region tends to be more accurate, and errors may accumulate to the downstream. (2) Local extinction and re-ignition are challenging to capture accurately, and they occur more frequently in the downstream region than in the upstream region.

6.3.5 Conditional Statistics

Since the two models predict very similar mixture fraction profiles as discussed in the previous two sections 6.3.3 and 6.3.4 (both axial and radial), their deviations in temperature and species profiles can mostly be represented by the conditional statistics in mixture fraction space. In addition, the conditional statistics can show more insight in turbulence/chemistry interactions, and can clearly show of the difference between FPV library table and FRC.

Figure 6.13 shows the conditional mean temperature at four different axial locations of x/d = 7.5, 15, 30, and 45. Results from the two models are close, but still contain noticeable deviations. In particular, results from the FRC-LES case agrees better with the experimental data than those from the FPV-LES approach for all locations, except for the rich side at x/d = 30, where the mean mixture fraction itself contains the

largest errors and is unreliable (Figure 6.10 and Figure 6.12). The predictability of the FRC-LES approach is better in the upstream region than in the downstream region. One possible reason is that the upstream region (near inlet) contains smaller turbulence intensity, and differential diffusion effects become important, which cannot be captured by the FPV-LES approach. In the upstream region (x/d = 7.5 and 15), the FRC-LES case agrees perfectly with the experimental data for almost all mixture fraction values. In the downstream (x/d = 30 and 45) region, both models agree very well with the experimental data on the fuel lean side, but significantly under-predict the mean temperature on the fuel rich side. In contrast, previous FPV studies [8] only slightly over-predict the mean temperature on the fuel rich side, possibly because they employed a more detailed chemical kinetics model (GRI 2.11 mechanism: 49 species and 279 reactions) than the one in the present work. The present FPV model employs a smaller kinetics model to be consistent with the present FRC model, which cannot afford very detailed kinetics model. Near the stoichiometric mixture fraction ($Z = 0.35$), comparing to the FRC-LES approach, the FPV-LES approach under-predicts the peak temperature, which is consistent with their comparison in the snapshots of temperature distribution (Figure 6.5 and Figure 6.6). In contrast, on the fuel rich side, temperature from the FPV-LES approach is always higher than that from the FRC-LES approach. During the evolution, the same location could be lean, stoichiometric, or rich at different time instances. Therefore, the time-averaged data at one location could be some averages of instantaneous lean, stoichiometric, and rich data, in which the opposite trends of the latter two could offset each other to some extent such that the time-averaged data between the two models have significantly smaller differences than the instantaneous data, as shown in Figure 6.5 and Figure 6.6. Due to the jet-breakup and consumption of fuel in the downstream region, all profiles end up with some mixture fraction values much smaller than one, and simulation data normally ends up with smaller mixture fraction values than experimental data.

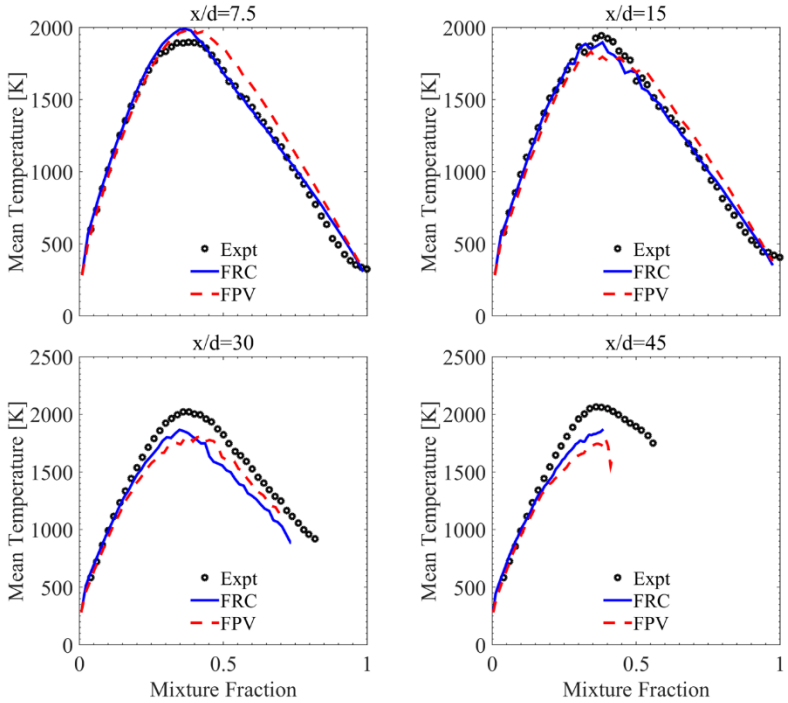

Figure 6.13: Conditional average of temperature at x/d = 7.5 (upper-left), 15 (upper-right), 30 (lower-left), 45 (lower-right), from the experiment, the FRC-LES approach, and the FPV-LES approach.

Figure 6.14 shows the conditional mean of Y_{H_2O} to represent major products. The profiles and performance of the two models are very similar to those of conditional mean temperature. This fact indicates that the major heat release is closely correlated with the formation of H_2O. The level of Y_{H_2O} at x/d = 45 is higher than that at x/d = 15, which indicates the occurrence of re-ignition. In addition, the strong partially premixed burning (i.e. the triple-flame structure) at x/d = 45 leads to a plateau region in the Y_{H_2O} profile from both simulation and experiment, which does not exist in pure diffusion flames. Again, results from the FRC-LES approach agrees with experimental data better (4% uncertainty) than those from the FPV-LES approach for all the locations, except the fuel

rich side at x/d = 30, where the mean mixture fraction itself contains the largest errors and is unreliable (Fig. 9 and Fig. 11). At x/d = 7.5, 15, and 45, the FRC-LES case agrees very well with the experimental data for almost all mixture fraction values. Near the stoichiometric mixture fraction ($Z = 0.35$), FPV-LES predicts less major products than FRC-LES. In contrast, on the fuel rich side, level of major products from the FPV-LES approach is always higher than that from the FRC-LES approach.

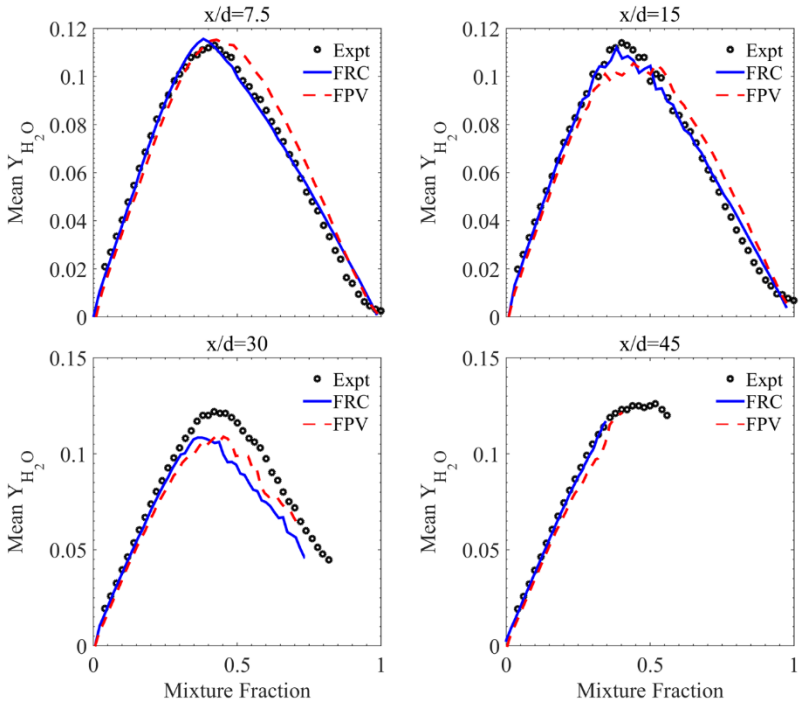

Figure 6.14: Conditional average of Y_{H_2O} at x/d = 7.5 (upper-left), 15 (upper-right), 30 (lower-left), 45 (lower-right), from the experiment, the FRC-LES approach, and the FPV-LES approach.

Figure 6.15 shows the conditional mean of Y_{CH_4} to represent major reactants. All models and experiment show monotonically increasing profiles, which follows the definition of mixture fraction. The FRC-LES case still shows advantages over the FPV-

LES case in upstream, but the deviations are smaller than those in temperature and Y_{H_2O}. At x/d = 7.5, 15, and 45, the FRC-LES case agrees perfectly with the experimental data for almost all mixture fraction values. At x/d = 30, both models over-predict the Y_{CH_4} level on the fuel rich side, which is consistent with their under-prediction of temperature at the same location. The large errors at this location are mainly due to the large errors in the mean mixture fraction at the same location (Figure 6.10 and Figure 6.12). On the fuel rich side, the FPV-LES approach predicts lower fuel level than the FRC-LES case, which further confirms that the FPV-LES approach over-predicts the reactant-to-product conversion, and thus over-predicts the temperature there.

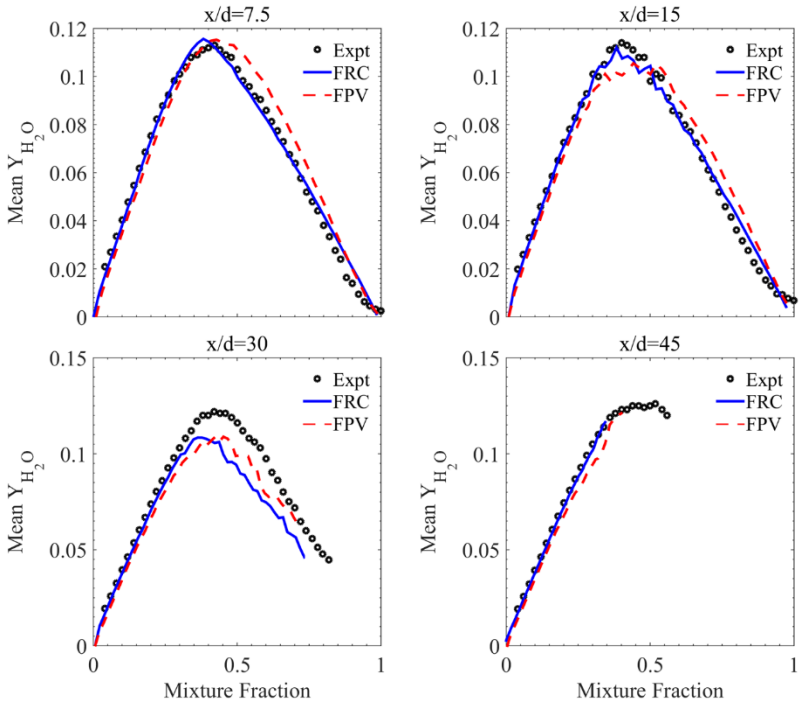

Figure 6.15: Conditional average of Y_{CH_4} at x/d = 7.5 (upper-left), 15 (upper-right), 30 (lower-left), 45 (lower-right), from the experiment, the FRC-LES approach, and the FPV-LES approach.

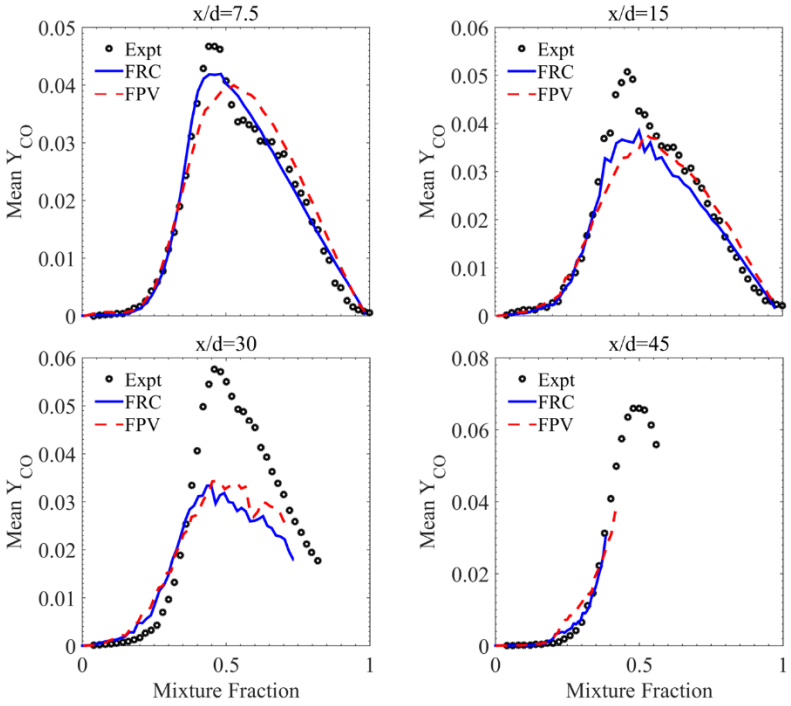

Figure 6.16: Conditional average of Y_{CO} at x/d = 7.5 (upper-left), 15 (upper-right), 30 (lower-left), 45 (lower-right), from the experiment, the FRC-LES approach, and the FPV-LES approach.

Figure 6.16 shows the conditional mean of Y_{CO} to represent intermediate species, in which experiment data contain 10% ~ 20% uncertainties. For all locations, very lean or very rich parts normally contain small errors, but both models under-predict the peak values near mixture fraction $Z = 0.5$, which explains the under-prediction of peak temperature (Figure 6.13) for all locations except the most upstream one (x/d = 7.5) near the inlet. In contrast, some previous FRC [202] and FPV [8] studies over-predict the peak values, both of which employed low Mach solvers. In particular, the FRC study employed a chemical kinetics (a 19 species mechanism, which is also globally reduced from GRI-Mech 3.0) similar to the present study, so these opposite trends is not likely due to different chemical kinetics models, but more likely due to the different choices of CFD solvers. At very upstream locations, the influence of piloted flame dominates, so the peak level of Y_{CO} cannot directly represent the temperature peak value. Similar to

temperature, Y_{H_2O}, and Y_{CH_4}, the FRC-LES approach predicts better than the FPV-LES case at all locations except the fuel rich side at x/d = 30, where the mean mixture fraction itself contains the largest errors and is unreliable (Figure 6.10 and Figure 6.12). Near the stoichiometric mixture fraction ($Z = 0.35$), FPV-LES predicts less CO than FRC-LES, which is consistent with the limiting effect of CO for FPV-LES observed in its snapshots (Figure 6.8). In contrast, on the fuel rich side, the CO level predicted from the FPV-LES approach is always higher than that from the FRC-LES approach. For this reason, the limiting effect of CO disappears on the fuel rich side, and FPV-LES approach predicts higher temperature than FRC-LES there (Figure 6.13).

6.4 Conclusion

An efficient finite-rate chemistry (FRC)-LES formulation is developed for the numerical modeling of turbulent combustion. A 20-species and 84-reactions methane/air kinetics model reduced from detailed GRI-3.0 is employed with point-implicit stiff ODE solver (ODEPIM) and a correlated dynamic adaptive chemistry (CoDAC) algorithm. In particular, the CoDAC method provides a very effective local mechanism reduction with negligible computational overhead. In FRC-LES, the techniques of ODEPIM and CoDAC provide a speed up of 8.6 times for chemistry, and 6.4 times for the total computation.

With this new framework, simulations using both FRC-LES and flamelet/progress-variable (FPV)-LES approaches are conducted for a piloted partially premixed methane/air flame, which contains low level of local extinction and re-ignition. The results of both approaches provide a good agreement with the experimental data. Although the two models have similar spatial distributions of time-averaged quantities, for instantaneous flame field, the FPV-LES approach predicts significantly smaller regions with high temperature than the FRC-LES approach, especially in the downstream intense flame region. This is because the FPV-LES approach predicts less CO level,

which becomes the rate controlling step for one of the primary heat release reactions $CO+OH=CO_2+H$. For axial profiles of time-averaged statistics, the FRC-LES approach is more accurate than the FPV-LES approach for both temperature and species, and this superiority is even larger for minor species. For radial profiles of time-averaged statistics, the two models have very similar predictions for temperature and mixture fraction, which also reasonably agree with the experimental data. The deviations in the upstream region are generally smaller than those in the downstream region. For conditional statistics, the FRC-LES approach provides better predictions for both temperature and species. Compared to the FRC-LES approach, the FPV-LES approach predicts lower temperature near the stoichiometric region due to the bottleneck effect of CO, but predicts higher temperature on the fuel rich side where the limiting effect disappears.

CHAPTER 7

SENSITIVITY OF PREDICTIONS TO CHEMICAL KINETICS

To investigate the sensitivity of predictions to chemical kinetics models, two different kinetics models, GRI-Mech 3.0 and an 11-species syngas model, are compared by performing 3D finite-rate kinetics-based direct numerical simulations (DNS) of a temporally evolving turbulent non-premixed syngas flame. Both chemical kinetics models, providing comparable qualitative trends, capture local extinction and re-ignition events. However, significant quantitative discrepancies (86~100 K difference in the temperature field) indicate high sensitivity to the chemical kinetics model. The 11-species model predicts a lower radicals-to-products conversion rate, causing statistically more local extinction and less re-ignition. This sensitivity to the chemical kinetics model is magnified relative to a 1D steady laminar simulation by the effects of unsteadiness and turbulence (up to 7 times for temperature, up to 12 times for CO, up to 13 times for H_2, up to 7 times for O_2, up to 5 times for CO_2, and up to 13 times for H_2O), with the deviations in species concentrations, temperature, and reaction rates forming a nonlinear positive feedback loop under reacting flow conditions. The differences between the results from the two models are primarily due to: (a) the larger number of species and related kinetic pathways in GRI-Mech 3.0; and (b) the differences in reaction rate coefficients for the same reactions in the two models. Both (a) and (b) are sensitive to unsteadiness and other turbulence effects, but (b) is dominant and is more sensitive to unsteadiness and other turbulence effects. At local extinction, the major differences between the results from the two chemical kinetics models are in the peak values and the volume occupied by the peak values, which is dominated by unsteady effects; at re-ignition, the differences are mainly observed in the spatial distribution of the reacting flow field, which is primarily dominated by the complex turbulence-chemistry interaction.

7.1 Introduction

It is unclear how different chemical kinetics models affect DNS/LES results on local extinction and re-ignition phenomena in turbulent combustion environments. These events may lead to increased emissions, combustion instability, or flame blowout; thus, accurate prediction of them is an important aspect of high-fidelity simulations. Accurate prediction will in turn require a quantitative understanding of the wide range of time and length scales involved, and of the complex interactions between turbulent mixing, molecular diffusion, and chemical reactions.

The sensitivity of simulation results to different chemical kinetics models is still unclear, particularly with regard to the prediction of local extinction and re-ignition events, which will be investigated in this chapter.

Most existing chemical kinetics models offer similar predictions of ignition and extinction in 0D/1D finite-rate simulations of laminar combustion processes. Is it appropriate, therefore, to extend this observation to a 3D turbulent combustion environment? This question is practically important because most large-scale combustion simulations were conducted using (globally reduced) chemical kinetics models validated/verified purely based on 0D/1D steady laminar tests. In order to answer this question, two different chemical kinetics models (GRI-Mech 3.0 [93] and an 11-species model [13]) are used to simulate a temporally evolving turbulent non-premixed syngas flame, and the results are compared.

7.2 Physical Model and Flow Conditions

In this study, we consider a canonical temporally evolving non-premixed flame (Figure 5.20). This type of flame has been extensively studied in the past, using DNS [12, 13, 15] and LES [14, 16]. The flow parameters and the grid information are provided in Table 5.5. We consider a reduced characteristic jet velocity U = 100 m/s to allow for simulations with a coarse grid. All the simulations are conducted at pressure P = 1 atm.

The canonical flow configuration comprises an inner fuel jet (50% CO, 10% H_2, and 40% N_2 by volume) and an outer oxidizer stream (25% O_2 and 75% N_2 by volume), which are counter-flowing in the stream-wise direction. The jet has a Reynolds number (Re_{jet}) of 2315 and a Damkohler number (Da) of 0.01, which is low enough to induce local extinction during turbulence-chemistry interaction and evolution. The extent of the computational domain is $L_x \times L_y \times L_z \equiv 12H \times 14H \times 8H$, where H = 0.96 mm is the initial width of the fuel jet. The simulations in this study employ about 18 uniformly spaced points along H, which leads to approximately 2.1M grid points total, with a minimum resolution of approximately 4η, where η is the Kolmogorov length-scale. A past DNS study [13] reports that η grows with time and becomes comparable to the grid size Δx; the grid resolution considered in this study is therefore adequate to capture the extinction and re-ignition dynamics. A grid convergence test (Figure 5.21) is included to show that the observations in this study are insensitive to grid resolution.

The reacting flow field is initialized with a laminar flamelet solution [53] at a bulk strain rate $\kappa = 0.75\kappa_q$, where $\kappa_q = 1295\ s^{-1}$ is the extinction bulk strain rate. Here, κ_q is obtained by gradually increasing the bulk strain rate in the laminar flamelet calculation until extinction occurs. To allow for the evolution of shear layer turbulence, broadband isotropic turbulence is superimposed on the mean flow with an initial integral length-scale of H/3, and turbulence intensity of 0.05U. A perfectly non-reflecting, characteristic-based outflow boundary condition is used in the transverse (y) direction, whereas a periodic boundary condition is specified along the streamwise (x) and spanwise (z) directions. The characteristic transient jet time is defined as $t_j = H/U$, and the simulations are conducted up to $40\ t_j$ to capture both the extinction and re-ignition events.

7.3 Chemical Kinetics Models

Two chemical kinetics models are compared in this study. The first model, GRI-Mech 3.0 [93], comprises 325 steps and 53 species, and serves as a detailed stiff mechanism for syngas. The second is a 21-step, 11-species non-stiff mechanism [13] developed by Hawkes et al., which has been used in past DNS [13] and LES [14, 16] studies. Predictions of the extinction strain rates and the laminar flame speeds by the 11-species model are within 1% and 5%, respectively, of those from GRI-Mech 3.0 (Figure 7.1). The two kinetics models predict very close adiabatic flame temperatures (~12 K difference). Further examination of the 11-species model and GRI-Mech 3.0 shows that most reaction rate coefficients for the same reactions are different for these two models. It should be emphasized that the 11-species model is independent of GRI-Mech 3.0. Since the transport data for these models are identical, any difference in simulation results must come from differences in the chemical reactions.

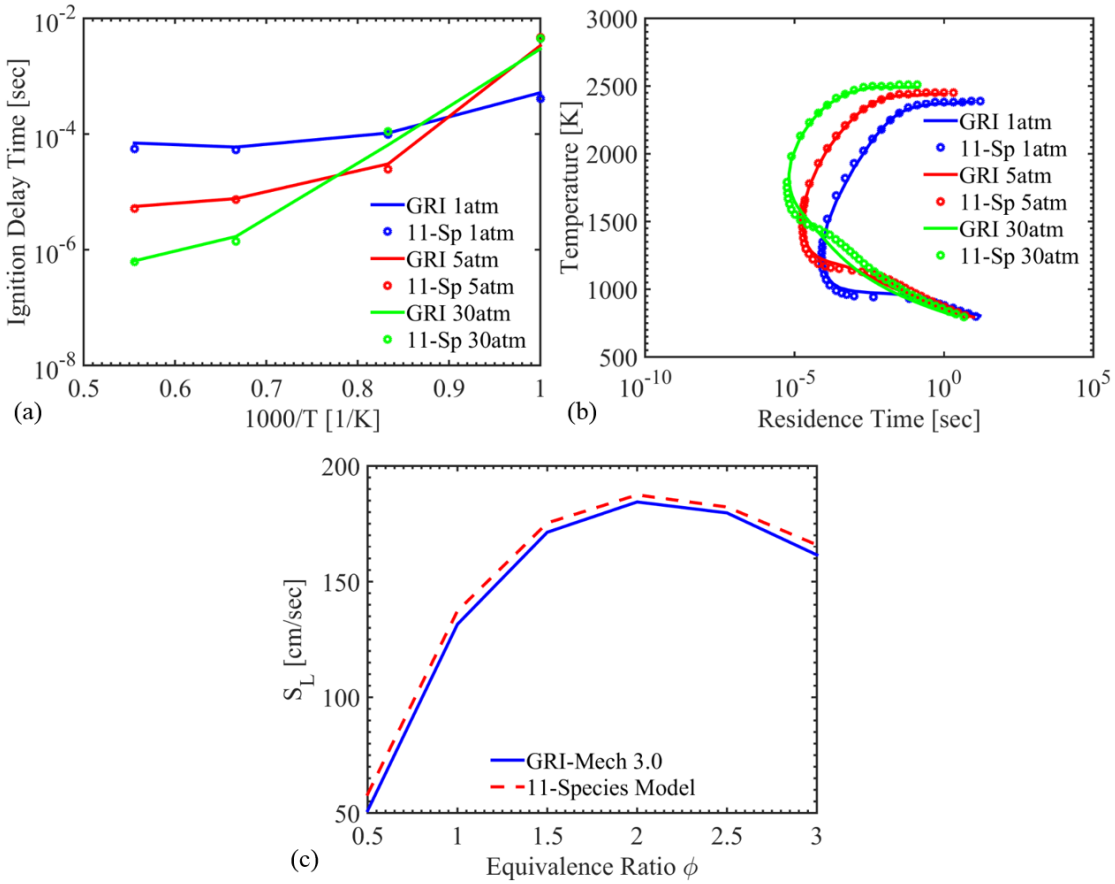

Figure 7.1: Comparison of GRI-Mech 3.0 and the 11-species model by (a) homogeneous ignition delay times, (b) extinction curves in the perfectly stirred reactor, and (c) laminar flame speeds.

7.4 Results and Discussions

7.4.1 Instantaneous Reacting Flow Features

Figure 7.2 (a-b) shows the contours of the OH mass fraction to illustrate the spatial evolution of the flame structure during local extinction and re-ignition processes. The flame location is identified using the stoichiometric mixture fraction iso-lines. Mixture fraction Z is defined as

$$Z = \left[\frac{sY_F - Y_O + Y_{O,0}}{sY_{F,0} + Y_{O,0}}\right], \tag{7.1}$$

where $s = AFR_{stoich} = (W_O \times \nu_O)/(W_F \times \nu_F)$, with $Y_{F,0}$ being the fuel mass fraction at the fuel stream inlet, $Y_{O,0}$ denoting the oxidizer mass fraction at the oxidizer stream inlet, and Y_O denoting the local oxidizer mass fraction. Here, W_F and W_O are the species molecular weights, and ν_F and ν_O are the fuel and oxygen stoichiometric coefficients, respectively.

At $20\ t_j$, only few discrete OH pockets survive and attach to the stoichiometric surfaces, indicating that local extinction is approached in most regions of the shear layers. However, at $40\ t_j$, the values of OH mass fraction increase sharply in most regions around the stoichiometric surfaces within the shear layers, indicating the approach of re-ignition. Some of the disconnected small radical pockets observed at $20\ t_j$ become the source of re-ignition at $40\ t_j$. The transverse movement of the flame occurs due to the spatial evolution of the shear layers in the transverse direction with time. Figure 7.2 (c-d) clearly substantiate this phenomenon, where the contours of the vorticity magnitude qualitatively illustrate the transverse spreading of the shear layers. Due to this spreading, we observe dominant large-scale structures at $40\ t_j$ as compared to $20\ t_j$, with reduced peak values of vorticity magnitude.

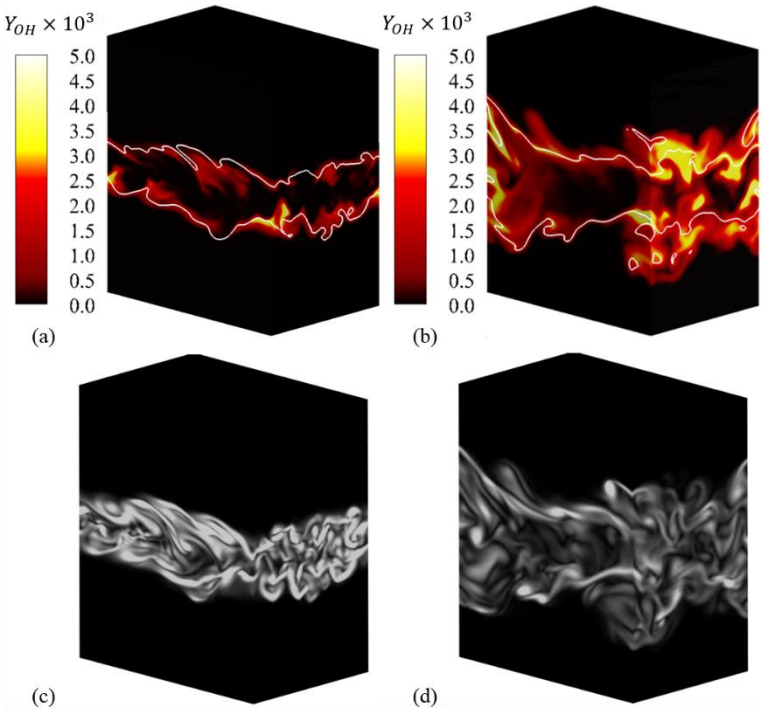

Figure 7.2: Contours of OH mass fraction overlaid with stoichiometric mixture fraction (upper) and vorticity magnitude (lower) in 3D computational domain at local extinction ($20\ t_j$, left) and re-ignition ($40\ t_j$, right) from GRI-Mech 3.0.

7.4.2 Comparison of the Two Kinetics Models

In this section, the predictions of local extinction and re-ignition from GRI-Mech 3.0 and the 11-species model are compared through the instantaneous flame structure, conditional statistics, syngas flame structure, and scalar dissipation rate statistics. The counterparts in all the comparisons have exact the same conditions except for chemical kinetics models: the same grid, initial conditions, initial turbulence perturbation, HPC system, processor count and topology, etc. Therefore, all the differences are attributed to the chemical kinetics models.

7.4.2.1 Instantaneous Flame Structure

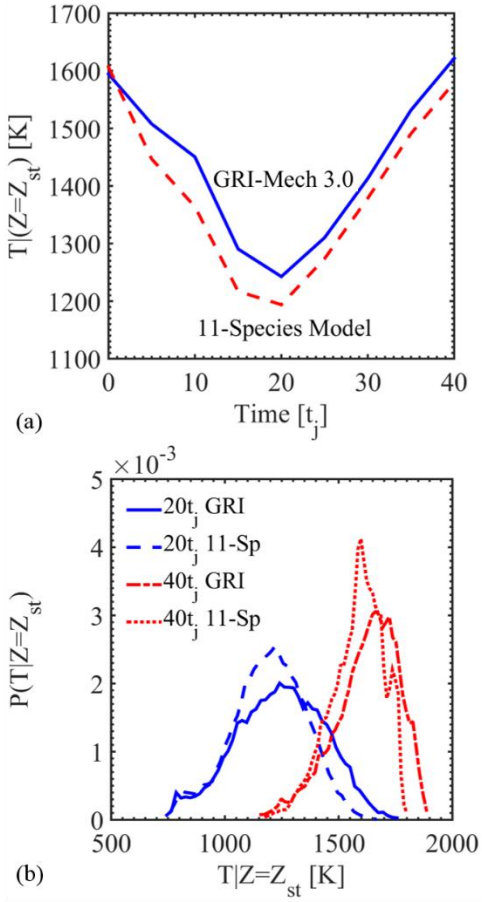

Figure 7.3: (a) Temporal evolution of mean temperature on the stoichiometric surface obtained from GRI-Mech 3.0 and 11-species model; (b) PDF of temperature on the stoichiometric surface at local extinction ($20\ t_j$) and re-ignition ($40\ t_j$) from GRI-Mech 3.0 and 11-species model.

Figure 7.3 compares the temporal evolution and PDF of the temperature field on the stoichiometric surface obtained from simulations using GRI-Mech 3.0 and the 11-species model. The mean stoichiometric temperature starts at approximately 1600 K, gradually drops to 1200 K ~ 1250 K at $20t_j$, and increases gradually to ~1600 K at $40t_j$. This evolution of the mean temperature clearly demonstrates the approach of local extinction followed by the subsequent re-ignition. Although the starting temperature and the trend are the same, the prediction from the 11-species model gradually deviates from

that of GRI-Mech 3.0. The deviation reaches its peak of 86 K (6%) near $20t_j$, but decreases slightly afterwards, stabilizes at ~50 K, and remains stable to the end of the simulation. Temperature from the 11-species model is always lower than that from GRI-Mech 3.0, as a result of different heat release pathways/rates.

The most probable temperatures in the PDF plots follow the temporal evolution of mean temperature. PDFs at re-ignition are much narrower than those at local extinction, which indicates that even at local extinction, there are some pockets of gas in a fully burning state. The two models show a qualitatively similar structure of the PDF, but their peak values and the right tails of high temperatures are quantitatively different, as shown in Table 7.1. Comparing with GRI-Mech 3.0, the PDFs from the 11-species model are biased toward lower temperatures, which is consistent with the mean temperature evolution, and the standard deviation is smaller, which indicates a narrower PDF.

Table 7.1: Statistics of the PDF of temperature on the stoichiometric surface (Z_{st}) for the two chemical kinetics models.

Statistics	GRI-Mech 3.0 ($20\ t_j$)	11-species model ($20\ t_j$)	GRI-Mech 3.0 ($40\ t_j$)	11-species model ($40\ t_j$)
Mean	1243 K	1194 K	1622 K	1580 K
Standard deviation	194 K	163 K	141 K	115 K
Skewness	-0.15	-0.21	-0.66	-0.58

The initial mean temperatures (Figure 7.3(a)) are generated from 1D steady laminar flamelet solutions (from a counter-flow configuration), and the values are close for the two chemical kinetics models (0.76% difference), indicating that the deviation is small in 1D steady laminar flames. The deviation between the two chemical kinetics models is magnified by the unsteady turbulent configuration.

Turbulence and unsteady turbulent reacting flows are chaotic dynamical systems that evolve on strange attractors of maximum dimension equal to the available degrees of freedom of the discretized system. By reducing the dimensionality of this system through elimination of governing equations, the attractor could be significantly altered, and the chaotic system may deviates and follows a different attractor. Therefore, this is one of the potential reasons to explain the observed deviation magnification. To directly investigate the effects of chaos in this system, Figure 7.4 shows the temporal evolution of mean temperature on the stoichiometric surface obtained from 11-species model with $\pm 5\%$ perturbations to the initial temperatures. In the evolution, the deviations are the same order of magnitude to the initial perturbations, with the largest deviation of ~7% (deviation magnification), and the smallest deviation of ~2% (deviation reduction). Therefore, there is no significant magnification of the initial perturbations. This prove that the system is insensitive to initial perturbations, and thus not a typical chaotic system.

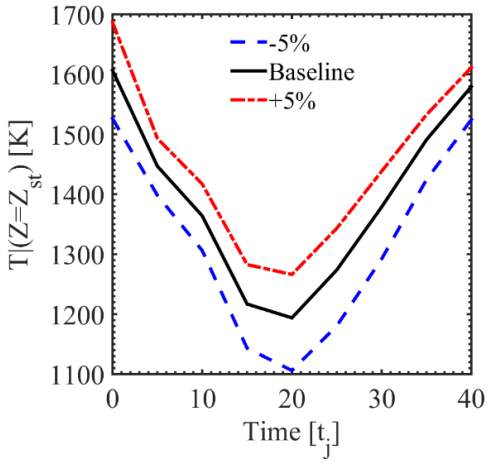

Figure 7.4: Temporal evolution of mean temperature on the stoichiometric surface obtained from 11-species model with $\pm 5\%$ perturbations to initial temperatures.

To quantitatively investigate this observation and compare with the flamelet solutions, absolute and relative mean deviations between the two chemical kinetics models (in mixture fraction space) of the 1D steady laminar flame, 3D unsteady laminar flame, and 3D turbulent flame are presented in Table 7.2. For an arbitrary quantity ϕ, its absolute mean deviation is defined as:

$$dev_{abs,st}^{\phi} = \max_{0 \le t \le 40 t_j} \left| \langle \phi_{GRI} | Z = Z_{st} \rangle(t) - \left\langle \phi_{11-sp} \middle| Z = Z_{st} \right\rangle(t) \right| \tag{7.2}$$

and its relative mean deviation is defined as:

$$dev_{rel,st}^{\phi} = \max_{0 \le t \le 40 t_j} \left| \frac{\langle \phi_{GRI} | Z = Z_{st} \rangle(t) - \left\langle \phi_{11-sp} \middle| Z = Z_{st} \right\rangle(t)}{\langle \phi_{GRI} | Z = Z_{st} \rangle(t)} \right| \tag{7.3}$$

Table 7.2: Maximal (over time) deviations/errors of the 11-species model (11-sp), GRI-Mech 3.0 using CoDAC+CoTran, and GRIred11, with respect to GRI-Mech 3.0. Mean values of temperature and mass fractions of representative species on the stoichiometric surface.

Abs. deviation	T (K)	Y_{CO}	Y_{H_2}	Y_{O_2}	Y_H	Y_O	Y_{OH}	Y_{CO_2}	Y_{H_2O}
1D steady laminar: 11-sp	12.22	0.0017	0.00001	0.0012	0.000007	0.00004	0.00044	0.0025	0.0001
3D unsteady laminar: 11-sp	89.00	0.0027	0.00002	0.0019	0.000101	0.00086	0.00044	0.0045	0.0024
3D turbulent: 11-sp	86.47	0.0038	0.00010	0.0026	0.000118	0.00143	0.00033	0.0054	0.0018
3D turbulent: CoDAC+CoTran	01.30	0.0002	3.44E-6	0.0002	0.000003	0.00004	0.00001	0.0004	3.1E-5
1D steady laminar: GRIred11	04.03	0.0004	1.65E-6	0.0003	7.40E-07	0.00004	0.00002	0.0008	0.0001
3D turbulent: GRIred11	11.25	0.0012	0.00002	0.0008	0.000006	0.00010	0.00004	0.0013	0.0002

Table 7.2 continued

Rel. dev. (%)	T	Y_{CO}	Y_{H_2}	Y_{O_2}	Y_H	Y_O	Y_{OH}	Y_{CO_2}	Y_{H_2O}
1D steady laminar: 11-sp	0.76	2.07	03.69	2.08	02.03	00.69	17.77	1.18	0.51
3D unsteady laminar: 11-sp	5.18	4.80	08.64	4.82	32.82	21.62	13.24	1.65	7.77
3D turbulent: 11-sp	5.96	2.82	21.09	2.80	49.55	33.86	14.11	5.00	8.51
3D turbulent: CoDAC+CoTran	0.09	0.19	00.45	0.19	01.23	01.10	00.83	0.34	0.15
1D steady laminar: GRIred11	0.25	0.45	00.48	0.44	00.20	00.76	00.62	0.35	0.51
3D turbulent: GRIred11	0.91	0.77	02.01	0.77	02.88	04.02	04.10	1.38	0.90

Since the 3D turbulent flame problem is of concern here, the same configuration is used for the 3D unsteady laminar case with the initial turbulence turned off and the Reynolds number reduced to 500 to avoid the generation of turbulence from the shear layers. Due to the lower mean strain rate, local extinction does not occur in this 3D unsteady laminar flame. As shown in Table 7.2, the deviations increase sharply from the 1D steady laminar flame to the 3D unsteady laminar flame to the 3D turbulent flame for most quantities, including temperature and major species. In particular, the absolute deviation magnification factor is 7 for temperature, 10 for H_2, and 13 for H_2O; the relative deviation magnification factor is 8 for temperature, 6 for H_2, 4 for CO_2, and 17 for H_2O. Turbulence and other unsteady effects significantly increase the deviations between the two chemical kinetics models. The 3D unsteady laminar case is a non-chaotic system, thus chaotic system and strange attractor cannot explain the deviation magnification due to general unsteadiness effects. Similar deviation enlargement has also been observed recently in an opposing-jet laminar flame impinged with unsteady vortex [206], which is also not a chaotic system.

The shear layers undergo unsteady growth, and the complex interaction of these unsteady effects with the kinetics significantly increases the discrepancies between the

two chemical kinetics models. For example, in 3D unsteady laminar simulations, the correlation coefficient of the two chemical kinetics models for the reaction rate of H_2O (defined as $\rho_{\dot{\omega}_{H_2O}^{GRI},\dot{\omega}_{H_2O}^{11-sp}} = \frac{cov\left(\dot{\omega}_{H_2O}^{GRI},\dot{\omega}_{H_2O}^{11-sp}\right)}{\sigma_{\dot{\omega}_{H_2O}^{GRI}} \cdot \sigma_{\dot{\omega}_{H_2O}^{11-sp}}}$, where cov is the covariance, and σ_X is the standard deviation of X) is 0.96. These deviations in reaction rates, and therefore heat release rate accumulate over time, which result in the above deviations in both mass fraction and temperature.

For most quantities (except for H_2 and CO_2), the deviations between the two chemical kinetics models in the unsteady laminar case is either close to or even larger than those in the turbulent case, which means that general unsteadiness effects are more significant than turbulence effects in the mixture fraction space. Therefore, the observed deviation magnification in turbulent case is not primarily due to the chaotic system and strange attractor. Comparing to the unsteady laminar case, the addition of turbulence amplifies the deviations for some quantities, but reduces the deviations for some others. The former ones may come from different attractors in the chaotic system. However, for the latter ones, either chaos is not the dominant factor, or the altered attractor is very close to the original attractor in the chaotic system. The most important effect of turbulence is on the spatial distribution of the shear layers and mixture fraction Z, but this effect is averaged out, as shown in Table 7.2. Note that the error quantification is much more stringent in Table 5.6 than in Table 7.2, because large local point-wise deviations can occur even if predictions from the two chemical kinetics models have similar means and PDFs on the stoichiometric surface. Table 7.2 provides better error quantification of CoDAC+CoTran using Eqs. (5.9-5.10). For the prediction of all quantities, the error introduced by CoDAC+CoTran is only 0.09~1.23%. Both the absolute and relative errors of CoDAC+CoTran are one to two orders of magnitude smaller than the corresponding deviations between the results from the two chemical kinetics models. This suggests that

CoDAC+CoTran introduces only negligible errors, which do not affect the observations discussed here.

The differences between the results using the two chemical kinetics models can be related to two major differences in the models: (a) GRI-Mech 3.0 contains 42 more species than the 11-species model, and thus contains 293 more kinetic reactions related to those 42 species, and (b) for those reactions included in both models, the reaction rate coefficients are different. To quantify the difference in the simulation results caused by the larger number of species in GRI-Mech 3.0, a globally reduced version of GRI-Mech 3.0 was created. The reduced version, which is referred to as 'GRIred11', only includes the 11 species treated in the 11-species model, and incorporates only those reactions related to these 11 species. Table 7.2 includes the deviations between detailed GRI-Mech 3.0 and GRIred11. Note that these deviations are always 2~10 times larger than the corresponding errors introduced by CoDAC+CoTran, which verifies that CoDAC is more accurate than the conventional global reduction.

Table 7.3 shows the contribution of (a) to the total absolute deviations between the two chemical kinetics models, and the absolute deviation magnification factors for (a), (b), and the total. The contribution of (a) is defined as the ratio of the deviations between GRI-Mech 3.0 and GRIred11 to the deviations between GRI-Mech 3.0 and the 11-species model: $C^{\phi}_{(a),st} = dev^{\phi,(GRI\ vs\ GRIred11)}_{abs,st} / dev^{\phi,(GRI\ vs\ 11-sp)}_{abs,st}$. In the 1D steady laminar case, (b) dominates the total deviations for most quantities (except O and H_2O). In the 3D turbulent case, (b) dominates the total deviations for all quantities. Both (a) and (b) are sensitive to unsteadiness and other turbulence effects for all quantities, but with only (a), even though the deviation magnification is significant (up to 12 times), the relative deviations are still within ~4% for all quantities. Therefore, the global mechanism reduction is still valid to use. For temperature and all species with more than 10 times total deviation magnification (H, O, H_2O), (b) is more sensitive, which results in the rise of its contribution to total deviations from 1D steady laminar case to 3D turbulent

case. In particular, for O and H_2O in the 1D steady laminar case, (a) and (b) cause deviations in opposite directions at Z_{st}. As a result, (a) contributes more than 100% deviations for O and H_2O in the 1D steady laminar case. However, the magnification factors of (b) for O and H_2O are 414 and 1329, respectively, which are 200~1000 times larger than those of (a) and makes (b) the dominant part in the 3D turbulent case. Essentially, (a) means the reaction rates of the globally reduced pathways are linearly removed. In contrast, (b) means that the difference in reaction rate coefficients (e.g. activation energy) can be nonlinearly (e.g. exponentially) enlarged. In summary, (b) is the dominant source of the discrepancies between the results using the two models, and is more sensitive to unsteadiness and other turbulence effects.

Table 7.3: Contribution from the global reduction of reaction pathways to the maximal (over time) absolute deviations between GRI-Mech 3.0 and 11-species model; absolute deviation magnification factors for (a) global reduction of reaction pathways, (b) different reaction rate coefficients, and total. Based on mean values of temperature and mass fractions of representative species on the stoichiometric surface.

Contribution from (a) to total deviation (%)	T	Y_{CO}	Y_{H_2}	Y_{O_2}	Y_H	Y_O	Y_{OH}	Y_{CO_2}	Y_{H_2O}
1D steady laminar	32.98	23.53	16.5	25.00	10.57	>100	04.55	32.00	>100
3D turbulent	13.01	31.58	20.0	30.77	05.08	6.99	12.12	24.07	11.11
Dev. magnification factor	T	Y_{CO}	Y_{H_2}	Y_{O_2}	Y_H	Y_O	Y_{OH}	Y_{CO_2}	Y_{H_2O}
(a) Reduced pathways	2.79	3.00	12.12	2.67	08.11	002.54	2.00	1.63	0001.38
(b) Different RR coefficients	9.18	2.00	09.58	2.00	17.89	414.12	0.69	2.41	1329.36
Total	7.08	2.24	10.00	2.17	16.86	039.59	0.75	2.16	0012.55

Figure 7.5 shows a comparison of 2D contours of temperature as computed using GRI-Mech 3.0 and the 11-species model. The stoichiometric mixture fraction iso-lines are marked as black curves. Local extinction and re-ignition are clearly captured by both

models. At $20\ t_j$, the extinction level is high (93% of the computational domain is below 1300 K), and only a few discrete flame pockets survive. At $40\ t_j$, most regions in the shear layers have been re-ignited and the flames are connected. In addition, the shear layers at $40\ t_j$ are spread much more widely than at $20\ t_j$. The peak combustion intensities (quantified by peak temperature), as modeled using GRI-Mech 3.0 (1627 K at $20\ t_j$, and 1882 K at $40\ t_j$), are higher than those from the 11-species model (1547 K at $20\ t_j$, and 1812 K at $40\ t_j$); this is consistent with the previously-discussed statistics of T conditioned on Z_{st}. Flame surface area varies by up to 26% (at $20\ t_j$) between the two chemical kinetics models, and the spatial distribution of combustion intensity is different, especially at $40\ t_j$. These differences are not revealed by comparison of T versus Z_{st}, because those analyses average out the differences in the spatial distribution of the shear layers and mixture fraction. For this reason, the average of the local point-wise deviation between the two chemical kinetics models is significantly larger than those shown in Table 5.6. These differences are particularly important in practice, as they can quickly affect the interplay of molecular diffusion, finite-rate kinetics, and turbulent mixing, thus altering the combustion dynamics.

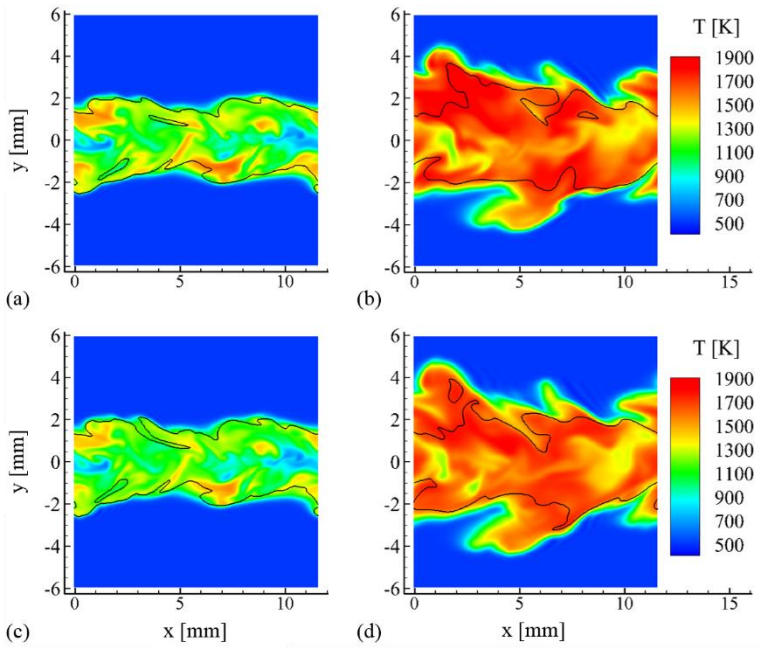

Figure 7.5: Instantaneous 2D contours of temperature at $20\,t_j$ (left) and $40\,t_j$ (right) on center plane (Z = 4H); GRI-Mech 3.0 (upper) and 11-species model (lower).

7.4.2.2 Conditional Statistics

Figure 7.6 shows the mixture-fraction conditioned mean values of temperature, and mass fractions of OH, O, and H at local extinction ($20\,t_j$) and re-ignition ($40\,t_j$). The initial values and the laminar flamelet data at extinction from both chemical kinetics models are obtained by gradually increasing the bulk strain rate in the laminar flamelet calculation until extinction occurs. As shown in Figure 7.6, for both chemical kinetics models, the temperature and mass fractions of OH and H decrease below the extinction values of the laminar flamelet solution at $20\,t_j$, indicating approach toward local extinction. Temperatures drop to ~1300 K, which is ~300 K lower than the initial temperatures, and rise again beyond the extinction values at $40\,t_j$, indicating re-ignition. The behavior of H is different from those of the other three quantities, as it increases continuously regardless of extinction and re-ignition. This is because most H_2 is

converted into H and OH radicals within the fuel stream, rather than reacting at the stoichiometric flame surface, and thus it is less affected by the change in the intensity of combustion.

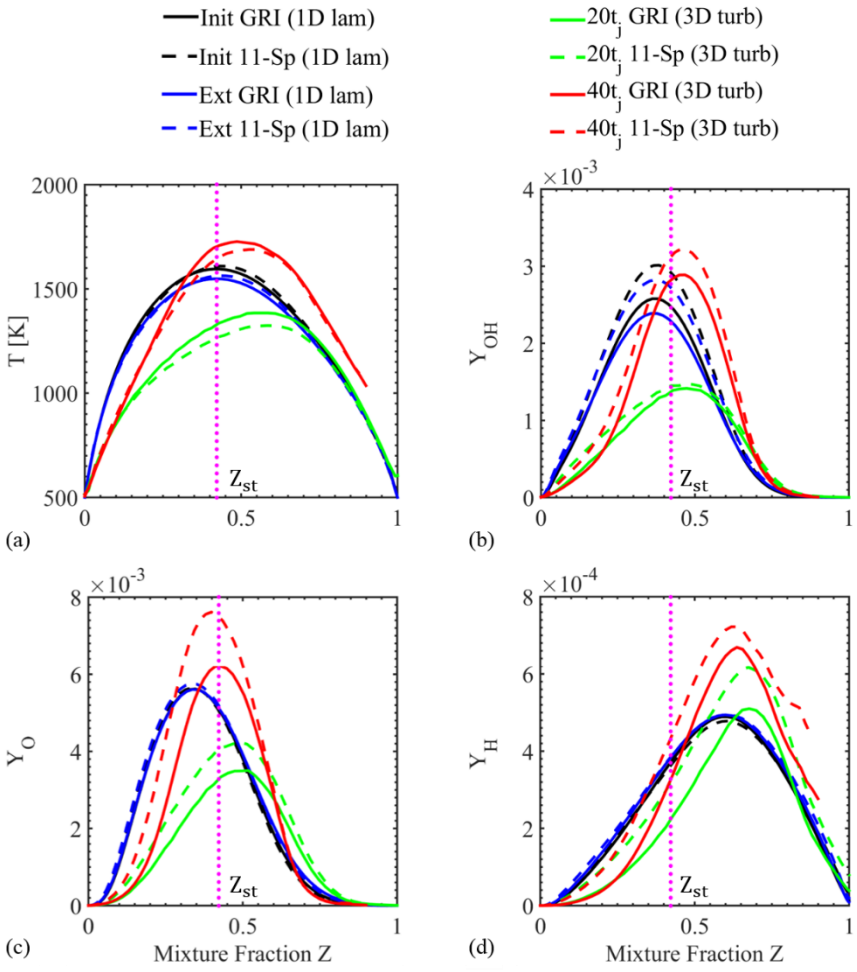

Figure 7.6 Comparison of GRI-Mech 3.0 (solid line) and 11-species model (dashed line) in 1D steady laminar solutions (initial data and laminar flamelet values at extinction) and 3D turbulent simulations (at $20t_j$ and $40t_j$): the conditional means of (a) T, (b) Y_{OH}, (c) Y_O, and (d) Y_H.

The comparison of heat release rates from the two models is shown in Figure 7.7. GRI-Mech 3.0 has a higher peak heat release rate than the 11-species model, which explains the higher temperature in the simulation using GRI-Mech 3.0.

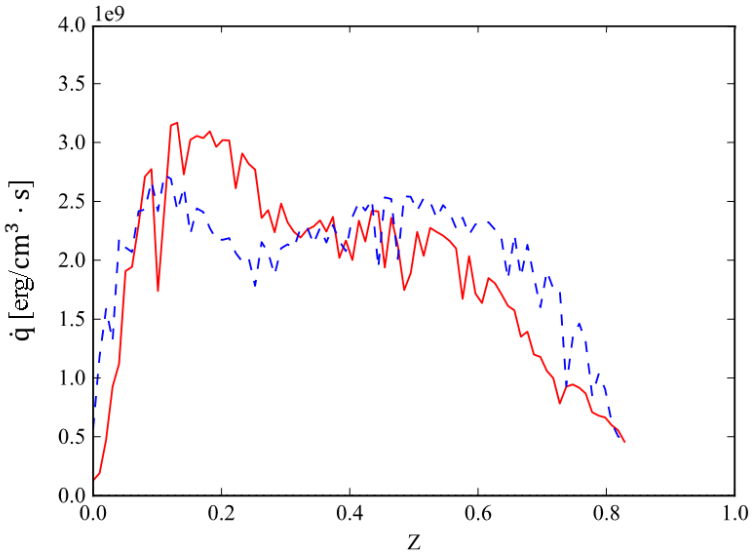

Figure 7.7 Comparison of GRI-Mech 3.0 (red solid line) and 11-species model (blue dashed line) in 3D turbulent simulations (at $40t_j$): conditional statistics of heat release rate.

Although the predictions from the two chemical kinetics models show the same trends, the 11-species model predicts lower temperature and higher radical levels at all mixture fractions. In other words, it predicts a lower radicals-to-products conversion rate for release heat. As a result, the 11-species model predicts more local extinction (mean $T|Z_{st}$ is 49 K smaller) but less re-ignition (mean $T|Z_{st}$ is 42 K smaller). The largest deviations and peak values of temperature, OH, and O in the 1D steady laminar case are located near the stoichiometric mixture fraction of 0.42. The mixture fractions corresponding to the largest deviations or peak values in 3D turbulent simulations, on the

other hand, are all on rich side (Z > 0.42), due to the relatively high diffusivities of fuels. For example, at 20 t_j, H peaks and deviates most at approximately Z = 0.7, a highly rich value. Moreover, all deviations in the 3D turbulent simulations are significantly larger than those in the 1D steady laminar solutions, except for the OH mass fraction, which has different laminar flamelet predictions in the two chemical kinetics models. In contrast, there are no observable errors in the same comparison between the results from the benchmark and from CoDAC+CoTran (not shown here); this demonstrates that CoDAC+CoTran technique does not affect the observations presented here. There are only minor deviations between GRI-Mech 3.0 and GRIred11 in the same comparison (not shown here).

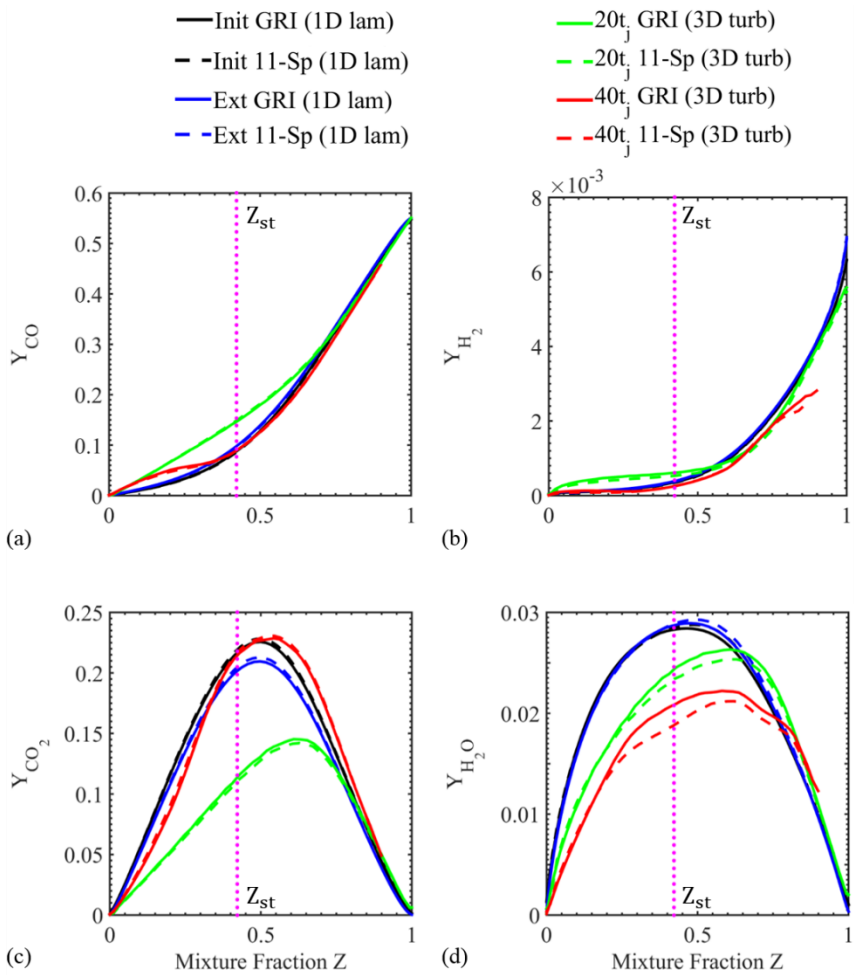

Figure 7.8 Mass fractions of (a) CO, (b) H_2, (c) CO_2, and (d) H_2O, in 1D steady laminar solution (initial data and laminar flamelet values at extinction) and 3D turbulent simulations (at $20t_j$ and $40t_j$); GRI-Mech 3.0 (solid line) and 11-species model (dashed line).

Figure 7.8 compares the conditional means of mass fractions of CO, H_2, CO_2, and H_2O with respect to mixture fraction from both chemical kinetics models. Profiles of the conditional Y_{CO} are close to linear, while those of Y_{H_2} contain significant variations of slope with respect to mixture fraction. More precisely, the slopes of Y_{H_2} are larger than those of Y_{CO} near Z=1 (the fuel stream) because the early consumption of H_2 inside the fuel stream provides H and OH radicals for the oxidation of CO. On the other hand, the

slopes of Y_{H_2} are smaller than those of Y_{CO} near Z=0 (the oxidizer stream), due to the recombination of radicals to reform H_2. Following the consumption of fuel, at approximately Z=0.9 at 40 t_j, the profiles of both Y_{CO} and Y_{H_2} end.

The behavior of Y_{CO_2} is similar to that of the OH and O radicals – it is lower than the extinction values at 20 t_j but higher at 40 t_j. In contrast, instead of recovering to values exceeding the extinction cutoff, H_2O levels further decrease at 40 t_j. There are two reasons for this phenomenon. On one hand, as shown in Figure 7.8 (a-b), the initial jet contains only 10% H_2 but 50% CO (by volume) so that at 40 t_j there is limited H_2 left in the fuel stream to generate H, OH and H_2O, but a significant amount of CO left for CO_2 generation. On the other hand, thermal decomposition of H_2O ($H_2O+M=H+OH+M$, $H_2O+O=2OH$) dominates the reactions at the high re-ignition temperature, as can be seen in the high level of H and OH at 40 t_j, as shown in Figure 7.6 (b, d).

At 20 t_j, as compared with H radical, both products peak and deviate most at above Z=0.6, a less-rich value, because of the smaller diffusivities. All predictions of the conditional Y_{CO} from the two chemical kinetics models match well, while there are slight deviations in Y_{H_2} and Y_{CO_2}. Moreover, the 11-species model predicts a significantly lower level of Y_{H_2O} in turbulent simulations (especially in the range of $0.2 < Z < 0.8$), but a slightly higher level in 1D steady laminar solutions. The reason for these opposite deviation trends is that the deviations in H_2O from (a) global reduction in kinetics pathways, and (b) different reaction rate coefficients, are in the opposite direction. Furthermore, (a) dominates the total deviations in 1D steady laminar flames, while (b) dominates in 3D turbulent flames, as discussed in section 7.4.2.1. For this reason, for H_2O in 1D steady laminar flames, the deviation between GRI-Mech 3.0 and GRIred11 (contribution from (a): $dev_{abs,st}^{H_2O,(GRI\ vs\ GRIred11)}$) is larger than the deviation between GRI-Mech 3.0 and the 11-species model (total deviation: $dev_{abs,st}^{H_2O,(GRI\ vs\ 11-sp)}$). As a result,

(a) contributes more than 100% of the total deviation of H_2O in 1D steady laminar flames, as shown in Table 7.3. Even though, both the total deviation and the contribution from (a) are actually very small (within 0.5%) in 1D steady laminar flames. According to the Arrhenius law, the reaction rate $RR = k(T)\prod_k [Y_k]^{\nu'_k}$, and the reaction rate constant $k(T) = A\,T^b \exp\left(-\frac{E_a}{RT}\right)$.

In 1D steady laminar solutions, the deviations in species concentration and temperature between the two chemical kinetics models (GRI-Mech 3.0 and the 11-species model) are negligible, so the additional reaction pathways in GRI-Mech 3.0 and the deviations of pre-exponential factor A dominate the total deviations. More precisely, both chemical kinetics models have exactly the same coefficients (A, b, E_a) for the major H_2O formation reaction (H_2+OH=H_2O+H), but the pre-exponential factor A of the major decomposition reaction of H_2O (the inverse of H+OH+M=H_2O+M) for GRI-Mech 3.0 is 72% higher than in the 11-species model. This is why the 11-species model predicts a slightly higher level of H_2O and a slightly lower level of H in the 1D steady laminar solution.

In unsteady simulations, the deviations in species concentration and temperature are significantly higher. In addition, according to Table 7.3 and a comparison of the same conditional statistics between GRI-Mech 3.0 and GRIred11 (not shown here), (a) is not the main driver for these large deviations. This suggests that, instead of deviations in pre-exponential factor A or deviations from (a), deviations in reactant concentration and the nonlinear temperature-dependent term $T^b \exp\left(-\frac{E_a}{RT}\right)$ are responsible for the total deviations. Note that the 11-species model predicts a lower H_2 level and significantly lower temperature than GRI-Mech 3.0, so that the major H_2O formation pathway (H_2+OH=H_2O+H) is significantly slower. In addition, this reaction (with E_a = 3430 cal/mole) is more sensitive to temperature than H_2O's major decomposition pathway (the inverse of H+OH+M=H_2O+M with E_a = 0), so that the H_2O decomposition rates in the

two chemical kinetics models are similar. These considerations explain why the 11-species model predicts a significantly lower H_2O level in unsteady simulations. In summary, the deviations in species concentration, temperature, and reaction rates form a nonlinear positive feedback loop in unsteady simulations, which significantly magnifies the sensitivity of simulation results to chemical kinetics models.

To provide further quantitative detail on the conditional mean deviations between the two chemical kinetics models, absolute and relative deviations of the 1D steady laminar flame (initial and at extinction), 3D unsteady laminar flame (both $20\ t_j$ and $40\ t_j$), and turbulent flame (both $20\ t_j$ and $40\ t_j$) using the two chemical kinetics models are presented in Table 7.4. The absolute conditional mean deviation of an arbitrary quantity ϕ is defined as:

$$dev_{abs}^{\phi} = \max_{0 \le Z \le 1} \left| \langle \phi_{GRI} | Z \rangle - \langle \phi_{11-sp} | Z \rangle \right| \tag{7.4}$$

and its relative conditional mean deviation is defined as:

$$dev_{rel}^{\phi} = \max_{0 \le Z \le 1} \left| \frac{\langle \phi_{GRI} | Z \rangle - \langle \phi_{11-sp} | Z \rangle}{\langle \phi_{GRI} | Z \rangle} \right| \tag{7.5}$$

Table 7.4: Maximal (over mixture fraction Z) deviations/errors of the conditional means in the 11-species model (11-sp), GRI-Mech 3.0 using CoDAC+CoTran, and GRIred11, with respect to GRI-Mech 3.0: temperature and mass fractions of representative species.

Absolute deviation	T (K)	Y_{CO}	Y_{H_2}	Y_{O_2}	Y_H	Y_O	Y_{OH}	Y_{CO_2}	Y_{H_2O}
Init. (1D steady laminar): 11-sp	23.28	0.002	0.00003	0.0013	0.00002	0.0002	0.00044	0.003	0.0006
Ext. (1D steady laminar): 11-sp	22.14	0.002	0.00006	0.0017	0.00002	0.0003	0.00044	0.003	0.0006
$20t_j$ (3D unsteady laminar): 11-sp	96.76	0.006	0.00003	0.0062	0.00006	0.0013	0.00057	0.006	0.0023
$40t_j$ (3D unsteady laminar): 11-sp	89.25	0.004	0.00006	0.0027	0.00004	0.0011	0.00060	0.006	0.0019
$20t_j$ (3D turbulent): 11-sp	70.97	0.004	0.00035	0.0085	0.00011	0.0007	0.00017	0.009	0.0022
$40t_j$ (3D turbulent): 11-sp	86.20	0.024	0.00039	0.0056	0.00019	0.0016	0.00057	0.016	0.0023
$20t_j$ (3D turbulent): CoDAC+CoTran	06.81	0.002	0.00009	0.0005	5.62E-6	5.6E-5	0.00002	0.001	0.0002
$40t_j$ (3D turbulent): CoDAC+CoTran	11.27	0.004	0.00008	0.0013	0.00002	9.7E-5	0.00004	0.003	0.0004
Init. (1D steady laminar): GRIred11	08.55	0.001	0.00005	0.0002	4.22E-6	4.5E-5	0.00002	0.001	0.0002
$20t_j$ (Turbulent): GRIred11	22.52	0.003	0.00019	0.0015	0.00001	0.0001	0.00006	0.004	0.0007
$40t_j$ (Turbulent): GRIred11	14.39	0.002	0.00006	0.0015	0.00002	9.9E-5	0.00005	0.002	0.0002
Rel. deviation (%)	T	Y_{CO}	Y_{H_2}	Y_{O_2}	Y_H	Y_O	Y_{OH}	Y_{CO_2}	Y_{H_2O}
Init. (1D steady laminar): 11-sp	1.52	01.36	31.18	4.11	30.69	08.89	17.61	01.16	02.47
Ext. (1D steady laminar): 11-sp	1.49	01.36	00.89	4.54	16.29	10.71	18.50	01.49	02.37
$20t_j$ (3D unsteady laminar): 11-sp	5.08	05.47	06.52	3.05	34.07	47.08	28.55	02.59	07.66
$40t_j$ (3D unsteady laminar): 11-sp	4.59	10.62	03.09	2.77	47.64	54.13	29.72	02.85	06.64

Table 7.4 continued

Rel. deviation (%)	T	Y_{CO}	Y_{H_2}	Y_{O_2}	Y_H	Y_O	Y_{OH}	Y_{CO_2}	Y_{H_2O}
$20t_j$ (3D turbulent): 11-sp	5.26	73.41	07.79	2.95	23.64	21.46	32.49	30.80	62.36
$40t_j$ (3D turbulent): 11-sp	5.46	05.21	14.51	5.56	58.99	33.51	26.05	14.56	11.16
$20t_j$ (3D turbulent): CoDAC+CoTran	1.02	00.35	02.28	0.002	01.15	01.60	01.44	04.23	04.57
$40t_j$ (3D turbulent): CoDAC+CoTran	1.00	01.00	02.98	0.011	05.44	02.34	03.53	06.30	02.40
Init. (1D steady laminar): GRIred11	0.99	00.20	01.23	00.78	02.16	00.83	00.76	02.80	0.57
$20t_j$ (Turbulent): GRIred11	3.68	00.50	03.26	00.48	03.22	04.52	04.68	04.76	03.86
$40t_j$ (Turbulent): GRIred11	1.00	00.38	02.25	01.11	06.99	01.60	02.63	01.78	01.12

For the 1D steady laminar case in Table 7.4, the ~31% relative deviation of H and H_2 happens near Z=1 (pure fuel) and Z=0 (pure oxidizer), where the concentrations of H and H_2 are close to zero (see Figure 7.6 and Figure 7.8) resulting in this large deviation. Similar to the trend shown in Table 7.2, the deviations in Table 7.4 increase sharply from the 1D steady laminar to the 3D unsteady laminar to the 3D turbulent for most quantities, including temperature and major species. As shown in Table 7.2, the relative deviation in 3D turbulent simulations is up to 50 times larger than that in the 1D steady laminar solutions for CO, almost 20 times for H_2, almost 30 times larger for CO_2 and H_2O, and nearly 4 times larger for temperature. The absolute deviation magnification factor is 4 for temperature, 12 for CO, 13 for H_2, 7 for O_2, 5 for CO_2, and 4 for H_2O. This further proves that the effects of unsteadiness and turbulence can significantly increase the deviations between the two chemical kinetics models, not only on the stoichiometric surface, but also for all values of mixture fraction. Again, the effect of unsteadiness is larger than that of turbulence for most quantities, because the major influence of turbulence is on the spatial distribution of the shear layer flow field and mixture fraction, and the spatial distribution is diminished in both Table 7.2 and Table 7.4. Therefore, the observed

deviation magnification in turbulent case is not primarily due to the chaotic system and strange attractor. Comparing to the unsteady laminar case, the addition of turbulence amplifies the deviations for some quantities, but reduces the deviations for some others. The former ones may come from different attractors in the chaotic system. However, for the latter ones, either chaos is not the dominant factor, or the altered attractor is very close to the original attractor in the chaotic system. At 20 t_j, the deviation in unsteady simulation is nearly 100 K, which is hardly acceptable for high-fidelity prediction, and could significantly affect the prediction of many important quantities, including NO_x emission.

To verify that CoDAC+CoTran does not affect the above observations, Table 7.4 also provides its error quantification using Eqs. (7.4) and (7.5). The errors are one half to three orders of magnitude smaller than the corresponding differences between the two chemical kinetics models. Table 7.4 also includes the differences between GRI-Mech 3.0 and GRIred11 to show the contribution from the global reduction of kinetics pathways to the total deviations.

To better understand the contribution to the total deviations from (a) the global reduction of kinetics pathways, and from (b) the differences in reaction rate coefficients, Table 7.5 shows the contribution of (a) to the total absolute deviations between the two chemical kinetics models, and the absolute deviation magnification factors for (a), (b), and total. The contribution of (a) is defined as the ratio of the deviations between GRI-Mech 3.0 and GRIred11 to the deviations between GRI-Mech 3.0 and the 11-species model: $C_{(a)}^{\phi} = dev_{abs}^{\phi,(GRI\ vs\ GRIred11)}/dev_{abs}^{\phi,(GRI\ vs\ 11-sp)}$. In the 1D steady laminar case, part (b) dominates the total deviations for most quantities except fuels (CO and H_2). In the 3D turbulent case, part (b) dominates the total deviations for all quantities. Both (a) and (b) are sensitive to unsteadiness and other turbulence effects, but for temperature and all major species, (b) is more sensitive than (a). In particular, (a) contributes

approximately 50% of the deviation for CO and more than 100% for H_2 in the 1D steady laminar case, which indicates that (a) and (b) cause deviations in opposite directions for H_2. However, the magnification factors of (b) for O and H_2O are 21 and 18, respectively, which are 6~7 times larger than those of (a) and makes (b) the dominant factor in the 3D turbulent case. In addition, with only (a), even after the large deviation magnification (up to 7.5 times), the deviations are still within ~2% for temperature and major species. The global mechanism reduction can thus still be considered appropriate for use. In summary, (b) dominates the deviations and is more sensitive to unsteadiness and other turbulence effects.

Table 7.5: Contribution from the global reduction of reaction pathways to the maximal (over mixture fraction Z) absolute deviations between GRI-Mech 3.0 and the 11-species model; absolute deviation magnification factors for (a) global reduction of reaction pathways, (b) different reaction rate coefficients, and total. Temperature and mass fractions of representative species.

Contribution from (a) to total deviation (%)	T	Y_{CO}	Y_{H_2}	Y_{O_2}	Y_H	Y_O	Y_{OH}	Y_{CO_2}	Y_{H_2O}
1D steady laminar	36.73	50.0	>100	15.38	21.10	22.50	04.55	33.33	33.33
3D turbulent	26.13	12.5	48.72	17.65	10.53	06.25	10.53	25.00	30.43
Deviation magnification factor	T	Y_{CO}	Y_{H_2}	Y_{O_2}	Y_H	Y_O	Y_{OH}	Y_{CO_2}	Y_{H_2O}
(a) Reduced kinetics pathways	2.63	03	03.8	7.50	04.74	2.22	3.00	4.00	3.50
(b) Different RR coefficients	4.32	21	10.0	6.36	10.77	9.68	1.21	6.00	4.00
Total	3.89	12	13.0	6.54	09.50	8.00	1.30	5.33	3.83

Note that the above observations were shown to be insensitive to grid resolution in the grid convergence test, as presented in Figure 5.21. When the grid resolution is increased by a factor of 2 in all spatial directions, the temperature and mass fractions of H_2O and H only change up to approximately 0.5% (7 K), 1%, and 5%, respectively. In contrast, for both grid resolutions, the deviations between the two chemical kinetics

models in temperature and mass fractions of H_2O and H are approximately 6% (84 K), 6%, and 20%, respectively, and these sizes are independent of the grid refinement. The spatially averaged transverse profiles provide similar mesh-independent results. When the grid resolution is increased by a factor of 2 in all spatial directions, the temperature and mass fractions of H_2O and H only change up to approximately 1% (10 K), 1%, and 6.5%, respectively. In contrast, for both grid resolutions, the deviations between the two chemical kinetics models in temperature and mass fractions of H_2O and H are approximately 5.3% (67 K), 5.5%, and 40%, respectively, and these sizes are independent of the grid refinement.

7.4.2.3 Syngas Flame Structure

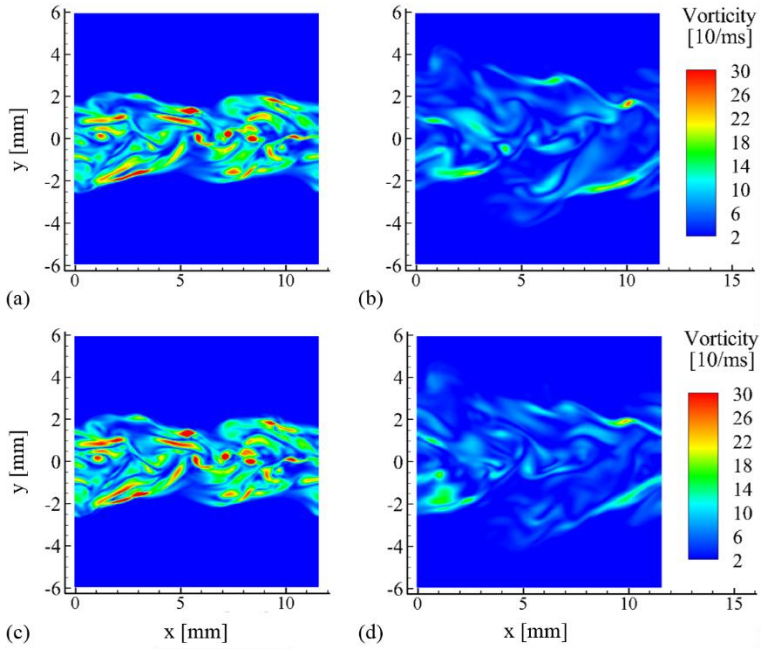

Figure 7.9: Comparison of GRI-Mech 3.0 (upper) and 11-species model (lower): instantaneous 2D contours of vorticity magnitude at 20 t_j (left) and 40 t_j (right) on center plane (Z = 4H).

To further investigate the effects of turbulence, which are not clear from the statistics in mixture fraction space, 2D contours of vorticity magnitude and mixture fraction obtained from turbulent simulations are shown in Figure 7.9 and Figure 7.10, respectively. The two chemical kinetics models produce similar vorticity magnitude and mixture fraction fields at $20\ t_j$ (local extinction), but significantly different fields at $40\ t_j$ (re-ignition). However, the same comparison for 3D unsteady laminar simulations (not shown here) shows almost identical vorticity magnitude and mixture fraction fields from both the chemical kinetics models, with less than 0.6% deviations in peak values. The deviations in flow and mixture fraction field seem therefore likely to be the result of the complex turbulence-chemistry interaction. Furthermore, the vorticity magnitude field does not contain the initial isotropic turbulence at both time instants, but is dominated by the shear-generated turbulence triggered by the initial turbulence. At both time instants, the stoichiometric mixture fraction value of 0.42 is found inside the shear layers.

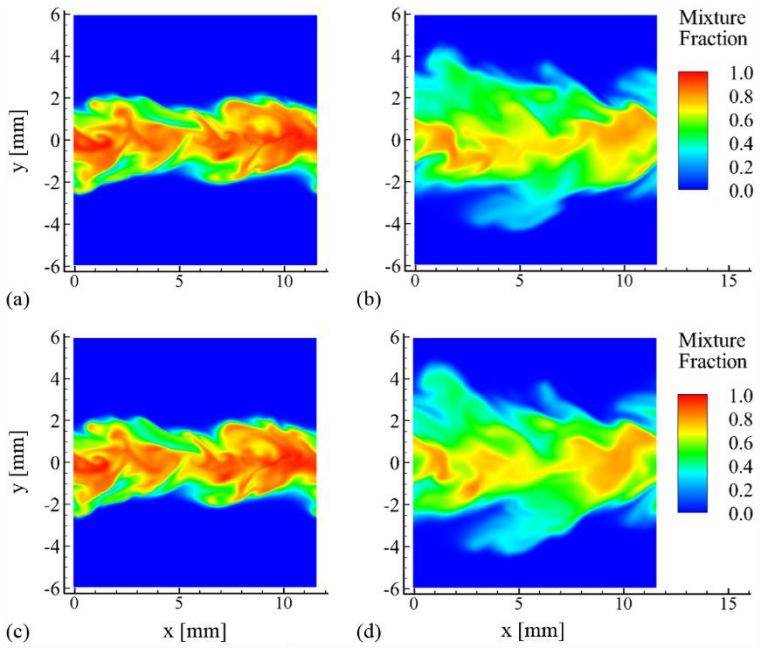

Figure 7.10: Comparison of GRI-Mech 3.0 (upper) and 11-species model (lower): instantaneous 2D contours of mixture fraction at 20 t_j (left) and 40 t_j (right) on center plane (Z = 4H).

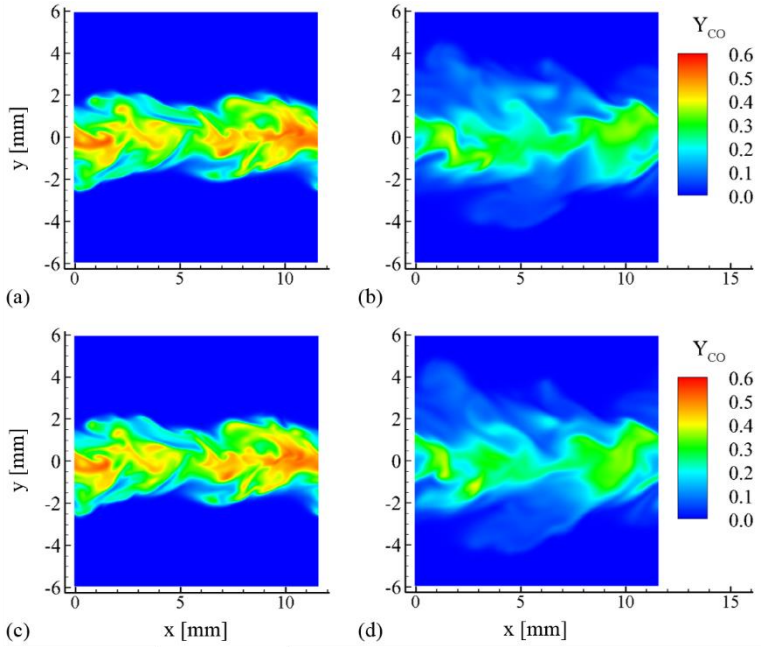

Figure 7.11: Instantaneous 2D contours of CO mass fraction at 20 t_j (left) and 40 t_j (right) on the center plane (Z = 4H): GRI-Mech 3.0 (upper) and 11-species model (lower).

The 2D contours of Y_{CO} and Y_{H_2} in turbulent simulations using the two chemical kinetics models are shown in Figure 7.11 and Figure 7.12, respectively. Due to fuel consumption, the levels of both CO and H_2 decrease significantly from $20\ t_j$ to $40\ t_j$. As shown in Figure 7.8, the consumption of H_2 is much faster than that of CO, as is consistent with the conditional statistics. This is because CO can only be consumed by combustion near the stoichiometric surface, but H_2 can be consumed inside the hot fuel stream by thermal decomposition (chain initiation reaction H_2+M=2H+M); this effect is also suggested by the spatial distribution of consumption rates of CO and H_2 (not shown here). In Figure 7.8, at $20\ t_j$, the major deviations between the two chemical kinetics models are in the peak values and the volume occupied by the peak values, as is further demonstrated by the conditional mean statistics. In contrast, the deviations at $40\ t_j$ are primarily in the spatial distribution, which is controlled by the flow field deviations shown in Figure 7.9.

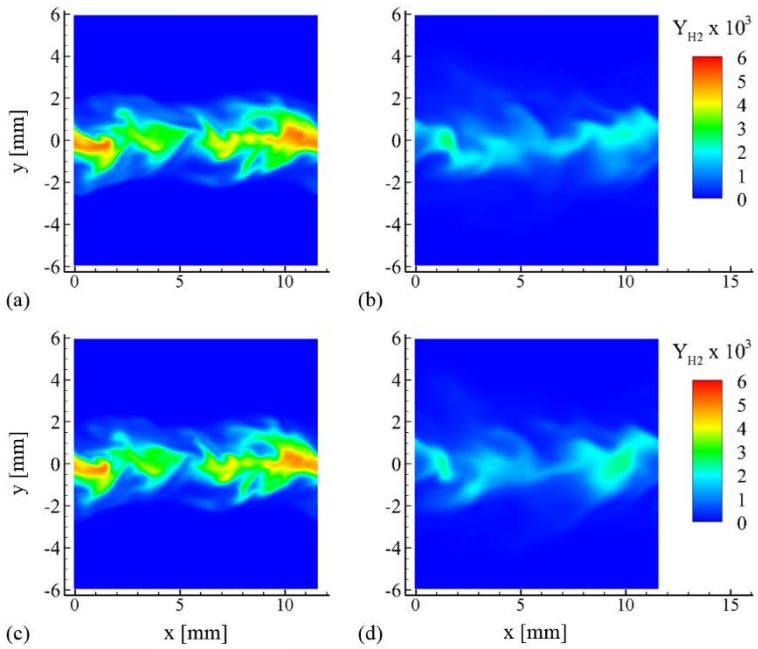

Figure 7.12: Instantaneous 2D contours of H_2 mass fraction at 20 t_j (left) and 40 t_j (right) on the center plane (Z = 4H): GRI-Mech 3.0 (upper) and 11-species model (lower).

Since OH is the key radical consuming CO and releasing heat, its 2D contours from the two chemical kinetics models are presented in Figure 7.13. Interestingly, the contours of OH roughly wrap around those of H_2 in Figure 7.12, which means that OH is mainly generated from the remaining H_2 in the fuel stream via chain branching reactions (i.e., $H+O_2=O+OH$, $O+H_2=H+OH$). The behavior of OH is similar to that of temperature in Figure 7.5, which indicates local extinction and re-ignition. Even at 20 t_j, however, a few disconnected small OH pockets survive and become the source of later re-ignition. A larger spread of OH in the transverse direction is clearly observed in the 11-species model as compared to GRI-Mech 3.0, especially at 40 t_j; this also demonstrates that the model with a lower radicals-to-products conversion rate (11-species model) can cause more local extinction and less re-ignition under the effect of turbulence.

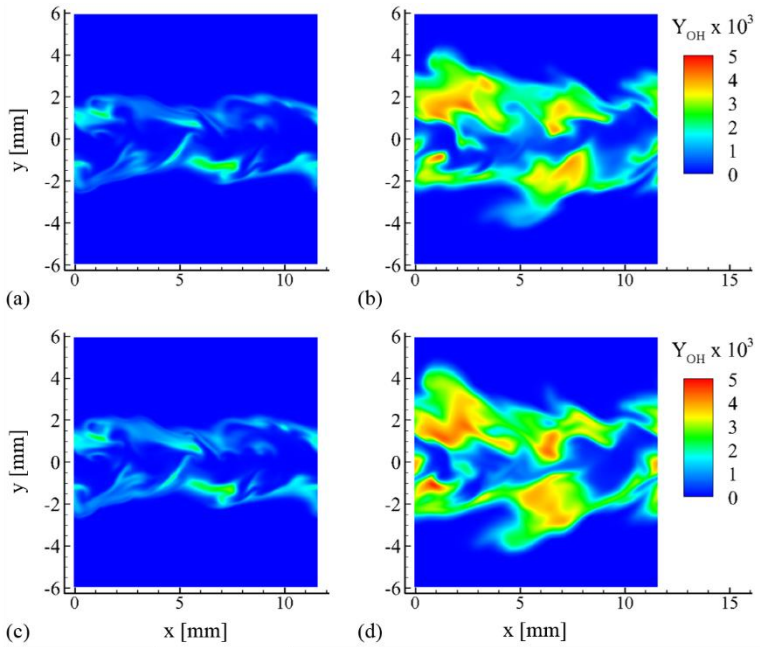

Figure 7.13: Instantaneous 2D contours of OH mass fraction at $20\ t_j$ (left) and $40\ t_j$ (right) on the center plane (Z = 4H): GRI-Mech 3.0 (upper) and 11-species model (lower).

7.4.2.4 Scalar Dissipation Rate Statistics

Figure 7.14 presents a comparison of the two chemical kinetics models through 2D contours in the symmetry plane of the scalar dissipation rate $\chi = 2D\nabla Z \cdot \nabla Z$, normalized by its extinction value χ_q = 961 sec^{-1}, where D is the mixture diffusivity, assuming unity Lewis numbers. A logarithmic scale is used here to account for the wide range of the scalar dissipation rate field. The stoichiometric mixture fraction iso-lines are marked as black curves. The contours clearly show that the flow is fully turbulent, and the high dissipation regions are concentrated in thin "laminar" sheets. The scalar dissipation rate is much more spatially distributed at $40\ t_j$ than at $20\ t_j$, due to more transverse spreading of the shear layers, but the peak values are similar. The thin sheets of peak values are generally located near the stoichiometric surface, where mixture

fraction has the largest gradients. As in the flow and mixture fraction fields, the two chemical kinetics models produce similar scalar dissipation rate distributions at $20\ t_j$ (local extinction) and different at $40\ t_j$ (re-ignition), but the two chemical kinetics models show almost identical scalar dissipation rate fields in the 3D unsteady laminar simulations (not shown here). This suggests that the deviations in scalar dissipation rate also come from the turbulence-chemistry interaction.

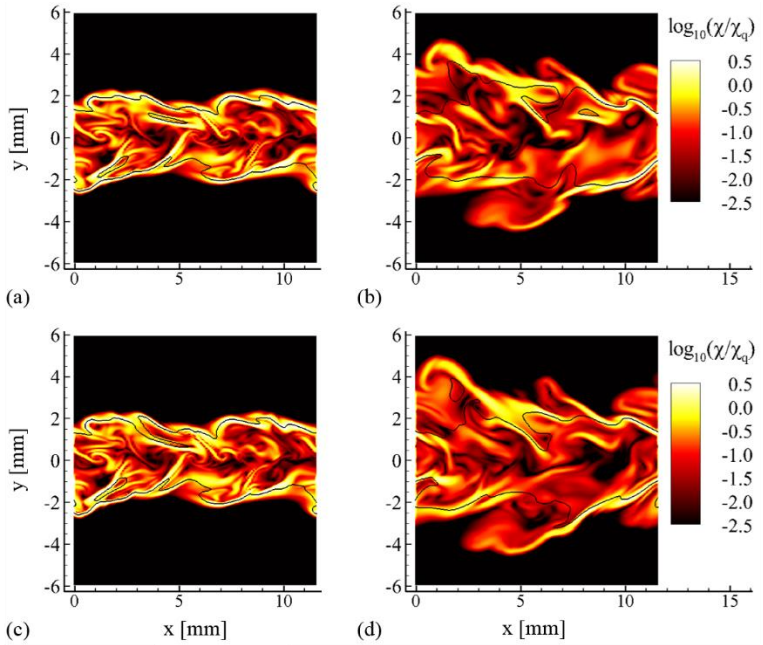

Figure 7.14: Instantaneous 2D contours of $\log_{10}(\chi/\chi_q)$ at $20\ t_j$ (left) and $40\ t_j$ (right) on the center plane (Z = 4H): GRI-Mech 3.0 (upper) and 11-species model (lower).

In order to remove possible bias resulting from the unmixed oxidizer fluid [207], Figure 7.15 shows a comparison of the normalized PDFs of scalar dissipation rate on the stoichiometric surface (Z_{st}) from both chemical kinetics models. Results from both chemical kinetics models match well, except for some slight deviations in the left tail

(normalized $\chi_{st} < -3$). The results from both chemical kinetics models match well even for the un-normalized PDF, with the detailed comparison shown in Table 7.6. Re-ignition ($40\ t_j$) has a slightly smaller mean scalar dissipation rate than local extinction ($20\ t_j$), due to the spreading of mixture fraction.

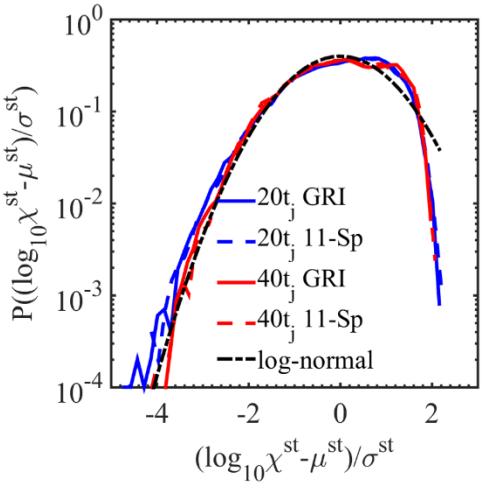

Figure 7.15: PDF of normalized logarithm of scalar dissipation rate on the stoichiometric surface at $20\ t_j$ (blue) and $40\ t_j$ (red): GRI-Mech 3.0 (solid lines), 11-species model (dashed lines), and log-normal distribution (dash-lot line).

Table 7.6: Statistics of non-normalized PDFs of scalar dissipation rate on stoichiometric surface (Z_{st}) from the two chemical kinetics models.

Statistics	GRI-Mech 3.0 ($20\ t_j$)	11-species model ($20\ t_j$)	GRI-Mech 3.0 ($40\ t_j$)	11-species model ($40\ t_j$)
Mean	3.25	3.23	2.64	2.59
2nd central moment	0.25	0.25	0.43	0.42
Standard deviation	0.50	0.50	0.66	0.65
3rd central moment	-0.06	-0.06	-0.10	-0.08
Skewness	-0.48	-0.45	-0.34	-0.31

Both chemical kinetics models show a negatively skewed mono-modal log-normal-like distribution with small departure from the ideal log-normal distribution on both tails [207]. With respect to the ideal log-normal distribution, they both over-predict the PDF at the left tail (normalized $\chi_{st} < -2$) and under-predict the PDF at the right tail (normalized $\chi_{st} > 2$). This is the so-called "scalar intermittency" in turbulent mixing theory [13]. Therefore, the log-normal distribution, which is applied in flamelet methods to model χ_{st} [208], has low accuracy at high and low values of χ_{st}, but good accuracy for the rest regions. Interestingly, re-ignition ($40\ t_j$) is slightly closer to the log-normal distribution than local extinction ($20\ t_j$), which indicates that the amount of intermittency decreases with the temporal evolution. Thus, the log-normal model in flamelet methods may perform better in long-term simulations of time-evolving problems, in which turbulence decays. The log-normal-like distribution is consistent with the results from the DNS study with over-resolved grid of Hawkes *et al.* [13] (this further confirms the use of reasonable grids in the present study). As tested, the continuous log-normal-like distribution of χ_{st} is only seen in turbulent combustion, while both 1D steady and 3D unsteady laminar simulations contain only one single value of χ_{st}.

The standard scalar dissipation rate χ is defined based on mixture fraction. At the same time, each species has its own scalar dissipation rate, defined as $\chi_k = 2D_k \nabla Y_k \cdot \nabla Y_k$ for the kth species, where D_k is its mass diffusivity. As in Figure 7.15, normalized PDFs of stoichiometric χ_{CO} and χ_{OH} in the turbulent cases also approximately follow the log-normal distribution, except in the two tails, while laminar cases only contain a few discrete values of stoichiometric χ_{CO} and χ_{OH} (not shown here).

Figure 17 presents the PDF of χ/χ_q, χ_{CO}, and χ_{OH} on the stoichiometric surface. The stoichiometric PDFs of χ and χ_{CO} are similar to that of temperature (Figure 7.3), but are different from that of χ_{OH} (which is more closely normally distributed). The most

likely χ_{st} of local extinction ($20\ t_j$) is 3.5 times larger than χ_q from the flamelet solution, while that of re-ignition ($40\ t_j$) is almost 2 times smaller than χ_q. This result is consistent with the theory that short local time-scales could prevent chemical reactions from releasing enough heat to sustain combustion, and would thus result in extinction [209]. On the other hand, re-ignition ($40\ t_j$) has narrower PDFs than local extinction ($20\ t_j$) for all three scalar dissipation rates, for the same reason as the PDFs of temperature in Figure 7.3.

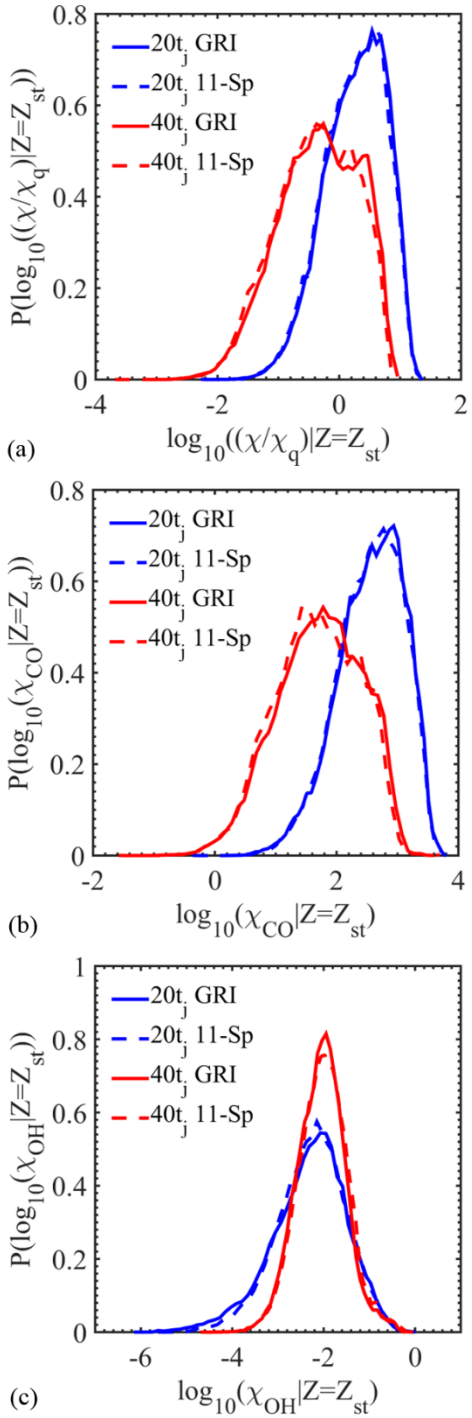

Figure 7.16: PDF of (a) χ/χ_q, (b) χ_{CO}, and (c) χ_{OH} on the stoichiometric surface at 20 t_j (blue) and 40 t_j (red), calculated using GRI-Mech 3.0 (solid lines) and 11-species model (dashed lines).

For the PDFs of all three scalar dissipation rates, the deviations between the two chemical kinetics models are small near the peak values. For both steady and unsteady laminar simulations, the PDFs of all scalar dissipation rates are mono-modal. Unlike 1D steady laminar simulations, however, the 3D unsteady laminar simulations using the two chemical kinetics models have different principal modes of scalar dissipation rates: only ~2% difference for χ, but 5%~6% for χ_{CO}, and 20%~55% for χ_{OH}, due to the unsteady shear layer expansion. The high sensitivity to (species-based) scalar dissipation rates results in large deviations in temperature and species concentrations in 3D unsteady laminar simulations.

7.4.3 Global Pathway Analysis (GPA)

Global Pathway Analysis (GPA) [91, 92] is applied in the present works to understand the 3D turbulent non-premixed syngas/air flame simulated with the two different kinetics models, GRI-Mech 3.0 and 11-species model.

Due to the large number of the temporal-spatial points in the 3D dataset, Global Pathways are firstly identified from the simulation results of auto-ignition in a 0D closed reactor. The reactants are stoichiometric mixture of the fuel and oxidizer used in 3D dataset. The simulation is conducted at 1 atm and initial temperature ranging from 700K to 1300K, using both GRI-Mech 3.0 and 11-species models. The following Global Pathways are identified as the major Global Pathways from H_2 to H_2O.

$$H_2 \rightarrow H \rightarrow OH \rightarrow H_2O \qquad \text{GP-}H_2\text{-1}$$

$$H_2 \rightarrow H \rightarrow HO_2 \rightarrow H_2O_2 \rightarrow OH \rightarrow H_2O \qquad \text{GP-}H_2\text{-2}$$

$$H_2 \rightarrow H \rightarrow HO_2 \rightarrow OH \rightarrow H_2O \qquad \text{GP-}H_2\text{-3}$$

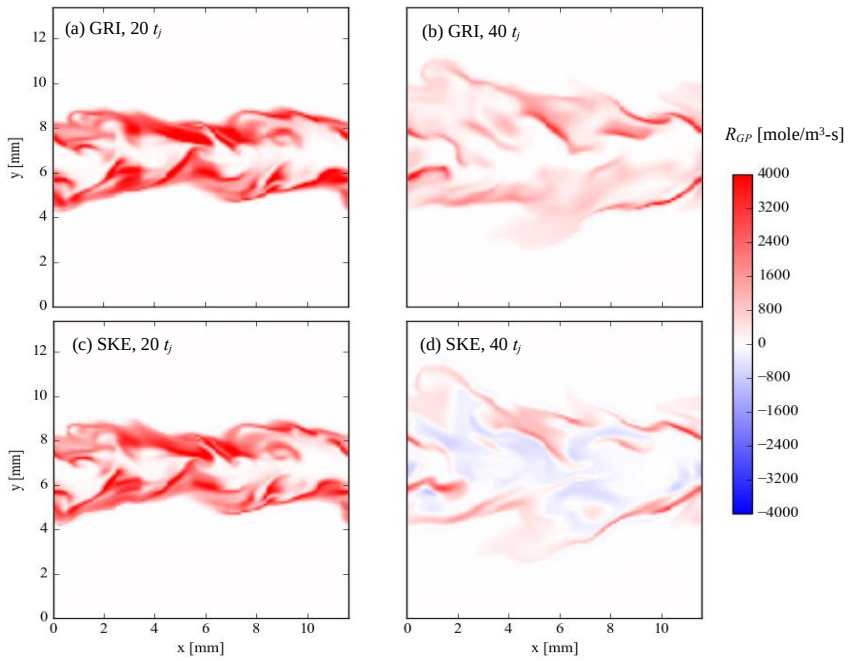

Figure 7.17: Instantaneous 2D contours of net radical production rate, R_{GP}, associated with GP-H_2-1, at 20 t_j (left) and 40 t_j (right) on center plane (Z = 4H): GRI-Mech 3.0 (upper) and 11-species model (=SKE: lower).

GP-H_2-2 is a major Global Pathway for the case of GRI-Mech 3.0, but it is not defined for the case of 11-species model as H_2O_2 is not included in 11-species model. The net radical production, R_{GP}, are illustrated in Figure 7.17 for GP-H_2-1 and Figure 7.18 for GP-H_2-3. At 20 t_j, two kinetics model predict similar R_{GP} for GP-H_2-1, which is producing radicals at this moment, as illustrated by the positive R_{GP} shown in Figure 7.17(a) and (c). However, for GP-H_2-3, two kinetics model shows large deviation. GRI-Mech 3.0 predicts weak radical consumption effect of GP-H_2-3, shown in Figure 7.18(a), but 11-sepcies model predicts the radical consumption effect is dominant, shown in Figure 7.18(c). This indicate that 11-species model predicts more radicals being consumed. This difference becomes more clear as time goes to 40 t_j. GRI-Mech 3.0 predicts that GP-H_2-1 is still producing radicals, shown in Figure 7.17(b), but 11-species model predicts that GP-H_2-1 is consuming radicals for a large region. For GP-H_2-3, GRI-

Mech 3.0 predicts that radicals are produced as well as consumed by this Global Pathway, depending on the local conditions, shown in Figure 7.18(b), but 11-species model predicts that GP-H_2-3 is almost always consuming radicals at this moment, shown in Figure 7.18(d). These observations show that, GRI-Mech 3.0 predicts faster net radical production comparing to 11-species model, and this is true for both moments (20 t_j and 40 t_j), which is consistent with the observation that GRI-Mech 3.0 statistically predicts less local extinction and more re-ignition comparing to 11-species model, shown in Figure 7.5.

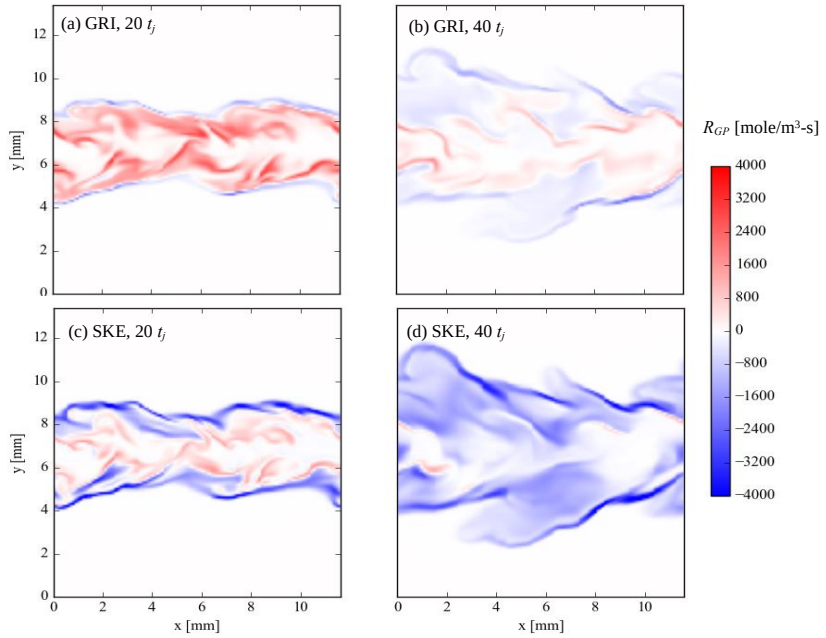

Figure 7.18: Instantaneous 2D contours of net radical production rate, R_{GP}, associated with GP-H_2-3, at 20 t_j (left) and 40 t_j (right) on center plane (Z = 4H): GRI-Mech 3.0 (upper) and 11-species model (=SKE: lower).

In summary, this complex reacting system is analyzed by GPA using several Global Pathways describing the oxidization process from H_2 to H_2O. GPA finds that

GRI-Mech 3.0 predicts more net radical production associated with the major Global Pathways, which explains the observation that GRI-Mech 3.0 predicts less local extinction and more re-ignition.

7.5 Conclusions

To study the sensitivity of predictions to chemical kinetics models, two chemical kinetics models, GRI-Mech 3.0 [93] and an 11-species syngas model [13], are compared in a 3D finite-rate simulation of a temporally evolving turbulent non-premixed syngas flame with extinction and re-ignition.

Local extinction and re-ignition are clearly captured by both chemical kinetics models, with similar qualitative trends. However, significant quantitative deviations are observed, indicating that simulation of turbulent combustion is highly sensitive to the choice of chemical kinetics model. In particular, the temperatures predicted by the 11-species model are consistently lower than those predicted by GRI-Mech 3.0 in stoichiometric PDFs and means (~86 K), conditional statistics (nearly 100 K), and 2D contours. This is due to the presence of fewer radicals-to-products conversions to release heat in the 11-species model. This is also manifested as prediction of more local extinction (mean $T|Z_{st}$ is 49 K smaller) and less re-ignition (mean $T|Z_{st}$ is 42 K smaller). As expected, the mixture-fraction conditioned mean deviations in major species are smaller than those in intermediate and minor species. In the conditional statistics on the major species, the deviations are significant for H_2O, moderate for H_2 and CO_2, and negligible for CO.

Although the two models start with almost identical 1D steady laminar flamelet solutions, the prediction of the 11-species model gradually deviates from that of GRI-Mech 3.0. The deviations in species concentration, temperature, and reaction rates form an interaction cycle to gradually reinforce each other under the effects of unsteadiness and turbulence. This reinforcement can change the dominant factors from the global

reduction of kinetics pathways to the deviations in reaction rate coefficients, causing deviations in directions opposite to those seen in 1D steady laminar solutions. In general, the deviations between the two chemical kinetics models increase sharply from the 1D steady laminar to the 3D unsteady laminar to the 3D turbulent simulations for most quantities, including temperature and major species. Thus, the absolute deviation in turbulent combustion simulations is up to 7 times larger than that in the 1D steady laminar solutions for temperature, up to 12 times larger for CO, up to 13 times larger for H_2, up to 7 times larger for O_2, up to 5 times larger for CO_2, and up to 13 times larger for H_2O. It can be concluded that the effects of unsteadiness and turbulence significantly magnify the sensitivity of turbulent combustion simulation to chemical kinetics. The deviations between the two chemical kinetics models include two major sources: (a) GRI-Mech 3.0 contains 42 more species than the 11-species model, and thus contains 293 more kinetic reactions related to those 42 species; and (b) for those reactions included in both models, their reaction rate coefficients are different. Both (a) and (b) are sensitive to unsteadiness and other turbulence effects, but (b) is the dominant part and is more sensitive to unsteadiness and other turbulence effects. Essentially, (a) means the reaction rates of those globally reduced kinetics pathways, which are linearly removed from the net path fluxes. In contrast, (b) the difference in reaction rate coefficients can grow exponentially.

In the stoichiometric means and conditional statistics of most quantities, the magnification of the deviations between the two chemical kinetics models due to unsteadiness is larger than that due to turbulence. Therefore, the effect of unsteadiness dominates the deviation in mixture fraction space. The two chemical kinetics models provide similar spatial distribution of vorticity magnitude, mixture fraction, and scalar dissipation rates at local extinction, but completely different fields at re-ignition, and these are dominated by the complex turbulence-chemistry interaction.

Both chemical kinetics models show negatively skewed mono-modal log-normal-like distributions for scalar dissipation rates, with small departures on both tails (that is, scalar intermittency). The log-normal distribution, which is used in flamelet methods to model χ_{st}, is not accurate enough at high and low values of χ_{st}, but should have good accuracy for the remaining regions. Interestingly, re-ignition is slightly closer to the log-normal distribution than local extinction, which tends to indicate that the amount of intermittency decreases with temporal evolution, so the log-normal model in flamelet methods might perform better for time-evolving problems with decaying turbulence. Due to the expansion of the unsteady shear layer, the two chemical kinetics models have different principal modes of the scalar dissipation rates. Consequently, the high sensitivity to scalar dissipation rates results in large deviations in temperature and species concentrations between the two models.

CHAPTER 8

CONCLUSIONS

This dissertation established a new framework for 3D DNS/LES of turbulent combustion by combining CoDAC, CoTran, and ODEPIM strategies. ODEPIM is a fast semi-implicit stiff ODE solver, which has accuracy approaching that of an implicit solver, and speed approaching that of an explicit solver. DAC utilizes the PFA method to reduce the kinetic mechanism for each location and time step, which significantly reduces the stiffness of the highly nonlinear kinetics system and greatly accelerates the calculation of the chemical source term. Thermo-chemical zones are introduced such that only one PFA calculation is required for each zone, which diminishes the CPU overhead of CoDAC to the point where it is negligible. CoTran uses a similar correlation technique to reduce the calculation of MAD transport properties, the dominant component of total CPU requirement after application of ODEPIM.

First, the framework was applied to accelerate the simulation of non-equilibrium plasma discharge of $C_2H_4/O_2/Ar$ mixtures in a low-temperature flow reactor. The accuracy and robustness of the new framework are extensively examined by comparing its results with those of previous simulations without the new methods. In particular, temporal evolution and spatial distribution of several key species and gas temperature are compared to verify the new framework. Temporal evolution of active species number shows periodic oscillation following that of gap voltage pulses. For this reason, CoDAC can efficiently reduce the size of ODE. Simulation results indicate that the new framework provides a speed up of 3.16 times in total, including 80 times for kinetics and 836 times for transport. Therefore, the new framework significantly enhances the computational efficiency for simulations of plasma-assisted pyrolysis/oxidation/combustion with detailed plasma-combustion kinetics.

Next, performance and accuracy of the framework was tested on a canonical turbulent premixed flame. Simulation results show that in this test, calculation of the chemical source term is 17 times faster with ODEPIM as compared to DVODE, a pure implicit solver. The kinetics in the cold unburnt side is reduced to zero reaction, which reveals that the DAC provides an optimized local reduction. Overall, in this test, with ODEPIM+CoDAC, the chemical source calculation is 2.7 times faster than ODEPIM, and 46 times faster than DVODE. In this test, calculation of the transport properties is 72 times faster, and the total calculation is 20 times faster than DVODE. In addition, parallel scaling tests show that the new framework has good weak scaling of speed-up and good strong scaling due to the minimization of MPI communication. Verifications of 2D contours, stream-wise spatially averaged flame structure, PDF profiles, and quantified errors illustrate that the new framework provides highly accurate results. In summary, the framework provides a significant speed-up of calculation of both chemistry and transport, which enables DNS with detailed kinetics, while maintaining high accuracy and good parallel scaling performance.

Based on above DNS framework, an efficient novel finite-rate chemistry (FRC)-LES formulation is developed for numerical modeling of turbulent combustion. With this framework, simulations using both FRC-LES and flamelet/progress-variable (FPV)-LES approaches are conducted for a piloted partially premixed methane/air flame, which contains low level of local extinction and re-ignition. A 20-species and 84-reactions methane/air mechanism reduced from detailed GRI-3.0 is employed. In FRC-LES, the techniques of ODEPIM and CoDAC provide a speed up of 8.6 times for chemistry, and 6.4 times for the total computation. The results of both approaches provide good agreement with experimental data. The two models have similar spatial distributions of time-averaged quantities. In terms of the instantaneous flame field, the FPV-LES approach predicts significantly smaller regions with high temperature than the FRC-LES approach, especially in the downstream intense flame region. This is because the FPV-

LES approach predicts less CO level, which becomes the rate controlling step for one of the primary heat release reactions $CO+OH=CO_2+H$. For axial profiles of time-averaged statistics, the FRC-LES approach is more accurate than the FPV-LES approach for both temperature and species, and this better fidelity is even more apparent for minor species. For radial profiles of time-averaged statistics, the two models have very similar predictions for temperature and mixture fraction, which agree reasonably with the experimental data. The deviations in the upstream region are generally smaller than those in the downstream region. For conditional statistics, the FRC-LES approach provides better predictions for both temperature and species. Compared to the FRC-LES approach, the FPV-LES approach predicts lower temperature near the stoichiometric region due to the bottleneck effect of CO, but predicts higher temperature on the fuel rich side where the limiting effect disappears.

To study the sensitivity of predictions to chemical kinetics models, two chemical kinetics models, GRI-Mech 3.0 and an 11-species syngas model, are compared in a 3D finite-rate simulation of a temporally evolving turbulent non-premixed syngas flame with extinction and re-ignition.

Local extinction and re-ignition are clearly captured by both chemical kinetics models with similar qualitative trends. However, significant quantitative deviations are observed, indicating that simulation of turbulent combustion is highly sensitive to the choice of chemical kinetics model. In particular, the temperatures predicted by the 11-species model are consistently lower than those predicted by GRI-Mech 3.0 in stoichiometric PDFs and means (~86 K), conditional statistics (nearly 100 K), and 2D contours. This is due to the presence of fewer radicals-to-products conversions to release heat in the 11-species model. This also manifests in the prediction of more local extinction (mean $T|Z_{st}$ is 49 K smaller) and less re-ignition (mean $T|Z_{st}$ is 42 K smaller). As expected, the mixture-fraction conditioned mean deviations in major species are smaller than those in intermediate and minor species. In the conditional statistics on the

major species, the deviations are significant for H_2O, moderate for H_2 and CO_2, and negligible for CO.

Although the two models start with almost identical 1D steady laminar flamelet solutions, the prediction of the 11-species model gradually deviates from that of GRI-Mech 3.0. The deviations in species concentration, temperature, and reaction rates form an interaction cycle to gradually reinforce each other under the effects of unsteadiness and turbulence. This reinforcement can change the dominant factors from the global reduction of kinetics pathways to the deviations in reaction rate coefficients, causing deviations in directions opposite to those seen in 1D steady laminar solutions. In general, the discrepancies between the two chemical kinetics models increase sharply from the 1D steady laminar to the 3D unsteady laminar to the 3D turbulent simulations for most quantities, including temperature and major species. Thus, the absolute deviation in turbulent combustion simulations is up to 7 times larger than that in the 1D steady laminar solutions for temperature, up to 12 times larger for CO, up to 13 times larger for H_2, up to 7 times larger for O_2, up to 5 times larger for CO_2, and up to 13 times larger for H_2O. We conclude that the effects of unsteadiness and turbulence significantly amplify the sensitivity of turbulent combustion simulation to chemical kinetics.

The deviations between the two chemical kinetics models include two major sources: (a) GRI-Mech 3.0 contains 42 more species than the 11-species model, and thus contains 293 more kinetic reactions related to those 42 species; and (b) for those reactions included in both models, the reaction rate coefficients are different. Both (a) and (b) are sensitive to unsteadiness and other turbulence effects, with (b) being the dominant part and is more susceptible to unsteadiness and other turbulence effects. Essentially, (a) means the reaction rates of those globally reduced kinetics pathways, which are linearly removed from the net path fluxes. In contrast, (b) the difference in reaction rate coefficients can grow exponentially.

In the stoichiometric means and conditional statistics of most quantities, the amplification of the deviations between the two chemical kinetics models due to unsteadiness is larger than that due to turbulence. Therefore, the effect of unsteadiness dominates the deviations in mixture fraction space. The two chemical kinetics models provide similar spatial distribution of vorticity magnitude, mixture fraction, and scalar dissipation rates at local extinction, but completely different fields during re-ignition, which are dominated by the complex turbulence-chemistry interaction.

CHAPTER 9

FUTURE RECOMMENDATION

9.1 More Efficient Approaches to Simulate Finite Rate Chemistry

The numerical framework developed in this dissertation, employing ODEPIM, CoDAC, and CoTran, has been proved both accurate and highly efficient for the simulations of turbulent combustion with detailed finite rate chemistry.

However, even with this framework, the finite rate simulations are still very expensive and are much slower than the corresponding simulations using FGM models. Therefore, based on the present framework, some further improvements are still needed for computational efficiency. Based on the results of the present study, the following are some recommendations for future work.

First, although ODEPIM adopted in this dissertation is an efficient iteration based (semi-)implicit stiff ODE solvers for chemical kinetics, the non-iteration based stiff ODE solver, such as analytic Jacobian solver [210, 211], could be more efficient than ODEPIM for many cases. In analytic Jacobian solver, the stiff ODE system is linearized to Jacobian matrices, and their analytic inversions are obtained and stored at the beginning of the simulation. Then only inverse matrices evaluation and matrix multiplication are required in all following time steps, and iteration operations become unnecessary. Analytic Jacobian solver requires fixed-size Jacobian matrices, but the CoDAC method dynamically varies the sizes of the Jacobian matrices in both space and time. This is why Analytic Jacobian solver has not been coupled with CoDAC method yet. One possible solution is to generate analytic inversions on the fly instead of pre-processing. This could introduce significant computational overhead to calculate the analytic inversions, but a space-time correlation method similar to CoDAC and CoTran could possibly reduce this overhead to small enough.

Second, the performance of CoDAC on HPC has loading balance issue. Generally, the classical domain decomposition distributes approximately equal number of grid points to each CPU core. However, when CoDAC is employed, some CPU cores have to solve relatively detailed chemical kinetics, while some others only need to solve relatively simplified chemical kinetics. Therefore, the workload of different CPU cores become very different, and many CPU cores waste a lot of time to wait for others. This issue is not very severe for DNS of canonical configurations, in which the orientations of the flames are well-know in advance. The user could decide to use Cartesian decomposition or pencil decomposition based on the orientations, and then the loading is roughly balanced again. However, for LES of complicated configurations, the orientations of the flames are complicated and vary dynamically. Therefore, the prescribed domain decomposition cannot solve the loading balance issue. This is a very challenging issue, and there is no obvious solution so far. Similar loading balance issue happens with adaptive mesh refinement (AMR) techniques and many new techniques to tackle the issue have been proposed during the past few years. Those techniques could be extended to CoDAC, and CoDAC could directly couple with AMR for better accuracy.

Third, CoTran could be generalized to efficiently evaluate both thermodynamics and transport properties of real fluids for supercritical mixing and combustion, with modified correlation criteria [212]. In addition, for transcritical and supercritical conditions, real fluid equations of state become necessary, and the key is to evaluate the compressibility factor Z=PV/(RT) via solving a cubic equation iteratively, which is also expensive. The time-space correlation idea could also be possibly applied to the evaluation of compressibility factor [212].

9.2 Future Development of FRC and FGM Models

The key for future development of FRC and FGM models is to find better balance between accuracy and efficiency. There are three major categories of attempts to improve

FRC and FGM models. The first category is improving the efficiency of FRC models. The second category is improving the accuracy and generality of FGM models. The third category is developing hybrid FRC/FGM models.

The first category has been discussed in details in Section 9.1. Although CoDAC effectively reduces the calculation of chemical source terms, the number of transport equations is still too large. As shown in Chapter 6, even the frozen FRC-LES without chemical source term is much slower than FGM-LES. For this reason, the next target is to reduce the number of transport equations. The simplest idea is to employ a small globally reduced chemical kinetics mechanism. However, to guarantee accuracy, even relatively small hydrocarbons require a reduced mechanism of ~40 species, which is still too large. Therefore, the first category alone cannot well handle this difficulty.

For the second category, normally each FGM model is designed and optimized for one single combustion regime. For this reason, how to handle the complicated multi-regime problems using FGM models become challenging. The conventional way is to determine which regime dominates this problem, and then select the corresponding FGM model. Obviously, this way sacrifices the accuracy for other regimes, and in many cases, there is no single dominant regime. To tackle this issue, one solution is to dynamically assign different FGM sub-models based on some regime indicators [33, 213]. However, the treatment of the boundary between different FGM sub-models is tricky, and some *ad hoc* "corrections" are needed. A better way is to develop a more general FGM formulation to cover all combustion regimes [214], which could be reduced to the corresponding FGM model for each regime.

Most formulations to generate FGM tables are steady state equations. For this reason, although the conservative scalars and progress-variables are transported unsteadily, the FGM tables themselves are still in steady state, and have difficulty to capture the unsteady evolution history of turbulent flames, as shown in Chapter 6. There are some attempts of unsteady FGM formulation [215], but they are analytically

challenging, and have difficulty for multi-regimes generalization. In the future, more theoretical and analytical efforts are required for the development of unsteady FGM models.

To capture more physics in more complicated configurations, high dimensional FGM models are proposed. For example, multiple injectors are very common in engine combustors, which often provide different definitions of mixture fraction. To cover all these injectors, multiple conservative scalars are included as FGM look-up table parameters [216], which enlarge the dimension of the table. However, high dimensional tables require larger computer memory and more pre-processing time. In addition, the higher-dimension table results in more complicated data retrieval process and coarser table grid, which could introduce higher interpolation errors. To resolve this difficulty, one idea is to solve the FGM formulations dynamically instead of pre-processing to build look-up tables, but this will result in a primitive version LEM model and large computational overhead. Again, time-space correlation idea could be employed here to reduce this overhead.

The third category contains two major ideas. The first idea is still to dynamically assign FGM or FRC sub-models based on some regime indicators [33, 213]. However, the treatment of the boundary between FGM and FRC sub-models is even more challenging than that between two FGM sub-models, and thus more *ad hoc* "corrections" are needed. More importantly, this idea creates great loading balance issue: the CPU cores assigned with FGM models need to wait for those assigned with FRC models, thus the net computational time is not much reduced from pure FRC models due to this bottleneck effect. A better idea without loading balance issue is the hybrid transported-tabulation strategy to downsize the number of species transport equations, proposed by Ribert *et al.* [217]. In this strategy, the detailed chemical kinetics mechanism is retained, but only species with non-zero concentration outside the flame layers are transported with the flow. Intermediate chemical species within the flame layers are expressed resorting to

their self-similar properties observed in a series of FGM formulations, and projected into an optimized progress variable defined from all transported species. Based on above discussion, the coupling between CoDAC and hybrid transported-tabulated strategy is a promising option for future attempts.

9.3 Better Selection and Global Reduction of Chemical Kinetics

Based on Chapter 7, deviations from reaction rate coefficients are much more sensitive to unsteadiness than global reduction; therefore, it is relatively safer to conduct global reduction. In contrast, it is very risky to modify the reaction rate coefficients, especially the activation energy. For most cases, even after the magnification of deviations due to unsteadiness, the deviations from global reduction are still small (e.g. within ~2%).

Chapter 7 also shows that the conventional 0D/1D steady laminar validation and verification procedure is not enough for both selection and global reduction of chemical kinetics mechanisms. Therefore, unsteady/turbulent CFD simulations should participate into the validation and verification procedures. To accelerate the validation/verification process, the new framework with ODEPIM, CoDAC, and CoTran should be employed in the unsteady/turbulent CFD simulations. However, this also create higher requirement for experimental measurement, because temporal evolution data instead of time-averaged data become necessary for model validation.

REFERENCES

[1] H. Pitsch, Large-eddy simulation of turbulent combustion, Annu. Rev. Fluid Mech. 38 (2006) 453-482.

[2] C. Bruno, V. Sankaran, H. Kolla, J.H. Chen, Impact of multi-component diffusion in turbulent combustion using direct numerical simulations, Combust. Flame 162 (11) (2015) 4313–4330.

[3] B. Yenerdag, N. Fukushima, M. Shimura, M. Tanahashi, T. Miyauchi, Turbulence–flame interaction and fractal characteristics of H 2–air premixed flame under pressure rising condition, Proc. Combust. Inst. 35 (2) (2015) 1277-1285.

[4] A. Aspden, M. Day, J. Bell, Lewis number effects in distributed flames, Proc. Combust. Inst. 33 (1) (2011) 1473-1480.

[5] Z. Nikolaou, N. Swaminathan, Direct Numerical Simulation of Complex Fuel Combustion with Detailed Chemistry: Physical Insight and Mean Reaction Rate Modeling, Combust. Sci. Technol. 187 (11) (2015) 1759-1789.

[6] A. Aspden, M. Day, J. Bell, Three-dimensional direct numerical simulation of turbulent lean premixed methane combustion with detailed kinetics, Combust. Flame 166 (2016) 266-283.

[7] M. Sheikhi, T. Drozda, P. Givi, F. Jaberi, S. Pope, Large eddy simulation of a turbulent nonpremixed piloted methane jet flame (Sandia Flame D), Proc. Combust. Inst. 30 (1) (2005) 549-556.

[8] M. Ihme, H. Pitsch, Prediction of extinction and reignition in nonpremixed turbulent flames using a flamelet/progress variable model: 2. Application in LES of Sandia flames D and E, Combust. Flame 155 (1) (2008) 90-107.

[9] Y.C. See, M. Ihme, Effects of finite-rate chemistry and detailed transport on the instability of jet diffusion flames, J. Fluid Mech. 745 (2014) 647-681.

[10] X. Wang, V. Yang, Supercritical Mixing and Combustion of Liquid-Oxygen/Kerosene Bi-Swirl Injectors, J. Propul. Power 33 (2) (2017) 316-322.

[11] C. Pantano, Direct simulation of non-premixed flame extinction in a methane–air jet with reduced chemistry, J. Fluid Mech. 514 (2004) 231-270.

[12] E.R. Hawkes, R. Sankaran, J.C. Sutherland, J.H. Chen, Direct numerical simulation of turbulent combustion: fundamental insights towards predictive models, Journal of Physics: Conference Series (2005), 16.

[13] E.R. Hawkes, R. Sankaran, J.C. Sutherland, J.H. Chen, Scalar mixing in direct numerical simulations of temporally evolving plane jet flames with skeletal CO/H 2 kinetics, Proc. Combust. Inst. 31 (1) (2007) 1633-1640.

[14] B.A. Sen, E.R. Hawkes, S. Menon, Large eddy simulation of extinction and reignition with artificial neural networks based chemical kinetics, Combust. Flame 157 (3) (2010) 566-578.

[15] D.O. Lignell, J.H. Chen, H.A. Schmutz, Effects of Damköhler number on flame extinction and reignition in turbulent non-premixed flames using DNS, Combust. Flame 158 (5) (2011) 949-963.

[16] Y. Yang, H. Wang, S.B. Pope, J.H. Chen, Large-eddy simulation/probability density function modeling of a non-premixed CO/H 2 temporally evolving jet flame, Proc. Combust. Inst. 34 (1) (2013) 1241-1249.

[17] R.W. Bilger, S.B. Pope, K.N.C. Bray, J.F. Driscoll, Paradigms in turbulent combustion research, Proc. Combust. Inst. 30 (1) (2005) 21-42.

[18] Y. Ju, J.K. Lefkowitz, C.B. Reuter, S.H. Won, X. Yang, S. Yang, W. Sun, Z. Jiang, Q. Chen, Plasma Assisted Low Temperature Combustion, Plasma Chem. Plasma Process. 36 (1) (2016) 85–105.

[19] A. Rousso, S. Yang, J. Lefkowitz, W. Sun, Y. Ju, Low Temperature Oxidation and Pyrolysis of n-Heptane in Nanosecond-pulsed Plasma Discharges, Proc. Combust. Inst. 36 (3) (2017) 4105–4112.

[20] H. Wang, K. Luo, J. Fan, Direct numerical simulation and conditional statistics of hydrogen/air turbulent premixed flames, Energy & Fuels 27 (1) (2012) 549-560.

[21] A. Gruber, J.H. Chen, D. Valiev, C.K. Law, Direct numerical simulation of premixed flame boundary layer flashback in turbulent channel flow, J. Fluid Mech. 709 (2012) 516-542.

[22] A.B. Bendtsen, P. Glarborg, K. Dam-Johansen, Visualization methods in analysis of detailed chemical kinetics modelling, Computers & Chemistry 25 (2) (2001) 161-170.

[23] T. Lu, C.K. Law, A directed relation graph method for mechanism reduction, Proc. Combust. Inst. 30 (1) (2005) 1333-1341.

[24] P. Pepiot-Desjardins, H. Pitsch, An efficient error-propagation-based reduction method for large chemical kinetic mechanisms, Combust. Flame 154 (1-2) (2008) 67-81.

[25] W. Sun, Z. Chen, X. Gou, Y. Ju, A path flux analysis method for the reduction of detailed chemical kinetic mechanisms, Combust. Flame 157 (7) (2010) 1298-1307.

[26] X. Gao, S. Yang, W. Sun, A global pathway selection algorithm for the reduction of detailed chemical kinetic mechanisms, Combust. Flame 167 (2016) 238-247.

[27] L. Liang, J.G. Stevens, J.T. Farrell, A dynamic adaptive chemistry scheme for reactive flow computations, Proc. Combust. Inst. 32 (1) (2009) 527-534.

[28] X. Gou, Z. Chen, W. Sun, Y. Ju, A dynamic adaptive chemistry scheme with error control for combustion modeling with a large detailed mechanism, Combust. Flame 160 (2) (2013) 225-231.

[29] H. Yang, Z. Ren, T. Lu, G.M. Goldin, Dynamic adaptive chemistry for turbulent flame simulations, Combustion Theory and Modelling 17 (1) (2013) 167-183.

[30] Y. Shi, L. Liang, H.-W. Ge, R.D. Reitz, Acceleration of the chemistry solver for modeling DI engine combustion using dynamic adaptive chemistry (DAC) schemes, Combustion Theory and Modelling 14 (1) (2010) 69-89.

[31] Z. Lu, L. Zhou, Z. Ren, T. Lu, C.K. Law, Effects of Spray and Turbulence Modelling on the Mixing and Combustion Characteristics of an n-heptane Spray Flame Simulated with Dynamic Adaptive Chemistry, Flow, Turbulence and Combustion 97 (2) (2016) 609–629.

[32] Y. Liang, S.B. Pope, P. Pepiot, A pre-partitioned adaptive chemistry methodology for the efficient implementation of combustion chemistry in particle PDF methods, Combust. Flame 162 (2015) 3236-3253.

[33] H. Wu, Y.C. See, Q. Wang, M. Ihme, A Pareto-efficient combustion framework with submodel assignment for predicting complex flame configurations, Combust. Flame 162 (11) (2015) 4208-4230.

[34] W. Sun, H.A. El-Asrag, Y. Ju, Correlated Dynamic Adaptive Chemistry and Multi-timescale Modeling of Ignition and Combustion of a n-Heptane/Air Mixture, 52nd AIAA Aerospace Sciences Meeting, National Harbor, Maryland, 2014, AIAA 2014-0821.

[35] W. Sun, X. Gou, H.A. El-Asrag, Z. Chen, Y. Ju, Multi-timescale and correlated dynamic adaptive chemistry modeling of ignition and flame propagation using a real jet fuel surrogate model, Combust. Flame 162 (4) (2015) 1530-1539.

[36] W. Sun, Y. Ju, Multi-timescale and Correlated Dynamic Adaptive Chemistry and Transport Modeling of Flames in n-Heptane/Air Mixtures, 53rd AIAA Aerospace Sciences Meeting (Jan. 2015), AIAA Paper 2015-1382.

[37] P. Brown, G. Byrne, A. Hindmarsh, VODE: A variable-coefficient ODE solver, SIAM J. Sci. Comput. 10 (8) (1989) 1038-1051.

[38] S.H. Lam, Model reductions with special CSP data, Combust. Flame 160 (12) (2013) 2707-2711.

[39] S.H. Lam, Using CSP to Understand Complex Chemical Kinetics, Combust. Sci. Technol. 89 (5-6) (1993) 375-404.

[40] U. Maas, S.B. Pope, Simplifying chemical kinetics: Intrinsic low-dimensional manifolds in composition space, Combust. Flame 88 (3-4) (1992) 239-264.

[41] T. Lu, C.K. Law, C.S. Yoo, J.H. Chen, Dynamic stiffness removal for direct numerical simulations, Combust. Flame 156 (8) (2009) 1542-1551.

[42] X. Gou, W. Sun, Z. Chen, Y. Ju, A dynamic multi-timescale method for combustion modeling with detailed and reduced chemical kinetic mechanisms, Combust. Flame 157 (6) (2010) 1111-1121.

[43] T.R. Bussing, E.M. Murman, Finite-volume method for the calculation of compressible chemically reacting flows, AIAA J. 26 (9) (1988) 1070-1078.

[44] V.R. Katta, W.M. Roquemore, Calculation of multidimensional flames using large chemical kinetics, AIAA J. 46 (7) (2008) 1640-1650.

[45] A. Potturi, J.R. Edwards, Investigation of Subgrid Closure Models for Finite-Rate Scramjet Combustion, 51st AIAA Aerospace Sciences Meeting (Jan. 2013), AIAA Paper 2013-2461.

[46] E. Gonzalez, A. Dasgupta, S. Arshad, M. Oevermann, Effect of the turbulence modeling in large-eddy simulations of nonpremixed flames undergoing extinction and reignition, 55th AIAA Aerospace Sciences Meeting (Jan. 2017), AIAA Paper 2017-0604.

[47] G. Goldin, Evaluation of LES subgrid reaction models in a lifted flame, 43rd AIAA Aerospace Sciences Meeting and Exhibit, 2005, 555.

[48] D.A. Lysenko, I.S. Ertesvåg, K.E. Rian, Numerical simulations of the sandia flame d using the eddy dissipation concept, Flow, turbulence and combustion 93 (4) (2014) 665-687.

[49] O.A. Marzouk, E.D. Huckaby, A comparative study of eight finite-rate chemistry kinetics for CO/H2 combustion, Engineering applications of computational fluid mechanics 4 (3) (2010) 331-356.

[50] S. Menon, A.R. Kerstein, in: Turbulent Combustion Modeling, Springer, Netherlands, 2011, p. 221-247.

[51] S.B. Pope, PDF methods for turbulent reactive flows, Prog. Energy Combust. Sci. 11 (2) (1985) 119-192.

[52] J.-P. Legier, T. Poinsot, D. Veynante, Dynamically thickened flame LES model for premixed and non-premixed turbulent combustion, Proceedings of the Summer Program, Stanford, CA, 2000, Center for Turbulence Research: 157-168.

[53] N. Peters, Laminar diffusion flamelet models in non-premixed turbulent combustion, Prog. Energy Combust. Sci. 10 (3) (1984) 319-339.

[54] H. Pitsch, H. Steiner, Large-eddy simulation of a turbulent piloted methane/air diffusion flame (Sandia flame D), Physics of Fluids (1994-present) 12 (10) (2000) 2541-2554.

[55] H. Pitsch, H. Steiner, Scalar mixing and dissipation rate in large-eddy simulations of non-premixed turbulent combustion, Proc. Combust. Inst. 28 (1) (2000) 41-49.

[56] C.D. Pierce, P. Moin, Progress-variable approach for large-eddy simulation of non-premixed turbulent combustion, J. Fluid Mech. 504 (2004) 73-97.

[57] X. Gao, J. Zhai, W. Sun, T. Ombrello, C. Carter, The Effect of Ozone Addition on Autoignition and Flame Stabilization, 54th AIAA Aerospace Sciences Meeting (Jan. 2016), AIAA Paper 2016-0960.

[58] X. Gao, W. Sun, T. Ombrello, C. Carter, The Effect of Ozonolysis Activated Autoignition on Jet Flame Dynamics, 55th AIAA Aerospace Sciences Meeting (Jan. 2017), AIAA Paper 2017-1776.

[59] S. Yang, X. Gao, W. Sun, The effects of ozonolysis activated autoignition on non-premixed jet flame dynamics: a numerical and experimental study, 53rd AIAA/SAE/ASEE Joint Propulsion Conference (Jul. 2017).

[60] H. Huo, V. Yang, Large-Eddy Simulation of Supercritical Combustion: Model Validation against Gaseous H2-O2 Injector, Journal of Propulsion and Power (submitted) (2016).

[61] S.-Y. Hsieh, V. Yang, A preconditioned flux-differencing scheme for chemically reacting flows at all Mach numbers, International Journal of Computational Fluid Dynamics 8 (1) (1997) 31-49.

[62] H. Meng, V. Yang, A unified treatment of general fluid thermodynamics and its application to a preconditioning scheme, J. Comput. Phys. 189 (1) (2003) 277-304.

[63] N. Zong, V. Yang, An efficient preconditioning scheme for real-fluid mixtures using primitive pressure–temperature variables, International Journal of Computational Fluid Dynamics 21 (5-6) (2007) 217-230.

[64] X. Wang, H. Huo, Y. Wang, L. Zhang, V. Yang, A Three-Dimensional Analysis of Swirl Injector Flow Dynamics at Supercritical Conditions, 53rd AIAA Aerospace Sciences Meeting (Jan. 2015), AIAA Paper 2015-1827.

[65] X. Wang, V. Yang, Supercritical Mixing Characteristics of Liquid Oxygen (LOX)/Kerosene Bi-Swirl Injectors, 54th AIAA Aerospace Sciences Meeting (Jan. 2016), AIAA Paper 2016-1933.

[66] Y. Li, X. Wang, L. Zhang, S.-T. Yeh, V. Yang, Flow Dynamics of Gaseous Oxygen/Kerosene Jet-Swirl Injectors at Supercritical Conditions, 55th AIAA Aerospace Sciences Meeting (Jan. 2017), AIAA Paper 2017-1107.

[67] S. Lam, D. Goussis, Understanding complex chemical kinetics with computational singular perturbation, Symposium (International) on Combustion, 1989, Elsevier: 931-941.

[68] S. Lam, D. Goussis, The CSP method for simplifying kinetics, International Journal of Chemical Kinetics 26 (4) (1994) 461-486.

[69] T. Lu, Y. Ju, C.K. Law, Complex CSP for chemistry reduction and analysis, Combustion and Flame 126 (1) (2001) 1445-1455.

[70] M. Valorani, F. Creta, D.A. Goussis, J.C. Lee, H.N. Najm, An automatic procedure for the simplification of chemical kinetic mechanisms based on CSP, Combustion and Flame 146 (1) (2006) 29-51.

[71] M. Valorani, H.N. Najm, D.A. Goussis, CSP analysis of a transient flame-vortex interaction: time scales and manifolds, Combustion and Flame 134 (1) (2003) 35-53.

[72] D.A. Goussis, H.N. Najm, Model reduction and physical understanding of slowly oscillating processes: the circadian cycle, Multiscale Modeling & Simulation 5 (4) (2006) 1297-1332.

[73] U. Maas, S.B. Pope, Simplifying chemical kinetics: intrinsic low-dimensional manifolds in composition space, Combustion and flame 88 (3) (1992) 239-264.

[74] U. Maas, Efficient calculation of intrinsic low-dimensional manifolds for the simplification of chemical kinetics, Computing and Visualization in Science 1 (2) (1998) 69-81.

[75] V. Bykov, U. Maas, The extension of the ILDM concept to reaction–diffusion manifolds, Combustion Theory and Modelling 11 (6) (2007) 839-862.

[76] V. Bykov, U. Maas, Problem adapted reduced models based on Reaction–Diffusion Manifolds (REDIMs), Proceedings of the Combustion Institute 32 (1) (2009) 561-568.

[77] T. Lu, C.S. Yoo, J. Chen, C.K. Law, Three-dimensional direct numerical simulation of a turbulent lifted hydrogen jet flame in heated coflow: a chemical explosive mode analysis, Journal of Fluid Mechanics 652 (2010) 45-64.

[78] Z. Luo, C.S. Yoo, E.S. Richardson, J.H. Chen, C.K. Law, T. Lu, Chemical explosive mode analysis for a turbulent lifted ethylene jet flame in highly-heated coflow, Combustion and Flame 159 (1) (2012) 265-274.

[79] R. Shan, C.S. Yoo, J.H. Chen, T. Lu, Computational diagnostics for n-heptane flames with chemical explosive mode analysis, Combustion and Flame 159 (10) (2012) 3119-3127.

[80] S. Yang, X. Wang, V. Yang, W. Sun, H. Huo, Comparison of Flamelet/Progress-Variable and Finite-Rate Chemistry LES Models in a Preconditioning Scheme, 55th AIAA Aerospace Sciences Meeting (Jan. 2017), AIAA Paper 2017-0605.

[81] X. Gao, J. Zhai, W. Sun, T. Ombrello, C. Carter, The Effect of Ozone Addition on Autoignition and Flame Stabilization, 54th AIAA Aerospace Sciences Meeting, 2016, 0960.

[82] X. Gao, W. Sun, T. Ombrello, C. Carter, The Effect of Ozonolysis Activated Autoignition on Jet Flame Dynamics, 55th AIAA Aerospace Sciences Meeting, Gaylord Texan, Grapevine, Texas, 2017.

[83] S. Yang, X. Gao, W. Sun, Effects of Ozonolysis Activated Autoignition on the Dynamics of Turbulent Non-Premixed Flame: A DNS Study, 53rd AIAA/SAE/ASEE Joint Propulsion Conference, Atlanta, Georgia, 2017.

[84] S.H. Won, S. Dooley, F.L. Dryer, Y. Ju, A radical index for the determination of the chemical kinetic contribution to diffusion flame extinction of large hydrocarbon fuels, Combustion and Flame 159 (2) (2012) 541-551.

[85] T. Turányi, Sensitivity analysis of complex kinetic systems. Tools and applications, Journal of Mathematical Chemistry 5 (3) (1990) 203-248.

[86] S. Yang, V. Yang, W. Sun, S. Nagaraja, W. Sun, Y. Ju, X. Gou, Parallel On-the-fly Adaptive Kinetics for Non-equilibrium Plasma Discharges of C2H4/O2/Ar Mixture, 54th AIAA Aerospace Sciences Meeting (Jan. 2016), AIAA Paper 2016-0195.

[87] S. Yang, R. Ranjan, V. Yang, S. Menon, W. Sun, Parallel On-the-fly Adaptive Kinetics in Direct Numerical Simulation of Turbulent Premixed Flame, Proc. Combust. Inst. 36 (2) (2017) 2025–2032.

[88] S. Yang, R. Ranjan, V. Yang, W. Sun, S. Menon, Sensitivity of predictions to chemical kinetics models in a temporally evolving turbulent non-premixed flame, Combustion and Flame (accepted) (2017).

[89] S. Coogan, X. Gao, A. McClung, W. Sun, Evaluation of Kinetic Mechanisms for Direct Fired Supercritical Oxy-Combustion of Natural Gas, ASME Turbo Expo 2016: Turbomachinery Technical Conference and Exposition, 2016, American Society of Mechanical Engineers: V04AT04A037-V04AT04A037.

[90] X. Gao, W. Sun, Global Pathway Analysis of the Autoignition and Extinction of Aromatic/Alkane mixture, 53rd AIAA/SAE/ASEE Joint Propulsion Conference, Atlanta, Georgia, 2017.

[91] X. Gao, S. Yang, W. Sun, Global Pathway Analysis of the Extinction and Re‐ignition of a Turbulent Non‐Premixed Flame, 53rd AIAA/SAE/ASEE Joint Propulsion Conference (Jul. 2017).

[92] X. Gao, S. Yang, W. Sun, Using Global Pathway to Understand Chemical Kinetics, 6th International Workshop on Model Reduction in Reacting Flow (Jul. 2017).

[93] G.P. Smith, D.M. Golden, M. Frenklach, N.W. Moriarty, B. Eiteneer, M. Goldenberg, C.T. Bowman, R.K. Hanson, S. Song, W.C. Gardiner Jr., V.V. Lissianski, Z. Qin http://www.me.berkeley.edu/gri_mech/

[94] L. Monchick, E. Mason, Transport properties of polar gases, The Journal of Chemical Physics 35 (5) (1961) 1676-1697.

[95] R.J. Kee, G. Dixon-Lewis, J. Warnatz, M.E. Coltrin, J.A. Miller, H.K. Moffat, Transport: a software package for the evaluation of gas-phase, multicomponent transport properties, Chemkin Collection, 1999.

[96] C.R. Wilke, A viscosity equation for gas mixtures, J. Chem. Phys. 18 (4) (1950) 517-519.

[97] S. Mathur, P. Tondon, S. Saxena, Thermal conductivity of binary, ternary and quaternary mixtures of rare gases, Mol. Phys. 12 (6) (1967) 569-579.

[98] U. Piomelli, Large-eddy simulation: achievements and challenges, Progress in Aerospace Sciences 35 (4) (1999) 335-362.

[99] P. Sagaut, Large eddy simulation for incompressible flows : an introduction, Springer, Berlin ; New York, 2001.

[100] P. Moin, K. Mahesh, Direct numerical simulation: a tool in turbulence research, Annual review of fluid mechanics 30 (1) (1998) 539-578.

[101] L. Vervisch, T. Poinsot, Direct numerical simulation of non-premixed turbulent flames, Annual review of fluid mechanics 30 (1) (1998) 655-691.

[102] W.-W. Kim, S. Menon, H.C. Mongia, Large-eddy simulation of a gas turbine combustor flow, Combust. Sci. Technol. 143 (1-6) (1999) 25-62.

[103] W.-W. Kim, S. Menon, Numerical modeling of turbulent premixed flames in the thin-reaction-zones regime, Combust. Sci. Technol. 160 (1) (2000) 119-150.

[104] V. Sankaran, S. Menon, Subgrid combustion modeling of 3-D premixed flames in the thin-reaction-zone regime, Proc. Combust. Inst. 30 (1) (2005) 575-582.

[105] V. Sankaran, S. Menon, LES of scalar mixing in supersonic mixing layers, Proc. Combust. Inst. 30 (2) (2005) 2835-2842.

[106] R.W. MacCormack, The effect of viscosity in hypervelocity impact cratering, J. Spacecraft Rockets 40 (5) (2003) 757-763.

[107] J. Kim, P. Moin, Application of a fractional-step method to incompressible Navier-Stokes equations, J. Comput. Phys. 59 (2) (1985) 308-323.

[108] S. Yang, A. Kurganov, Y. Liu, Well-Balanced Central Schemes on Overlapping Cells with Constant Subtraction Techniques for the Saint-Venant Shallow Water System, J. Sci. Comput. 63 (3) (2015) 678-698.

[109] E.P.N. Duque, B.J. Whitlock, S.M. Legensky, C.P. Stone, R. Ranjan, S. Menon, The Impact of In Situ Data Processing and Analytics upon Weak Scaling of CFD Solvers and Workflows, 27th International Conference on Parallel Computational Fluid Dynamics (2015).

[110] S.B. Pope, Turbulent flows, Cambridge University Press, Cambridge ; New York, 2000.

[111] D.R. Chapman, Computational aerodynamics development and outlook, AIAA J. 17 (12) (1979) 1293-1313.

[112] W. Cabot, Large-eddy simulations with wall models, 1995.

[113] E. Balaras, C. Benocci, U. Piomelli, Two-layer approximate boundary conditions for large-eddy simulations, AIAA J. 34 (6) (1996) 1111-1119.

[114] P.R. Spalart, Detached-eddy simulation, Annual review of fluid mechanics 41 (2009) 181-202.

[115] A. Leonard, Energy cascade in large-eddy simulations of turbulent fluid flows, Advances in geophysics 18 (1975) 237-248.

[116] S. Ghosal, P. Moin, The basic equations for the large eddy simulation of turbulent flows in complex geometry, J. Comput. Phys. 118 (1) (1995) 24-37.

[117] H. van der Ven, A family of large eddy simulation (LES) filters with nonuniform filter widths, Phys. Fluids 7 (5) (1995) 1171-1172.

[118] C. Le Ribault, S. Sarkar, S. Stanley, Large eddy simulation of a plane jet, Phys. Fluids 11 (10) (1999) 3069-3083.

[119] P. Moin, Progress in large eddy simulation of turbulent flows, 35th Aerospace Sciences Meeting and Exhibit, 1997, 749.

[120] A. Favre, Statistical equations of turbulent gases (Statistical equations for compressible gas, discussing turbulent quantities separated into fluctuating and macroscopic parts), (1969).

[121] U. Unnikrishnan, X. Wang, S. Yang, V. Yang, Subgrid Scale Modeling of the Equation of State for Turbulent Flows under Supercritical Conditions, 53rd AIAA/SAE/ASEE Joint Propulsion Conference (Jul. 2017).

[122] J. Smagorinsky, General Circulation Experiments with the Primitive Equations. I-the Basic Experiment. , Monthly Weather Review 91 (1963) 99-164.

[123] D.K. Lilly, The representation of small scale turbulence in numerical simulation experiments, (1967).

[124] G. Erlebacher, M. Hussaini, C. Speziale, T.A. Zang, Toward the large-eddy simulation of compressible turbulent flows, J. Fluid Mech. 238 (1992) 155-185.

[125] P. Moin, J. Kim, Numerical investigation of turbulent channel flow, J. Fluid Mech. 118 (1982) 341-377.

[126] M. Martin, U. Piomelli, G. Candler, A PRIORI TEST OF SGS MODELS IN COMPRESSIBLE TURBULENCE, Proceedings of the 3rd ASME/JSME Joint Fluid Engineering Conference, , San Francisco, California, USA, 1999.

[127] M. Germano, U. Piomelli, P. Moin, W.H. Cabot, A dynamic subgrid‐scale eddy viscosity model, Physics of Fluids A: Fluid Dynamics 3 (7) (1991) 1760-1765.

[128] A. Juneja, J.G. Brasseur, Characteristics of subgrid-resolved-scale dynamics in anisotropic turbulence, with application to rough-wall boundary layers, Phys. Fluids 11 (10) (1999) 3054-3068.

[129] M. Germano, Turbulence: the filtering approach, J. Fluid Mech. 238 (1992) 325-336.

[130] D.K. Lilly, A proposed modification of the Germano subgrid‐scale closure method, Physics of Fluids A: Fluid Dynamics 4 (3) (1992) 633-635.

[131] J.C. Oefelein, V. Yang, Modeling high-pressure mixing and combustion processes in liquid rocket engines, J. Propul. Power 14 (5) (1998) 843-857.

[132] M. Masquelet, S. Menon, Large-eddy simulation of flame-turbulence interactions in a shear coaxial injector, J. Propul. Power 26 (5) (2010) 924-935.

[133] A. Klimenko, Multicomponent diffusion of various admixtures in turbulent flow, Fluid Dynamics 25 (3) (1990) 327-334.

[134] R. Bilger, Conditional moment closure for turbulent reacting flow, Physics of Fluids A: Fluid Dynamics 5 (2) (1993) 436-444.

[135] N. Peters, Turbulent combustion, Cambridge University Press, Cambridge, England, 2000.

[136] A.R. KERSTEIN, Linear-eddy modeling of turbulent transport. Part 4. Structure of diffusion flames, Combust. Sci. Technol. 81 (1-3) (1992) 75-96.

[137] A.R. Kerstein, Linear-eddy modelling of turbulent transport. Part 7. Finite-rate chemistry and multi-stream mixing, J. Fluid Mech. 240 (1992) 289-313.

[138] P. McMurtry, S. Menon, A. Kerstein, Linear eddy modeling of turbulent combustion, Energy & fuels 7 (6) (1993) 817-826.

[139] J. Légier, T. Poinsot, D. Veynante, Dynamically thickened flame LES model for premixed and non-premixed turbulent combustion, Proceedings of the Summer Program, 2000, 12.

[140] P.E. DesJardin, S.H. Frankel, Large eddy simulation of a nonpremixed reacting jet: Application and assessment of subgrid-scale combustion models, Phys. Fluids 10 (9) (1998) 2298-2314.

[141] A.W. Cook, J.J. Riley, Subgrid-scale modeling for turbulent reacting flows, Combust. Flame 112 (4) (1998) 593-606.

[142] S.S. Girimaji, Y. Zhou, Analysis and modeling of subgrid scalar mixing using numerical data, Phys. Fluids 8 (5) (1996) 1224-1236.

[143] H. Pitsch, E. Riesmeier, N. Peters, Unsteady flamelet modeling of soot formation in turbulent diffusion flames, Combust. Sci. Technol. 158 (1) (2000) 389-406.

[144] T. Poinsot, D. Veynante, Theoretical and numerical combustion, Edwards, Philadelphia, 2005.

[145] H. Huo, X. Wang, V. Yang, A general study of counterflow diffusion flames at subcritical and supercritical conditions: Oxygen/hydrogen mixtures, Combust Flame (2014).

[146] X. Wang, H. Huo, V. Yang, Counterflow Diffusion Flames of Oxygen and N-Alkane Hydrocarbons (CH4-C16H34) at Subcritical and Supercritical Conditions, Combust Sci Technol 187 (1-2) (2014) 60-82.

[147] H. Pitsch, N. Peters, A consistent flamelet formulation for non-premixed combustion considering differential diffusion effects, Combust Flame 114 (1-2) (1998) 26-40.

[148] G. Ribert, N. Zone, V. Yang, L. Pons, N. Darabiha, S. Candel, Counterflow Diffusion Flames of General Fluids: Oxygen/Hydrogen Mixtures, 45th AIAA Aerospace Sciences Meeting and Exhibit, Reno, NV, 8-11 Jan. 2007, 2007, American Institute of Aeronautics and Astronautics, 1801 Alexander Bell Drive, Suite 500, Reston, VA, 20191-4344, USA, [URL:http://www.aiaa.org].

[149] Y.H. Choi, C.L. Merkle, The Application of Preconditioning in Viscous Flows, Journal of Computational Physics 105 (2) (1993) 207-223.

[150] J.S. Shuen, K.H. Chen, Y.H. Choi, A Coupled Implicit Method for Chemical Nonequilibrium Flows at All Speeds, Journal of Computational Physics 106 (2) (1993) 306-318.

[151] E. Turkel, Review of Preconditioning Methods for Fluid-Dynamics, Applied Numerical Mathematics 12 (1-3) (1993) 257-284.

[152] S.Y. Hsieh, V. Yang, A preconditioned flux-differencing scheme for chemically reacting flows at all Mach numbers, Int J Comput Fluid D 8 (1) (1997) 31-49.

[153] N. Zong, V. Yang, An efficient preconditioning scheme for real-fluid mixtures using primitive pressure-temperature variables, International Journal of Computational Fluid Dynamics 21 (5-6) (2007) 217-230.

[154] N. Zong, Modeling and simulation of cryogenic fluid injection and mixing dynamics under supercritical conditions, Thesis (Ph D), Pennsylvania State University, 2005.

[155] P.E.O. Buelow, Convergence enhancement of Euler and Navier-Stokes algorithms, Thesis (Ph D), Pennsylvania State University., 1995.

[156] S. Venkateswaran, C. Merkle, Dual time-stepping and preconditioning for unsteady computations, 33rd Aerospace Sciences Meeting and Exhibit, 1995, 78.

[157] P.E.O. Buelow, S. Venkateswaran, C.L. Merkle, Effect of Grid Aspect Ratio on Convergence, AIAA Journal 32 (12) (1994) 2401-2408.

[158] K.A. Hoffmann, S.T. Chiang, Computational fluid dynamics, Engineering Education System, Wichita, Kan., 1998.

[159] W. Kordulla, M. Vinokur, Efficient Computation of Volume in Flow Predictions, Aiaa Journal 21 (6) (1983) 917-918.

[160] M. RAI, S. Chakrvarthy, Conservative high-order-accurate finite-difference methods for curvilinear grids, 11th Computational Fluid Dynamics Conference, 1993, 3380.

[161] A. Fosso, H. Deniau, F. Sicot, P. Sagaut, Curvilinear finite-volume schemes using high-order compact interpolation, Journal of Computational Physics 229 (13) (2010) 5090-5122.

[162] R.C. Swanson, E. Turkel, On Central-Difference and Upwind Schemes, Journal of Computational Physics 101 (2) (1992) 292-306.

[163] P. Jorgenson, E. Turkel, Central Difference Tvd Schemes for Time-Dependent and Steady-State Problems, Journal of Computational Physics 107 (2) (1993) 297-308.

[164] S. Apte, V. Yang, Unsteady flow evolution in porous chamber with surface mass injection, part 1: Free oscillation, AIAA Journal 39 (8) (2001) 1577-1586.

[165] T.J. Poinsot, S.K. Lele, Boundary-Conditions for Direct Simulations of Compressible Viscous Flows, Journal of Computational Physics 101 (1) (1992) 104-129.

[166] D.H. Rudy, J.C. Strikwerda, A Nonreflecting Outflow Boundary-Condition for Subsonic Navier-Stokes Calculations, Journal of Computational Physics 36 (1) (1980) 55-70.

[167] M. Baum, T. Poinsot, D. Thevenin, Accurate Boundary-Conditions for Multicomponent Reactive Flows, Journal of Computational Physics 116 (2) (1995) 247-261.

[168] Y. Ju, W. Sun, Plasma assisted combustion: Progress, challenges, and opportunities, Combust. Flame 162 (3) (2015) 529-532.

[169] Y. Ju, W. Sun, Plasma assisted combustion: Dynamics and chemistry, Prog. Energy Combust. Sci. 48 (2015) 21-83.

[170] W. Sun, Y. Ju, Nonequilibrium Plasma-Assisted Combustion: A Review of Recent Progress, J. Plasma Fusion Res. 89 (4) (2013) 208-219.

[171] T. Ombrello, Y. Ju, Kinetic Ignition Enhancement of H2 Versus Fuel-Blended Air Diffusion Flames Using Nonequilibrium Plasma, IEEE Trans. Plasma Sci. 36 (6) (2008) 2924-2932.

[172] S. Yang, S. Nagaraja, W. Sun, V. Yang, A Detailed Comparison of Thermal and Nanosecond Plasma Assisted Ignition of Hydrogen-Air Mixtures, 53rd AIAA Aerospace Sciences Meeting (Jan. 2015), AIAA Paper 2015-1615.

[173] S. Nagaraja, V. Yang, Z. Yin, I. Adamovich, Ignition of hydrogen–air mixtures using pulsed nanosecond dielectric barrier plasma discharges in plane-to-plane geometry, Combust. Flame 161 (4) (2014) 1026-1037.

[174] W. Sun, M. Uddi, T. Ombrello, S.H. Won, C. Carter, Y. Ju, Effects of non-equilibrium plasma discharge on counterflow diffusion flame extinction, Proc. Combust. Inst. 33 (2) (2011) 3211-3218.

[175] S.H. Won, M.S. Cha, C.S. Park, S.H. Chung, Effect of electric fields on reattachment and propagation speed of tribrachial flames in laminar coflow jets, Proc. Combust. Inst. 31 (1) (2007) 963-970.

[176] H. Oshia, I. Kimura, H. Horisawa, Control of Soot Emission of a Turbulent Diffusion Flame by DC or AC Corona Discharges, Combust. Flame 116 (4) (1999) 653-661.

[177] M. Cha, S. Lee, K. Kim, S. Chung, Soot suppression by nonthermal plasma in coflow jet diffusion flames using a dielectric barrier discharge, Combust. Flame 141 (4) (2005) 438-447.

[178] Z. Yin, I.V. Adamovich, W.R. Lempert, OH radical and temperature measurements during ignition of H2-air mixtures excited by a repetitively pulsed nanosecond discharge, Proc. Combust. Inst. 34 (2) (2013) 3249-3258.

[179] Z. Yin, A. Montello, C.D. Carter, W.R. Lempert, I.V. Adamovich, Measurements of temperature and hydroxyl radical generation/decay in lean fuel–air mixtures excited by a repetitively pulsed nanosecond discharge, Combust. Flame 160 (9) (2013) 1594-1608.

[180] J.K. Lefkowitz, B.C. Windom, W. MacDonald, S. Adams, T. Chen, M. Uddi, Y. Ju, Time Dependent Measurements of Species Formation in Nanosecond-Pulsed Plasma Discharges in C2H4/O2/Ar Mixtures, 52nd AIAA Aerospace Science Meeting (2014), 1179.

[181] J.K. Lefkowitz, M. Uddi, B. Windom, G.F. Lou, Y. Ju, In situ species diagnostics and kinetic study of plasma activated ethylene pyrolysis and oxidation in a low temperature flow reactor, Proc. Combust. Inst. 35 (2015) 3505-3512.

[182] S. Nagaraja, V. Yang, I. Adamovich, Multi-scale modelling of pulsed nanosecond dielectric barrier plasma discharges in plane-to-plane geometry, J. Phys. D: Appl. Phys. 46 (15) (2013) 155205.

[183] S. Yang, X. Gao, V. Yang, W. Sun, S. Nagaraja, J.K. Lefkowitz, Y. Ju, Nanosecond Pulsed Plasma Activated C2H4/O2/Ar Mixtures in a Flow Reactor, J. Propul. Power 32 (5) (2016) 1240-1252.

[184] Y. Zhang, S. Yang, W. Sun, V. Yang, Effects of Non-Equilibrium Plasma Discharge on Ignition and LTC of DME/O2/Ar Mixtures: A Numerical Investigation, 10th U. S. National Combustion Meeting (2017), usncm10-1F05.

[185] W. Sun, S.H. Won, X. Gou, Y. Ju, Multi-scale modeling of dynamics and ignition to flame transitions of high pressure stratified n-heptane/toluene mixtures, Proc. Combust. Inst. 35 (1) (2015) 1049-1056.

[186] S. Nagaraja, V. Yang, A 'frozen electric-field' approach to simulate repetitively pulsed nanosecond plasma discharges and ignition of hydrogen–air mixtures, J. Phys. D: Appl. Phys. 47 (38) (2014) 385201.

[187] M.P. Burke, M. Chaos, Y. Ju, F.L. Dryer, S.J. Klippenstein, Comprehensive H2/O2 kinetic model for high‐pressure combustion, Int. J. Chem. Kinet. 44 (7) (2012) 444-474.

[188] P. Diévart, X. Yang, T. Tan, N. Labee, S. Klippenstein, Y. Georgievski, L. Harding, R. Sivaramakrishnan, W. Liu, M. Davis, On the Pyrolysis and Oxidation Chemistry of Methyl Formate and Methanol, Combust. Flame (2014).

[189] X. Shen, X. Yang, J. Santner, J. Sun, Y. Ju, Experimental and kinetic studies of acetylene flames at elevated pressures, Proc. Combust. Inst. 35 (1) (2015) 721-728.

[190] S. Pancheshnyi, B. Eismann, G. Hagelaar, L. Pitchford, Computer code ZDPlasKin, University of Toulouse, LAPLACE, CNRS-UPS-INP, Toulouse, France, 2008.

[191] W. Sun, M. Uddi, S.H. Won, T. Ombrello, C. Carter, Y. Ju, Kinetic effects of non-equilibrium plasma-assisted methane oxidation on diffusion flame extinction limits, Combust. Flame 159 (1) (2012) 221-229.

[192] T.J. Poinsot, S.K. Lele, Boundary conditions for direct simulations of compressible viscous flows, J. Comput. Phys. 101 (1) (1992) 104-129.

[193] R.H. Kraichnan, Diffusion by a random velocity field, Phys. Fluids 13 (1) (1970) 22-31.

[194] S. Ferraris, J.X. Wen, LES of the sandia flame D using laminar flamelet decomposition for conditional source-term estimation, Flow, turbulence and combustion 81 (4) (2008) 609-639.

[195] M.E. Mueller, G. Iaccarino, H. Pitsch, Chemical kinetic uncertainty quantification for large eddy simulation of turbulent nonpremixed combustion, Proc. Combust. Inst. 34 (1) (2013) 1299-1306.

[196] X. Xu, Y. Chen, H. Wang, Detailed numerical simulation of thermal radiation influence in Sandia flame D, Int. J. Heat Mass Transfer 49 (13) (2006) 2347-2355.

[197] A. Vreman, B. Albrecht, J. Van Oijen, L. De Goey, R. Bastiaans, Premixed and nonpremixed generated manifolds in large-eddy simulation of Sandia flame D and F, Combust. Flame 153 (3) (2008) 394-416.

[198] V. Raman, H. Pitsch, A consistent LES/filtered-density function formulation for the simulation of turbulent flames with detailed chemistry, Proc. Combust. Inst. 31 (2) (2007) 1711-1719.

[199] M. Nik, S. Yilmaz, P. Givi, M. H. Sheikhi, S. Pope, Simulation of Sandia flame D using velocity-scalar filtered density function, AIAA J. 48 (7) (2010) 1513-1522.

[200] V. Hiremath, S.R. Lantz, H. Wang, S.B. Pope, Large-scale parallel simulations of turbulent combustion using combined dimension reduction and tabulation of chemistry, Proc. Combust. Inst. 34 (1) (2013) 205-215.

[201] R. Mustata, L. Valiño, C. Jiménez, W. Jones, S. Bondi, A probability density function Eulerian Monte Carlo field method for large eddy simulations: application to a turbulent piloted methane/air diffusion flame (Sandia D), Combust. Flame 145 (1) (2006) 88-104.

[202] W. Jones, V. Prasad, Large Eddy Simulation of the Sandia Flame Series (D–F) using the Eulerian stochastic field method, Combust. Flame 157 (9) (2010) 1621-1636.

[203] R.S. Barlow, J.H. Frank, Effects of turbulence on species mass fractions in methane/air jet flames, Symposium (International) on Combustion 27 (1) (1998) 1087-1095.

[204] S. Coogan, X. Gao, A. McClung, W. Sun, Evaluation of Kinetic Mechanisms for Direct Fired Supercritical Oxy-Combustion of Natural Gas, ASME Turbo Expo 2016: Turbomachinery Technical Conference and Exposition (Jun. 2016), Paper GT2016-56658.

[205] X. Gao, Y. Zhang, S. Adusumilli, J. Seitzman, W. Sun, T. Ombrello, C. Carter, The effect of ozone addition on laminar flame speed, Combust. Flame 162 (10) (2015) 3914-3924.

[206] V.R. Katta, W.M. Roquemore, Evaluation of Kinetics Models for JP-8 in Predicting Unsteady Flames, 55th AIAA Aerospace Sciences Meeting (Jan. 2017), AIAA Paper 2017-0608.

[207] L.K. Su, N.T. Clemens, The structure of fine-scale scalar mixing in gas-phase planar turbulent jets, J. Fluid Mech. 488 (2003) 1-29.

[208] P. Sripakagorn, S. Mitarai, G. Kosály, H. Pitsch, Extinction and reignition in a diffusion flame: a direct numerical simulation study, J. Fluid Mech. 518 (2004) 231-259.

[209] D. Veynante, L. Vervisch, Turbulent combustion modeling, Prog. Energy Combust. Sci. 28 (3) (2002) 193-266.

[210] F. Perini, E. Galligani, R.D. Reitz, An analytical Jacobian approach to sparse reaction kinetics for computationally efficient combustion modeling with large reaction mechanisms, Energy & Fuels 26 (8) (2012) 4804-4822.

[211] K.E. Niemeyer, N.J. Curtis, C.-J. Sung, pyJac: Analytical Jacobian generator for chemical kinetics, Comput. Phys. Commun. 215 (2017) 188-203.

[212] S. Yang, Y. Li, X. Wang, U. Unnikrishnan, V. Yang, W. Sun, Comparison of Tabulation and Correlated Dynamic Evaluation of Real Fluid Properties for Supercritical Mixing and Combustion, 53rd AIAA/SAE/ASEE Joint Propulsion Conference (Jul. 2017).

[213] H. Wu, M. Ihme, Compliance of combustion models for turbulent reacting flow simulations, Fuel 186 (2016) 853-863.

[214] B.A. Perry, M.E. Mueller, A Flamelet Modeling Approach for Multi-Modal Combustion with Inhomogeneous Inlets, APS Meeting Abstracts, 2016.

[215] H. Pitsch, Improved pollutant predictions in large-eddy simulations of turbulent non-premixed combustion by considering scalar dissipation rate fluctuations, Proc. Combust. Inst. 29 (2) (2002) 1971-1978.

[216] B.A. Perry, M.E. Mueller, A.R. Masri, A two mixture fraction flamelet model for large eddy simulation of turbulent flames with inhomogeneous inlets, Proc. Combust. Inst. (2016).

[217] G. Ribert, L. Vervisch, P. Domingo, Y.-S. Niu, Hybrid transported-tabulated strategy to downsize detailed chemistry for numerical simulation of premixed flames, Flow, turbulence and combustion 92 (1-2) (2014) 175-200.